James Cook University
College of Science & Engineering
Mechanical Engineering

Conjugate natural convection boundary layers

Mehdi Khatamifar

Submitted in part fulfilment of the requirements for the degree of
Doctor of Philosophy in the College of Science & Engineering
James Cook University, January 2018

Statement of access

I, the undersigned, author of this work, understand that James Cook University will make this thesis available for use within the University Library and, via the Australian Digital Theses network, for use elsewhere.

I understand, that, as an unpublished work, a thesis has significant protection under the Copyright Act and;

I do not wish to place any further restriction on access to this work.

Mehdi Khatamifar

January 18, 2018

Statement of sources declaration

I declare that this thesis is my own work and has not been submitted in any form for another degree or diploma at any university or other institution of tertiary education. Information derived from the published or unpublished work of others has been acknowledged in the text and a list of references is given.

Mehdi Khatamifar

January 18, 2018

Electronic copy

I, the undersigned and author of this work, declare that the electronic copy of this thesis provided to the James Cook University Library is an accurate copy of the print thesis submitted, within the limits of the technology available.

Mehdi Khatamifar

January 18, 2018

Statement of the contribution of others

This thesis has been made possible through the support of the following people:

Supervisors	
	Principal Supervisor: 1. Professor Wenxian Lin, School Science & Engineering, James Cook University Co-Supervisors: 1. Dr. David Holmes, School Science & Engineering, Queensland University of Technology 2. Professor Steven W. Armfield, School of Aerospace, Mechanical and Mechatronic Engineering, The University of Sydney 3. Associate Professor Michael Kirkpatrick, School of Aerospace, Mechanical and Mechatronic Engineering, The University of Sydney
Financial Assistance	
	1. James Cook University Postgraduate Research Scholarship (JCUPRS) 2. Australian Research Council (ARC) Scholarship

Abstract

In this study, the unsteady behavior of conjugate natural convection flow and heat transfer in a differentially-heated square cavity divided by a partition with finite thickness and thermal conductivity is studied using direct numerical simulation. A series of numerical simulation is carried out for three values of dimensionless partition thickness (*i.e.*, $T_P = 0.05, 0.1$, and 0.2), two values of dimensionless partition position (*i.e.*, $X_P = 0.25$ and 0.5), five values of the thermal conductivity ratio (*i.e.*, $k_r = 0.1, 1, 100, 500$ and 1000) and six values of the Rayleigh value (*i.e.*, $Ra = 10^3, 10^4, 10^5, 10^6, 10^7$ and 10^8). For all these cases, the aspect ratio of the cavity $A = H/L = 1$, and the Prandtl number $Pr = 0.71$ were used.

A computer code written in Visual $C\#$ programming language is developed in this study for all numerical simulations. The code operates by solving the conservation equations for heat, mass and momentum with the finite volume method. The main variables used throughout the code are velocities and pressure, and the SIMPLE algorithm is employed to solve the velocity and pressure fields. Each equation can be solved by TDMA (as a default algorithm) or other methods. The developed code can solve steady/unsteady, compressible/incompressible, and turbulent/laminar flows in a Cartesian coordinate system. The nomenclature of the TEACH code (originated at the Imperial Collage) is mainly used in this code to increase readability. To further improve the readability of this code, the code structure has been designed to have separate and independent sections. Another code has been written in Visual $C\#$ to do the post-processing of data using already produced binary files by the main code. The code is verified and validated against the published results of partitioned (data from two studies) and non-partitioned (data from 14 studies) cavities.

Empirical correlations are developed for the average Nusselt number by the iterative non-linear curve fitting (*i.e.*, the Levenberg-Marquardt algorithm) which include the effects of Ra, T_P and X_P. It is found that the effect of X_P is negligible. For high k_r cases, the number of isotherms in the partition is very low or is not present. The low temperature difference in the partition leads to a negligible heat flux through the partition. In this situation, the partition can be considered as an isothermal wall and the heat transfer characteristics are similar to those of non-partitioned cavity cases, and consequently, the scaling relations for isothermals of a non-partitioned cavity can be used. However, higher temperature gradients are present in the partition in the low k_r cases, compared to that in the high k_r cases. Therefore, the temperature

difference between the left and right sides of the partition is dependent on both k_r and T_P. In this situation, the thermal behavior of the partition shifts from an isothermal wall like to isoflux wall type. This type of partition has uniform heat flux, and the thermal resistance parameter role becomes important and the scaling relations extracted for isoflux wall in a non-partitioned cavity are more appropriate.

The overall behaviour of Nu_{Ave} as k_r varies is identified to have three distinctive regions; thermal resistance, thermal transient and isothermal regions. The effect of T_P on Nu_{Ave} is trivial for low Ra values. T_P and k_r have opposite effects on the thermal resistance parameter of the partition. Therefore, there is a point where k_r nullifies the effect of T_P and the increased thermal conductivity of the partition overcomes the thermal damping effect of the partition thickness. This situation happened around $k_r = 100$ for both the centrally positioned and off-centre partitioned cavities.

The transient Nu_{Ave} at the hot sidewall (or cold sidewall) of a centrally partitioned cavity characterized by four regimes; conduction, quasi-steady, decaying and steady-state regimes. For cavities with off-centre partitions (in this study partition is close to the hot sidewall) this classification is different. The cold sidewall was characterized by the same four regimes presented for a centrally partitioned cavity. However, for the hot sidewall, a regime identified after decaying region and is called filling regime. Consequently, the five distinct regimes of Nu_{Ave} at the hot wall of an off-centre partitioned cavity are conduction, quasi-steady, decaying, filling and steady-state.

List of Associated Publications

Refereed Journal Papers

1. M. Khatamifar, W. Lin, S. W. Armfield, D. Holmes, M. P. Kirkpatrick, Conjugate natural convection heat transfer in a partitioned differentially-heated square cavity, *International Communications in Heat and Mass Transfer*, $81 : 92 - 103$, 2017.

2. M. Khatamifar, E. L. Wood, W. Lin, S. W. Armfield, D. Holmes, M. P. Kirkpatrick, A multigrid accelerated code for simulating unsteady conjugate natural convection boundary layers, *Applied Mechanics & Materials*, $846 : 30 - 35$, 2016.

Refereed Conference Papers

1. M. Khatamifar, W. Lin, D. Holmes, S. W. Armfield, and M. P. Kirkpatrick. Transient laminar conjugate natural convection in a cavity with a finite thickness and conductivity partition, *In Proceedings of the* 20^{th} *Australasian Fluid Mechanics Conference*, pp. $1 - 4$. Australasian Fluid Mechanics Society, Perth, Australia, 2016.

2. M. Khatamifar, R. DUrso, W. Lin, D. Holmes, S. W. Armfield, and M. P. Kirkpatrick. A numerical and experimental study on the unsteady conjugate natural convection boundary layers in a water filled rectangular cavity with a conducting partition wall at varied locations. *In Proceedings of the* 19^{th} *Australasian Fluid Mechanics Conference*, pp. $1 - 4$. Australasian Fluid Mechanics Society, Melbourne, Australia, 2014.

Papers In Preparation

1. M. Khatamifar, W. Lin, S. W. Armfield, D. Holmes, M. P. Kirkpatrick, Transient conjugate natural convection flow and heat transfer in a differentially-heated, partitioned square cavity with finite thickness and conductivity.

2. M. Khatamifar, W. Lin, S. W. Armfield, D. Holmes, M. P. Kirkpatrick, Effect of partition characteristics on the conjugate natural convection boundary layers in a water filled rectangular cavity.

Acknowledgements

Firstly, I would like to express my sincere gratitude to my supervisor Prof. Wenxian Lin for the continuous support during my Ph.D. study and related research, for his patience, motivation, and immense knowledge. His guidance helped me in all the time of research and writing of this thesis. I could not have imagined having a better advisor and mentor for my Ph.D. study.

Besides my advisor, I would like to thank the rest of my thesis committee: Prof. Steven W. Armfield, A/Prof. Michael Kirkpatrick, and Dr. David Holmes, for their insightful comments and encouragement, but also for the hard question which incented me to widen my research from various perspectives.

A very special gratitude goes out to all down at James Cook University and also Australian Research Council for helping and providing the funding for the work.

Many thanks also to all the staff at the Collage of Science and Engineering, the James Cook University, for creating a thoroughly enjoyable place to do research. There are several colleagues I would like to mention and to whom I am indebted: Mr. Liqiang Dong, Mr. Yuan Xiao, among many others.

I am grateful to my family: my parents, my wife, Hadis, and to my brother for supporting me spiritually throughout writing this thesis and my life in general.

Dedication

To my parents and my wife.

'The important work of moving the world forward does not wait to be done by perfect men.'

George Eliot

List of Symbols

Alphabet

A	aspect ratio of the cavity
Bo	Boussinesq number
f_n	dimensionless natural frequency of the time-varying temperature
g	acceleration due to gravity
Gr	Grashof number
H	height of the cavity
k_f	thermal conductivity of fluid
k_r	thermal conductivity ratio
k_s	thermal conductivity of partition
L	width of the cavity
p	dimensionless pressure
P_0	characteristic pressure
Pr	Prandtl number
Ra	Rayleigh value
Ra^*	modified Rayleigh value
S	source term

t time

T_0 characteristic temperature

T_c temperature of the cold sidewall

T_h temperature of the hot sidewall

T_p partition thickness

U, V velocity components in the X and Y directions

u, v dimensionless velocity components in the x and y directions

U_{ref} reference velocity

X, Y coordinates

x, y dimensionless coordinates

X_p partition distance from the left sidewall

Greek symbol

β_f coefficient of volumetric expansion of fluid

χ dimensionless thermal resistance

ΔT temperature difference between hot and cold sidewalls

ΔT^* temperature difference between sidewall and partition

Γ diffusion coefficient

κ_f thermal diffusivity of fluid

ν_f kinematic viscosity of fluid

ϕ transport variable

τ dimensionless time

θ dimensionless temperature

Contents

Abstract **xi**

List of Associated Publications **xiii**

Acknowledgements **xv**

1 Introduction **1**

1.1 Background 1

1.2 Problem description and motivation 6

1.3 Objectives 9

1.4 Thesis outline 10

2 Literature review **12**

2.1 Introduction 12

2.2 Natural convection over a vertical plate 13

2.2.1 In an initially thermally stratified fluid 13

2.2.2 In an initially constant temperature fluid 15

2.3 Natural convection in an open cavity 16

2.3.1 Numerical studies 16

2.3.2 Experimental studies 17

2.4 Natural convection in a closed cavity 18

2.4.1 Scaling analysis 18

2.4.2 Effect of the governing parameters and boundary conditions 19

2.4.3 Effect of cavity shape and inclination 22

2.4.4 Benchmark studies 25

2.4.5 Transient studies 25

2.4.6 Experimental studies 27

2.5 Conjugate natural convection heat transfer 30

2.6 Conjugate natural convection in closed cavity 33

2.6.1 Numerical studies 33

2.6.2 Experimental studies 36

3 Numerical method **39**

3.1 Introduction 39

3.2 Governing equations 39

3.3 Heat transfer analysis 42

3.4 Numerical method 44

3.4.1 Discretization of the governing equations 44

4 Numerical implementation **55**

4.1 Introduction 55

4.2 Code verification and validation 67

4.2.1 Non-partitioned cavity 67

4.2.2 Partitioned cavity 77

5 Steady-state natural convection in a partitioned cavity 81

5.1 Introduction 81

5.2 Centrally positioned partition 82

5.2.1 Qualitative analysis of flow and heat transfer behaviour 82

5.2.2 Quantitative analysis of flow and heat transfer behaviour 109

5.3 Off-centre partition 127

5.3.1 Qualitative analysis of flow and heat transfer behaviour 127

5.3.2 Quantitative analysis of flow and heat transfer behaviour 154

5.4 Empirical correlations for the average Nusselt number 166

6 Transient natural convection heat transfer in a partitioned cavity 170

6.1 Centrally positioned partition 170

6.2 Off-centre partition 185

7 Conclusion 204

7.1 Summary of Thesis Outcomes 204

7.2 Future Work 208

Bibliography 208

Appendix 240

A Variables in the code 241

B Code **245**

B.1 Horizontal velocity method (u) 245

B.2 Vertical velocity method (v) 253

B.3 Pressure method (p) 261

B.4 Temperature method (θ) 265

C TDMA method **272**

List of Tables

2.1 List of the selected studies on natural convection using scaling analysis. 20

2.2 List of the selected experimental studies on natural convection of nanofluids. . . 22

2.3 List of the selected studies on natural convection in cavities with different shapes. 24

2.4 List of the selected benchmark studies on natural convection in differentially heated cavities. 26

2.5 List of the selected experimental studies on natural convection. 30

2.6 List of some of studies on the conjugate natural convection. 36

4.1 Variable used in the code and their specifications 56

4.2 Grid independence tests. 68

4.3 Comparison between the average Nusselt number obtained from the present code and those available in the literature for a differentially heated square cavity at various Rayleigh values. 74

4.4 Comparison of the maximum horizontal velocity at the mid-width and its location obtained from the present code with those available in the literature for a differentially heated square cavity at various Rayleigh values. 75

4.5 Comparison of the maximum vertical velocity at the mid-height and its location obtained from the present code with those available in the literature for a differentially heated square cavity at various Rayleigh values. 75

4.6 Comparison of the maximum Nusselt number on the hot wall and its location obtained from the present code with those available in the literature for a differentially heated square cavity at various Rayleigh values. 76

4.7 Comparison of the minimum Nusselt number on the hot wall and its location obtained from the present code with those available in the literature for a differentially heated square cavity at various Rayleigh values. 76

4.8 Grid independence tests of a partitioned cavity. 78

4.9 Comparison between the average Nusselt number obtained from the present code and those available in the literature for a differentially heated partitioned cavity at various Rayleigh values. 80

5.1 Characteristics of the correlations presented in some previous studies. 167

A.1 Global variables in the code with their description. 241

A.2 Main local variables in the code with their description. 243

List of Figures

1.1 Common heat transfer modes and their performances [1]. 3

1.2 Schematic diagram of cooling electronic circuit (on the left) and its simplified geometry (on the right). 3

1.3 Schematic diagram of the reactor containment (on the left) and the simplified geometry (on the right) [2]. 4

1.4 Schematic diagram of a hollow block (on the left) and two adjacent rooms (on the right) and the simplified geometry (on the bottom). 5

1.5 Schematic diagram of a supertanker [3]. 6

1.6 Schematic of flow pattern in a differentially heated partitioned cavity. 8

1.7 Schematic of the computational domain and boundary conditions. 10

2.1 Schematic of natural convection over a vertical plate in an initially thermally stratified fluid. 13

2.2 Schematic of the conjugate natural convection boundary layer. 31

3.1 Schematic of the computational domain with initial and boundary conditions. . 40

3.2 Schematic presentation of heat transfer in a partitioned cavity. 43

3.3 The staggered mesh locations as well as the control volume used to descretise the governing equations. 44

3.4 Illustration of the extrapolation used in the Adams-Bashforth method. 46

3.5 Control volume and nodes for QUICK method. 48

3.6 The line by line procedure. 52

3.7 The SIMPLE Algorithm flowchart. 53

4.1 Flowchart for explaining main procedure of the code. 57

4.2 Grid mapping using a sin function. 58

4.3 Grid mapping using a linear function. 58

4.4 Grid quantities calculations. 59

4.5 Finding stretching factor of the grid in the x direction. 60

4.6 Drawing mesh pattern in the graphical outputs. 60

4.7 Allocating the partition in the mapped grid and evaluating the accuracy. 61

4.8 Piece of the code for initializing main variables. 62

4.9 Sample of the code for the pause section. 62

4.10 Calling main variable methods in the internal iteration. 63

4.11 Saving a variable (*e.g.* temperature) in a binary file by an appropriate name and address. 64

4.12 Saving a variable (*e.g.* PHI, a general name for any assigned variable) in a txt file by an appropriate name and address. 65

4.13 Flowchart for explaining the main procedure of the code. 66

4.14 Methods written for graphical representation of main variables. 66

4.15 Methods written for data saving and generating. 67

4.16 The grid distribution for a non-partitioned cavity with the mesh of 100×100. . 68

4.17 Time series of the average Nusselt number on the hot wall for the non-partitioned cavity at different meshes. 69

4.18 Time series of the average Nusselt number on the hot wall for the non-partitioned cavity for different time steps. 69

4.19 Schematic of the differentially heated cavity with the initial and boundary conditions. 71

4.20 Comparison of temperature contours presented by Corzo *et al.* [4] (left column) and by this study (right column) for a non-partitioned cavity. 72

4.21 Grid distribution for a partitioned cavity with the mesh of 100×100. 77

4.22 Time series of (a) the average Nusselt number on the hot wall and (b) temperature at $(0.05, 0.5)$ for different time steps of case the $T_P = 0.2$, $X_P = 0.5$, $k_r = 1000$, $Pr = 0.71$ and $Ra = 10^8$. 78

4.23 Comparison of temperature contours for $k_r = 1$ (top row) and $k_r = 100$ (bottom row) presented by Kahveci [5] (left column), Choi [2] (middle column) and the present study (right column) for $Ra = 10^6$. 79

4.24 Comparison of stream function contours for $k_r = 1$ (top row) and $k_r = 100$ (bottom row) presented by Kahveci [5] (left column), Choi [2] (middle column) and the present study (right column) for $Ra = 10^6$. 80

5.1 Temperature contours at $k_r = 0.1$ and $X_p = 0.5$ for different Ra values ($10^3 \leq Ra \leq 10^8$) and T_p ($T_p = 0.05$, 0.1 and 0.2). 85

5.2 Stream function contours at $k_r = 0.1$ and $X_p = 0.5$ for different Ra values ($10^3 \leq Ra \leq 10^8$) and T_p ($T_p = 0.05$, 0.1 and 0.2). 86

5.3 Temperature contours at $k_r = 1$ and $X_p = 0.5$ for different Ra values ($10^3 \leq Ra \leq 10^8$) and T_p ($T_p = 0.05$, 0.1 and 0.2). 87

5.4 Stream function contours at $k_r = 1$ and $X_p = 0.5$ for different Ra values ($10^3 \leq Ra \leq 10^8$) and T_p ($T_p = 0.05$, 0.1 and 0.2). 88

5.5 Temperature contours at $k_r = 100$ and $X_p = 0.5$ for different Ra values ($10^3 \leq Ra \leq 10^8$) and T_p ($T_p = 0.05$, 0.1 and 0.2). 89

5.6 Stream function contours at $k_r = 100$ and $X_p = 0.5$ for different Ra values ($10^3 \leq Ra \leq 10^8$) and T_p ($T_p = 0.05$, 0.1 and 0.2). 90

5.7 Temperature contours at $k_r = 500$ and $X_p = 0.5$ for different Ra values ($10^3 \leq Ra \leq 10^8$) and T_p ($T_p = 0.05$, 0.1 and 0.2). 91

5.8 Stream function contours at $k_r = 500$ and $X_p = 0.5$ for different Ra values ($10^3 \leq Ra \leq 10^8$) and T_p ($T_p = 0.05$, 0.1 and 0.2). 92

5.9 Temperature contours at $k_r = 1000$ and $X_p = 0.5$ for different Ra values ($10^3 \leq Ra \leq 10^8$) and T_p ($T_p = 0.05$, 0.1 and 0.2). 93

5.10 Stream function contours at $k_r = 1000$ and $X_p = 0.5$ for different Ra values ($10^3 \leq Ra \leq 10^8$) and T_p ($T_p = 0.05$, 0.1 and 0.2). 94

5.11 A schematic of the typical flow pattern in the upper left corner region of the rectangular cavity. 95

5.12 Dividing stream function in the left half-cavity. 95

5.13 Vertical velocity contours at $k_r = 0.1$ and $X_p = 0.5$ for different Ra values ($10^3 \leq Ra \leq 10^8$) and T_p ($T_p = 0.05$, 0.1 and 0.2). 99

5.14 Horizontal velocity contours at $k_r = 0.1$ and $X_p = 0.5$ for different Ra values ($10^3 \leq Ra \leq 10^8$) and T_p ($T_p = 0.05$, 0.1 and 0.2). 100

5.15 Vertical velocity contours at $k_r = 1$ and $X_p = 0.5$ for different Ra values ($10^3 \leq Ra \leq 10^8$) and T_p ($T_p = 0.05$, 0.1 and 0.2). 101

5.16 Horizontal velocity contours at $k_r = 1$ and $X_p = 0.5$ for different Ra values ($10^3 \leq Ra \leq 10^8$) and T_p ($T_p = 0.05$, 0.1 and 0.2). 102

5.17 Vertical velocity contours at $k_r = 100$ and $X_p = 0.5$ for different Ra values ($10^3 \leq Ra \leq 10^8$) and T_p ($T_p = 0.05$, 0.1 and 0.2). 103

5.18 Horizontal velocity contours at $k_r = 100$ and $X_p = 0.5$ for different Ra values ($10^3 \leq Ra \leq 10^8$) and T_p ($T_p = 0.05$, 0.1 and 0.2). 104

5.19 Vertical velocity contours at $k_r = 500$ and $X_p = 0.5$ for different Ra values ($10^3 \leq Ra \leq 10^8$) and T_p ($T_p = 0.05$, 0.1 and 0.2). 105

5.20 Horizontal velocity contours at $k_r = 500$ and $X_p = 0.5$ for different Ra values ($10^3 \leq Ra \leq 10^8$) and T_p ($T_p = 0.05$, 0.1 and 0.2). 106

5.21 Vertical velocity contours at $k_r = 1000$ and $X_p = 0.5$ for different Ra values ($10^3 \leq Ra \leq 10^8$) and T_p ($T_p = 0.05$, 0.1 and 0.2). 107

5.22 Horizontal velocity contours at $k_r = 1000$ and $X_p = 0.5$ for different Ra values ($10^3 \leq Ra \leq 10^8$) and T_p ($T_p = 0.05$, 0.1 and 0.2). 108

5.23 Horizontal temperature profiles at the mid-height ($y = 0.5$) for different values of Ra (10^3, 10^4, 10^5, 10^6, 10^7 and 10^8), k_r (0.1, 1, 100, 500 and 1000) and T_p (0.05, 0.1, and 0.2). 110

5.24 Average Nusselt number on the hot wall for a partitioned cavity with different partition thermal conductivity ratio ($1 \leq k_r \leq 1000$), $T_p = 0.1$ and $X_p = 0.5$ for $10^4 \leq Ra \leq 10^6$. 113

5.25 Average Nusselt number on the hot wall for a partitioned cavity with different partition thicknesses and thermal conductivity ratios for $10^3 \leq Ra \leq 10^8$. 114

5.26 Schematic representation of Nu_{Ave} behaviour as k_r changes. 115

5.27 The vertical profiles of the local Nusselt number on the hot sidewall for different values of Ra (10^3, 10^4, 10^5, 10^6, 10^7 and 10^8), k_r (0.1, 1, 100, 500 and 1000) and T_p (0.05, 0.1, and 0.2). 117

5.28 The vertical profiles of the local Nusselt number on the left side of partition ($x = X_p - 0.5T_p$) for different values of Ra (10^3, 10^4, 10^5, 10^6, 10^7 and 10^8), k_r (0.1, 1, 100, 500 and 1000) and T_p (0.05, 0.1, and 0.2). 119

5.29 Vertical temperature profiles on the left side of partition ($x = X_p - 0.5T_p$) and horizontal temperature drops ($\theta_{D,x}$) for different values of Ra (10^3, 10^4, 10^5, 10^6, 10^7 and 10^8), k_r (0.1, 1, 100, 500 and 1000), $X_p = 0.5$ and T_p (0.05, 0.1, and 0.2). 121

5.30 Horizontal temperature drop ($\theta_{D,x}$) for different values of Ra (10^3, 10^4, 10^5, 10^6, 10^7 and 10^8), k_r (0.1, 1, 100, 500 and 1000), $X_p = 0.5$ and T_p (0.05, 0.1, and 0.2). 123

5.31 Vertical temperature profiles on the middle of the centrally positioned partition for different values of Ra (10^3, 10^4, 10^5, 10^6, 10^7 and 10^8), k_r (0.1, 1, 100, 500 and 1000) and T_p (0.05, 0.1, and 0.2). 125

5.32 Vertical temperature drop ($\theta_{D,y}$) at the middle of the partition for different values of Ra (10^3, 10^4, 10^5, 10^6, 10^7 and 10^8), k_r (0.1, 1, 100, 500 and 1000) and T_p (0.05, 0.1, and 0.2). 126

5.33 Temperature contours at $k_r = 0.1$ and $X_p = 0.25$ for different Ra values ($10^3 \leq Ra \leq 10^8$) and T_p ($T_p = 0.05$, 0.1 and 0.2). 128

5.34 Stream function contours at $k_r = 0.1$ and $X_p = 0.25$ for different Ra values ($10^3 \leq Ra \leq 10^8$) and T_p ($T_p = 0.05$, 0.1 and 0.2). 129

5.35 Temperature contours at $k_r = 1$ and $X_p = 0.25$ for different Ra values ($10^3 \leq Ra \leq 10^8$) and T_p ($T_p = 0.05$, 0.1 and 0.2). 130

5.36 Stream function contours at $k_r = 1$ and $X_p = 0.25$ for different Ra values ($10^3 \leq Ra \leq 10^8$) and T_p ($T_p = 0.05$, 0.1 and 0.2). 131

5.37 Temperature contours at $k_r = 100$ and $X_p = 0.25$ for different Ra values ($10^3 \leq Ra \leq 10^8$) and T_p ($T_p = 0.05$, 0.1 and 0.2). 132

5.38 Stream function contours at $k_r = 100$ and $X_p = 0.25$ for different Ra values ($10^3 \leq Ra \leq 10^8$) and T_p ($T_p = 0.05$, 0.1 and 0.2). 133

5.39 Temperature contours at $k_r = 500$ and $X_p = 0.25$ for different Ra values ($10^3 \leq Ra \leq 10^8$) and T_p ($T_p = 0.05$, 0.1 and 0.2). 134

5.40 Stream function contours at $k_r = 500$ and $X_p = 0.25$ for different Ra values ($10^3 \leq Ra \leq 10^8$) and T_p ($T_p = 0.05$, 0.1 and 0.2). 135

5.41 Temperature contours at $k_r = 1000$ and $X_p = 0.25$ for different Ra values ($10^3 \leq Ra \leq 10^8$) and T_p ($T_p = 0.05$, 0.1 and 0.2). 136

5.42 Stream function contours at $k_r = 1000$ and $X_p = 0.25$ for different Ra values ($10^3 \leq Ra \leq 10^8$) and T_p ($T_p = 0.05$, 0.1 and 0.2). 137

5.43 Vertical velocity contours at $k_r = 0.1$ and $X_p = 0.25$ for different Ra values ($10^3 \leq Ra \leq 10^8$) and T_p ($T_p = 0.05$, 0.1 and 0.2). 142

5.44 Horizontal velocity contours at $k_r = 0.1$ and $X_p = 0.25$ for different Ra values ($10^3 \leq Ra \leq 10^8$) and T_p ($T_p = 0.05$, 0.1 and 0.2). 143

5.45 Vertical velocity contours at $k_r = 1$ and $X_p = 0.25$ for different Ra values ($10^3 \leq Ra \leq 10^8$) and T_p ($T_p = 0.05$, 0.1 and 0.2). 144

5.46 Horizontal velocity contours at $k_r = 1$ and $X_p = 0.25$ for different Ra values ($10^3 \leq Ra \leq 10^8$) and T_p ($T_p = 0.05$, 0.1 and 0.2). 145

5.47 Vertical velocity contours at $k_r = 100$ and $X_p = 0.25$ for different Ra values ($10^3 \leq Ra \leq 10^8$) and T_p ($T_p = 0.05$, 0.1 and 0.2). 146

5.48 Horizontal velocity contours at $k_r = 100$ and $X_p = 0.25$ for different Ra values ($10^3 \leq Ra \leq 10^8$) and T_p ($T_p = 0.05$, 0.1 and 0.2). 147

5.49 Vertical velocity contours at $k_r = 500$ and $X_p = 0.25$ for different Ra values ($10^3 \leq Ra \leq 10^8$) and T_p ($T_p = 0.05$, 0.1 and 0.2). 148

5.50 Horizontal velocity contours at $k_r = 500$ and $X_p = 0.5$ for different Ra values ($10^3 \leq Ra \leq 10^8$) and T_p ($T_p = 0.05$, 0.1 and 0.2). 149

5.51 Vertical velocity contours at $k_r = 1000$ and $X_p = 0.25$ for different Ra values ($10^3 \leq Ra \leq 10^8$) and T_p ($T_p = 0.05$, 0.1 and 0.2). 150

5.52 Horizontal velocity contours at $k_r = 1000$ and $X_p = 0.25$ for different Ra values ($10^3 \leq Ra \leq 10^8$) and T_p ($T_p = 0.05$, 0.1 and 0.2). 151

5.53 Horizontal temperature profiles at the mid-height ($y = 0.5$) of the case $X_p = 0.25$ for different values of Ra (10^3, 10^4, 10^5, 10^6, 10^7 and 10^8), k_r (0.1, 1, 100, 500 and 1000) and T_p (0.05, 0.1, and 0.2). 153

5.54 Average Nusselt number on the hot wall for an off-centre partitioned cavity with different partition thicknesses and thermal conductivity ratios for $10^3 \leq Ra \leq 10^8$.155

5.55 The vertical profiles of the local Nusselt number on the hot and cold sidewalls of the case $X_p = 0.25$ for different values of Ra (10^3, 10^4, 10^5, 10^6, 10^7 and 10^8), k_r (0.1, 1, 100, 500 and 1000) and T_p (0.05, 0.1, and 0.2). 157

5.56 The vertical profiles of the local Nusselt number on the both sides of the partition of the case $X_p = 0.25$ for different values of Ra (10^3, 10^4, 10^5, 10^6, 10^7 and 10^8), k_r (0.1, 1, 100, 500 and 1000) and T_p (0.05, 0.1, and 0.2). 158

5.57 Vertical temperature profiles on both sides of the partition of the case $X_p = 0.25$ for different values of Ra (10^3, 10^4, 10^5, 10^6, 10^7 and 10^8), k_r (0.1, 1, 100, 500 and 1000) and T_p (0.05, 0.1, and 0.2). 161

5.58 Horizontal temperature drop on the partition of the case $X_p = 0.25$ for different values of Ra (10^3, 10^4, 10^5, 10^6, 10^7 and 10^8), k_r (0.1, 1, 100, 500 and 1000) and T_p (0.05, 0.1, and 0.2). 163

5.59 Vertical temperature profiles at the middle of the partition ($x = X_p$) of the case $X_p = 0.25$ for different values of Ra (10^3, 10^4, 10^5, 10^6, 10^7 and 10^8), k_r (0.1, 1, 100, 500 and 1000) and T_p (0.05, 0.1, and 0.2). 164

5.60 Vertical temperature drop at the middle of partition of the case $X_p = 0.25$ for different values of Ra (10^3, 10^4, 10^5, 10^6, 10^7 and 10^8), k_r (0.1, 1, 100, 500 and 1000) and T_p (0.05, 0.1, and 0.2). 165

5.61 Average Nusselt number for three values of T_p (T_p = 0.05, 0.1, and 0.2), two values of X_p (X_p = 0.25 and 0.5), five values of k_r ($k_r = 0.1, 1, 100, 500$ and 1000) and six values of Ra ($Ra = 10^3, 10^4, 10^5, 10^6, 10^7$ and 10^8). 168

5.62 Comparison of the correlations for the average Nusselt number obtained in the current study with some others available over the Rayleigh number range considered for the case of $X_p = 0.5$, $r_k = 0.01(i.e., k_r = 100)$, $N = 1$ and $T_p = 0.05$. . 169

6.1 Regimes of transient Nu_{Ave} at the hot wall for the case of $X_p = 0.5$,$Ra = 10^8$, $k_r = 1000$ and $T_p = 0.2$. 172

6.2 Time series of average Nusselt number on the hot sidewall and the partition ($x = X_p - 0.5T_p$) of the case $X_p = 0.5$ for different values of Ra (10^3, 10^4, 10^5, 10^6, 10^7 and 10^8), k_r (0.1, 1, 100, 500 and 1000) and T_p (0.05, 0.1, and 0.2). . . . 173

6.3 Temperature contours of the case $k_r = 0.1$, $T_p = 0.1$, $Ra = 10^8$ and $X_p = 0.5$ at different times. 175

6.4 Temperature contours of the case $k_r = 1000$, $T_p = 0.1$, $Ra = 10^8$ and $X_p = 0.5$ at different times. 176

6.5 Time series of θ of the case $X_p = 0.5$ at $x = 0.05$ and $y = 0.5$ for different values of Ra (10^3, 10^4, 10^5, 10^6, 10^7 and 10^8), k_r (0.1, 1, 100, 500 and 1000) and T_p (0.05, 0.1, and 0.2). 178

6.6 Time series of $\theta_{D,x}$ at $y = 0.5$ of the case $X_p = 0.5$ for different values of Ra (10^3, 10^4, 10^5, 10^6, 10^7 and 10^8), k_r (0.1, 1, 100, 500 and 1000) and T_p (0.05, 0.1, and 0.2). 179

6.7 Time series of $\theta_{D,y}$ of the case $X_p = 0.5$ for different values of Ra (10^3, 10^4, 10^5, 10^6, 10^7 and 10^8), k_r (0.1, 1, 100, 500 and 1000) and T_p (0.05, 0.1, and 0.2). . . . 181

6.8 Position of u_{max} at the top half of the left half-cavity ($0 \leq x \leq X_p$ and $0.5 \leq y \leq 1$) and v_{max} at the left half of the left half-cavity ($0 \leq x \leq 0.25$ and $0 \leq y \leq 1$) by passing time for different values of Ra (10^3, 10^4, 10^5, 10^6, 10^7 and 10^8), k_r ($0.1(a,b)$, $1(c,d)$, $100(e,f)$, $500(g,h)$ and $1000(i,j)$) and T_p (0.05, 0.1, and 0.2). . 183

6.9 Position of the maximum stream function at the left half-cavity by passing time for different values of Ra (10^3, 10^4, 10^5, 10^6, 10^7 and 10^8), k_r (0.1, 1, 100, 500 and 1000) and T_p (0.05, 0.1, and 0.2). 184

6.10 Regimes of transient Nu_{Ave} at the hot and cold sidewalls for the case $X_p = 0.25$,$Ra = 10^8$, $k_r = 1000$ and $T_p = 0.2$. 187

6.11 Time series of the average Nusselt number on the cold and hot sidewalls and the partition ($x = X_p - 0.5T_p$) for the case of $X_p = 0.25$ and $T_p = 0.05$ for different values of Ra (10^3, 10^4, 10^5, 10^6, 10^7 and 10^8), k_r (0.1, 1, 100, 500 and 1000). . . 188

6.12 Time series of the average Nusselt number on the cold and hot sidewalls and the partition ($x = X_p - 0.5T_p$) for the case of $X_p = 0.25$ and $T_p = 0.1$ for different values of Ra (10^3, 10^4, 10^5, 10^6, 10^7 and 10^8), k_r (0.1, 1, 100, 500 and 1000). . . 189

6.13 Time series of the average Nusselt number on the cold and hot sidewalls and the partition ($x = X_p - 0.5T_p$) for the case of $X_p = 0.25$ and $T_p = 0.2$ for different values of Ra (10^3, 10^4, 10^5, 10^6, 10^7 and 10^8), k_r (0.1, 1, 100, 500 and 1000). . . 190

6.14 Temperature contours of the case $k_r = 0.1$, $T_p = 0.1$, $Ra = 10^8$ and $X_p = 0.25$ at different times. 193

6.15 Temperature contours of the case $k_r = 1000$, $T_p = 0.1$, $Ra = 10^8$ and $X_p = 0.25$ at different times. 194

6.16 Time series of θ of the case $X_p = 0.25$ at $x = 0.05$ and $y = 0.5$ for different values of Ra (10^3, 10^4, 10^5, 10^6, 10^7 and 10^8), k_r (0.1, 1, 100, 500 and 1000) and T_p (0.05, 0.1, and 0.2). 195

6.17 Time series of $\theta_{D,x}$ at $y = 0.5$ of the case $X_p = 0.25$ for different values of Ra (10^3, 10^4, 10^5, 10^6, 10^7 and 10^8), k_r (0.1, 1, 100, 500 and 1000) and T_p (0.05, 0.1, and 0.2). 197

6.18 Time series of $\theta_{D,y}$ of the case $X_p = 0.25$ for different values of Ra (10^3, 10^4, 10^5, 10^6, 10^7 and 10^8), k_r (0.1, 1, 100, 500 and 1000) and T_p (0.05, 0.1, and 0.2). . . . 198

6.19 Position of u_{max} at the top half of cavity ($0 \leq x \leq 1$ and $0.5 \leq y \leq 1$) by passing time for different values of Ra (10^3, 10^4, 10^5, 10^6, 10^7 and 10^8), k_r (0.1, 1, 100, 500 and 1000) and T_p (0.05, 0.1, and 0.2). 200

6.20 Position of v_{max} at the left half of the left half-cavity ($0 \leq x \leq 0.5(X_p - 0.5T_p)$) and the left half of the right half-cavity ($X_p \leq y \leq 0.5 + X_p - 0.25T_p$) by passing time for different values of Ra (10^3, 10^4, 10^5, 10^6, 10^7 and 10^8), k_r (0.1, 1, 100, 500 and 1000) and T_p (0.05, 0.1, and 0.2). 201

6.21 Position of the maximum stream function at the left and right half-cavities by passing time for different values of Ra (10^3, 10^4, 10^5, 10^6, 10^7 and 10^8), k_r (0.1, 1, 100, 500 and 1000) and T_p (0.05, 0.1, and 0.2). 203

Chapter 1

Introduction

1.1 Background

Natural convection is a result of the change in the density of a fluid. Such a density difference may be caused by a temperature difference, which is the most common case, or a concentration or phase difference in a fluid. With the presence of gravity, the fluid possesses buoyancy, which causes the motion of fluid without any externally applied force. It is customary for researchers to idealize natural convection problems present in nature or industry, with simple physical models, such as natural convection adjacent to horizontal or vertical thermal flat plates, in a differentially heated cavity or in a differentially heated partitioned cavity. Natural convection in a differentially heated partitioned cavity is widely present in various situations in nature and engineering, such as solar thermal systems, electronic equipment, chemical and nuclear reactors and buildings, to name just a few. Due to its fundamental significance and practical application importance, natural convection in a differentially heated partitioned cavity has attracted extensive research interest.

Electronic devices and equipment are now present in every aspect of our daily life. Electronic computers, as an example, play a crucial role in producing modern equipment and have various sizes, from the hand-held personal digital assistant to large-scale servers. In many cases, computers are embedded within some other devices controlling their functions. New techniques and

inventions lead to a trend towards higher circuit density. This increase needs further packaging density accompanied by increasing power dissipation per a circuit which is the main reason for the signal delay between communicating circuits. It is reported that the reliability of a silicon chip will be decreased by about 10% for every 2 $^{\circ}C$ temperature rise. In fact, the major cause of an electronic chip failure is the temperature rise (55%) and other factors have smaller effects such as vibration (20%), humidity (19%) and dust (6%) [6]. Therefore, the importance of cooling systems which enhances the module performance, and reliability is increasing. In addition, it is important not only to keep the maximum temperature of the circuit below a certain limit but also to maintain a uniform temperature. To meet the challenge of removing heat from the electronic devices, several different technologies have been suggested. Figure 1.1 graphically presents a comparison of common heat transfer modes and their performances. As figure 1.1 illustrates, natural convection is one of the cooling methods for electronic equipment. Although it has a small working range of heat flux (up to about $5W$ of power can be cooled effectively by natural convection [7]), it is desirable because of its simplicity and maintenance-free feature. There are many cases of embedded circuits in other equipment that can be simplified to a differentially heated partitioned cavity, as schematically illustrated in figure 1.2, as an example.

Another application is related to nuclear reactors [8–10]. The safety systems of a nuclear power plant are designed to protect the plant in the case of accidents and to minimize the radioactivity release. The hydrogen risk in light-water reactors can happen during severe accidents in which hydrogen can be generated by the metal-steam reaction. As containment is the last barrier to safety in a reactor, releasing hydrogen into the containment and forming combustible or even detonable gas mixture can impose the danger of destroying its integrity. Three main options considered to mitigate the hydrogen risk are inerting the containment atmosphere, mixing the containment atmosphere to prevent high local concentrations of hydrogen and consuming hydrogen by recombining or deliberate ignition [11–13]. The complex geometry and problem of the hydrogen risk in a reactor containment can be reduced to a scientific heat transfer test case of a differentially heated fully partitioned cavity. The schematic diagram of containment and the simplified geometry are shown in figure 1.3.

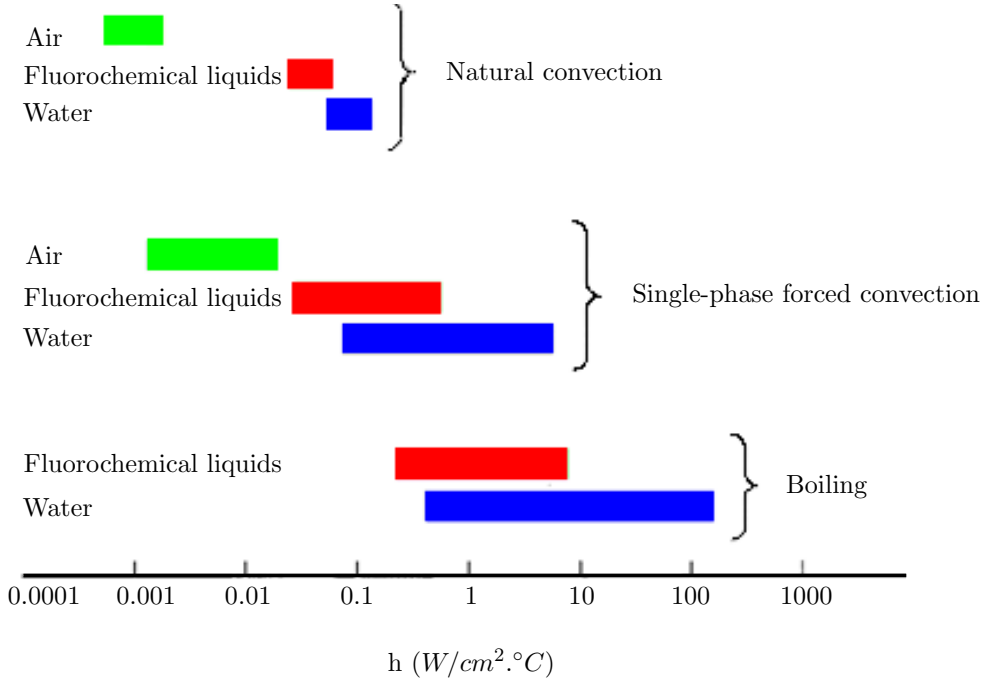

Figure 1.1: Common heat transfer modes and their performances [1].

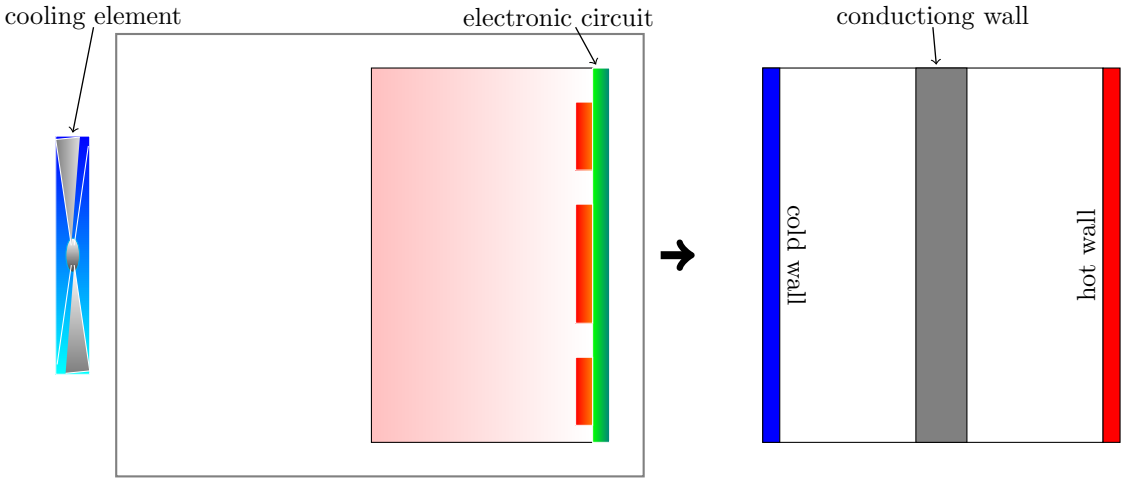

Figure 1.2: Schematic diagram of cooling electronic circuit (on the left) and its simplified geometry (on the right).

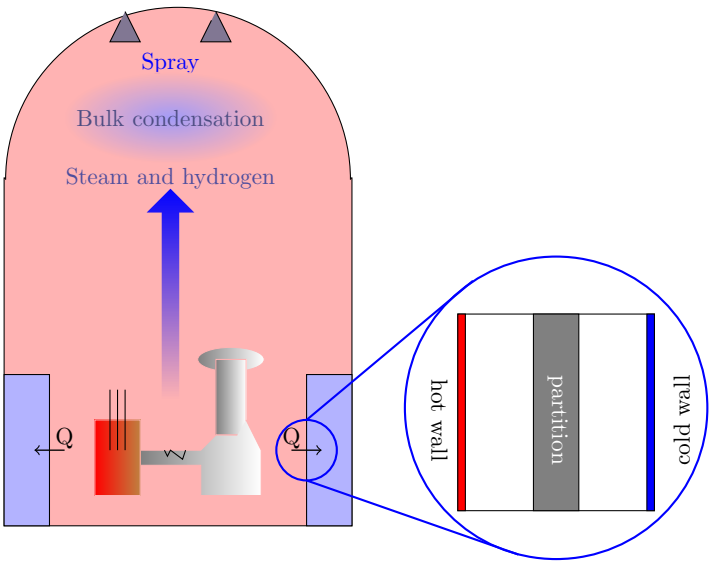

Figure 1.3: Schematic diagram of the reactor containment (on the left) and the simplified geometry (on the right) [2].

Moreover, the interaction between indoor spaces and the environment is highly influenced by the type of building materials, and a great amount of energy is consumed to compensate for the heat loss through building walls and ceilings. To achieve internal thermal comfort conditions, it is necessary to calculate cooling/heating load and specify the amount of heat that needs to be removed from or added to buildings. Many thermal element's arrangements in a building can be simplified by a differentially heated partitioned cavity. For instance, a typical hollow block used for walls can be a good example of a conjugate heat transfer system. The left and right side walls may have different temperatures, and typically a block has at least one wall in the middle (see, figure 1.4(a)) [14]. Two adjacent rooms in a building also can be considered as a system of conjugate heat transfer, as illustrated on a larger scale. The case of the heated left sidewall of the left room (by the sun for instance) and the cooled right sidewall of the right room (by Air conditioner) is illustrated in figure 1.4(b). The conjugate heat transfer happens between two neighboring rooms through the middle shared wall, which serves as a partition. There are many other parts of a building that can be simplified to a partitioned cavity [15–19].

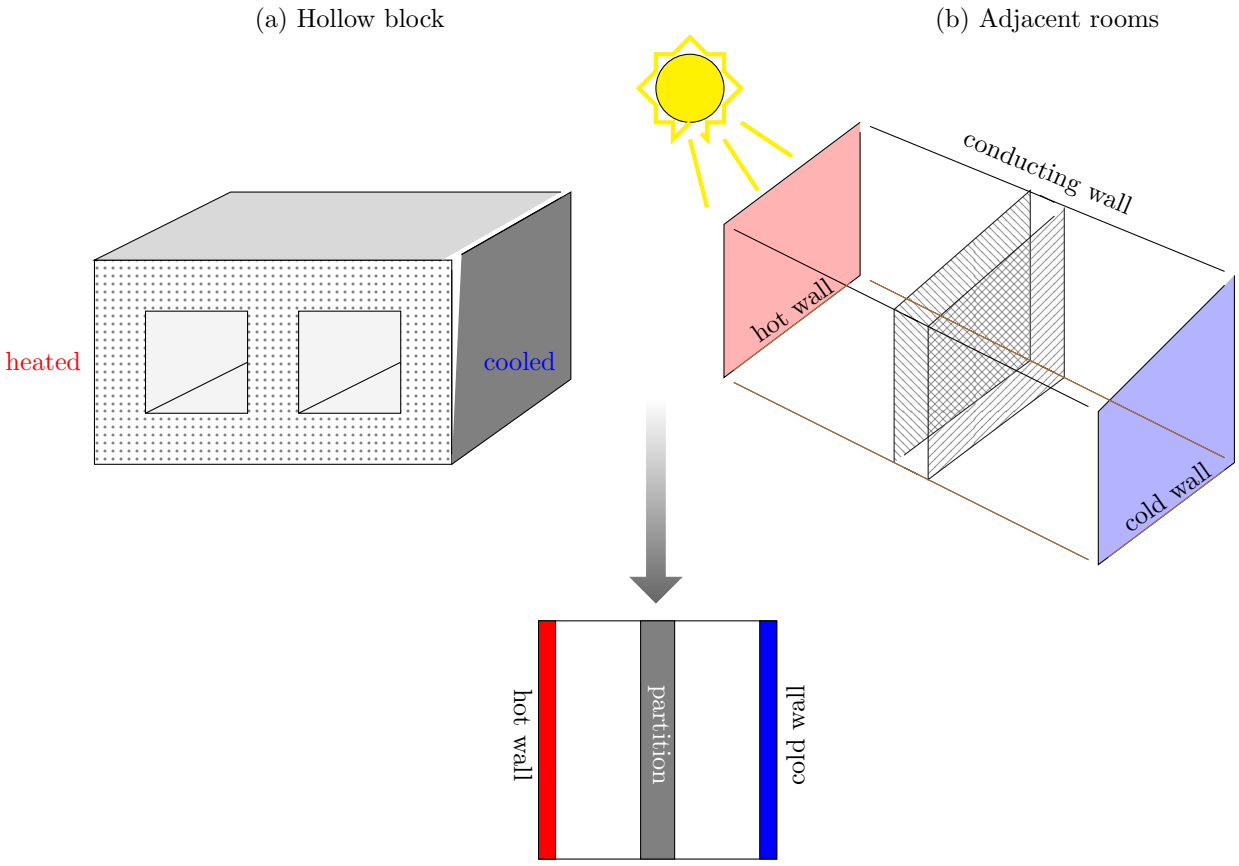

Figure 1.4: Schematic diagram of a hollow block (on the left) and two adjacent rooms (on the right) and the simplified geometry (on the bottom).

Heat transfer in a partitioned cavity is also useful for the specific cooling studies such as the cooling process of fuel oil in a wrecked ship. In 2002, the supertanker Prestige with more than $37,500Tm$ of heavy fuel oil inside the tanks sank off the northern coast of Spain. To prevent the oil spill from tanks, it is important to predict the fuel oil evolution inside the tanks of the sunken ship. For the supertanker Prestige, authorities needed to know if the fuel oil would be frozen in Atlantic Ocean (2.6 $°C$), if this was the case, how long it would take to reach this state. To do the numerical simulation, the thermal arrangement of a sunk fuel oil tank can be simplified to a differentially heated partitioned cavity [3]. Figure 1.5 illustrates the schematic of a supertanker and a simplified geometry of the tank.

All these cases require a full understanding of the transient flow and heat transfer in a differentially heated partitioned cavity. Although there are numerous studies on this topic, as will be reviewed in the next chapter, such an understanding is still in its early developing stage, which motivates this thesis.

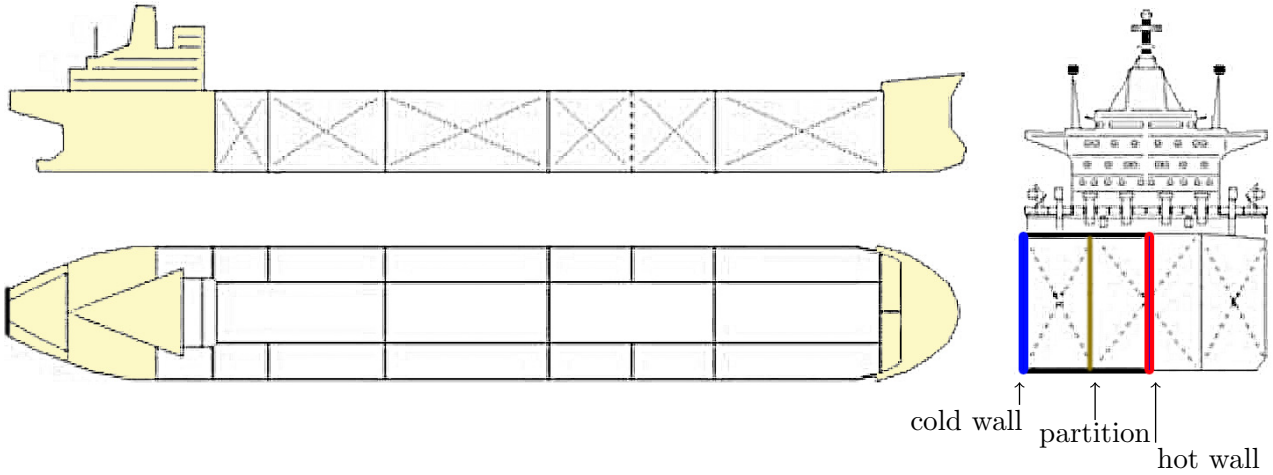

Figure 1.5: Schematic diagram of a supertanker [3].

1.2 Problem description and motivation

The physical system under consideration is a two-dimensional partitioned rectangular cavity (with height H and width L and the aspect ratio $A = H/L$), as illustrated in Figure 1.6. The

top and bottom walls of the cavity are adiabatic and the left and right opposing vertical sidewalls are isothermal fixed at temperatures T_h and T_c ($T_h > T_c$), respectively. A partition of thickness T_p is placed on the location X_p from the left wall (both T_p and X_p are dimensionless, made dimensionless by L). The working fluid is assumed to be air, which is initially quiescent and at a temperature of $(T_h + T_c)/2$ with a constant thermal conductivity (k_f). All the interior walls and the partition surfaces are rigid and no-slip. The partition wall is heat conducting, with finite thermal conductivity k_s. At a specific time, by abruptly heating/cooling the left/right vertical sidewall, a rising/falling natural convection boundary layer forms on the side walls of the cavity. By intensifying convective heat transfer, the Rayleigh value Ra is large enough, the sidewall natural convection boundary layer discharges heated/cooled fluid as a hot/cold intrusion below/over the ceiling/floor as shown in figure 1.6 (a). The created intrusions move from the sidewalls to the partition and impinge on it. Subsequently, a stratification and filling process starts in each of the two half-cavities, as illustrated in figure 1.6 (b). This filling process continues until it reaches a steady state and the heated/cooled fluids in the left/right half-cavity are in contact with the partition, producing temperature differences across the partition, and consequently, a falling/rising conjugate natural convection boundary layer discharging into a cool/hot intrusion at the bottom/top of the half-cavity. For cavities with low convective heat transfer, the impinging intrusions on the partition and the stratification process may not take place. Such an interaction of cooled and heated fluids and the partition is a key phenomenon in the cavity and the main design constraint in many industrial applications, such as building, industrial equipment (gas turbine, electric equipment, reactors, *etc.*), as well as is of significant theoretical importance [20–26].

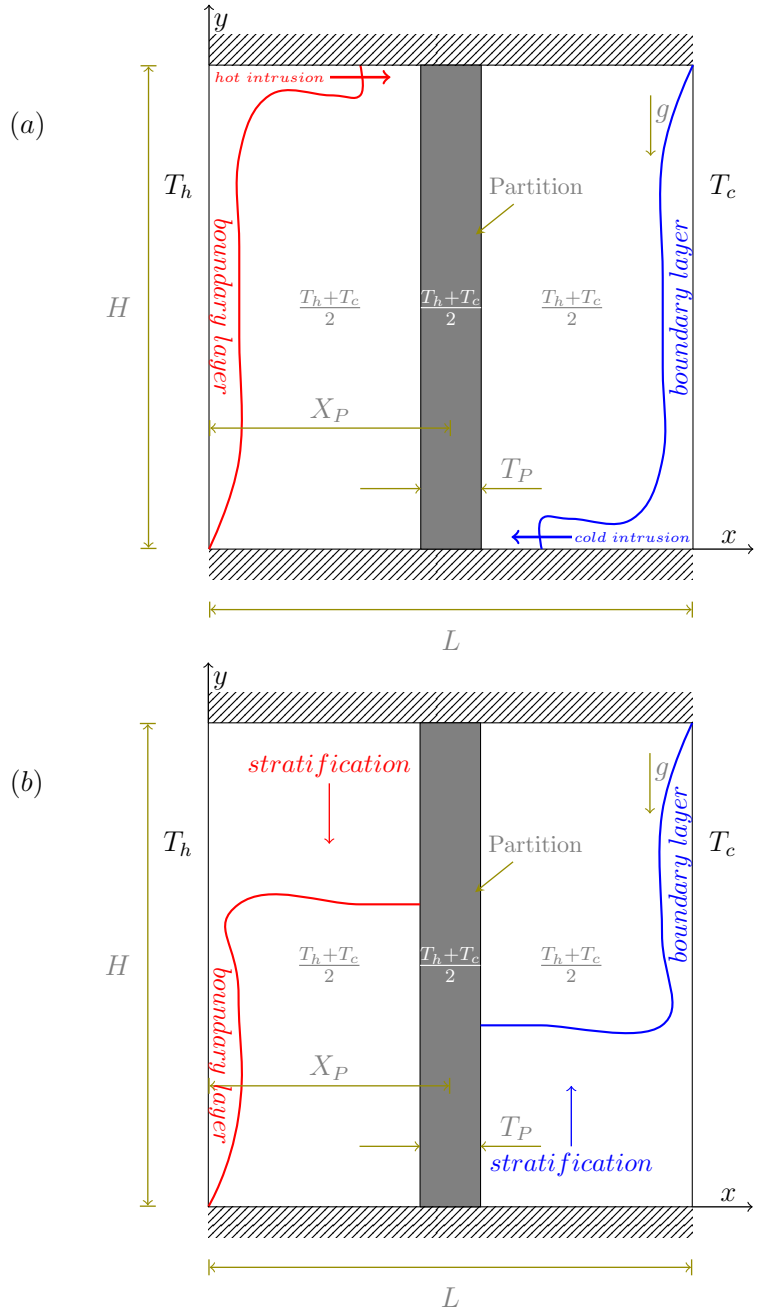

Figure 1.6: Schematic of flow pattern in a differentially heated partitioned cavity.

1.3 Objectives

Early studies on conjugate heat transfer mainly focused on applying different assumptions about the velocity distribution in the conjugate natural convection boundary layers such as the linear velocity distribution to simplify the problem [27]. Some other investigations analytically solved the conjugate heat transfer problem in the form of the generalized power series [28]. The assumptions of constant partition temperature (*e.g.*, [29, 30]), constant heat flux (*e.g.*, [31]) and power-law temperature distributions (*e.g.*, [32, 33]) made in these early studies helped to simplify the problem.

The existing developed tools are mainly for chained and steady rather than coupled and transient phenomena. Therefore, the majority of the past studies have focused on the steady effect of natural convection in a partitioned cavity with a thin partition or a partition with infinite thermal conductivity and simplified initial thermal conditions. The objective of the present study is to numerically analyze transient heat transfer through coupled thermal boundary layers in a partitioned cavity with more realistic assumptions; that is, with a partition which has a finite thickness and thermal conductivity.

The computational domain and the boundary conditions for the differentially heated cavity with a partition which has a finite thickness, and thermal conductivity are schematically shown in figure 1.7.

The specific objectives of this investigation are:

- To develop an in-house code in Visual $C\#$ to solve the discretized governing equations generated by the finite volume method and to post-process the data;
- To verify and validate the developed code with available numerical and experimental results;
- To use the direct numerical simulation results to demonstrate the behavior of transient conjugate natural convection and heat transfer in a partitioned cavity;

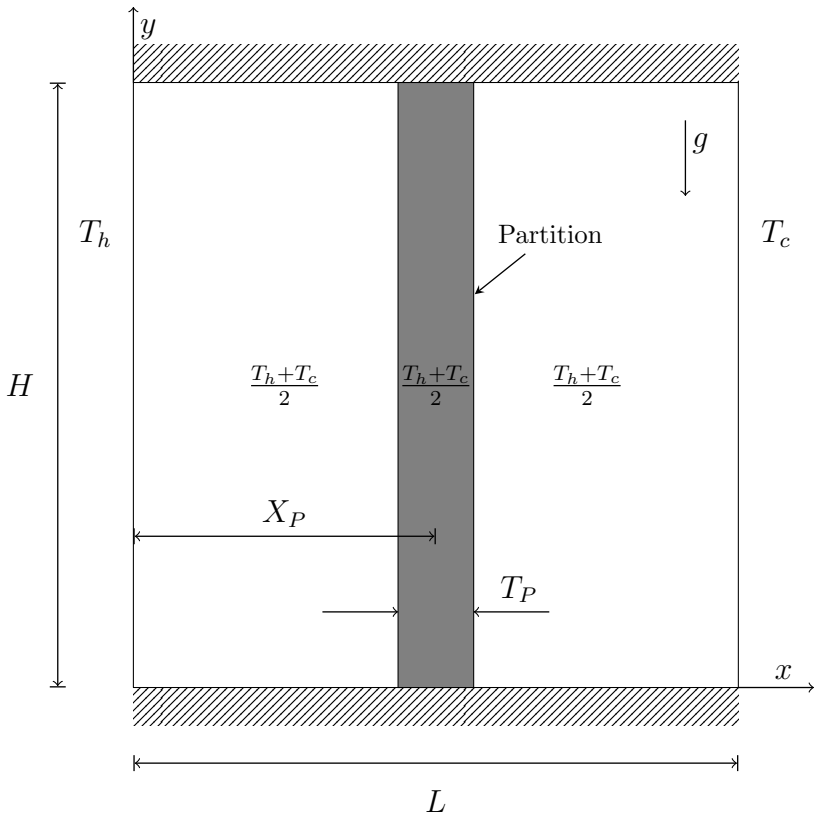

Figure 1.7: Schematic of the computational domain and boundary conditions.

- To investigate the effect of partition properties (*e.g.*, partition position, thickness and thermal conductivity) on the flow patterns and the conjugate natural convection heat transfer in a partitioned cavity for a wide range of the Rayleigh value; and
- To obtain empirical relations to quantify the conjugate natural convection heat transfer in a partitioned cavity.

1.4 Thesis outline

The remaining parts of this thesis are outlined as follows:

- Chapter 2 presents the literature review on the relevant previous studies on the topics of this work, which include natural convection over a plate, in an open cavity, and in a closed cavity, conjugate natural convection heat transfer, and conjugate natural convection in a closed cavity.

- Chapter 3 presents the governing equations and the appropriate boundary and initial conditions. In addition, the finite-volume numerical method used for direct numerical simulation is also described.

- Chapter 4 details the developed code of current work. It includes details of how the code is written and how the code works. It also presents the details about the post-processing of data produced from direct numerical simulations. The details of the verification and validation of the developed code against the available experimental and numerical results are also presented for both the partitioned and non-partitioned cases.

- Chapter 5 presents the steady-state results of natural convection in a partitioned cavity. The effects of different parameters on the steady-state heat transfer and flow patterns are detailed and empirical relations are obtained with the numerical results over a wide range of the Rayleigh value.

- Chapter 6 presents the transient results of natural convection in a partitioned cavity. The evolution of the unsteady behavior of the flow and heat transfer is presented for both centrally positioned and off-centred partitioned cavities. The effect of different parameters on the heat transfer and flow pattern is studied, and several heat transfer regimes are identified and classified, with several empirical relations developed with the obtained numerical results.

- Chapter 7 concludes the thesis by summarizing the major findings of this thesis and discussing some future work.

Chapter 2

Literature review

2.1 Introduction

Natural convection flow and heat transfer vary widely under various boundary conditions, geometries, fluids and flow regimes. There have been a great number of analytical, experimental and numerical studies on the various types of natural convection flow and heat transfer, with some reviewed in *e.g.*, [34–40]. In the current literature review, only the types closely related to the current study are discussed. These include the natural convection flow and heat transfer and conjugate natural convection flow and heat transfer under three different geometries: over a vertical plate, in a cavity with differentially heated sidewalls, and in a partitioned cavity with differentially heated sidewalls. It is well known that the general behaviors of natural convection flow and heat transfer are characterized and quantified mainly by three dimensionless parameters, i.e., the Rayleigh value (Ra) (or the Grashof number (Gr)), the Prandtl number (Pr) and the aspect ratio of the cavity (A), defined as follows,

$$Ra = \frac{\beta_f g \Delta T H^3}{\nu_f \kappa_f} = Gr \times Pr, \tag{2.1}$$

$$Pr = \frac{\nu_f}{\kappa_f}, \tag{2.2}$$

$$A = \frac{H}{L}, \tag{2.3}$$

although other parameters may also be important to govern the flow and heat transfer as well.

2.2 Natural convection over a vertical plate

2.2.1 In an initially thermally stratified fluid

Natural convection flow over a vertical plate in a thermally stratified medium has been extensively studied due to its application importance (*e.g.*, the cooling of nuclear reactors) [41]. Figure 2.1 shows the basic configuration of natural convection over a plate in an initially thermally stratified fluid.

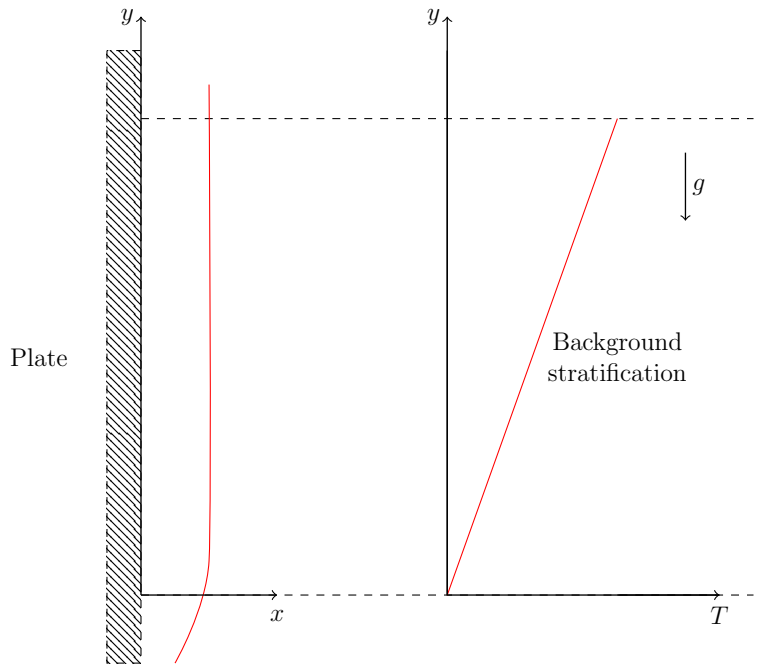

Figure 2.1: Schematic of natural convection over a vertical plate in an initially thermally stratified fluid.

For the case of a mountain and valley winds in the stratified air; a seminal analytical solution was presented by Prandtl [42] to supply the exact solution for natural convection along a slope that is maintained with a constant temperature excess with respect to the outer air linear stratification. As shown by Tanny and Cohen [43], a plane parallel flow was observed along the slope.

Many analytical methods were employed previously to solve the problem of a vertical wall immersed in a thermally stratified environment. For instance, similarity solutions are used to extract a set of ordinary differential equations [44]. This method has been used in many cases such as non-isothermal vertical flat plate [45], an isothermal wall immersed in a particular polynomial profile of thermal stratification [46], fixed wall temperatures [47], prescribed linearly increasing temperatures on both wall and the medium [48] and uniform heat flux [49]. Cheesewright [50] analytically studied natural convection heat transfer over a semi-infinite vertical plate immersed in a thermally stratified medium. The existing similarity solutions were generalized to include the effect of a non-isothermal surroundings. Scaling analysis was performed by Armfield *et al.* [51] on the natural convection boundary layer adjacent to an evenly heated semi-infinite plate with stratified ambient fluid. They obtained the scaling relations for the start-up, transitional and full development and reported that at full development, the stratified case had a region of two-dimensional flow near to the plate origin, while the remainder of the flow, far from the plate origin, was one-dimensional. The scaling relations were confirmed by their numerical solutions, especially for the case of the one-dimensional region of the start-up, transitional and the fully developed flow as well as the two- to one-dimensional transition location.

Many numerical studies have been conducted on the laminar natural convection from an isothermal vertical surface in a stable thermally stratified medium using different numerical schemes [52–54]. The natural convection on a vertical plate with uniform and constant heat flux in a thermally stable and stratified micropolar fluid was numerically studied by Chang and Lee [55]. It was reported that an increase in the stratification parameter reduces the wall temperature, the skin friction parameter, and the wall couple stress. Shapiro and Fedorovich [56] studied unsteady laminar natural convection in a stratified flow along an infinite vertical plate. They considered the induced flow due to an impulsive (step) change in plate temperature; a sudden application of a plate heat flux, and arbitrary temporal variations in plate temperature or plate heat flux. Turbulent natural convection along a vertical plate immersed in a stably stratified fluid is investigated by Fedorovich and Shapiro [57]. It is found that the transition from a laminar to a turbulent regime shows a quasi-stationary oscillatory phase due to the in-

teraction between turbulence and the ambient stable stratification. The turbulent fluctuations gradually fade out by increasing distance from the wall, while periodic laminar oscillations persist over much larger distances before disappearing.

2.2.2 In an initially constant temperature fluid

Lin and Armfield [58] used scaling analysis to investigate the transient behavior of the natural convection boundary-layer flow adjacent to a vertical plate heated with a uniform flux in a quiescent homogeneous ambient fluid with the Prandtl number less than one. The induced flow was classified as a startup stage, a short transitional stage and a steady state. The velocity boundary layer divides to the inner region and the outer region with each having different behavior and consequently, different scaling relations. It was found that the applicability of the scaling is limited by both distance from the plate origin and the Boussinesq number ($Bo = Pr \times Ra$) as close to the origin and/or at low Boussinesq numbers the flows are no longer self-similar. Lin *et al.* [59] recently also conducted a scaling analysis for the unsteady natural convection boundary layer (NCBL) of a homogeneous Newtonian fluid with $Pr > 1$ adjacent to a vertical plate evenly heated with a time-dependent sinusoidal temperature.

Hossain *et al.* [60] studied the effect of a fluctuating surface temperature and surface concentration on surface heat flux and surface mass flux from a vertical flat plate. The linearized theory [61–63] was used to solve the unsteady natural convection flow from a vertical plate, and it was reported that the amplitude and phase angles of the surface heat flux as well as of the surface mass-flux predicted by the perturbation and asymptotic methods are in good agreement with the finite difference solutions. Furthermore, the effect of the streamwise temperature and species concentration variations on a steady natural convection flow from a vertical plate was investigated by Hossain and Roy [64]. Direct numerical simulation was used to investigate boundary-layer instability of a natural convection flow on a uniformly heated vertical plate submerged in a homogeneous quiescent environment by Aberra *et al.* [65]. The two-dimensional investigation was conducted for the local Rayleigh value over the range of $0 \leq Ra_x \leq 2.4 \times 10^{10}$ and the working fluid of air and water and the critical Rayleigh values were reported separately

for both the temperature and velocity signals.

Due to the wide application of natural convection over a vertical plate, various working fluids have been studied previously. Effect of nanoparticles on natural convective boundary-layer flow over a vertical plate for the case of actively and passively controlled nanofluid particle fraction on the boundary was studied by Kuznetsov and Nield [66, 67] using similarity transformation. Teymourtash *et al.* [68] numerically investigated laminar natural convection with uniform or non-uniform prescribed surface heat flux over a vertical flat plate in the supercritical fluid. It was reported that by increasing and decreasing wall heat flux, the local Nusselt number increases and decreases, respectively.

2.3 Natural convection in an open cavity

Open cavities exist in various engineering systems, such as solar thermal receivers and collectors, electronic chips, passive systems, etc. An open cavity can be total [69], partial [70] or partial with screens or slots [71].

2.3.1 Numerical studies

There are numerous numerical studies on natural convection in open cavities (see, e.g., [70, 72–87]). Laminar steady natural convection in an inclined shallow cavity was numerically studied by Polat and Bilgen [88]. The side facing the opening has a constant heat flux, the sides perpendicular to the heated side are adiabatic and the opening is in contact with a fluid ($Pr = 1$) at constant temperature and pressure. The volumetric flow rate and heat transfer were found to increase with the increase of the aspect ratio and the Rayleigh value. Bilgen and Oztop [89] numerically investigated laminar natural convection in an inclined partially open square cavity in which the wall facing the opening was isothermal and in contact with air. For $10^3 \leq Ra \leq 10^6$ it was found that the volume flow rate and the Nusselt number increase with the Rayleigh value, the aperture size, and the general aperture position. They also reported

that the Nusselt number was affected by the inclination angle, although the relation is not linear. The results also showed that it is possible to maximize or minimize heat transfer by selecting appropriate parameters (*i.e.*, aperture size, aperture position and inclination angle) at a given operation Rayleigh value. Airflow due to natural convection in a partially open square two-dimensional cavity with internal heat source, adiabatic bottom and top walls, and vertical walls maintained at different constant temperatures was numerically investigated by Fontana *et al.* [90], which showed that the heat source was dominant at low Rayleigh value, but as the Rayleigh value increases the flow becomes being dominated by the temperature difference between the sidewalls.

2.3.2 Experimental studies

Chakroun *et al.* [91] and Elsayed and Chakroun [92] experimentally investigated natural convection in a rectangular partially or fully open from one side tilted cavity. The wall facing the cavity opening was heated to a constant heat flux and the other walls were adiabatic. The experiments were carried out for air as a working fluid and $Gr = 5.5 \times 10^8$, the tilt angle measured from the vertical direction between -90 deg to $+90$ deg in 15 deg increments, the aspect ratio (height-to-width of cavity) of $1, 0.5$ and 0.25 and the opening ratio (opening height to cavity height) of $1, 0.5$ and 0.25. The average Nusselt number was reported for different experimental parameters. Combined natural convection and surface radiative exchange in a solar open cubic cavity-type receiver was theoretically and experimentally investigated by Montiel-Gonzlez [93]. It was reported that as the Rayleigh value increases over the range of $10^4 \leq Ra \leq 10^6$, the total average Nusselt number in the cavity increases by 331% to 411%. The experimental and numerical results were in fairly good agreement near the top and bottom walls whereas near the isothermal wall, there are some differences between the temperatures obtained numerically and experimentally. Maytorena *et al.* [94] investigated experimentally and numerically the turbulent natural convection in an open cubic cavity with the air as the heat transfer fluid and the vertical wall opposite to the aperture was subjected to uniform heat flux, with Ra over the range of $1.66 \times 10^{11} - 7.1 \times 10^{11}$, resulting in the Nusselt number over the range of $185.94 - 243.31$ and

the heat transfer coefficient over the range of $4.88 - 6.83\ W/m^2K$. The maximum differences between the experimental and numerical data for heat transfer coefficient and Nusselt number were 10.8% and 14%, respectively.

2.4 Natural convection in a closed cavity

The two-dimensional convective motions in boundary layers of a rectangular cavity were studied by Gill [95] and an approximate solution obtained in large Prandtl numbers was found to be in good agreement of experimental results. Steady laminar natural convection of cold water in a vertical annulus with a constant-heat-flux heated inner wall and an isothermally cooled outer wall was studied by Ho and Lin [96]. Over the ranges of $0.5 \leq$ aspect ratio ≤ 8, $1.2 \leq$ radius ratio ≤ 10, $-2 \leq$ density inversion parameter ≤ 1 and $10^3 \leq Ra \leq 10^6$), they found that the Nusselt number increases as the radius ratio increases and in a tall annulus (aspect ratio = 8) multicellular flow behavior intensifies. The multicellular solution in natural convection in a vertical air-filled tall cavity with differentially heated sidewalls was studied by Wakitani [97,98]. It was found that flow structure depends on the initial conditions. Kimura and Bejan [99] analytically and numerically investigated natural convection in a rectangular cavity with a constant uniform heat flux (heating and cooling) at the vertical sidewalls. They reported that the boundary-layer thickness was independent of height, and the vertical wall temperature gradient is similar to the motionless linearly stratified core region.

2.4.1 Scaling analysis

Patterson and Imberger [100] investigated unsteady natural convection in a rectangular cavity with differentially heated and cooled side walls. With their pioneering scaling analysis, they classified flow development through several transient flow regimes to one of three steady-state types of flow based on the relative values of the Rayleigh value, the Prandtl number, and the aspect ratio of the cavity. Their scaling relations were in agreement with two- and three-dimensional numerical simulations of the transient flow in a side-heated cavity conducted by

Schladow *et al.* [101]. Since then, further extensive scaling analyses have been performed by many researchers to extend the scaling analysis by Patterson and Imberger [100] to numerous cases with wide ranges of governing parameter values and different flow configurations (see, *e.g.*, [51, 58, 102–112]). For example, Lin and Armfield [58] investigated the transient behavior of the natural convection boundary-layer flow adjacent to a vertical plate heated with a uniform flux in a quiescent homogeneous ambient fluid with the Prandtl number less than one by scaling analysis and direct numerical simulation. To further extend their research, they carried out scaling analysis for fluids with the Prandtl number larger than one under isothermal heating [112]. They reported a strong Prandtl number dependency in the characteristic quantities for the velocity in both the developing and fully developed structures of the natural convection boundary layer. Scaling for the unsteady natural convection boundary layer (NCBL) of a homogeneous Newtonian fluid with $Pr > 1$ adjacent to a finite vertical plate evenly heated with a time-varying sinusoidal temperature was developed recently by Lin and Armfield [59]. They carried out direct numerical simulation with the similar ranges of Ra, Pr, and f_n to that for the time-varying sinusoidal heat flux case [113], and used a simple three-region structure proposed in [104, 112] to develop the scaling relations, and found that the developed scaling relations agree with the numerical results very well. Some of the previous studies on natural convection using scaling analysis are summarized in Table 2.1.

2.4.2 Effect of the governing parameters and boundary conditions

The Prandtl number is one of the dimensionless parameters governing the flow patterns and thermal behavior in natural convection flows. To compare the experimental results with the numerical results, Viskanta *et al.* [114] conducted a numerical research on two- and three-dimensional cavities filled with a low Prandtl number fluid (gallium). They found a good agreement between the experimental and numerical results. Natural convection in an internally heated square cavity with a low-Prandtl number fluid was studied by Arcidiacono *et al.* [115]. A left-right symmetry and steady flow were observed in the Grashof number up to 10^7. Asymmetric steady-state flow patterns were observed in the Grashof number of 3×10^7 and it becomes

Table 2.1: List of the selected studies on natural convection using scaling analysis.

Authors	**Steady/unsteady**	**Configuration**
Patterson and Imberger [100]	Unsteady	Differentially heated rectangular cavity
Lin and Armfield [102]	Unsteady	Cooling of fluid ($Pr < 1$) in a vertical cylinder
Lin *et al.* [103]	Unsteady	A linearly-stratified fluid with $Pr < 1$ on an evenly heated semi-infinite vertical plate
Patterson *et al.* [104]	Unsteady	A vertical wall following non-instantaneous heating
Tomasz *et al.* [105, 106]	Unsteady	Paramagnetic fluids with the Prandtl number greater than one in a square cavity
Armfield *et al.* [51]	Unsteady	An evenly heated semi-infinite plate with stratified ambient fluid
Aberra *et al.* [107]	Steady	An evenly heated vertical plate (Pr > 1)
Saha *et al.* [108]	Unsteady	An inclined plate with uniform heat flux
Saha *et al.* [109]	Unsteady	An inclined plate subject to sudden cooling
Saha *et al.* [110]	Unsteady	A triangular cavity subject to a non-instantaneous heating on the inclined walls
Saha *et al.* [111]	Unsteady	Semi-infinite vertical plate heated with a uniform ramp heat flux
Lin and Armfield [58]	Unsteady	A vertical plate heated with a uniform flux
Lin *et al.* [112]	Unsteady	A vertical plate
Lin and Armfield [59]	Unsteady	Time-dependent temperature on a vertical plate

time-periodic at the Grashof number of 5×10^7 and finally chaotic at the Grashof number higher than 10^8. The same configuration of Arcidiacono *et al.* [115] was used for another study for the cavity aspect ratio of 4, and different flow regimes of steady-state, periodic and chaotic were obtained [116]. Koca *et al.* [117] tested the effect of the Prandtl number on natural convection in a triangular cavity with localized heating from below and observed that the Prandtl number, the location and the length of the heater, as well as the Rayleigh value, affect flow and temperature fields. The Rayleigh value as another dimensionless parameter influencing natural convection has also been widely investigated (see, *e.g.*, [118–121]). Dixit and Babu [122]

numerically simulated high Rayleigh values (up to 10^{10}) natural convection in a square differentially heated cavity. Their results were in very good agreement with the benchmark results. In another research, Kulacki and Emara [123] experimentally studied high Rayleigh value (up to 2.17×10^{12}) natural convection with internal heat sources in a horizontal fluid layer with an insulated lower boundary and a constant-temperature upper boundary.

Natural convection heat transfer subjected to different boundary conditions has been the topic of many studies (see, *e.g.*, [124–127]). Sathiyamoorthy *et al.* [128] numerically analyzed the steady natural convection flow in a square cavity with a sinusoidal heated bottom wall, linearly heated sidewalls and insulated top wall. They presented their results for the Prandtl number from 0.01 to 10 and the Rayleigh value of 10^5. Natural convection in a cavity heated from bellow was numerically and experimentally investigated by Calcagni [129], with the heat source length varying from 1/5 to 4/5 of the height and sidewalls acting as cooling elements while the other surfaces being adiabatic. It was revealed that at low Rayleigh values ($Ra \leq 10^4$) heat transfer mechanism was mainly developed conduction and convective heat transfer at $Ra \cong 10^5$ and heat source length increase causes an increase in heat transfer especially for high Rayleigh values. To examine the cooled ceiling application, natural convection in a rectangular enclosure heated from one side and cooled from the ceiling was studied numerically by Aydin *et al.* [130]. For $10^3 \leq Ra \leq 10^7$, the effect of the aspect ratio on the flow pattern and energy transport was analyzed. They found that in shallow cavities, the effect of Rayleigh value on the heat transfer is more significant, and the influence of the aspect ratio is stronger for tall cavities with high Rayleigh values.

A partially heated cavity is an important subject in natural convection problems due to wide applications and has been extensively investigated for different thermal conditions (see, *e.g.*, [117, 131–139]). The effect of the heater size, location, aspect ratio and boundary condition in a rectangular air-filled enclosure was studied both experimentally and numerically by Chu *et al.* [140]. They reported that the heater size and location were very important parameters on temperature fields and heat transfer as the maximum Nusselt number is obtained almost for all Rayleigh values when the heater is located in the middle of the wall. The effects of the heater and cooler locations on natural convection in cavities were numerically examined by

Turkoglu and Yucel [141]. They observed that the mean Nusselt number increases as the heater moves closer to the bottom wall for a given cooler location and as the cooler moves closer to the top horizontal wall for a given heater location. Valencia and Frederick [142] investigated an air-filled square cavity with partially thermally active side walls for five different heating locations. They reported that heat transfer rate increases when the heating section is in the middle of the hot wall.

It is well known that heat transfer coefficient for natural convection is low. Geometry optimization is one method to enhance heat transfer performance. Another way for scaling up of heat transfer capacity is nanofluids. Dilute suspensions of nanoparticles (such as Al_2O_3, CuO, Cu, SiO and TiO_2) smaller than 100 nm are nanofluids and due to their wide application, nanofluids are the centre of attention for many researchers. For example, Hwang *et al.* [143] used nanofluids to investigate natural convection in a differentially heated cavity and found that the ratio of heat transfer coefficient of nanofluids to that of the base fluid decreases as the size of nanoparticles increases. The heat transfer enhancement by utilizing nanofluids was also well investigated in some of the previous studies (see, *e.g.*, [144–147]), as summarized in Table 2.2.

Table 2.2: List of the selected experimental studies on natural convection of nanofluids.

Authors	**Rayleigh value**	**Nanoparticle**
Putra *et al.* [148]	$10^7 - 10^9$	Al_2O_3, CuO
Wen and Ding [149]	$10^4 - 10^6$	TiO_2
Nnanna [150]	$0.9 \times 10^7 - 3.0 \times 10^7$	Al_2O_3
Li and Peterson [151]	$8 \times 10^3 - 2.8 \times 10^4$	Al_2O_3
Ho *et al.* [152]	$6.21 \times 10^5 - 25.6 \times 10^8$	Al_2O_3
Jahanshahi *et al.* [153]	$10^5 - 10^7$	SiO_2

2.4.3 Effect of cavity shape and inclination

Flow and consequently heat transfer in a cavity strongly depend on the enclosure shape. The main cavity shapes investigated include rectangular [154, 155], cylindrical [156, 157], triangular [158, 159], spherical [160], trapezoidal [161], parallelogram [162, 163], octagonal [164], hemi-

spherical [165,166] and pentagonal [167]. Each cavity shape and boundary condition represents a possible application in nature or industry. For instance, Hyun and Choi [168] studied the natural convective heat transfer in a parallelogram-shaped enclosure at large Rayleigh values. They reported that it was possible to use a parallelogram-shaped enclosure as a transient thermal diode to control the tilt angle of the partition walls. Natural convection heat transfer was studied in a trapezoidal enclosure with parallel cylindrical top and bottom walls at different temperatures and adiabatic sidewalls by Iyican *et al.* [169], who presented the average and local Nusselt numbers for Ra up to 2.7×10^6 and the inclination angle from 0 to 180 degrees (measured from the vertical). Kent [170] investigated two-dimensional laminar natural convection in an isosceles triangular enclosure for the cold base and hot inclined walls. The cavity was filled with air and the effect of Ra and the aspect ratio on the flow pattern and heat transfer were analyzed over the ranges 15 to 75 degree for the base angle and $10^3 - 10^5$ for Ra. It is reported that as the base angle decreases isotherms compresses towards the bottom wall and consequently a low aspect ratio shows a higher heat transfer rate from the bottom of the triangular cavity. Kent *et al.* [171] further studied natural convection in triangular cavities by investigating a right-angled triangular cavity. For the same Ra range of [170] and the aspect ratio from 0.1 to 4, they observed that at the higher aspect ratio, the effect of the hot bottom wall at the upper portion of the cavity is negligible, and a single circulation cell was formed at the middle and bottom parts of the cavity. They also found that for the various thermal boundary conditions the mean Nusselt number of the hot wall increases with increasing Ra.

By tilting cavities, the induced natural convection behavior changes and the inclination angle plays a key role in the heat transfer and flow pattern. Hart [172] studied the effect of inclination angle on the flow characteristics in a differentially heated rectangular cavity and reported that the instability types predominantly depend on the inclination angle. The study by Kuyper *et al.* [173] showed that the Nusslet number has a strong dependence on the inclination angle and its relation with Ra is in power-law fashion. Hollands and Konicek [174] studied different flow regimes in angled cavities in terms of the critical Rayleigh value related to the stability of air layers in the conduction regime. More studies conducted on inclined cavities to find the effect of the aspect ratio [175] and the Nusselt number [176]. Kalendar and Oosthuizen [177]

Table 2.3: List of the selected studies on natural convection in cavities with different shapes.

Authors	**Shape**
Anderson and Lauriat [154]	rectangle
Arpino *et al.* [155]	rectangle
Bari [156]	cylinder
Edwards and Catton [157]	cylinder
Lei *et al.* [158]	triangle
Basak *et al.* [159]	triangle
Kent [170]	triangle
Kent *et al.* [171]	triangle
Chiu and Chen [160]	sphere
Varol *et al.* [161]	trapeze
Iyican *et al.* [169]	trapeze
Almeida and Naylor [162]	parallelogram
Aldridge and Yao [163]	parallelogram
Hyun and Choi [168]	parallelogram
Saleh *et al.* [164]	octagonal
Bari and de Mara [165]	hemisphere
Shiina *et al.* [166]	hemisphere
Ridouane and Campo [167]	pentagon

studied natural convection heat transfer in an isothermal inclined cylinder with a square cross-section which was an approximate model of that which occurs in some electrical and electronic component cooling problems. The influence of Rayleigh value, inclination angle and the ratio of the width to the height of the heated cylinder on the Nusslet number presented. The effect of the inclination angle on the critical Rayleigh value in an air-filled open cavity was studied by Nateghi and Armfield [178]. They obtained the critical Rayleigh value over the range of $10^5 \leq Ra \leq 10^{10}$ and the inclination angle over the range of 0 to 90 degrees and reported that the critical Rayleigh value decreases as the inclination angle increases. The flow structure, stability, and heat transfer in an inclined differentially heated cavities were investigated by Williamson *et al.* [179]. The attached jet/plumes formed adjacent to the adiabatic walls was

observed in the inclined cavity and the same relation between the critical Rayleigh value and the inclination angle as that from [178] was reported.

2.4.4 Benchmark studies

To validate numerical results, several benchmark investigations on natural convection have been carried out (see, *e.g.*, [180–184]). A numerical benchmark investigation was done by Davis [185] on natural convection in an air-filled square cavity. Ampofo and Karayiannis [186] conducted an experimental study on low-level turbulence natural convection in an air-filled vertical square cavity. The vertical isothermal sidewalls were at 50 and $10°C$ respectively giving the Rayleigh value of 1.58×10^9. The local velocity and temperature, the local and average Nusselt numbers, the wall shear stress as well as the turbulent kinetic energy and the dissipation rates of the temperature variance were reported. A three-dimensional benchmark numerical research was performed on natural convection in a differentially heated cavity by Wakashima and Saitoh [187]. Three Rayleigh values of $10^4, 10^5$ and 10^6 and the fixed Prandtl number of 0.71 were chosen for the numerical study. Flow visualization was used to examine natural convection in a rectangular inclined cavity by Linthorst *et al.* [188]. Different ranges of the aspect ratio ($0.25 \leq A \leq 7$), the inclination angle (0 to 90 degree) and Ra (5×10^3 to 2.5×10^5) were selected for an air-filled cavity. They identified transition from stationary to nonstationary flow and the transition from two-dimensional to three-dimensional flow for the considered ranges of the parameters. The list of discussed benchmark studies with their specification is presented in Table 2.4.

2.4.5 Transient studies

LeQuere and Alziary de Roquefort [189] numerically investigated the transient behavior of air-filled cavities with isothermal side walls and adiabatic horizontal walls. They reported that there were oscillations due to the internal gravity waves which were eventually damped out when the steady state obtained. In a subsequent research, LeQuere and Alziary de Roquefort [190]

Table 2.4: List of the selected benchmark studies on natural convection in differentially heated cavities.

Reference	**Method**	**Rayleigh value**	**Working fluid**
Leong *et al.* [180]	Experimental	$10^4 - 10^8$	air
Pepper and Hollands [181]	Numerical	$10^5 - 10^8$	air
Le Quéré *et al.* [182]	Numerical	$10^6 - 10^7$	air
Cheikh *et al.* [184]	Numerical	$10^5 - 10^9$	air
Davis [185]	Numerical	$10^3 - 10^6$	air
Ampofo and Karayiannis [186]	Experimental	1.58×10^9	air
Wakashima and Saitoh [187]	Numerical	$10^4 - 10^6$	air
Linthorst *et al.* [188]	Experimental	$10^3 - 10^5$	air

determined the critical value of the Rayleigh value for the transition to periodic flow as a function of the aspect ratio. The transient natural convective flow in a rectangular cavity with a uniformly heated vertical wall was investigated by Kuhn and Oosthuizen [191]. Mohamad and Viskanta [192] found the oscillation reported by LeQuere and Alziary de Roquefort [189] at the critical Grashof numbers, which were dependent on the Prandtl number (Prandtl number of 0.001, 0.005 and 0.01). Numerical and experimental results for transient two-dimensional natural convection initiated by instantaneously heating and cooling the opposing vertical walls of a square cavity containing a stationary and isothermal fluid were compared by Patterson and Armfield [193]. Unsteady natural convection has also been extensively investigated for different cavity shapes and configurations. Scaling analysis and direct numerical simulations was used to investigate transient flows in a differently heated cavity with a fin at different positions on the sidewall by Ma and Xu [194]. It was reported that the development of transient flows around the fin is dependent on the fin position and the Rayleigh value. To explore the transient behavior of isoflux side walls in a square cavity, Jiracheewanun *et al.* [195] conducted a numerical simulation and revealed that transient flow features obtained for the isoflux cavity were similar to the flow features for the isothermal case but the fully developed flow features were very different. Rostami [196] and Hasan *et al.* [197] presented numerical predictions for unsteady heat transfer and fluid flow characteristics in enclosures with vertical wavy side walls and sinusoidal corrugated side walls, respectively. Nithyadevi *et al.* [198] and Kizildag *et al.* [199] studied transient natural convection in a square cavity with partly thermally active side

walls and a rectangular cavity of the 7:1 aspect ratio under transient boundary conditions, respectively. Younis *et al.* [200] described a numerical analysis of the effects of thermal boundary conditions, fluid variable viscosity and wall conduction on unsteady laminar natural convection of a high Prandtl number fluid ($Pr = 4 \times 10^4$). The time evolutions of heat transfer and flow pattern of eight different cases of cooling were presented and analyzed. Furthermore, Lin [201] and Lin and Armfield [202–204] investigated unsteady natural convection cooling of an initially homogeneous fluid in a vertical circular cylinder and in a rectangular container and showed analytical and numerical features of transient heat transfer and flow pattern. The transitory features of natural convection in a triangular enclosure have also been extensively studied in the previous studies (*e.g.*, [158, 205–215]).

2.4.6 Experimental studies

Experimental studies on natural convection are much less than forced convection. The main reason for this scarcity is experimental difficulties in terms of low-velocity measurements and experimental device's design to maintain boundary conditions. Imberger [216] performed an experimental study on natural convection in a water filled deferentially heated rectangular cavity. Temperature and velocity profiles were presented for the aspect ratio (depth to length) of 10^{-2} and 1.9×10^{-2} and the Rayleigh value from 1.31×10^6 to 1.11×10^8. An experimental study of natural convection in a parallelepiped enclosure induced by a single vertical wall was conducted by Fills and Poulikakos [217]. The upper half of the wall was hot while the lower half was cold, and the other enclosure walls were insulated. The experiment was performed at $10^{10} < Ra < 5 \times 10^{10}$ and flow and temperature measurements were reported for water as the working fluid. Due to a significant difference between their results from previous studies, careful examination of temperature boundary conditions suggested. Ramesh and Venkateshan [218] studied laminar natural convection heat transfer in a differentially heated square enclosure and used a differential interferometer (DI) to visualize boundary conditions on the wall. A flow visualization technique was introduced by Tanasawa [219] and used for flow visualization of natural convection in a horizontal rectangular liquid layer driven by surface tension and buoyancy. The

flow patterns were visualized by suspended fine aluminum flakes in liquid. To investigate a problem of interest in the thermal control of electronic equipment, an experimental study was carried out by Ramos *et al.* [220]. Since in the case of component failure natural convection is the main cooling process, the effects of natural convection on the flow and heat transfer in a cavity with two flush mounted heat sources on the left vertical wall were analyzed. Experimental results showed a good agreement with the numerical data. 2D-PIV (two-dimensional particle image velocimetry) and holographic interferometry techniques were used to examine the natural convection heat transfer in an air-filled square cavity heated from below and cooled by the sidewalls by Corvaro and Paroncini [221]. Those techniques were used for investigation of velocity and temperature fields in a Hele-Shaw convection cell (HSC) by Lee and Kim [222]. Some other experiments were carried out to obtain velocity and temperature of air in an enclosed cavity (see, *e.g.*, [223–226]). A few experimental researches have been performed to investigate the transient effect of natural convection in a cavity. To confirm the classification scheme presented by Patterson and Imberger [100], a series of experiments was done by Jeevaraj and Patterson [227] in a square cavity with initially stationary glycerol-water mixture as the working fluid and isothermal sidewalls. They confirmed the classification as well as some aspects of the flow development. Transient flow characteristics in a differentially heated air-filled tall cavity were investigated numerically and experimentally by Kolsi *et al.* [228]. A Rayleigh value range of $2929 - 11772$ was selected for the experiment and reported that as the Rayleigh value increases the flow becomes unstable. Ivey [229] experimentally investigated the transient natural convection in a cavity with isothermal side walls and reported oscillations which were due to the inertia of the flow entering the interior of the cavity induced by side walls boundary layers. The effect of the inclination angle of a cavity on the transient natural convection in a cavity was experimentally studied by Upton and Watt [230]. In their study, the evolution of the flow to steady-state was investigated for a Prandtl number of 6.38, a Rayleigh value of 1.5×10^5 and an aspect ratio of 1.0, at angles of inclination $\pi/4$, $\pi/2$ and $3\pi/4$. They found that the angle of inclination has a significant effect on the flow and heat transfer in natural convection in an enclosure. Laser Doppler velocimetry and dye flow visualizations were used to obtain velocity profiles and flow pattern of natural convection in open cavities by Hess and Henze [231]. For

$3 \times 10^{10} \leq Ra \leq 2 \times 10^{11}$, boundary-layer transition to turbulence, flow patterns in the cavity, and flow outside of the cavity were discussed. Yewell *et al.* [232] experimentally investigated transient natural convection in enclosures at high Rayleigh values (*i.e.*, $1.28 \times 10^9 - 1.49 \times 10^9$) and low aspect ratios (*i.e.*, 0.0625 and 0.112). Turbulent natural convection has been investigated experimentally and numerically in a differentially heated cavity by Salat *et al.* [233]. At the Rayleigh value of 1.5×10^9 temperature was measured by 25 m micro-thermocouples and velocity by a Laser Doppler Anemometer. Results in the median vertical plan were presented and compared with numerical data. Jeng *et al.* [234] conducted experimental and numerical research on transient natural convection flow and transport process caused by mass transfer in the inclined enclosures at different angles. For $1.126 \times 10^8 \leq Ra \leq 1.157 \times 10^{11}$, the aspect ratio from 0.6 to 1 and the angles of inclination from 30 to 90 degrees, flow structure was visualized by particle tracers and shadowgraph. The concentration and its fluctuations were measured with the non-intrusive optical method and results were compared with numerical data.

The list of experimental studies mentioned in this section is presented in Table 2.5.

Table 2.5: List of the selected experimental studies on natural convection.

Authors	**Rayleigh value**	**Working fluid**
Imberger [216]	$1.31 \times 10^6 - 1.11 \times 10^8$	water
Fills and Poulikakos [217]	$10^{10} - 5 \times 10^{10}$	water
Ramesh and Venkateshan [218]	$10^4 - 10^6$	air
Ramos *et al.* [220]	-	air
Corvaro and Paroncini [221]	$10^4 - 10^5$	air
Tian and Karayiannis [223]	1.58×10^9	air
Betts and Bokhari [225]	$0.86 \times 10^6 - 1.43 \times 10^6$	air
Saury *et al.* [226]	up to 1.2×10^{11}	air
Jeevaraj and Patterson [227]	$10^7 - 10^8$	glycerol-water
Kolsi *et al.* [228]	$2929 - 11772$	glycerol-water
Ivey [229]	$10^8 - 10^9$	glycerol-water & water
Upton and Watt [230]	1.5×10^5	water
Hess and Henze [231]	$3 \times 10^{10} \leq Ra \leq 2 \times 10^{11}$	-
Yewell *et al.* [232]	$1.28 \times 10^9 - 1.49 \times 10^9$	water
Salat *et al.* [233]	1.5×10^9	air
Jeng *et al.* [234]	$1.126 \times 10^8 - 1.157 \times 10^{11}$	$CuSO_4 + H_2SO_4$

2.5 Conjugate natural convection heat transfer

Conjugate natural convection in a differentially-heated, partitioned cavity with heat-conducting partition wall has been presented in various situations in nature and engineering, such as in solar thermal systems, electronic equipment, chemical reactors and buildings, and has attracted extensive research interest (see, *e.g.*, [235–240]).

As figure 2.2 illustrates, conjugate natural convection boundary layers (CNCBLs) occurs when a temperature difference ($T_h - T_c$, $T_h > T_c$) is created at sides of a vertical conducting partition. Due to heat transfer across the partition, two areas of heated (on the right side of the partition) and cooled (on the left side of the partition) are created. Those thermal boundary layers induce a downward (on the left) and upward (on the right) flows at sides of the partition. The fact that

in this arrangement, natural convection boundary layers are coupled through the conduction in the partition and the presence of different sub-domains make this problem complicated and interesting.

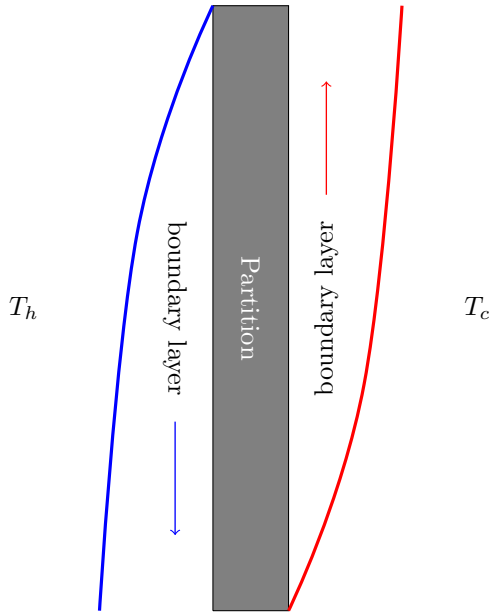

Figure 2.2: Schematic of the conjugate natural convection boundary layer.

A general analysis of laminar conjugate natural convection boundary layers was first conducted by Viskanta and Abrams [241]. They obtained an exact solution for the temperature distribution and the heat transfer in the case of constant properties, concurrent and inviscid flow. They also found that the omission of the thermal interaction between the fluid streams on both sides of the separating wall can lead to a serious inaccuracy. The local similarity concept and the method of interaction were used by Lock and Ko [242] to examine the problem of the thermal interaction through a wall between two free convective systems. The effect of the plate resistance was taken into account in their study. In another study of this problem, an analytical investigation was performed for laminar natural convection and the value of the Prandtl number was assumed to approach infinity [243]. Interestingly, the results revealed that the vertical wall can be approximated as a constant heat flux surface and the overall heat transfer rate is almost independent of the Prandtl number. Furthermore, the authors studied a system with two saturated porous reservoirs at different temperatures separated by a partition [244, 245]. The heat transfer rate between coupled natural convections at two sides of the

vertical conductive wall separating two infinite reservoirs at different temperatures was studied by Chen and Chang [246]. The separating wall was assumed to have a very small thickness-to-height aspect. The non-similarity transformation technique was used to solve the laminar form and cast dimensionless governing equations and extracted equations were solved by using the finite difference method. They approximated wall heat conduction by using one-dimensional heat conduction equation and their results were in good agreement with the predicted results of Viskanta and Lankford [247]. An analytical and numerical investigation was conducted by Higuera and Pop [248] on conjugate natural convection heat transfer. Their system consisted of two semi-infinite fluid-saturated porous reservoirs at different temperatures separated by a vertical plate. Unlike Chen and Chang [246], they tried to apply two-dimensional wall conduction both across and along it while the wall aspect ratio was small.

The conjugate natural convection on a vertical surface when each side of it was maintained at a different temperature was examined by Merkin and Pop [249]. They used a finite difference scheme to solve the governing equations for Pr of 0.7, 0.72, and 0.733. They found that the asymptotic expansion gives trustworthy results. Solving conjugate heat transfer problems using SIMPLE-like algorithms in an undivided computational domain (domain consisting of the both solid and fluid region) has some difficulties. The main issue is to ensure the physical realism of the extracted results. The methods of the 'pseudo-density' and the 'pseudo-solid -specific-heat' were suggested by Chen and Han [250] to avoid any possible errors. The effects of heat generation on coupling of laminar natural convection flow along conducting vertical flat plate and plate conduction were investigated by Mamun, *et al.* [251]. They used a local non-similar transformation to form dimensionless governing equations. Numerical results depicted that the fluid velocity and skin friction at the solid-fluid interface increased by increasing heat generation parameter and decreased by increasing Pr and conduction factor. Furthermore, when the rate of heat transfer is decreased, heat generation and conduction parameters rise and lead to a reduction of Pr. A numerical investigation was conducted to examine the effect of conduction in the wall on the natural convection flow by Belazizia, *et al.* [252]. The studied system was a square enclosure that had a vertical wall at the left with a finite thermal conductivity. The numerical study was performed at Ra between 500 and 10^7, the thermal conductivity of wall

to fluid between 0.1 and 10, Pr of 0.70, and the proportion of wall thickness to the height of the wall of 0.2. Wall conduction was found to have a strong effect on natural convection flow and when the Rayleigh value and conductivity ratio increased, fluid velocity and the heat transfer rate go up. The effect of wall conduction on natural convection heat transfer in a porous enclosure was the main focus of study performed by Saeid [253]. Steady conjugate natural convection-conduction heat transfer was analyzed at the same physical model as that of Belazizia, *et al.* [252]. The calculation of governing equations was in Ra between 10 and 1000, the wall to the porous thermal conductivity ratio from 0.1 to 10 and the ratio of wall thickness to its height between 0.02 and 0.5. It was concluded that the average Nusselt number increased by increasing Ra and the thermal conductivity ratio or decreasing the thickness of the conducting wall.

2.6 Conjugate natural convection in closed cavity

2.6.1 Numerical studies

Many practical applications require considering a partitioned cavity as an investigation system (see, figure 1.7). Conjugate heat transfer problem in a partitioned cavity is of great interest due to containing two or more subdomains which heat transfer phenomena describes by different differential equations (elliptical Laplace equation or parabolic differential equation in solid while elliptical Navier-Stokes equation in fluid) [27].

Transient laminar natural convection in a partitioned enclosure with an adiabatic baffle has been studies by Fu *et al.* [254]. Also, Fu *et al.* [255] numerically investigated the transient laminar natural convection in an enclosure partitioned by an adiabatic baffle in which the enclosure was heated by uniform heat flux from the left wall and cooled from the right wall. They observed that the adiabatic baffle had important influences on the transient heat transfer mechanism. Numerical simulations of unsteady natural convection in a differentially heated cavity with a thin fin of different lengths on a sidewall at $Ra = 3.8 \times 10^9$ performed by Xu

et al. [256]. They reported that the fin length significantly influenced the transient thermal flow around the fin and heat transfer through the finned sidewall in the early stage. Xu [257] also investigated the transition from steady to unsteady coupled thermal boundary layers induced by a fin on the partition of a differentially heated cavity and demonstrated that the fin may induce a transition to unsteady coupled thermal boundary layers and the critical Rayleigh value for the occurrence of the transition was between $3.5 \times 10^8 - 3.6 \times 10^8$.

Stability characteristics of conjugate natural convection boundary layers in a differentially heated rectangular cavity, partitioned in the middle by a very thin and infinite thermal conductivity wall were studied by Williamson and Armfield [258]. They found the critical Rayleigh number for the flow to become oscillatory. Xu *et al.* [259] classified unsteady natural convection flows in a partitioned cavity (thin and infinite thermal conductivity partition) into three distinct stages: the initial, transient and steady stages. They examined the transient start-up characteristics of unsteady natural convection flow in both sides of the partition and found that the temperature distribution on the partition surrounded by the coupled convection boundary layers is like an isothermal cavity. However, due to the presence of the partition, the volumetric flow rate and heat transfer are reduced by 37% and 50%, respectively. Additionally, they reported that the partition has approximately isoflux wall behavior at the steady state. In another research conducted by Saha *et al.* [260], the transient natural convection in a partitioned isosceles triangular cavity has been examined. Their results supported the flow classification and partition thermal behavior reported by Xu *et al.* [259]. The same thermal conditions selected by Xu *et al.* [259] was assumed by Saha *et al.* [260], that is, the initial temperatures of the left and right chests of cavities were the same as that on the left and right side walls, respectively. This assumption simplifies the investigation of the thermal behavior of the partition; however, it deviates from the actual conditions in industries or nature.

The numerical results of Ho and Yin [261] show that heat transfer in an air-filled partitioned rectangular cavity is considerably lower than that in a non-partitioned cavity, while the numerical study of Acharya and Tsang [262] shows that inclination angle also has a strong influence on the maximum Nusselt number. Turkoglu and Yucel [263] numerically simulated the flow and conjugate natural convection heat transfer in cavities with multiple conducting partitions

and conducting side walls and found that the increase of the partition number results in the decrease of heat transfer whereas on the other hand the increase of the Rayleigh value results in increased heat transfer. However, they also found that the cavity aspect ratio has no significant bearing on heat transfer within the range considered.

The effect of partition characteristics has been examined in some previous studies. Ghosh *et al.* [264] analyzed the effect of the partition position on the flow structure and heat transfer in a rectangular cavity with a single thin partition, and found that for Ra over $10^3 - 10^7$, the partition location does not have a significant effect on the heat transfer. Tong and Gerner [265] investigated the effect of the position of vertical partition in an air-filled rectangular enclosure. In the study, the partition was assumed to have negligible thermal resistance and the Rayleigh value was in the range of $10^4 - 10^5$. The results show that placing the partition in the middle will result in the largest reduction in heat transfer. Kahveci [5] extended the investigation by making more realistic assumptions on the conducting partitions and examined the effect of partition thickness, conductivity, and position on the Nusselt number of the steady-state laminar natural convection heat transfer at relatively low Rayleigh values, over the range of $10^4 - 10^6$. It is found that when the distance of the partition increases from the left wall towards the middle of the cavity, the average Nusselt number decreases asymptotically towards a constant value and the partition thickness has a negligible effect on the heat transfer. It is also found that the variation of the thermal resistance of the partition leads to substantially different heat transfer changes, which was also found by Kangi *et al.* [266], who studied the effect of the thermal resistance of the partition in a divided tall cavity with a finite thickness partition. Additionally, Kahveci [267] examined the effect of the aspect ratio on natural convection heat transfer in a partitioned cavity and reported that the increase in the aspect ratio leads to an enhanced heat transfer. The transition from the steady to the unsteady coupled thermal boundary layers around a partition in a differentially heated partitioned cavity was investigated numerically by Xu *et al.* [268]. The transition from the steady to the unsteady coupled thermal boundary layers in the water filled cavity over a wide range of Rayleigh numbers from $Ra = 10^9$ to 10^{11} was reported. The dependency of Ra number and heat transfer through the partitioned cavity on the traveling waves in the unsteady coupled thermal boundary layers was characterized and

quantified. Table 2.6 shows some of the studies conducted on the conjugate natural convection.

Table 2.6: List of some of studies on the conjugate natural convection.

Authors	Ra	Pr	**Number of partitions**	A
Williamson and Armfield [258]	0.6×10^{10}– 1.6×10^{10}	7.5	1	2
Xu *et al.* [259]	9.2×10^{8}	6.63	1	1
Acharya and Tsang [262]	up to 10^{7}	0.71	1	$1-2$
Turkoglu and Yucel [263]	$10^{5}-10^{7}$	0.71	$0-4$	$0.5-1.5$
Cuckovic-Dzodzo *et al.* [269]	$10^{4}-10^{6}$	$2700-7000$	$0-1$	1
Nishimura *et al.* [270]	$10^{8}-10^{10}$	6	$0-4$	4
Ghosh *et al.* [264]	$10^{3}-10^{6}$	1	1	$1, 0.8, 0.5$ and 0.4
Tong and Gerner [265]	$10^{4}-10^{5}$	0.71	1	$5, 7.5, 10, 12.5$ and 15
Kahveci [5]	$10^{4}-10^{6}$	0.71	1	1
Kangi *et al.* [266]	$10^{3}-10^{7}$	0.72	$1-5$	$5-20$
Kahveci [267]	$10^{4}-10^{6}$	0.71	1	$0.25-4$
Hanjali *et al.* [271]	$10^{10}-10^{12}$	air & water	$0-1$	$0.5, 0.33$ and 0.66
Nansteel and Greif [272]	$10^{10}-10^{11}$	$3.5-7$	$0-1$	0.5
Xu *et al.* [268]	$10^{9}-10^{11}$	7.8	1	1

2.6.2 Experimental studies

Anderson and Bejan [30] conducted an experimental and theoretical study of natural convection in a differentially heated single or double partitioned cavity. The experiment was carried out in a water-filled cavity, and the overall temperature difference between vertical sidewalls varied

in the range of $6 - 35°C$ with Ra varying in the range $10^9 - 10^{10}$. It is found that the heat transfer can be reduced by inserting vertical partitions. Thermal stratification was observed on both sides of the partition the temperature of the partition steadily increased with altitude. The following expression was extracted for the heat transfer rate,

$$Nu_{Ave} = 0.167 Ra^{1/4}(n+1)^{-0.61}, \tag{2.4}$$

Cuckovic-Dzodzo *et al.* [269] made a numerical and experimental study on the laminar conjugate natural convection flow and heat transfer in a cubic enclosure with and without a heat conducting partition with glycerol as the working medium and the partition placed in the middle of the enclosure. Their results also show that the convective heat transfer in the partitioned cavity is reduced in comparison to that in the cavity without a partition, from 59.1% to 63.6% for the Rayleigh value in the range of 38000 to 369000. Similarly, Nishimura *et al.* [270] conducted a numerical and experimental study on the laminar conjugate natural convection in a rectangular enclosure divided by multiple vertical partitions. In this study, the thickness of the partitions was neglected in the numerical simulation and the partitions were equally spaced in the enclosure. Their results reveal that the Nusselt number was inversely proportional to $(1+N)$, where N is the number of partitions, which is in agreement with their experimental results as well as the results obtained by Cuckovic-Dzodzo *et al.* [269]. Nishimura *et al.* [273] conducted some experimental and numerical computational studies for explaining the heat transfer mechanism and presenting correlations for heat transfer rates in a differentially heated partitioned cavity. They found that heat transfer rate is not sensitive to the partition position. An experiments were carried out over $2.428 \times 10^9 \leq Ra \leq 2.458 \times 10^{10}$ and $5.3701 \leq Pr \leq 6.1697$, with the partition wall placed at the center of the cavity. The temperatures at eight locations in the cavity were measured by Resistance Temperature Detectors (RTDs) and compared with the numerical results [274]. The shadowgraph technique was used by Xu *et al.* [275] to investigate the coupled thermal boundary layers next to a vertical partition placed in the middle of a differentially heated cavity. Water was used as a working fluid for the Rayleigh numbers from 2.6×10^9 to 10^{10}. It was found that the transition from steady to unsteady natural convection flow was from $Ra = 7.9 \times 10^9$ and 10^{10} for $Pr = 7.8$ and $A = 1$ in the fully developed stage.

The instability in the coupled thermal boundary layers adjacent to the partition was described and quantified.

Chapter 3

Numerical method

3.1 Introduction

In this chapter, the governing equations of the natural convection problem in a partitioned cavity with appropriate initial and boundary conditions are described. Numerical procedures for solving the governing equations using finite volume method are also presented.

3.2 Governing equations

The physical system under consideration in this thesis is a two-dimensional partitioned rectangular cavity (with height H and width L and the aspect ratio $A = H/L$), as illustrated in Fig. 3.1. The top and bottom walls of the cavity are adiabatic, and the left and right vertical walls are isothermal fixed at T_h and T_c respectively ($T_h > T_c$, with the dimensionless temperatures $\theta = 1.0$ and $\theta = 0.0$, respectively, where $\theta = (T - T_c)/(T_h - T_c)$). A partition of thickness T_p is placed at the location X_p from the left wall (both T_p and X_p are dimensionless, made dimensionless by L). The working fluid is assumed to be air (Pr=0.71, where Pr is the Prandtl number as will be defined by Eq.(3.10)), which is initially quiescent and at a temperature of $(T_h + T_c)/2$ (*i.e.*, at the dimensionless temperature $\theta = 0.5$). All the interior walls and the par-

tition surfaces are rigid and no-slip. The partition wall is heat conducting, with finite thermal conductivity k_s.

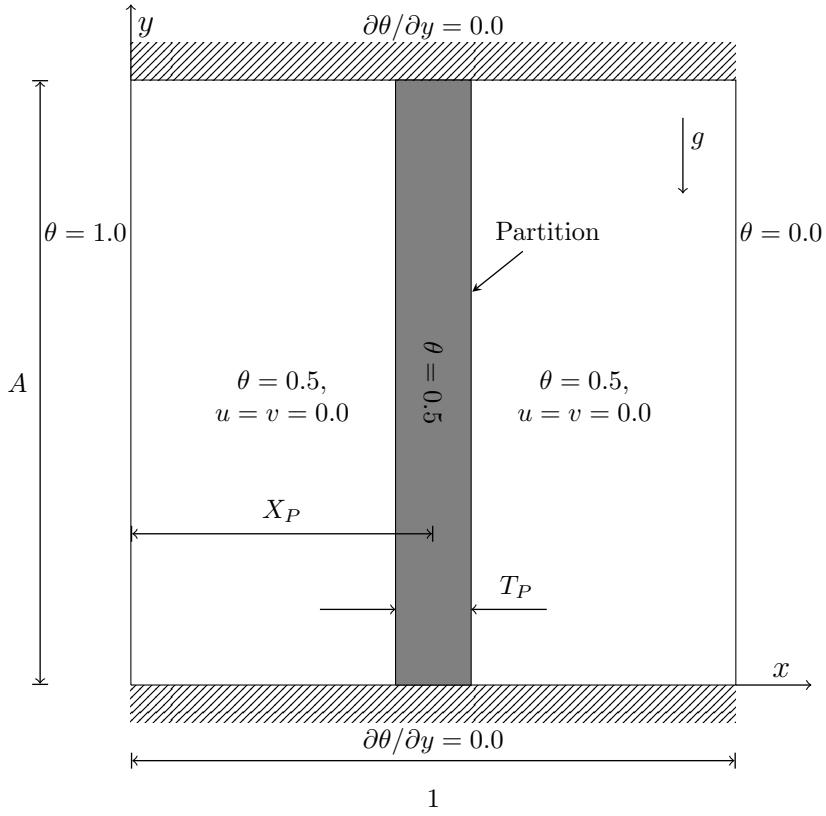

Figure 3.1: Schematic of the computational domain with initial and boundary conditions.

The transient flow of fluid within the cavity is governed by the two-dimensional Navier-Stokes equations with the Boussinesq approximation for buoyancy; that is, density can be assumed to have a linear relation with the temperature and changes in fluid properties are negligible,

$$\rho(T) = \rho(P_0, T_0)[1 - \beta(T - T_0)]. \tag{3.1}$$

This is an appropriate assumption for the current study as the temperature difference between sidewalls of the cavity in the natural convection studies is not large. The Navier-Stokes equations, together with the temperature equation, can be written in dimensionless forms in Cartesian coordinates as follows,

$$\frac{\partial U}{\partial X} + \frac{\partial V}{\partial Y} = 0, \tag{3.2}$$

$$\frac{\partial U}{\partial t} + \frac{\partial (UU)}{\partial X} + \frac{\partial (VU)}{\partial Y} = -\frac{1}{\rho}\frac{\partial P}{\partial X} + \nu \left(\frac{\partial^2 U}{\partial X^2} + \frac{\partial^2 U}{\partial Y^2} \right), \tag{3.3}$$

$$\frac{\partial V}{\partial t}+\frac{\partial (UV)}{\partial X}+\frac{\partial (VV)}{\partial Y}=-\frac{1}{\rho}\frac{\partial P}{\partial Y}+\nu\left(\frac{\partial^2 V}{\partial X^2}+\frac{\partial^2 V}{\partial Y^2}\right)+g\beta(T-T_0), \tag{3.4}$$

$$\frac{\partial T}{\partial t}+\frac{\partial (UT)}{\partial X}+\frac{\partial (VT)}{\partial Y}=\alpha\left(\frac{\partial^2 T}{\partial X^2}+\frac{\partial^2 T}{\partial Y^2}\right). \tag{3.5}$$

The above governing equations can be written in the following dimensionless form,

$$\frac{\partial u}{\partial x}+\frac{\partial v}{\partial y}=0, \tag{3.6}$$

$$\frac{\partial u}{\partial \tau}+\frac{\partial (uu)}{\partial x}+\frac{\partial (vu)}{\partial y}=-\frac{\partial p}{\partial x}+\sqrt{\frac{Pr}{Ra}}\left(\frac{\partial^2 u}{\partial x^2}+\frac{\partial^2 u}{\partial y^2}\right), \tag{3.7}$$

$$\frac{\partial v}{\partial \tau}+\frac{\partial (uv)}{\partial x}+\frac{\partial (vv)}{\partial y}=-\frac{\partial p}{\partial y}+\sqrt{\frac{Pr}{Ra}}\left(\frac{\partial^2 v}{\partial x^2}+\frac{\partial^2 v}{\partial y^2}\right)+\theta, \tag{3.8}$$

$$\frac{\partial \theta}{\partial \tau}+\frac{\partial (u\theta)}{\partial x}+\frac{\partial (v\theta)}{\partial y}=\sqrt{\frac{1}{RaPr}}\left(\frac{\partial^2 \theta}{\partial x^2}+\frac{\partial^2 \theta}{\partial y^2}\right), \tag{3.9}$$

where x and y are the dimensionless coordinates , u and v are the dimensionless velocity components in the x and y directions, and τ , p and θ are the dimensionless time, pressure and temperature, respectively, which are made dimensionless by their respective scales as follows,

$$x=\frac{X}{H},\quad y=\frac{Y}{H},\quad u=\frac{U}{U_{ref}},\quad v=\frac{V}{U_{ref}},$$

$$\tau=\frac{U_{ref}}{H}t,\quad p=\frac{P}{\rho_f U_{ref}^2},\quad \theta=\frac{T-T_c}{T_h-T_c},$$

in which the dimensional quantities X and Y are the coordinates, U and V are the velocity components in the X and Y directions, and t, P, T and ρ_f are the time, pressure, temperature, and density of fluid, respectively. $U_{ref}=\frac{\kappa_f}{H}\sqrt{PrRa}$ is the velocity scale, where the Prandtl number (Pr) and the Rayleigh value (Ra) are defined as follows,

$$Pr=\frac{\nu_f}{\kappa_f},\quad Ra=\frac{g\beta_f(T_h-T_c)H^3}{\nu_f\kappa_f}, \tag{3.10}$$

in which g is the acceleration due to gravity, ν_f , κ_f and β_f are the kinematic viscosity, thermal diffusivity and the coefficient of volumetric expansion of fluid, respectively. The heat transfer

within the heat-conducting partition is governing by the following dimensionless equation,

$$\frac{\partial \theta}{\partial \tau} = \frac{k_r}{\sqrt{RaPr}} \left(\frac{\partial^2 \theta}{\partial x^2} + \frac{\partial^2 \theta}{\partial y^2} \right), \tag{3.11}$$

where k_r is the thermal conductivity ratio defined as follows,

$$k_r = \frac{k_s}{k_f}. \tag{3.12}$$

The initial conditions (when $\tau = 0$) are $u = v = 0$ and $\theta = 0.5$ everywhere within the cavity and the partition, and for $\tau > 0$ the boundary conditions for fluid are $u = v = 0$ on all solid surfaces, $\partial\theta/\partial y = 0$ on the top and bottom walls, and $\theta = 1$ and $\theta = 0$ on the left and right vertical walls, respectively, and the boundary conditions for the partition wall are,

$$\left.\begin{aligned} u = v = 0, \quad k_r \left(\frac{\partial \theta}{\partial y} \right)_{x_1^-} &= \left(\frac{\partial \theta}{\partial y} \right)_{x_1^+}, \quad \text{at } x = x_1, \\ u = v = 0, \quad k_r \left(\frac{\partial \theta}{\partial y} \right)_{x_2^-} &= \left(\frac{\partial \theta}{\partial y} \right)_{x_2^+}, \quad \text{at } x = x_2, \end{aligned}\right\} \tag{3.13}$$

where x_1 and x_2 are the locations of the left and right sides of the partition wall and the associated superscripts '-' and '+' denote their nearest left and right cells, respectively. Figure 3.1 shows the initial and boundary conditions in a partitioned cavity used in this study.

3.3 Heat transfer analysis

The convective heat transfer behavior can be characterized by the Nusselt number. This dimensionless parameter is defined as the ratio of convection heat transfer to fluid conduction heat transfer under the same condition as follows,

$$Nu_{Ave} = \frac{Qconvection}{Qconduction}. \tag{3.14}$$

By considering the cavity illustrated in figure 3.1, the average Nusselt number can be presented as,

$$Nu_{Ave} = \int_0^1 Nu_{Local} dy, \tag{3.15}$$

where Nu_{Local} is local Nusselt number at the specific location x which is calculated by

$$Nu_{Local} = \left(\frac{\partial \theta}{\partial x}\right)\Big|_x. \tag{3.16}$$

Figure 3.2 schematically shows the heat transfer process in a partitioned cavity. Heat transfers from the hot wall (at T_h) on the left side of the cavity through conduction (at low Ra) or convection (at high Ra) to the left side of the partition (at $x = x_1$). The heated left side of the partition (T_{x_1}) transfers energy through conduction to the right side of the partition (T_{x_2}). Subsequently, there is a heat transfer phenomenon between the right side of the partition and the cold wall (at T_c).

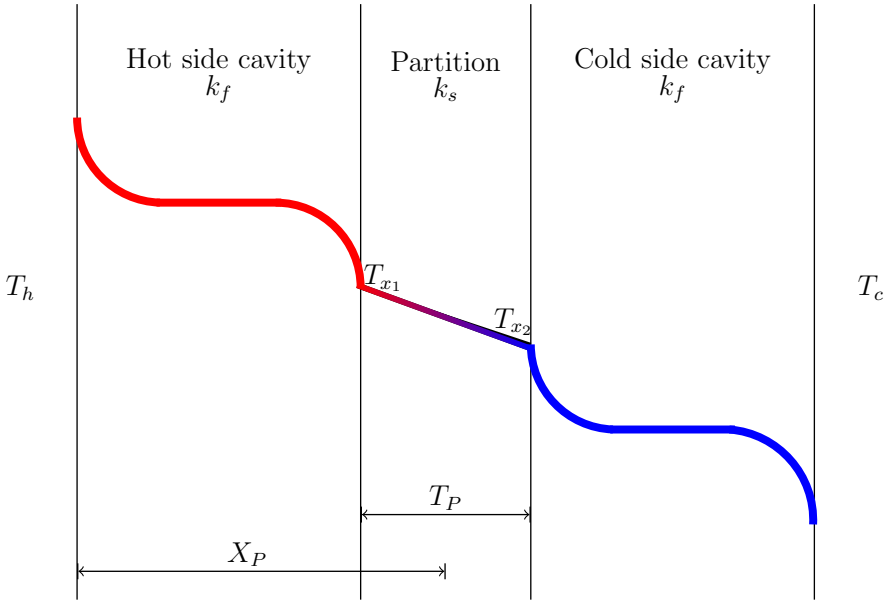

Figure 3.2: Schematic presentation of heat transfer in a partitioned cavity.

3.4 Numerical method

The governing equations (3.6) to (3.9) and (3.11) were discretized on a staggered mesh [276] using the finite volume method and solved by the SIMPLE algorithm [277]. The location of the staggered mesh with 7×7 grids, as an example, are illustrated in figure 3.3. The staggered mesh concept is based on having offsetted one-half of a mesh spacing to the left and below for the horizontal and vertical velocity points respectively. The QUICK scheme [278] and the central difference scheme were employed for the advection and diffusion terms and the Adam-Bashforth scheme [279] was used for time integration.

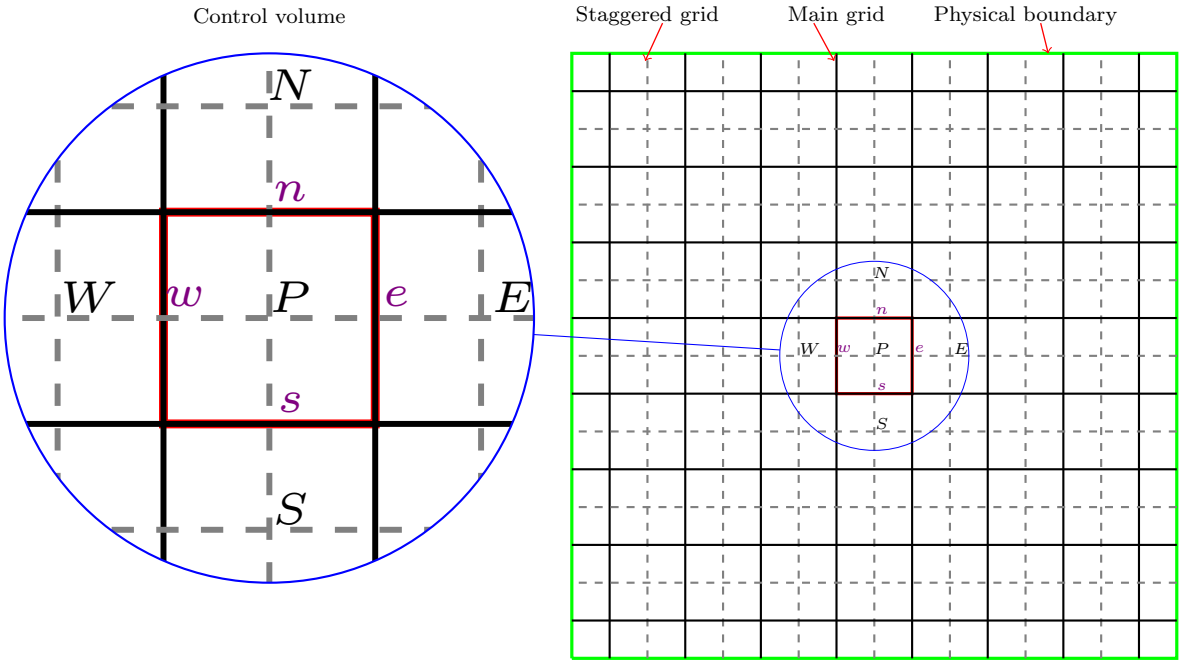

Figure 3.3: The staggered mesh locations as well as the control volume used to descretise the governing equations.

3.4.1 Discretization of the governing equations

The transport equations (3.7) to (3.9) can be represented generally as,

$$\rho\frac{\partial\phi}{\partial t} + \rho u\frac{\partial\phi}{\partial x} + \rho v\frac{\partial\phi}{\partial y} = \Gamma\left(\frac{\partial^2\phi}{\partial x^2} + \frac{\partial^2\phi}{\partial y^2}\right) + S, \tag{3.17}$$

The two-dimensional control volume illustrated in figure 3.3 is used in the discretisetion of the general transport equation. The grid point P has east (E), west (W), north (N) and south (S) neighbours and cell faces of e, w, n and s are placed midway between grid points and the corresponding neighbours. The integration is performed over the control volume and also temporally over a time increment Δt, as follows,

$$\begin{aligned}\int_t^{t+\Delta t}(\int_{CV}\rho\frac{\partial\phi}{\partial t}dV)dt+\int_t^{t+\Delta t}(\int_{CV}\rho u\frac{\partial\phi}{\partial x}dV)dt+\int_t^{t+\Delta t}(\int_{CV}\rho v\frac{\partial\phi}{\partial y}dV)dt=\\ \int_t^{t+\Delta t}(\int_{CV}\Gamma\frac{\partial^2\phi}{\partial x^2}dV)dt+\int_t^{t+\Delta t}(\int_{CV}\Gamma\frac{\partial^2\phi}{\partial y^2}dV)dt+\int_t^{t+\Delta t}(\int_{CV}SdV)dt.\end{aligned} \tag{3.18}$$

By changing the order of integration for the unsteady term, this term becomes,

$$\int_t^{t+\Delta t}(\int_{CV}\rho\frac{\partial\phi}{\partial t}dV)dt=\int_{CV}(\int_t^{t+\Delta t}\rho\frac{\partial\phi}{\partial t}dt)dV=\rho(\phi_P-\phi_P^0)\Delta V, \tag{3.19}$$

where ϕ_P and ϕ_P^0 are the value of transport variable at time $t+\Delta t$ and t respectively. The unsteady term can be descretised by using higher order schemes. The Adams-Bashforth scheme (AB2) is an explicit, second order, three-level scheme which extrapolates forward-in-time from known values to give a mid-point value. Figure 3.4 shows the linear extrapolation from known values to a mid-point in the time-stepping interval, which takes the following form,

$$\phi^{n+1}-\phi^n=\Delta t(\frac{3}{2}\phi^n-\frac{1}{2}\phi^{n-1}). \tag{3.20}$$

For the diffusion term, the volume integrals are converted to surface integrals by the divergence theorem [280] and can be presented for the x direction as,

$$\int_t^{t+\Delta t}(\int_{CV}\Gamma\frac{\partial^2\phi}{\partial x^2}dV)dt=\int_t^{t+\Delta t}[(\Gamma A\frac{\partial\phi}{\partial x})_e-(\Gamma A\frac{\partial\phi}{\partial x})_w]dt. \tag{3.21}$$

By assuming the diffusion coefficient as a constant value equal surface area for the eastern and western control surfaces, equation (3.21) becomes,

$$\int_t^{t+\Delta t}(\int_{CV}\Gamma\frac{\partial^2\phi}{\partial x^2}dV)dt=\Gamma A\int_t^{t+\Delta t}[(\frac{\partial\phi_E-\phi_P}{\Delta x_{PE}})-(\frac{\partial\phi_P-\phi_W}{\Delta x_{WP}})]dt. \tag{3.22}$$

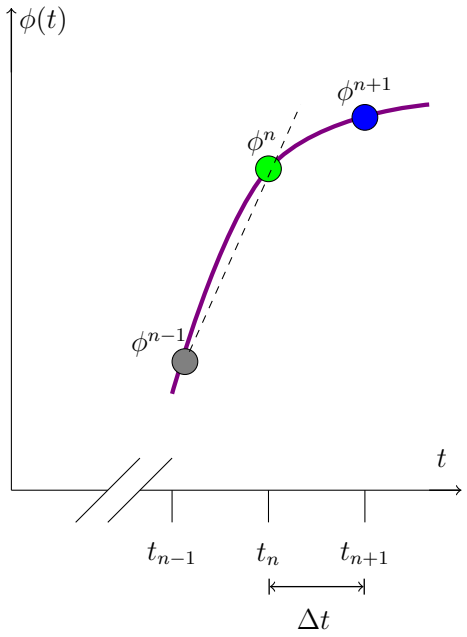

Figure 3.4: Illustration of the extrapolation used in the Adams-Bashforth method.

Similarly the same method is applied for the y direction. The divergence theorem is also utilized for the convective term as follows,

$$\begin{aligned} &\int_t^{t+\Delta t}(\int_{CV}\rho u\frac{\partial\phi}{\partial x}dV)dt = \\ &\int_t^{t+\Delta t}[(\rho uA\phi)_e-(\rho uA\phi)_w]dt = \\ &\rho u_eA\phi_e\Delta t-\rho u_wA\phi_w\Delta t. \end{aligned} \tag{3.23}$$

The control surface values of ϕ (ϕ_e and ϕ_w) presented in equation (3.23) must be interpolated from the grid point values by a suitable scheme. Many interpolation schemes have been developed previously, such as the central difference scheme, the upwind scheme (donor-cell method), the hybrid difference scheme [281], the power law scheme [277], and the quadratic upstream interpolation for convective kinetics (QUICK) scheme [282]. The simplest differencing scheme used for the convective term is the upwind scheme. In this method, the face values are equal to the value of the upstream grid point and can be presented as,

$$\phi_e=\phi_P\frac{max(u_e,0)}{u_e}-\phi_E\frac{max(-u_e,0)}{u_e}, \tag{3.24}$$

$$\phi_w = \phi_W \frac{max(u_w, 0)}{u_w} - \phi_P \frac{max(-u_w, 0)}{u_w}, \tag{3.25}$$

where the function $max(x, y)$ is defined to be equal to x if $x > y$ and to y if $x < y$.

Finally the source term is descritised as,

$$\int_t^{t+\Delta t} (\int_{CV} S dV) dt = \bar{S} \Delta t \Delta V, \tag{3.26}$$

where $\bar{S}$ is the average value of S over the control volume. To avoid writing complex and long equations, two new variables are defined as follows,

$$\begin{aligned} F &= \rho u A_{CS}, \\ D &= \frac{\Gamma A_{CS}}{\Delta x}, \end{aligned} \tag{3.27}$$

where A_{CS} is the corresponding control surface area. By applying the same method for the y direction and plugging the descretised terms into the general transport finite volume equation and using equation (3.27), the following equation is obtained,

$$\begin{aligned} a_P \phi_P &= a_E \phi_E + a_W \phi_W + a_N \phi_N + a_S \phi_S + b \\ &= \sum_{nb} a_{nb} \phi_{nb} + b, \end{aligned} \tag{3.28}$$

where nb stands for the neighbour cell and the coefficients of the transport variable are defined as,

$$\left.\begin{aligned} a_E &= max(-F_e, 0) + D_e, \quad a_W = max(-F_w, 0) + D_w, \\ a_N &= max(-F_n, 0) + D_n, \quad a_S = max(-F_s, 0) + D_s, \\ b &= \rho \phi_P^0 \frac{\Delta V}{\Delta t} + \bar{S} \Delta V, \quad a_P^0 = \rho \frac{\Delta V}{\Delta t}, \\ a_P &= a_E + a_W + a_N + a_S + a_P^0 + (F_e - F_w) + (F_n - F_s). \end{aligned}\right\} \tag{3.29}$$

By using different interpolation schemes, the coefficients presented in the final descretised equation change. In the case of choosing hybrid differencing scheme the neighbouring nodal coeffi-

cients are as follows,

$$\left.\begin{aligned} a_E &= max[-F_e, (D_e - \frac{F_e}{2}), 0], \quad a_W = max[F_w, (D_w + \frac{F_w}{2}), 0], \\ a_N &= max[-F_n, (D_n - \frac{F_n}{2}), 0], \quad a_S = max[F_s, (D_s + \frac{F_s}{2}), 0]. \end{aligned}\right\} \tag{3.30}$$

The QUICK method, as another method, is a three-point upstream weighted quadratic interpolation scheme which can be used to calculate the discrete fluxes entering or leaving a control volume (face values). Figure 3.5 shows the control volume for the node i as well as the upstream and downstream nodes. The subscripts FW, W, P, E, and FE refer to the far west, west, central, east, and far east nodes. The subscripts w and e refer to the left and right faces.

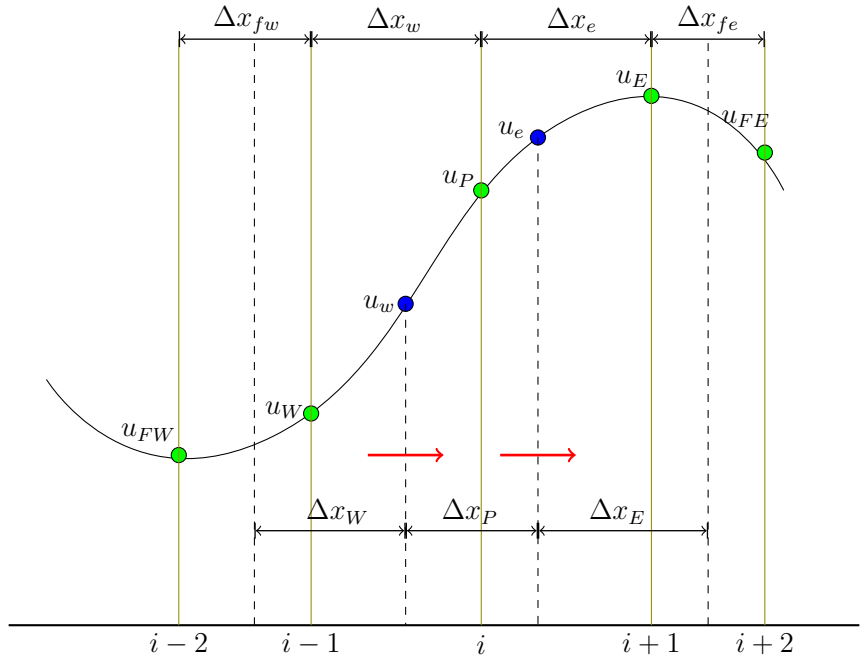

Figure 3.5: Control volume and nodes for QUICK method.

For uniform grids, the face values of a flow to the right can be presented as follows,

$$u_w = \frac{1}{2}(u_W + u_P) - \frac{1}{8}(u_{FW} + u_P - 2u_W), \tag{3.31}$$

$$u_e = \frac{1}{2}(u_P + u_E) - \frac{1}{8}(u_W + u_E - 2u_P). \tag{3.32}$$

This scheme can be simply interpreted as a combination of a linear interpolation (the fist term

on the right hand side) and a correction obtained by the upstream-weighted curvature (the second term on the right hand side).

For the case of non-uniform grid the face values can be estimated as,

$$u_w = \frac{1}{2}(u_W + u_P) - \frac{\Delta x_w^2}{8}\frac{1}{\Delta x_W}(\frac{u_P - u_W}{\Delta x_w} - \frac{u_W - u_{FW}}{\Delta x_{fw}}), \tag{3.33}$$

$$u_e = \frac{1}{2}(u_P + u_E) - \frac{\Delta x_e^2}{8}\frac{1}{\Delta x_P}(\frac{u_E - u_P}{\Delta x_e} - \frac{u_P - u_W}{\Delta x_w}). \tag{3.34}$$

Adding the pressure gradient term to the equation (3.28) (extracting from the source term) changes it to the following form,

$$\begin{aligned} a_e u_e &= \sum_{nb} a_{nb} u_{nb} + (P_P - P_E)A_e + b_e, \\ a_n u_n &= \sum_{nb} a_{nb} u_{nb} + (P_P - P_N)A_n + b_n. \end{aligned} \tag{3.35}$$

To calculate transport variables, pressure should be known. The SIMPLE algorithm indicates that discrete continuity equation should be substituted into the momentum equations containing the pressure terms which result in an equation for discrete pressure. The SIMPLE solves pressure correction by guessing an initial flow field and pressure distribution in the domain. The guessed pressure (P^*) form the previous iteration helps to solve velocities,

$$\begin{aligned} a_e u_e^* &= \sum_{nb} a_{nb} u_{nb}^* + (P_P^* - P_E^*)A_e + b_e, \\ a_n u_n^* &= \sum_{nb} a_{nb} u_{nb}^* + (P_P^* - P_N^*)A_n + b_n. \end{aligned} \tag{3.36}$$

These guessed velocities do not satisfy the continuity due to the guessed pressure. Consequently, pressure and velocities should be corrected as follows,

$$\begin{aligned} u &= u^* + u', \\ v &= v^* + v', \\ p &= p^* + p', \end{aligned} \tag{3.37}$$

where the superscript prime is for the correction and the superscript star for the guessed variables.

By subtracting equations (3.36) from equations (3.35), the following equation are obtained,

$$\begin{aligned} a_e u'_e &= \sum_{nb} a_{nb} u'_{nb} + (P'_P - P'_E) A_e, \\ a_n u'_n &= \sum_{nb} a_{nb} u'_{nb} + (P'_P - P'_N) A_n. \end{aligned} \tag{3.38}$$

Finally the velocity correction equations are obtained by omitting the first terms on the right hand side of the equations (3.38) and become as follows,

$$\begin{aligned} u'_e &= \frac{A_e}{a_e}(P'_P - P'_E), \\ u'_n &= \frac{A_n}{a_n}(P'_P - P'_N). \end{aligned} \tag{3.39}$$

Using equation (3.39) in equation (3.37) leads to,

$$\begin{aligned} u_e &= u^*_e + \frac{A_e}{a_e}(P'_P - P'_E), \\ u_n &= u^*_n + \frac{A_n}{a_n}(P'_P - P'_N). \end{aligned} \tag{3.40}$$

The pressure correction can be obtained by substituting equation (3.40) in the discrete continuity equation and can be presented as,

$$a_P p'_P = a_E p'_E + a_W p'_W + a_N p'_N + a_S p'_S + b, \tag{3.41}$$

where

$$\left.\begin{aligned} a_E &= \rho_e \frac{A_e}{a_e}\Delta y, \quad a_W = \rho_w \frac{A_w}{a_w}\Delta y, \\ a_N &= \rho_n \frac{A_n}{a_n}\Delta x, \quad a_S = \rho_s \frac{A_s}{a_s}\Delta x, \\ a_P &= a_E + a_W + a_N + a_S, \\ b &= \frac{(\rho^0_P - \rho_P)\Delta x \Delta y}{\Delta t} + [(\rho u^*)_w - (\rho u^*)_e]\Delta y + [(\rho v^*)_s - (\rho v^*)_n]\Delta x. \end{aligned}\right\} \tag{3.42}$$

Using the SIMPLE algorithm, there are four partial differential equations to be solved. There are many methods introduced for solving a linear system of equations such as matrix inversion, Gauss elimination, Gauss-Seidel, TDMA (tridiagonal matrix algorithm), BiCgSta (Bi-Conjugate Gradient stabilized iterative matrix solver), GpBiCg (Generalized Product Bi-Conjugate Gradient iterative matrix solver), MlkBiCgStab (Multiple-Lanczos Bi-Conjugate Gradient stabilized iterative matrix solver), TFQMR (Transpose Free Quasi-Minimal Residual iterative matrix solver), as presented in (3.28). The tridiagonal matrix algorithm or Thomas algorithm is usually the preferred method. The one-dimensional discretised equation can be written as,

$$a_{W_i}\phi_{i-1} + a_{P_i}\phi_i + a_{E_i}\phi_{i+1} = b_i. \tag{3.43}$$

This method consists of a forward elimination and a backward substitution procedure. The coefficients for the forward sweep are as follows,

$$A_i = \begin{cases} \dfrac{a_{E_1}}{a_{P_1}} & i = 1, \\ \dfrac{a_{E_i}}{a_{P_i} - A_{i-1}a_{W_i}} & i = 2, 3, ..., N, \end{cases} \tag{3.44}$$

$$B_i = \begin{cases} \dfrac{b_1}{a_{P_1}} & i = 1, \\ \dfrac{b_i - B_{i-1}a_{W_i}}{a_{P_i} - A_{i-1}a_{W_i}} & i = 2, 3, ..., N. \end{cases} \tag{3.45}$$

By the backward substitution the sweep solution can be obtained,

$$\phi_i = \begin{cases} B_N & i = N, \\ B_i - A_i\phi_{i+1} & i = N-1, N-2, ..., 1. \end{cases} \tag{3.46}$$

This method can be applied to equation (3.28) by rearranging it to the tridiagonal system of equations and assuming $N - S$ direction to be constant for every sweep,

$$-a_W\phi_W + a_P\phi_P - a_E\phi_E = a_N\phi_N + a_S\phi_S + b, \tag{3.47}$$

The line by line solution procedure is illustrated in figure 3.6. To solve the equations for the

points along each line (*e.g.*, $W - E$ line), the values on the neighboring lines are assumed to be temporarily known. Therefore, the equation for each point of the line reduces to a one-dimensional equation with three unknowns (*e.g.*, ϕ_W, ϕ_E and ϕ_P). The obtained set of equations for all points are much simpler and can produce a tridiagonal matrix. The equations of this type are easy to be solved by the TDMA method.

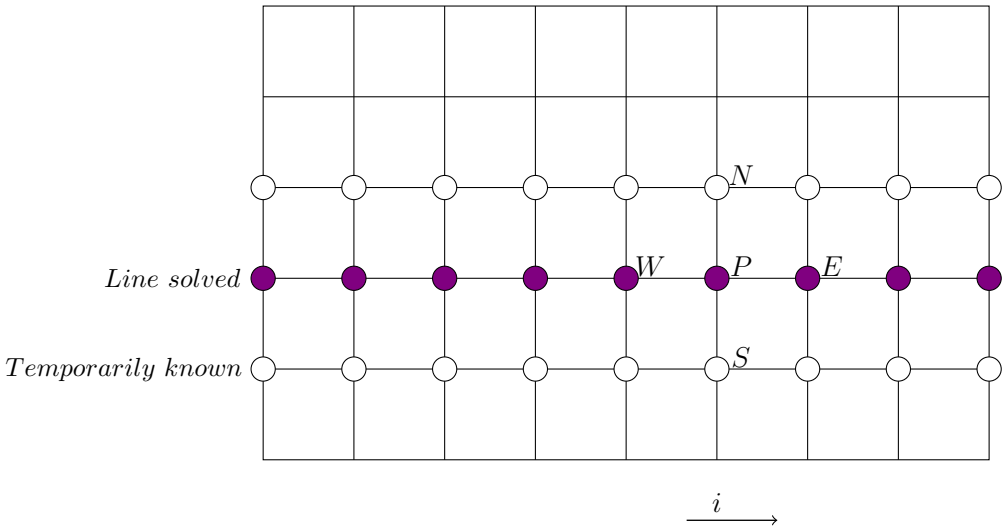

Figure 3.6: The line by line procedure.

It is essential to monitor the convergence of the solution within a time step in order to be able to advance in time. The convergence monitoring can be achieved by checking how well the equation (3.28) is satisfied. The residual can be obtained as follows,

$$R_\phi = a_E\phi_E + a_W\phi_W + a_N\phi_N + a_S\phi_S + b - a_P\phi_P. \tag{3.48}$$

It is expected that the residuals decay to small values. Various convergence criteria have been selected for different studies. It is commonly acknowledged that 10^{-6} is suitable for most of the natural convection studies. The SIMPLE algorithm flowchart is presented in figure 3.7.

To prevent divergence, it is necessary to restrain the speed of solution by balancing the newly achieved result with the previous one. The generally successful practice is called under-

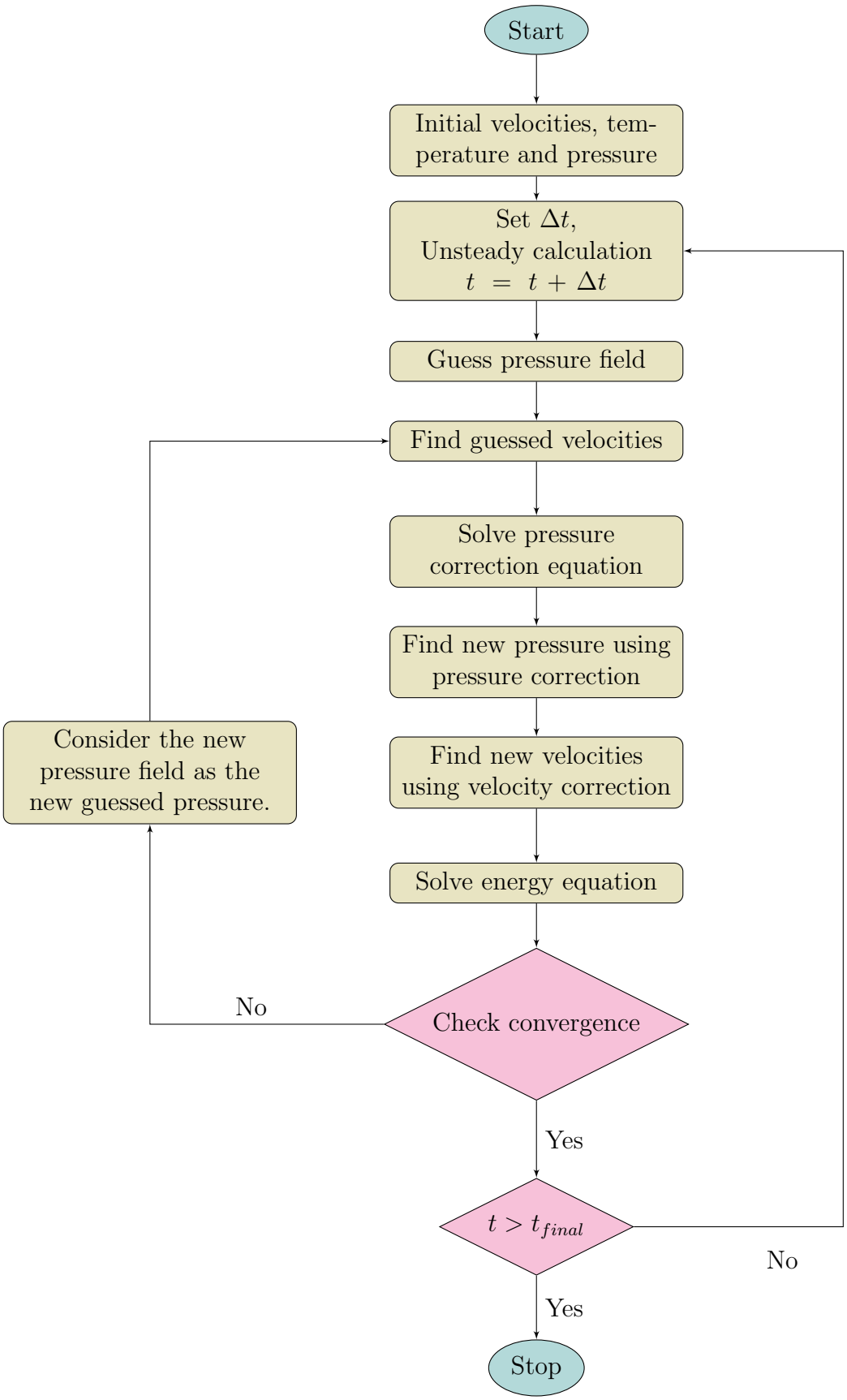

Figure 3.7: The SIMPLE Algorithm flowchart.

relaxation and can be described as follows,

$$\begin{aligned} p &= p^* + \alpha_p p', \\ u^{new} &= \alpha_u u + (1-\alpha_u) u^{old}, \\ v^{new} &= \alpha_v v + (1-\alpha_v) v^{old}, \\ T^{new} &= \alpha_T T + (1-\alpha_T) T^{old}. \end{aligned} \tag{3.49}$$

Chapter 4

Numerical implementation

4.1 Introduction

The computer code written in Visual *C#* programming language was developed for this thesis by implementing the numerical methods presented in the previous chapter.

The programming language Visual *C#* is simple, modern, general-purpose and object-oriented. Visual *C#* has a strong type checking, array bounds checking, detection of attempts to use uninitialized variables, and automatic garbage collection which increases software robustness and durability. The code can be edited in the Microsoft Visual Studio platform or other similar editors. To use and run the code, having the Microsoft Visual Studio is not necessary if the inputs are entered and compiled. Users can simply run the *exe* file in the *Release* folder of the code. Therefore, the code is easily portable and executable in any Windows operating system.

The Nomenclature of the TEACH code [283] (originated at the Imperial College), which is similar to the TEAM (Turbulent Elliptic Algorithm of Manchester) codes [284] (developed at the University of Manchester), is mainly adopted in the current code to increase readability. To further improve the readability of this code, the structure of the code was designed to have separate and independent sections (called methods in Visual *C#*). Each method is a code block that contains a series of statements and can be executed in the program by calling them and

designating the required arguments which are specific to that method. Consequently, methods help code developers or users to have better understanding and control of the code and easier editing and debugging processes.

The flowchart of the code is illustrated in figure 4.1. Prior to the main calculation section of the code, it is necessary to define variables and their initial their values or sizes. Table 4.1 lists the main variable types used in the code with their specifications.

Table 4.1: Variable used in the code and their specifications

Integers		
Name	Range	
int	$-2,147,483,648 - 2,147,483,647$	
short	$-32,768 - 32,767$	
long	$-9,223,372,036,854,775,808 - 9,223,372,036,854,775,807$	
Floating point numbers		
Name	Approximate range	Precision
double	$\pm 5.0 \times 10^{324} - \pm 1.7 \times 10^{308}$	15-16 digits
float	$-3.4 \times 10^{38} - +3.4 \times 10^{38}$	7 digits
decimal	$1.0 \times 10^{-28} - 7.9 \times 10^{28}$	28-29 digits
Boolean values		
Name	Value	
bool	true or false	
Strings and chars		
Name	Value	
string	textual data	

A variable can be defined as a local or global one. A global variable in the code has the $G.$ prefix and is accessible for all methods. The main global variables defined are grid variables and main calculation variables. Tables A.1 and A.2 in the appendix section list the main global and local variables with their types and description. Hence, before running the code, it is needed to decide the maximum size of grids (*i.e.*, IT and JT) which consequently defines the

size of all grids and main variable arrays. The code automatically generates the needed folders and sub-folders for saving results. Depends on the selected solution platform ($x32$ or $x64$) the $OUTPUT$ folder is created at $bin\backslash Release$ or $bin\backslash x64$, respectively. Figure 4.11 shows the details regarding creating the necessary folder at the requested address.

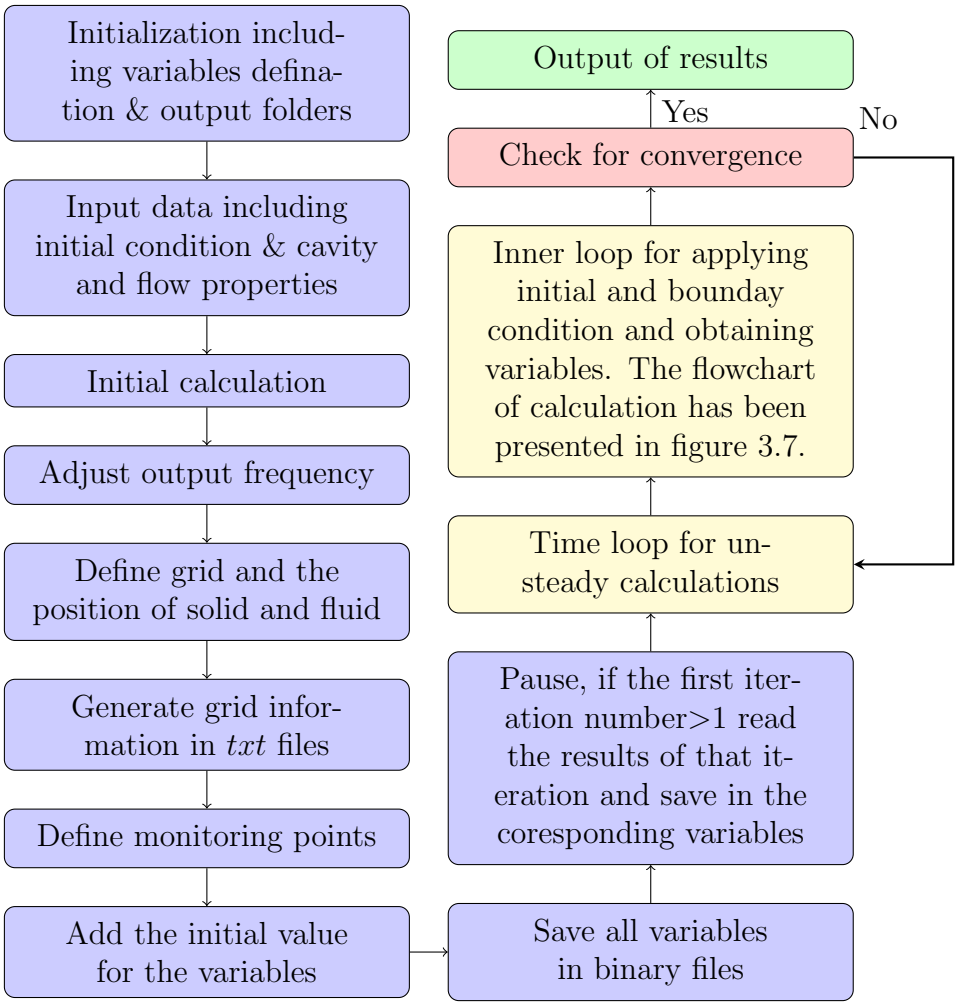

Figure 4.1: Flowchart for explaining main procedure of the code.

At the input section of the code, all information regarding grid, partition, time step, fluid and solid properties and solvers should be provided. For the next step, the code calculates some necessary initial data such as converting some input data to the dimensionless or dimensional form. The output frequency is the next section of the code which initiates an array to decide how often output should be generated. This section has a default data but can be edited.

The grid section of the code is responsible to generate arrays for the main and staggered grid points and sizes. As grid mapping has four options of uniform, manual non-uniform, non-

uniform Sin function, and non-uniform linear function, users can select one of them in the input section by variable $MESH\_TYPE1$. Figures 4.2 and 4.3 show how grid spacings are developed by the specified functions.

```
// Sin function
for (int i = 2; i <= G.NI; i++)
{
G.XU[i] = ELBYH * ((i - 2) / ((float)NIM2) - MeshParCoef2 / (MeshParCoef1
    * Math.PI) * Math.Sin(MeshParCoef1 * Math.PI * (i - 2) /
    ((float)NIM2)));
}
for (int j = 2; j <= G.NJ; j++)
{
G.YV[j] = ELBYH * ((j - 2) / ((float)NJM2) - MeshParCoef2 / (2 * Math.PI)
    * Math.Sin(2 * Math.PI * (j - 2) / ((float)NJM2)));
}
```

Figure 4.2: Grid mapping using a sin function.

```
    // Liear function
    // Changing sign location
    double IXC = 0.5;
    double JXC = 0.5;
    // Strength of grid , Strength>0 gives concentrated points inside
        cavity and strength<0 gives concentrated points at the ends.
    double JSTRENGTH = 1.0;
    for (int i = 2; i <= G.NI; i++)
    {
    G.XU[i] = ((i - 2) / ((float)NIM2)) + (IXC - ((i - 2) / ((float)NIM2)))
        * (1 - ((i - 2) / ((float)NIM2))) * ((i - 2) / ((float)NIM2)) *
        ISTRENGTH;
    }
    for (int J = 2; J <= G.NJ; J++)
    {
    G.YV[J] = ((J - 2) / ((float)NJM2)) + (JXC - ((J - 2) / ((float)NJM2)))
        * (1 - ((J - 2) / ((float)NJM2))) * ((J - 2) / ((float)NJM2)) *
        JSTRENGTH;
    }
```

Figure 4.3: Grid mapping using a linear function.

As the grid mapping figures 4.2 and 4.3 show, the code first develops the staggered grid points (*i.e.*, XU and YV) using one of the mapping methods provided. Then, using staggered points, the main grid points are calculated. Figure 4.4 presents the method of calculating the main

grid points and arrays related to grid thickness.

```
1       G.X[1] = G.XU[2]; G.X[G.NI]
            = G.XU[G.NI];
2       for (int i = 2; i <= NIM1;
            i++)
3       {
4       G.X[i] = 0.5 * (G.XU[i + 1]
            + G.XU[i]);
5       }
6       G.Y[1] = G.YV[2]; G.Y[G.NJ]
            = G.YV[G.NJ];
7       for (int j = 2; j <= NJM1;
            j++)
8       {
9       G.Y[j] = 0.5 * (G.YV[j + 1]
            + G.YV[j]);
10      }
11      G.DXPW[1] = 0.0;
            G.DXEP[G.NI] = 0.0;
12      for (int i = 1; i <= NIM1;
            i++)
13      {
14      G.DXEP[i] = G.X[i + 1] -
            G.X[i]; G.DXPW[i + 1] =
            G.DXEP[i];
15      }
16      G.DYPS[1] = 0.0;
            G.DYNP[G.NJ] = 0.0;
17      for (int j = 1; j <= NJM1;
            j++)
18      {
19      G.DYNP[j] = G.Y[j + 1] -
            G.Y[j]; G.DYPS[j + 1] =
            G.DYNP[j];
20      }
21      G.DXPWU[1] = 0.0; G.DXPWU[2]
            = 0.0;
22      G.DXEPU[1] = 0.0;
            G.DXEPU[G.NI] = 0.0;
23      for (int I = 2; I <= NIM1;
            I++)
24      {
25      G.DXEPU[I] = G.XU[I + 1] -
            G.XU[I]; G.DXPWU[I + 1] =
            G.DXEPU[I];
26      }
27      G.DYPSV[1] = 0.0; G.DYPSV[2]
            = 0.0;
28      G.DYNPV[1] = 0.0;
            G.DYNPV[G.NJ] = 0.0;
29      for (int J = 2; J <= NJM1;
            J++)
30      {
31      G.DYNPV[J] = G.YV[J + 1] -
            G.YV[J]; G.DYPSV[J + 1] =
            G.DYNPV[J];
32      }
33      for (int I = 1; I <= G.NI;
            I++)
34      {
35      G.SEW[I] = G.DXEPU[I];
36      }
37      for (int J = 1; J <= G.NJ;
            J++)
38      {
39      G.SNS[J] = G.DYNPV[J];
40      }
41      for (int I = 1; I <= G.NI;
            I++)
42      {
43      G.SEWU[I] = G.DXPW[I];
44      }
45      for (int J = 1; J <= G.NJ;
            J++)
46      {
47      G.SNSV[J] = G.DYPS[J];
48      }
```

Figure 4.4: Grid quantities calculations.

It is important to make sure that the grid stretching factor is not high. Consequently, the code has a section to evaluate this factor. As figure 4.5 shows, the array *stretchingF* contains the stretching factor of the cavity in the x direction.

```
// Check grid stretching factor
double[] stretchingF = new double[G.NI];
for (int i = 2; i < G.NI; i++)
{
    if (G.DXEP[i] > G.DXEP[i + 1])
    {
       stretchingF[i] = (G.DXEP[i] / G.DXEP[i + 1]);
    }
    else
    {
       stretchingF[i] = (G.DXEP[i + 1] / G.DXEP[i]);
    }
}
```

Figure 4.5: Finding stretching factor of the grid in the x direction.

The grid pattern can also be visually investigated. This option can be available by activating the following piece of code presented in figure 4.6 in the requested output method.

```
      // Draw mesh pattern
      Pen transPen = new Pen(Color.FromArgb(145, 150, 150, 150), 2);
      g.DrawRectangle(transPen, (float)centerPoint.X,
      (float)centerPoint.Y,
      (float)XCellDimension[i, j],
      (float)YCellDimension[i, j]);
```

Figure 4.6: Drawing mesh pattern in the graphical outputs.

In the case of the partition presence ($INPART = true$ declared in the input section), the code finds the position of the partition cells based on the input specifications of the partition (the distance from the left wall and the thickness) and the mapped grid. Figure 4.7 shows how a partition is placed in the mapped domain. It is necessary to ensure the placing quality by comparing the requested partition thickness (T_P) with the final partition thickness on the mapped cavity which is presented in this figure.

Additionally, a part of the initial calculation is finding the position of the monitoring points in the mapped cavity. Then, the initial values of all main parameters are assigned to avoid any possible error. Figure 4.8 shows how main variables are initialized. It is worth noting that for some variables $G.SMALL = 1.0E-20$ is used to prevent division by zero.

```
// Partition definition
if (G.INPART)
{
  // Find starting grid
  double SUMMM1 = 0.0; double SUMMM2 = 0.0;
  int IIII = 0;  int MP = 0;
  bool FIND = false;
  for (int i = 2; i <= G.NI; i++)
    {
      if (G.XU[i] >= XP && FIND == false)
        {
          MP = i; IIII = i;
          do
          {
            G.EPa = i;  SUMMM1 += G.DXPWU[i]; i = i + 1;
          } while (SUMMM1 <= TP / 2);
          FIND = true;  SUMMM2 = 0.0;  i = MP;
          do
          {
             G.SPa = IIII - 1; SUMMM2 += G.DXPWU[IIII - 1];
             IIII = IIII - 1;
          } while (SUMMM2 <= TP / 2);
      }
   }
}
// Check the final partition thickness on the domain
double THICKNESS_P = 0.0;
for (int I = G.SPa; I <= G.EPa; I++)
{
   THICKNESS_P += G.DXPWU[I];
}
Console.WriteLine("THICKNESS DIFFERENCE : " + (TP - THICKNESS_P));
```

Figure 4.7: Allocating the partition in the mapped grid and evaluating the accuracy.

Finally, the pause section is the last preparation step before reaching the calculation loops. This part of the code is written to be able to continue the calculation after stopping the code. Since unsteady simulations ($G.STEADY = false$) usually take a long time, unexpected accidents may interrupt the calculation process. In this case, by activating the pause section ($VALUE = 0$), it monitors the current iteration number ($NFTSTP$ in the code) and if this number is bigger than one (the starting point), it asks code to read results of the previous calculation from the default folder ($OUTPUT\backslash DATABANK$) and copy those in their corresponding variables and continue the calculation from the breaking point. Figure 4.9 shows a sample of the code for

```
for (int I = 1; I <= G.NI; I++)
{
  for (int J = 1; J <= G.NJ; J++)
  {
    G.U[I, J] = G.SMALL; G.UO[I, J] = G.SMALL; G.UOO[I, J] = G.SMALL;
    G.V[I, J] = G.SMALL; G.VO[I, J] = G.SMALL; G.VOO[I, J] = G.SMALL;
    G.P[I, J] = G.SMALL; G.PO[I, J] = G.SMALL; G.PP[I, J] = G.SMALL;
    G.T[I, J] = 0.5;      G.TO[I, J] = 0.5;     G.TOO[I, J] = 0.5;
    G.DEN[I, J] = 1.0 + G.SMALL;      G.VIS[I, J] = 1.0 + G.SMALL;
    G.DU[I, J] = 0.0;    G.DV[I, J] = 0.0;
  }
}
```

Figure 4.8: Piece of the code for initializing main variables.

reading the last saved results from binary files and copies their values to the array.

```
if (VALUE == 0)
     {
         // Find the address of binary file
         string pathTr = string.Concat(Environment.CurrentDirectory,
             @"\OUTPUT\DATABANK\T\ " + "T" + NFTSTP + ".bin");
         // Initiate file stream and binary reader
         FileStream fstr = new FileStream(pathTr, FileMode.Open,
             FileAccess.Read);
         BinaryReader bwtr = new BinaryReader(fstr);
         // Copy the values into the array
         for (int i = 0; i <= G.NI; i++)
         {
             for (int j = 0; j <= G.NJ; j++)
             {
                 G.T[i, j] = (bwtr.ReadDouble());
             }
         }
         //Close file stream and binary reader.
         bwtr.Close(); fstr.Close();
     }
```

Figure 4.9: Sample of the code for the pause section.

The main calculation loop starts after the pause section and velocity, pressure and temperature variables are solved by calling appropriate methods. Calculation methods for main variables are separated. Those methods are $CALCU$ for the u velocity component, $CALCV$ for the v velocity component, $CALCT$ for the θ temperature and $CALCP$ for the p pressure and are

presented in appendix B.

Due to having separate and independent methods, the calling process is very easy and is presented in figure 4.10.

```
1       // Calculate U
2       if (G.INCALU) { CALCU(R1, NSWPU, ITSTEP); }
3       // Calculate V
4       if (G.INCALV) { CALCV(R1, NSWPV, TREF, ITSTEP); }
5       // Calculate P
6       if (G.INCALP) { CALCP(IPREF, JPREF, NSWPP, ITSTEP); }
7       // Calculate T
8       if (G.INCALT) { CALCT(R2, NSWPT, ITSTEP); }
```

Figure 4.10: Calling main variable methods in the internal iteration.

After converging (with the convergence criteria $SORMAX$) the calculations, the results of the main variables are saved in binary files according to the defined output frequency. Results have a separate folder and are named based on the variable and its iteration. For instance, in folder $OUTPUT\backslash DATABANK\backslash T$ the file name $T1200.bin$ represents the results of temperature variable at the iteration number 1200. The $DUMP$ method which is responsible for saving binary files is presented in figure 4.11 for the case of the variable T.

In addition to binary files, data for monitoring points, the Nusselt number and other types of results are produced to check the simulation progress. Since these results should be directly available for the users, they are saved in txt files with appropriate format, which can be imported to $Microsoft\ Excel$ or other data processing software. Figure 4.12 shows the universal code written for saving any type of variable in its specific address.

Furthermore, it is possible to turn on other types of outputs in the main code; however, a separate code has been written for solely post-processing purpose. The monitoring of the code can be done by analyzing the txt files of the monitoring points (at least 7 points) or the Nusselt numbers. As those files are time series, the code writes on those files during the simulation and should have access to them. Therefore, for monitoring, the users should pause the code through the Microsoft Visual Studio and then open those files. Opening time series files during

```
static void DUMP(int ITSTEP)
{
    // Create the necessary folder at the requested address
    string path1 = @"OUTPUT\DATABANK" + "\\" + "T";
    try
    {
      DirectoryInfo di = Directory.CreateDirectory(path1);
    } catch (Exception e)
    {
      Console.WriteLine("The process of creating the folder failed: {0}",
          e.ToString());
    }
    // Specify the address of binary file
    string pathT = string.Concat(Environment.CurrentDirectory, @
        "\OUTPUT\DATABANK\T\"" + "T" + ITSTEP + ".bin" );
    FileStream fsT = new FileStream(pathT, FileMode.OpenOrCreate,
        FileAccess.Write);
    BinaryWriter bT = new BinaryWriter(fsT);
    // Write the binary file
    for (int i = 0; i <= G.NI; i++)
    {
     for (int j = 0; j <= G.NJ; j++)
       {
          bT.Write((G.T[i, j]));
       }
    }
    // Close file streaming
    bT.Close(); fsT.Close();
}
```

Figure 4.11: Saving a variable (*e.g.* temperature) in a binary file by an appropriate name and address.

the simulation without pause may cause an error in the simulation and stop the process. After finishing work with the files and closing them, the users can simply press 'continue' button to carry on the rest of simulation.

It is usually preferred to generate the requested outputs after finishing simulations to save space and time. Another code is written in visual $C\#$ to do the post-processing of data using already produced binary files. This program needs the same preparation steps of the main program; however in the calculation loop; it has the output generating code. This code can handle all binary files or a range of them or just specific file of results. Therefore, users can select one of those options based on their needs. The main flowchart of the post-processing code is presented

```
1       static void PRINT(List<string> PHI, string NAME, int ITSTEP)
2       {
3         // Create a folder for the requested variable inside the $OUTPUT$
              folder
4         string path = @"OUTPUT\" + NAME + "\\"";
5         try
6         {
7            DirectoryInfo di = Directory.CreateDirectory(path);
8         } catch (Exception e)
9         {
10           Console.WriteLine("The process of creating the folder failed: {0}",
                 e.ToString());
11        }
12        // Write the results in a text file
13        string pathX = string.Concat(Environment.CurrentDirectory, @"\OUTPUT\
              " + NAME + "\\" + NAME + "_" + ITSTEP + ".txt");
14        FileStream fX = new FileStream(pathX, FileMode.OpenOrCreate,
              FileAccess.Write);
15        using (StreamWriter writer = new StreamWriter(fX))
16        {
17           foreach (string x in PHI)
18           {
19           writer.WriteLine(x);
20           }
21        }
22      }
```

Figure 4.12: Saving a variable (*e.g.* PHI, a general name for any assigned variable) in a *txt* file by an appropriate name and address.

in figure 4.13.

The output section can be classified into two parts. The first part is graphical outputs which include contour pictures of variables and the second part is numerical outputs which are saved in *txt* files. The first part includes many methods, such as *Line* which defines lines and *LineGenerator* which draws lines on a picture or *ColorMap* which defines colours and their gradients. All the methods related to the graphical outputs are illustrated in figure 4.14. These graphical presentations have several options such as adding isolines, selecting the colour range (full colours or two colours gradients) and adapting to uniform or non-uniform grids.

The numerical outputs are mainly generated in response to the requested data for a specific position of a condition and saved in *txt* files. Those results could be time dependent or for

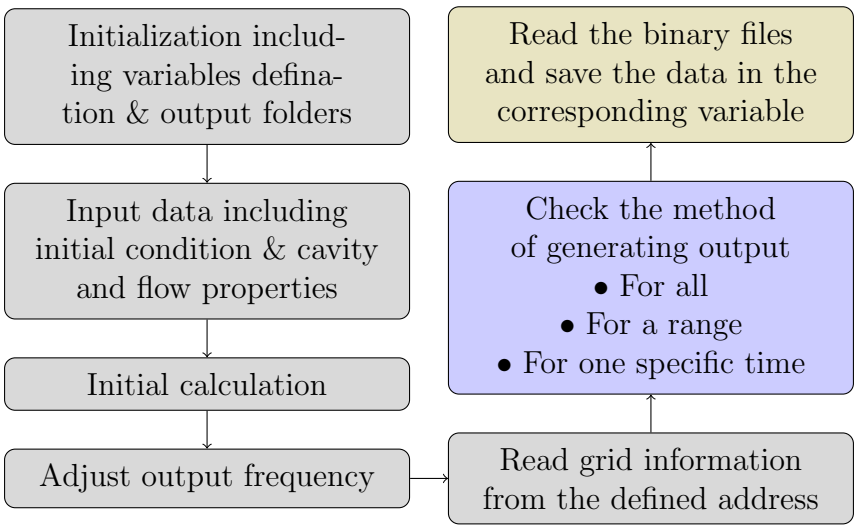

Figure 4.13: Flowchart for explaining the main procedure of the code.

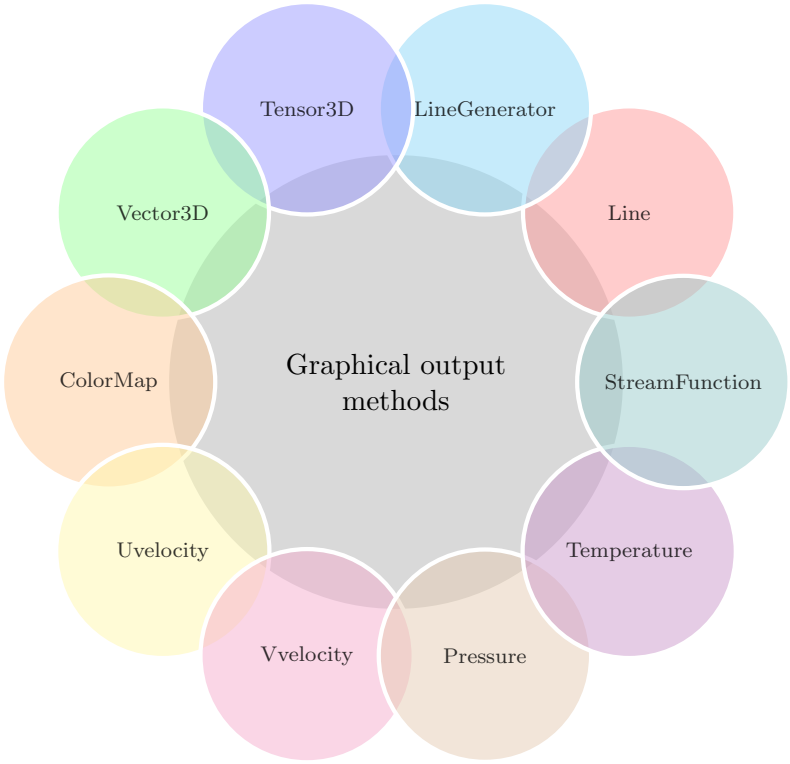

Figure 4.14: Methods written for graphical representation of main variables.

particular time steps. In case of time series, there is always an extra column beside the original data for the time in the result files and for position dependent data that an additional column is for the distance of cells from the origin of the domain. The main methods defined are depicted in figure 4.15.

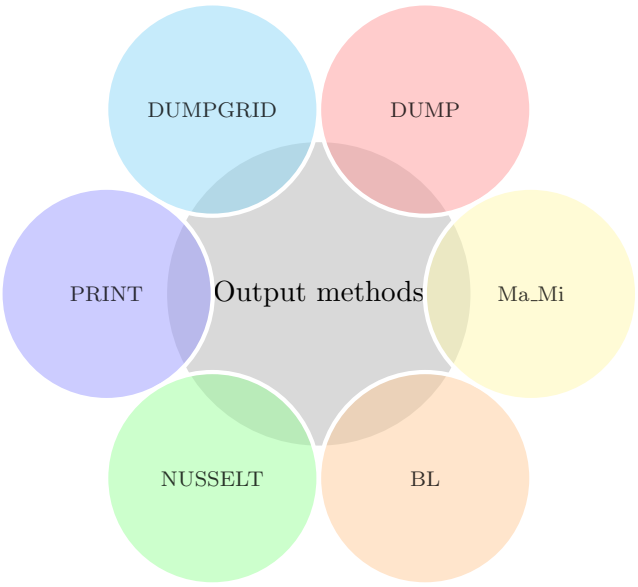

Figure 4.15: Methods written for data saving and generating.

4.2 Code verification and validation

4.2.1 Non-partitioned cavity

A. Time and grid independence test

Accuracy and simulation time are important factors for any numerical simulations. Therefore, obtaining the optimum grid size and time step is essential steps to get an accurate and time-efficient result. The non-uniform grid distribution is selected for mapping the non-partitioned cavity. The domain has finer grids near the walls and coarser grids in the middle. Figure 4.16 shows a schematic of the non-uniform mesh distribution in a non-partitioned cavity.

The grid independence test for $Ra = 10^8$ was performed for four different meshes of 100×100, 160×160, 200×200 and 250×250 and the time step of $\tau = 0.005$. To verify the grid independent solution; a study was carried out on the average and time series of the Nusselt number on the hot wall, which are presented in figure 4.17.

As figure 4.17 shows, as expected, the variation of the average Nusselt number gradually decreases by increasing the mesh size. Since the variation for all cases is less than 1%, the mesh of

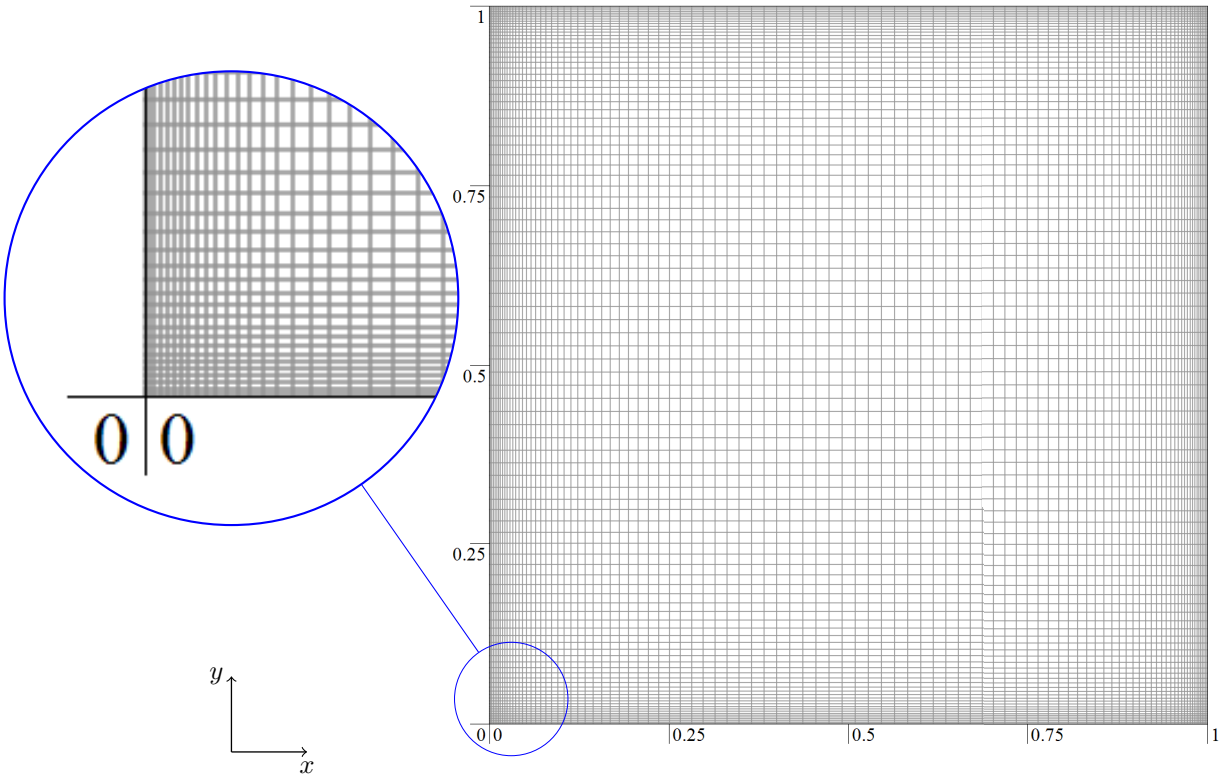

Figure 4.16: The grid distribution for a non-partitioned cavity with the mesh of 100×100.

200×200 was selected as the mesh that produces results with suitable resolution. The smallest grid size is 0.0007 whereas the largest grid size is 0.0093 in the x and y directions, and the maximum grid expansion ratio (or stretching factor) is 1.0524. Table 4.2 quantitatively shows the steady-state results of the temperature at the point $(0.05, 0.5)$ and the average Nusselt number on the hot wall. These results also confirm the selected grid size for the non-partitioned cavity.

Table 4.2: Grid independence tests.

Grid size	Temperature at point $(0.05, 0.5)$	Steady-state average Nusselt number on the hot wall
100×100	0.47125	30.38639
160×160	0.47884	30.27983
200×200	0.47913	30.25848
250×250	0.48075	30.24565

In order to do the time step independence test, the simulations were carried out with different time steps of $d\tau = 10^{-2}$, 5×10^{-3} and 10^{-3}. It is clear from figure 4.18 that the variation of results due to the selected time steps is negligible. Therefore, $d\tau = 10^{-2}$ was chosen for the code validation tests.

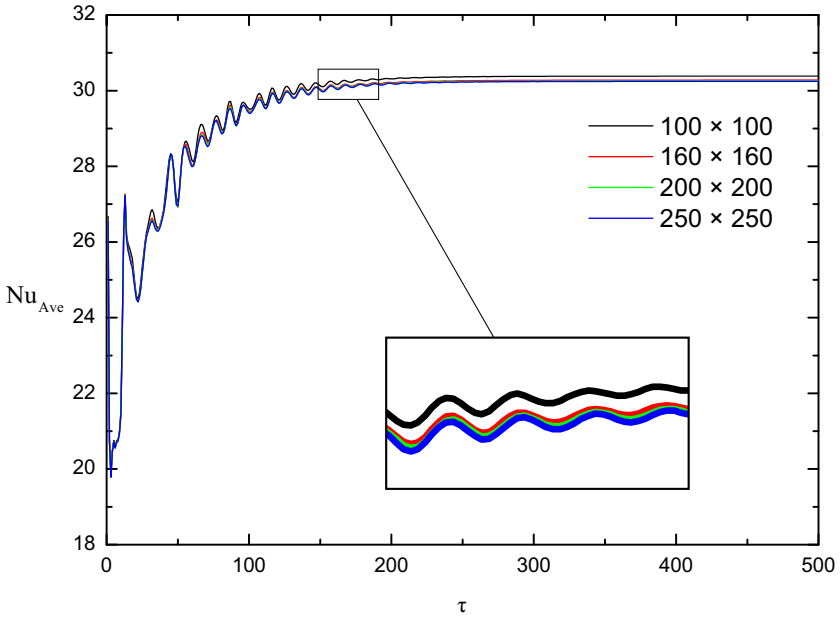

Figure 4.17: Time series of the average Nusselt number on the hot wall for the non-partitioned cavity at different meshes.

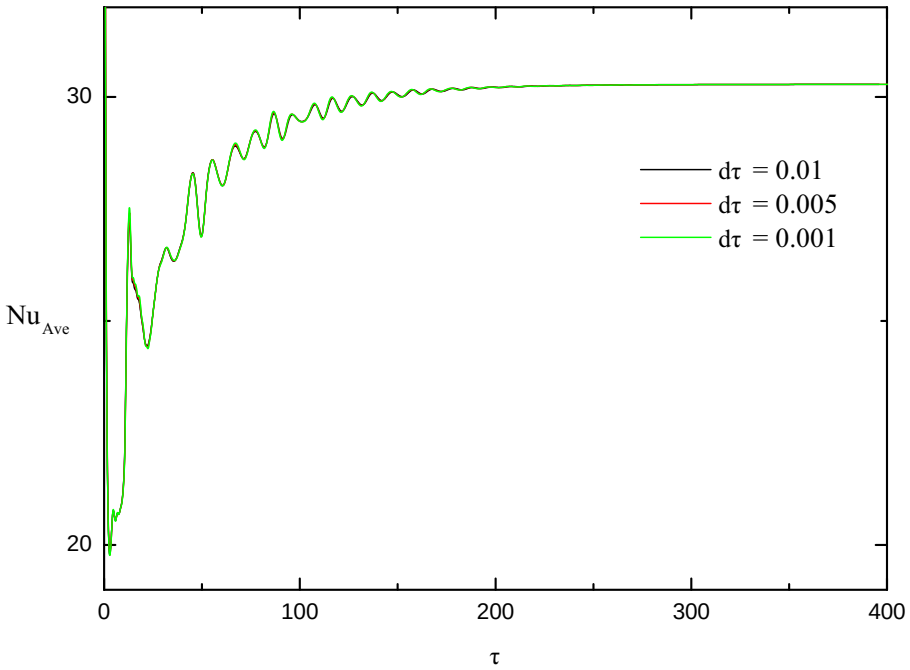

Figure 4.18: Time series of the average Nusselt number on the hot wall for the non-partitioned cavity for different time steps.

B. Validation with a two-dimensional non-partitioned cavity

The code validation was performed by benchmarking the available results for two-dimensional natural convection in a differentially heated square cavity without partition. The thermal flow in the two-dimensional heated square cavity filled by air ($Pr = 0.71$) was a numerical benchmark problem for testing accuracy and efficiency of numerical methods for solving the incompressible Navier-Stokes equations since the pioneering work of de Vahl Davis and Jones [185, 285]. The cavity is closed and top and bottom walls are adiabatic. The left and right sidewalls are isothermally heated (*e.g.*, $\theta = 1.0$) and cooled (*e.g.*, $\theta = 0.0$) respectively. The working fluid is air and initially quiescent and at the mean temperature of sidewalls (*e.g.*, $\theta = 0.5$). The dimensionless forms of the initial and boundary conditions for this cavity are presented in figure 4.19 and the governing equations are as follows,

$$\frac{\partial u}{\partial x} + \frac{\partial v}{\partial y} = 0, \tag{4.1}$$

$$\frac{\partial u}{\partial \tau} + \frac{\partial (uu)}{\partial x} + \frac{\partial (vu)}{\partial y} = -\frac{\partial p}{\partial x} + \sqrt{\frac{Pr}{Ra}} \left(\frac{\partial^2 u}{\partial x^2} + \frac{\partial^2 u}{\partial y^2} \right), \tag{4.2}$$

$$\frac{\partial v}{\partial \tau} + \frac{\partial (uv)}{\partial x} + \frac{\partial (vv)}{\partial y} = -\frac{\partial p}{\partial y} + \sqrt{\frac{Pr}{Ra}} \left(\frac{\partial^2 v}{\partial x^2} + \frac{\partial^2 v}{\partial y^2} \right) + \theta, \tag{4.3}$$

$$\frac{\partial \theta}{\partial \tau} + \frac{\partial (u\theta)}{\partial x} + \frac{\partial (v\theta)}{\partial y} = \sqrt{\frac{1}{RaPr}} \left(\frac{\partial^2 \theta}{\partial x^2} + \frac{\partial^2 \theta}{\partial y^2} \right). \tag{4.4}$$

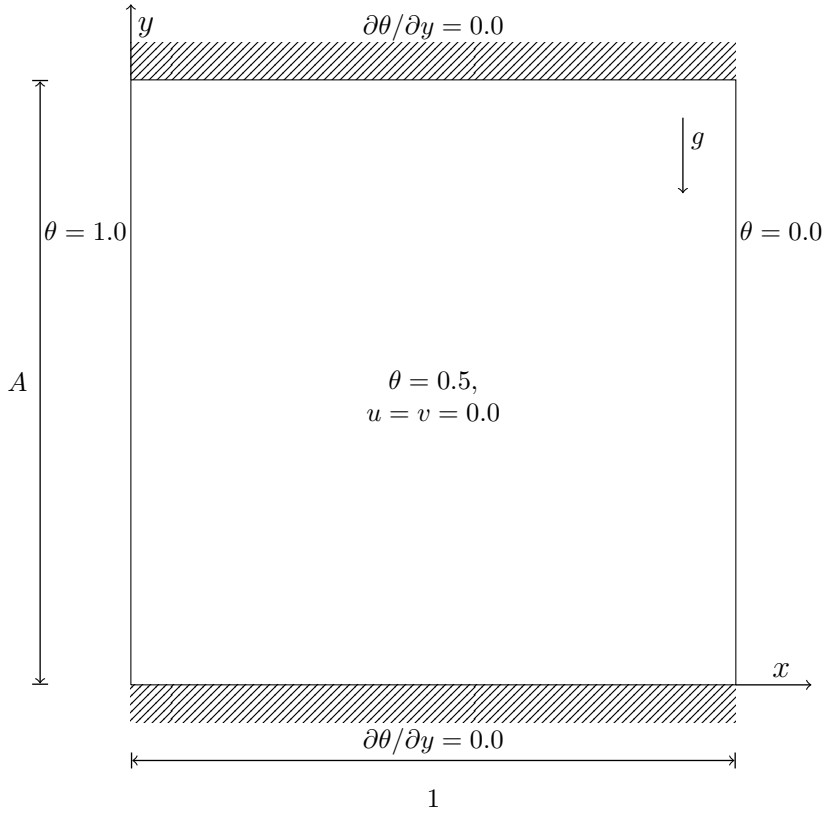

Figure 4.19: Schematic of the differentially heated cavity with the initial and boundary conditions.

The comparison of temperature contours for a range of Ra ($10^3 \leq Ra \leq 10^8$) shows satisfactory agreement with the results by Corzo *et al.* [4], as shown in figure 4.20.

Moreover, the predicted average Nusslet number from the present code was compared with several numerical and experimental studies, as presented in table 4.3. As can be seen from the table, the results of the present study agree well with those numerical data reported in the literature up to $Ra = 10^6$. However, for higher Ra values, there is a discrepancy with some of the presented data in the literature (*e.g.*, by Wan *et al.* [286](DSC)). Nevertheless, in terms of the experimental results (*i.e.*, [180]), the higher Ra cases show well agreement with the numerical ones, but a discrepancy at lower Ra cases found. This outcome is expected as lower Ra cases are more sensitive to the experiment errors.

To validate the results presented in this study, four more additional parameters are also investigated. The quantities under study are as follows,

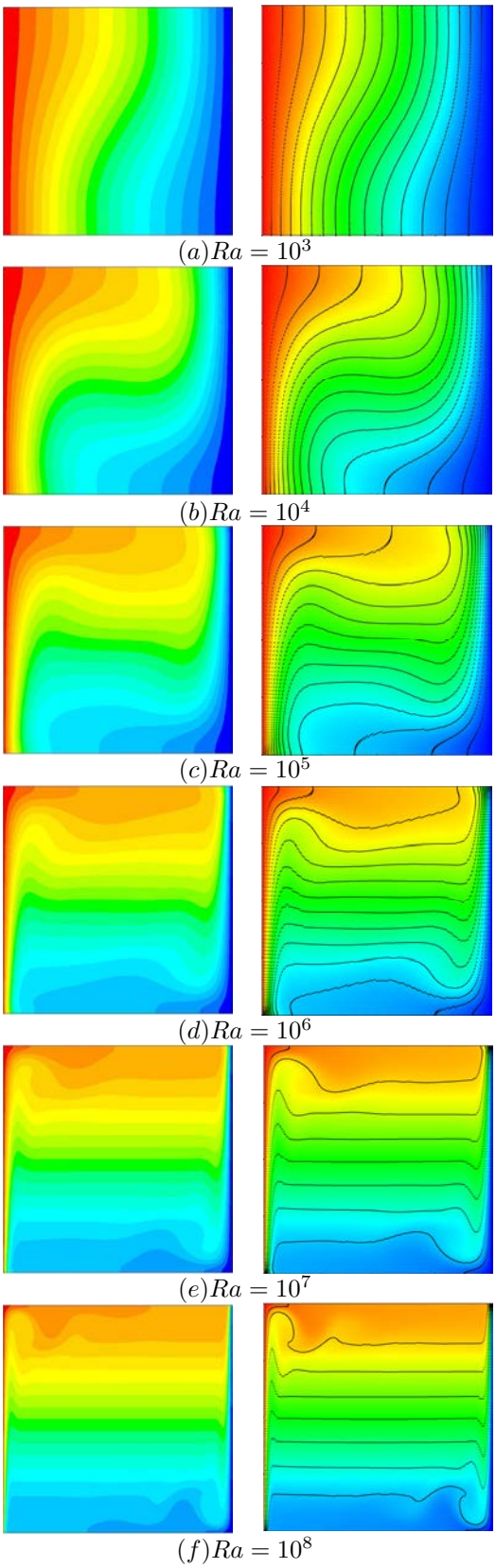

Figure 4.20: Comparison of temperature contours presented by Corzo *et al.* [4] (left column) and by this study (right column) for a non-partitioned cavity.

1. u_{max}, the maximum horizontal velocity on the vertical mid-plane of the cavity,

2. v_{max}, the maximum vertical velocity on the horizontal mid-plane of the cavity,

3. Nu_{max}, the maximum value of the local Nusselt number on the hot wall,

4. Nu_{min}, the minimum value of the local Nusselt number on the hot wall.

These parameters were obtained for $10^3 \leq Ra \leq 10^8$ and compared with several other studies, with the results presented in Tables 4.4 to 4.7.

By analysing tables 4.4 to 4.7, it can be seen that the uncertainties and complexities grow with the increase in the Rayleigh value. Nevertheless, a good agreement is observed among the investigations up to $Ra = 10^6$. For high Ra cases ($10^7 \leq Ra \leq 10^8$), results obtained from the code are closer to the data calculated by Fluent and OpenFOAM software. Similar to the average Nusselt number results, the calculated data by DSC method (Wan *et al.* [286]) shows the biggest differences.

Table 4.3: Comparison between the average Nusselt number obtained from the present code and those available in the literature for a differentially heated square cavity at various Rayleigh values.

	$Ra = 10^3$	$Ra = 10^4$	$Ra = 10^5$	$Ra = 10^6$	$Ra = 10^7$	$Ra = 10^8$
This study	1.117	2.244	4.521	8.825	16.528	30.245
Leong *et al.* [180] (experimental)	-	1.246	3.916	7.883	15.38	31.22
Choi [2]	1.117	2.243	4.519	8.820	16.504	-
Chenoweth and Paolucci [287]	1.118	2.244	4.520	8.822	16.82	-
Dixit and Babu [122]	1.121	2.244	4.520	8.822	16.79	30.506
Khanafer *et al.* [145]	1.118	2.286	4.546	8.652	-	-
De Vahl Davis [185]	1.118	2.243	4.519	8.799	-	-
Le Quéré and De Roquefortt [288]	1.1178	2.245	4.522	8.825	16.52	-
Le Quéré [289]	-	-	-	-	16.523	30.225
Puragliesi [290]	-	-	4.521	8.825	16.523	-
Corzo *et al.* [4] (Fluent)	1.113	2.246	4.535	8.861	16.645	28.52
Corzo *et al.* [4] (OpenFOAM)	1.109	2.222	4.498	8.786	16.502	30.1425
Manzari [291]	1.074	2.084	4.3	8.743	13.99	-
Wan *et al.* [286] (FEM)	1.117	2.254	4.598	8.976	16.656	31.486
Wan *et al.* [286] (DSC)	1.073	2.155	4.352	8.632	13.86	23.67

Table 4.4: Comparison of the maximum horizontal velocity at the mid-width and its location obtained from the present code with those available in the literature for a differentially heated square cavity at various Rayleigh values.

		$Ra = 10^3$	$Ra = 10^4$	$Ra = 10^5$	$Ra = 10^6$	$Ra = 10^7$	$Ra = 10^8$
u_{max}	this study	3.648 (0.807)	16.176 (0.819)	34.736 (0.855)	64.767 (0.855)	147.029 (0.883)	313.198 (0.926)
	[4] (Fluent)	3.643 (0.817)	16.139 (0.817)	34.469 (0.855)	64.433 (0.846)	146.00 (0.888)	304.015 (0.922)
	[4] (OpenFOAM)	3.640 (0.812)	16.281 (0.822)	34.928 (0.859)	64.558 (0.851)	145.84 (0.884)	299.156 (0.921)
	[185]	3.634 (0.813)	16.2 (0.823)	34.81 (0.855)	65.33 (0.851)	-	-
	[291]	3.68 (0.817)	16.1 (0.817)	34.0 (0.857)	65.4 (0.875)	139.7 (0.919)	-
	[292]	3.6493 (0.8125)	16.1798 (0.8235)	34.7741 (0.8535)	64.6912 (0.8460)	145.2666 (0.8845)	283.689 (0.9455)
	[286] (FEM)	3.489 (0.813)	16.122 (0.815)	33.39 (0.835)	65.40 (0.86)	143.56 (0.922)	296.71 (0.93)
	[286] (DSC)	3.6434 (0.8167)	15.967 (0.8167)	33.51 (0.85)	65.55 (0.86)	145.06 (0.92)	295.67 (0.94)

Table 4.5: Comparison of the maximum vertical velocity at the mid-height and its location obtained from the present code with those available in the literature for a differentially heated square cavity at various Rayleigh values.

		$Ra = 10^3$	$Ra = 10^4$	$Ra = 10^5$	$Ra = 10^6$	$Ra = 10^7$	$Ra = 10^8$
v_{max}	this study	3.701 (0.181)	19.674 (0.122)	68.584 (0.064)	221.122 (0.036)	700.240 (0.020)	2217.47 (0.011)
	[4] (Fluent)	3.690 (0.182)	19.619 (0.119)	68.817 (0.064)	220.970 (0.0379)	695.36 (0.0196)	2199.51 (0.011)
	[4] (OpenFOAM)	3.700 (0.177)	19.547 (0.123)	68.878 (0.067)	221.572 (0.0670)	704.094 (0.0217)	2233.35 (0.012)
	[185]	3.679 (0.179)	19.51 (0.12)	68.22 (0.066)	216.75 (0.0387)	-	-
	[291]	3.73 (0.1827)	19.9 (0.1246)	70.0 (0.068)	228 (0.039)	698 (0.0235)	-
	[292]	3.6962 (0.1790)	19.6177 (0.1195)	68.6920 (0.0665)	220.8331 (0.0380)	703.2536 (0.0215)	2223.4424 (0.013)
	[286] (FEM)	3.686 (0.188)	19.79 (0.12)	70.63 (0.072)	227.11 (0.040)	714.48 (0.022)	2259.08 (0.012)
	[286] (DSC)	3.686 (0.183)	19.98 (0.117)	70.81 (0.070)	227.24 (0.040)	714.47 (0.021)	2290.13 (0.013)

Table 4.6: Comparison of the maximum Nusselt number on the hot wall and its location obtained from the present code with those available in the literature for a differentially heated square cavity at various Rayleigh values.

		$Ra = 10^3$	$Ra = 10^4$	$Ra = 10^5$	$Ra = 10^6$	$Ra = 10^7$	$Ra = 10^8$
Nu_{max}	this study	1.506 (0.090)	3.532 (0.144)	7.723 (0.086)	17.571 (0.0408)	39.537 (0.018)	88.808 (0.007)
	[4] (Fluent)	1.506 (0.090)	3.539 (0.144)	7.767 (0.083)	17.717 (0.0379)	40.619 (0.015)	96.47 (0.0074)
	[4] (OpenFOAM)	1.505 (0.001)	3.538 (0.085)	7.765 (0.080)	17.708 (0.0404)	40.594 (0.017)	90.294 (0.008)
	[185]	1.50 (0.092)	3.53 (0.143)	7.71 (0.08)	17.92 (0.039)	-	-
	[291]	1.47 (0.109)	3.47 (0.125)	7.71 (0.08)	17.46 (0.039)	30.46 (0.024)	-
	[292]	1.5062 (0.08956)	3.5305 (0.1426)	7.7084 (0.08353)	17.5308 (0.03768)	41.0247 (0.03899)	91.2095 (0.067)
	[286] (FEM)	1.501 (0.08)	3.579 (0.13)	7.945 (0.08)	17.86 (0.03)	38.6 (0.015)	91.16 (0.010)
	[286] (DSC)	1.444 (0.0917)	3.441 (0.1333)	7.662 (0.085)	17.39 (0.04)	31.02 (0.02)	68.73 (0.010)

Table 4.7: Comparison of the minimum Nusselt number on the hot wall and its location obtained from the present code with those available in the literature for a differentially heated square cavity at various Rayleigh values.

		$Ra = 10^3$	$Ra = 10^4$	$Ra = 10^5$	$Ra = 10^6$	$Ra = 10^7$	$Ra = 10^8$
Nu_{min}	this study	0.691 (0.998)	0.586 (0.998)	0.729 (0.998)	0.981 (0.998)	1.366 (0.999)	1.916 (0.999)
	[4] (Fluent)	0.691 (1.000)	0.691 (1.000)	0.691 (1.000)	0.983 (1.000)	1.394 (0.990)	2.0536 (0.999)
	[4] (OpenFOAM)	0.691 (1.000)	0.691 (1.000)	0.726 (1.000)	0.977 (0.998)	1.365 (0.998)	1.906 (0.999)
	[185]	0.692 (1.0)	0.586 (1.0)	0.729 (1.0)	0.989 (1.0)	-	-
	[291]	0.623 (1.0)	0.497 (1.0)	0.614 (1.0)	0.716 (1.0)	0.787 (1.0)	-
	[292]	0.6913 (1.0)	0.5850 (1.0)	0.7282 (1.0)	0.9845 (1.0)	1.3799 (1.0)	2.044 (1.0)
	[286] (FEM)	0.691 (1.0)	0.577 (1.0)	0.698 (1.0)	0.9132 (1.0)	1.298 (1.0)	1.766 (1.0)
	[286] (DSC)	0.665 (1.0)	0.528 (1.0)	0.678 (1.0)	0.903 (1.0)	0.997 (1.0)	1.428 (1.0)

4.2.2 Partitioned cavity

A. Time and grid independence test

The non-uniform mesh was used for mapping partitioned cavities. The domain has finer grids near the walls and the partition and coarser grids at the core. Figure 4.21 shows a schematic of the non-uniform mesh distribution in a partitioned cavity.

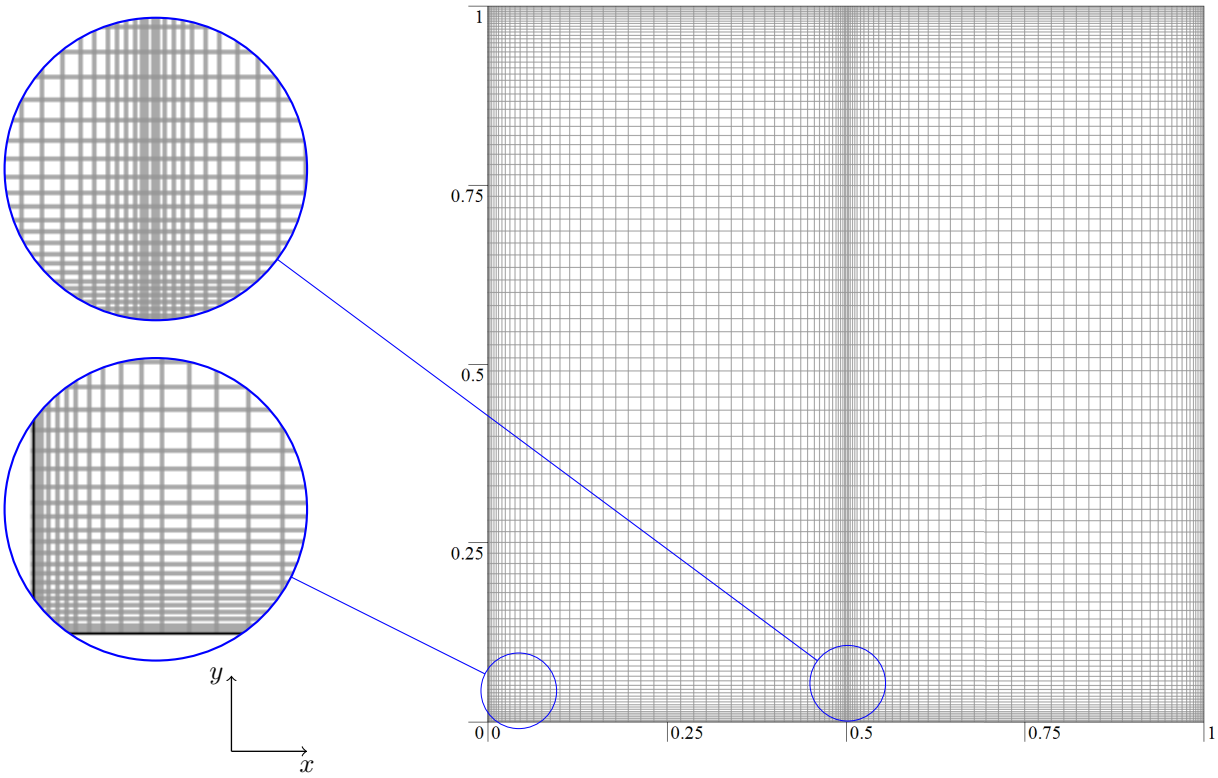

Figure 4.21: Grid distribution for a partitioned cavity with the mesh of 100×100.

Results of the grid independence tests for several meshes from 100×100 to 300×300 are listed in Table 4.8. Other parameters of the partitioned cavity are $T_P = 0.2$, $X_P = 0.5$, $k_r = 1000$, $Pr = 0.71$ and $Ra = 10^8$. The presented results include steady-state data for the temperature at the point $(0.05, 0.5)$ and the average Nusselt number on the hot wall. Since the variation of results from meshes of 250×250 to 300×300 is less than 2% for the average Nusselt number and less than 1% for the temperature, the 250×250 mesh is selected as an optimum mesh for the partitioned cavity. The smallest grid size is $\Delta x = 0.000807$ in the x direction

and $\Delta y = 0.000806$ in the y direction whereas the largest grid sizes are $\Delta x = 0.007256$ and $\Delta y = 0.007255$ and the maximum grid expansion ratio (or stretching factor) is 1.0697.

Table 4.8: Grid independence tests of a partitioned cavity.

Grid size	Temperature at point $(0.05, 0.5)$	Steady-state average Nusselt number on the hot wall
100×100	0.61743	17.43051
150×150	0.65790	15.87343
230×230	0.69663	14.52101
250×250	0.70103	14.38578
270×270	0.70453	14.25898
300×300	0.70748	14.12233

In order to have the time step independence test, the simulations were carried out with different time steps of $d\tau = 10^{-2}$, 5×10^{-3} and 10^{-3}. It is clear from figure 4.22 that the variation of results due to the selected time steps are negligible. Therefore, $d\tau = 5 \times 10^{-3}$ was chosen for the code validation tests.

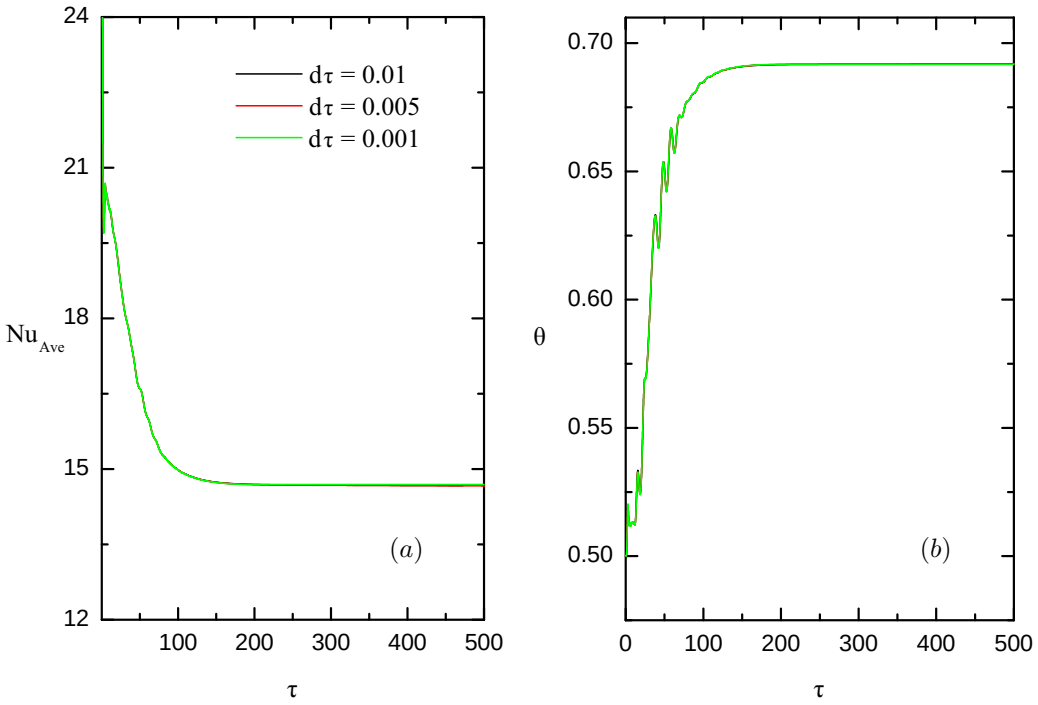

Figure 4.22: Time series of (a) the average Nusselt number on the hot wall and (b) temperature at $(0.05, 0.5)$ for different time steps of case the $T_P = 0.2$, $X_P = 0.5$, $k_r = 1000$, $Pr = 0.71$ and $Ra = 10^8$.

B. Validation with a two-dimensional partitioned cavity

The accuracy of the code was also validated for the case of a partitioned cavity. The same dimensionless governing equations, initial and boundary conditions presented in section 3.2 was used for this validation. The partition thickness (T_P) and position (X_P) are 0.1 and 0.5 and the thermal conductivity ratio (k_r) of 1 and 100 were selected. The temperature and stream function obtained for $Ra = 10^6$ of the code are compared against the results presented by Kahveci [5] and Choi [2] in figures 4.23 and 4.24.

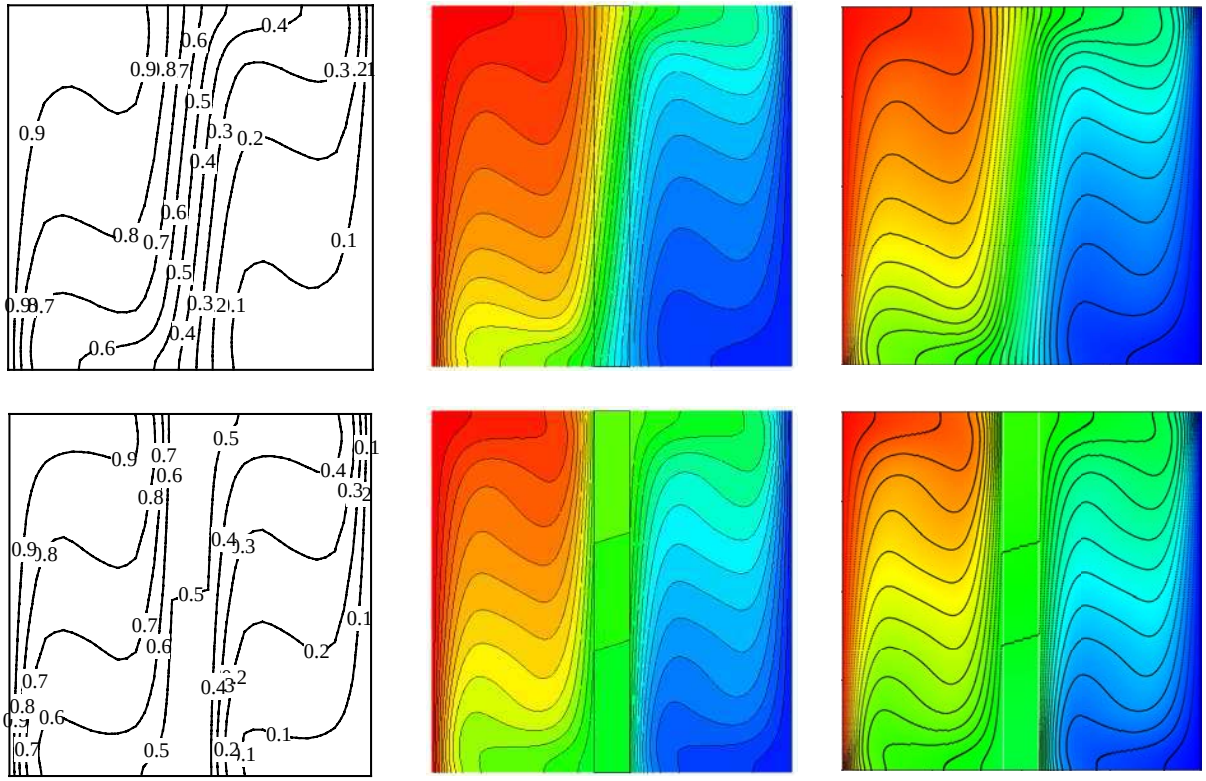

Figure 4.23: Comparison of temperature contours for $k_r = 1$ (top row) and $k_r = 100$ (bottom row) presented by Kahveci [5] (left column), Choi [2] (middle column) and the present study (right column) for $Ra = 10^6$.

Comparing temperature and stream function contours reveal that results presented by Kahveci [5] are almost identical to data obtained from the current code. However, the contours reported by Choi [2] show less convective behavior.

Further investigation of the partitioned cavities over a range of Rayleigh value between 10^4 and 10^6 shows the same underestimation observed in the results reported by Choi [2]. The average

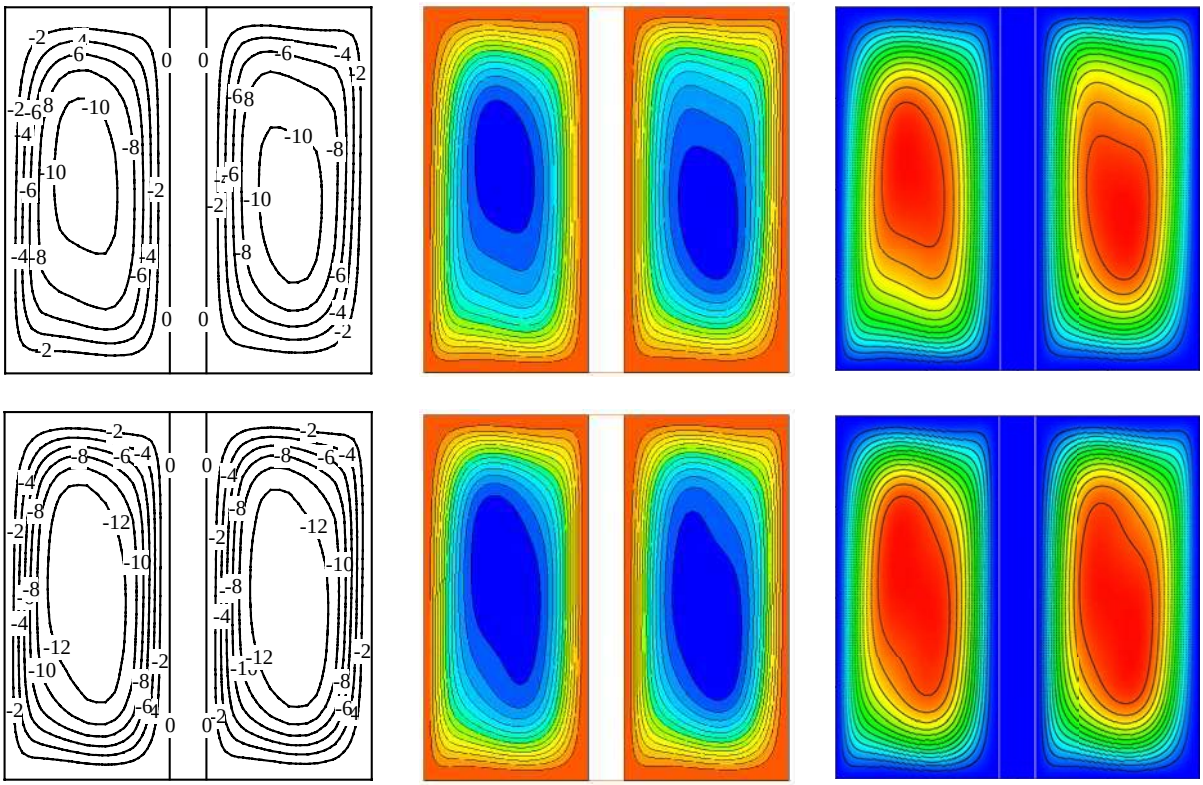

Figure 4.24: Comparison of stream function contours for $k_r = 1$ (top row) and $k_r = 100$ (bottom row) presented by Kahveci [5] (left column), Choi [2] (middle column) and the present study (right column) for $Ra = 10^6$.

Nusselt number obtained for $10^4 \leq Ra \leq 10^6$ and $k_r = 1$ and 100 is presented in table 4.9.

Table 4.9: Comparison between the average Nusselt number obtained from the present code and those available in the literature for a differentially heated partitioned cavity at various Rayleigh values.

	$Ra = 10^4$	$Ra = 10^5$	$Ra = 10^6$
	$k_r = 1$		
This study	1.09	1.76	2.82
Choi [2]	1.05	1.74	2.79
Kahveci [5]	1.06	1.79	2.8
	$k_r = 100$		
This study	1.17	2.11	4.03
Choi [2]	1.05	1.87	3.51
Kahveci [5]	1.19	2.14	3.93

Chapter 5

Steady-state natural convection in a partitioned cavity

5.1 Introduction

Heat transfer and flow structures in a partitioned cavity usually depend on both the geometrical parameters (*e.g.*, aspect ratio, partition thickness, partition position, thermal conductivity, etc.) and the flow control parameters (*e.g.*, the Rayleigh value, the Prandtl number). In the present study, natural convection in a partitioned cavity is investigated for three values of the dimensionless partition thickness (*i.e.*, $T_p = 0.05$, 0.1, and 0.2), two values of the dimensionless partition position (*i.e.*, $X_p = 0.25$ and 0.5), five values of the thermal conductivity ratio (*i.e.*, $k_r = 0.1$, 1, 100, 500 and 1000), and six values of the Rayleigh value (*i.e.*, $Ra = 10^3$, 10^4, 10^5, 10^6, 10^7 and 10^8). For all these cases, $A = H/L = 1$ (*i.e.*, the aspect ratio is $A = 1$), and $Pr = 0.71$ are used.

The thermal conductivity ratio selected for this work covers a wide range of materials with different applications in the industry. $k_r \approx 0.1$ represents a range of super insulating materials such as fiber fillings or powder filled panels [293]. By selecting $k_r \approx 1$, the partition represents the thermal behavior of materials such as polyurethane foam, extruded polystyrene, some gases such as nitrogen, oxygen, water vapor, redwood bark or silica aerogel. For instance, silica

aerogels have a wide range of uses, mostly in high-tech science and engineering. Some of the current applications include insulation on the Mars exploration rovers, hypervelocity particle capture in the stardust probe, high-energy Cherenkov radiation particle counters, remediating oil from water, and transparent window insulation [294]. Granite, sandstone, ice, fused silica, thorium dioxide and zirconium dioxide are some of the materials that have $k_r \approx 100$. Aluminum oxide and stainless steel have $k_r \approx 500$ and beryllium oxide (a well known electrical insulator), bronze, titanium, monel, constantan, solder have $k_r \approx 1000$. For example, beryllium oxide, owing to its high thermal conductivity and good electrical resistivity, can be an effective heat sink in high-power devices or high density electronic circuits for high-speed computers. Beryllium oxide is transparent to microwaves and x-rays and can be used as windows, radomes and antennas in microwave communication systems and microwave ovens, as an x-ray window, particularly for severe operating conditions or in high-power laser tubes. Beryllium oxide also has specific nuclear properties (low neutron capture cross-section and high neutron moderating ability) which make it attractive material for nuclear-power reactors.

5.2 Centrally positioned partition

5.2.1 Qualitative analysis of flow and heat transfer behaviour

A. Isotherms and streamlines

Figures 5.1, 5.3, 5.5, 5.7 and 5.9 present the temperature contours and figures 5.2, 5.4, 5.6, 5.8 and 5.10 show the streamlines at the fully developed stage obtained numerically for $T_p = 0.05$, 0.1, and 0.2, and $k_r = 0.1$, 1, 100, 500 and 1000, each at $X_p = 0.5$ and at $Ra = 10^3$, 10^4, 10^5, 10^6, 10^7 and 10^8, respectively. Isolines of the color-coded contour figures presented in this thesis are defined in a way that the maximum and minimum values of the parameter of the interest are assigned to the red and blue colors on the top and bottom of the plot key bar respectively and divided to 30 equally spaced sections.

The general flow pattern for all convection dominated cases (equal to and higher than $Ra = 10^5$)

shown is that in the left enclosure, the heated air close to the hot wall moves upward and impinges on the top wall to form a hot intrusion which moves horizontally along the top wall until it strikes on the top edge of the left side of the partition wall, which moves subsequently downward along the left side of the partition wall; a similar process occurs in the right enclosure, although there it is a cold intrusion that impinges on the bottom edge of the right side of the partition wall and moves upward. With the continuous passing of these hot and cold intrusions on either side of the partition wall, heat is transferred by conduction through the partition wall from the left enclosure to the right one, resulting in the coupling of the flow and heat transfer between the two enclosures. For the cases of conduction-dominated heat transfer phenomenon, such a movement induced in the high Ra cases does not exist. Heat transfers from the left wall mainly by conduction to the partition and then through conduction transfers to the other side.

By studying the temperature contours for all cases, it is clear that as Ra increases isotherms change from being completely vertical and parallel to the side walls (*i.e.*, the $Ra = 10^3$ case) to angled and finally horizontal (perpendicular to the side walls) at the middle of side-cavity. This observation implies that the heat transfer mechanism changes gradually from a conduction-dominated form to a convective heat transfer. The next overall observation is regarding isotherms distribution in the fluid region of the cavity. The low Ra cases show more uniformly spaced in the horizontal direction isotherms, indicating the temperature varies almost linearly with distance along the x-axis. However, the high Ra cases have non-uniformly spaced isotherms. The areas with denser isotherms are mainly close to the side walls and the partition, indicating a steep temperature gradient and thermal boundary layers formation in the vicinity of all walls for high Ra cases. The temperature variation within the fluid layer diminishes inward from the sidewalls into the center of the enclosure which forms the circulation, indicating that the heat transfer regime changes from conduction to convection with increases in Ra.

The stream function contours of $Ra = 10^3$ show a symmetrical oval shape flow pattern and the eye of the vortex is located at the center of the enclosure. As Ra increases flow pattern becomes asymmetrical and gradually transforms from an oval shape (*i.e.*, $Ra = 10^3$) to an egg shape (*i.e.*$10^4 \leq Ra \leq 10^5$) and finally an elongated shape (*i.e.*, $10^6 \leq Ra \leq 10^8$) with more vortex eyes. Flow patterns in the half-cavity for $Ra \geq 10^4$ are not symmetrical and the

vortex eyes are mainly shifted to the sidewalls. By inspecting the streamlines for high Ra cases (10^7 or 10^8), clearly the 180-degree rotational symmetry which exists in the flow pattern of a non-partitioned cavity, cannot be observed in each half-cavity of a partitioned cavity. For instance, the intensity of stream function close to the top-left corner is higher than that at the opposite corner (bottom-right) in the left half-cavity.

To investigate how the flow structure evolves in an enclosure for increasing Ra, figure 5.11 presents a schematic of the observed typical flow pattern in the upper left corner region of the enclosure for the range of Ra covered in this study, where figure 5.11(a), (b), (c) and (d) represent $Ra = 10^3$, $10^4 \leq Ra \leq 10^6$, $10^6 \leq Ra \leq 10^7$ and $10^7 \leq Ra \leq 10^8$, respectively. Comparing the flow patterns illustrated in figures 5.2, 5.4, 5.6, 5.8 and 5.10 it is shown that the partition specification affects the patterns and for low Ra cases (figure 5.11(a) and (b)) fluid is bounded by the boundary-layer flow with a single cell in each half-cavity and flow travels around the corner without any evidence of separation. By increasing Ra streamlines move closer to the sidewalls. A further increase in Ra causes streamlines in the core region to be almost horizontal and the boundary-layer type regions formed close to the horizontal and vertical walls are more recognizable (mainly for $Ra = 10^7$ and 10^8). It is clear that flow from the corner moves into the core more sharply. This sudden discharge into the interior forms a flow separation from the top wall near the corner (*i.e.*, figure 5.11(c)). At these high Ra cases flow, while passing the corner area (turning process which follows by separation), is compressed (with denser streamlines), which is similar to a jet behavior spreading to a wide area of the enclosure (almost covers the half height of the enclosure). By further increasing Ra, the turning process gets sharper and consequently, the separation jump increases. This observed inverse S-shape pattern (figure 5.11(d)) causes a block of fluid to trap between the upcoming boundary-layer fluid of sidewall and the spreading fluid into the core. This block of fluid forms a re-circulation region and as Ra increases it moves closer to the corner.

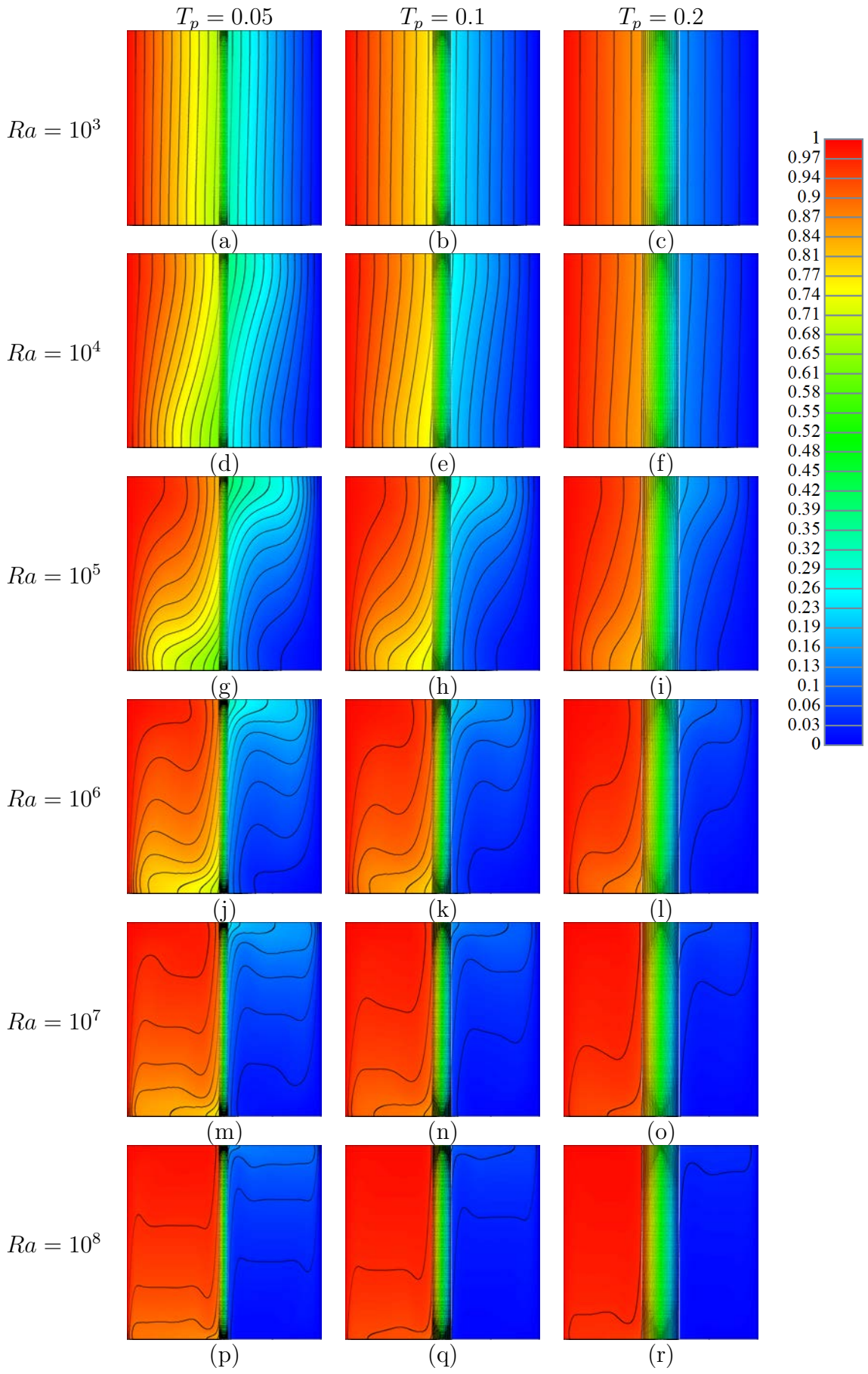

Figure 5.1: Temperature contours at $k_r = 0.1$ and $X_p = 0.5$ for different Ra values ($10^3 \leq Ra \leq 10^8$) and T_p ($T_p = 0.05$, 0.1 and 0.2).

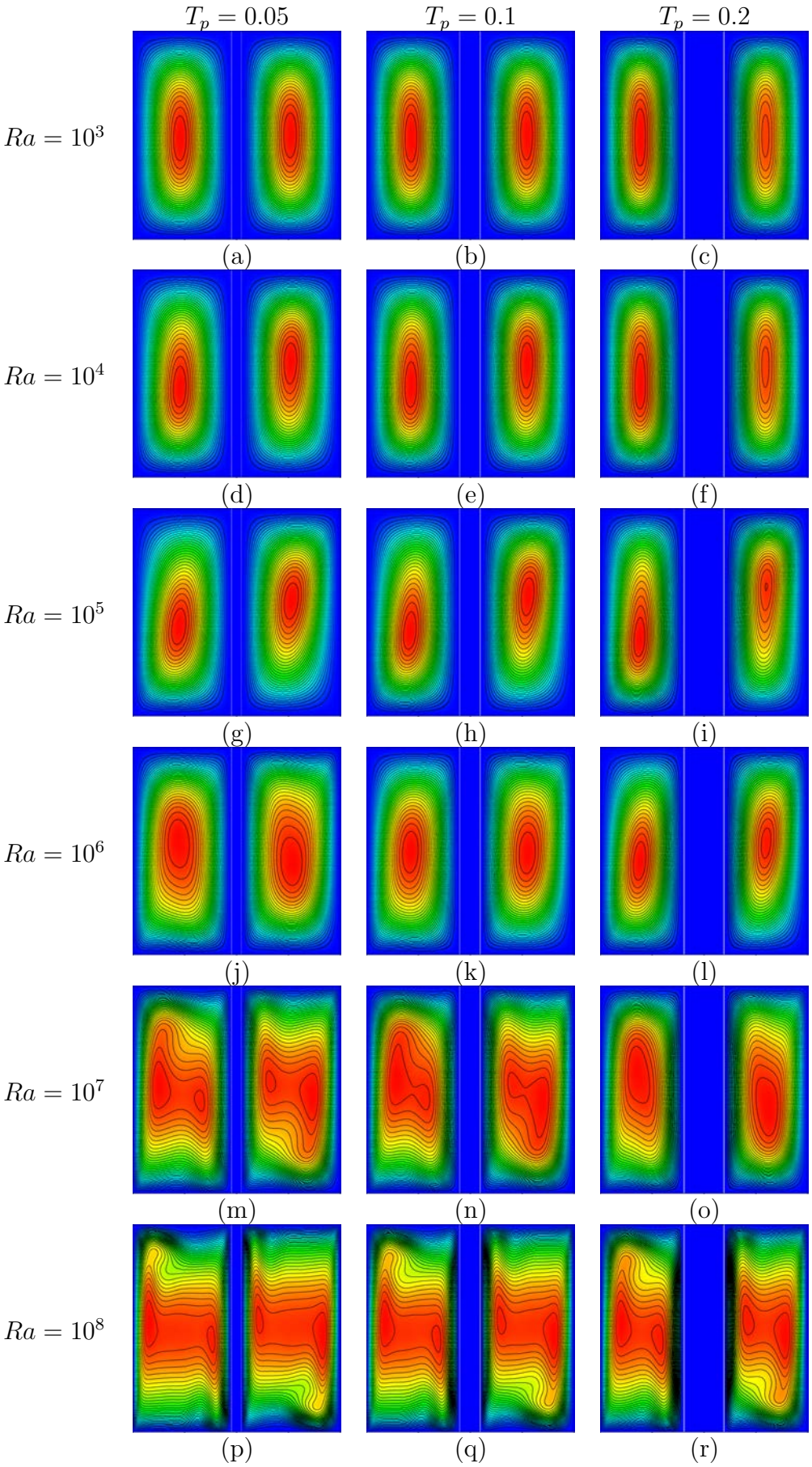

Figure 5.2: Stream function contours at $k_r = 0.1$ and $X_p = 0.5$ for different Ra values ($10^3 \leq Ra \leq 10^8$) and T_p ($T_p = 0.05$, 0.1 and 0.2).

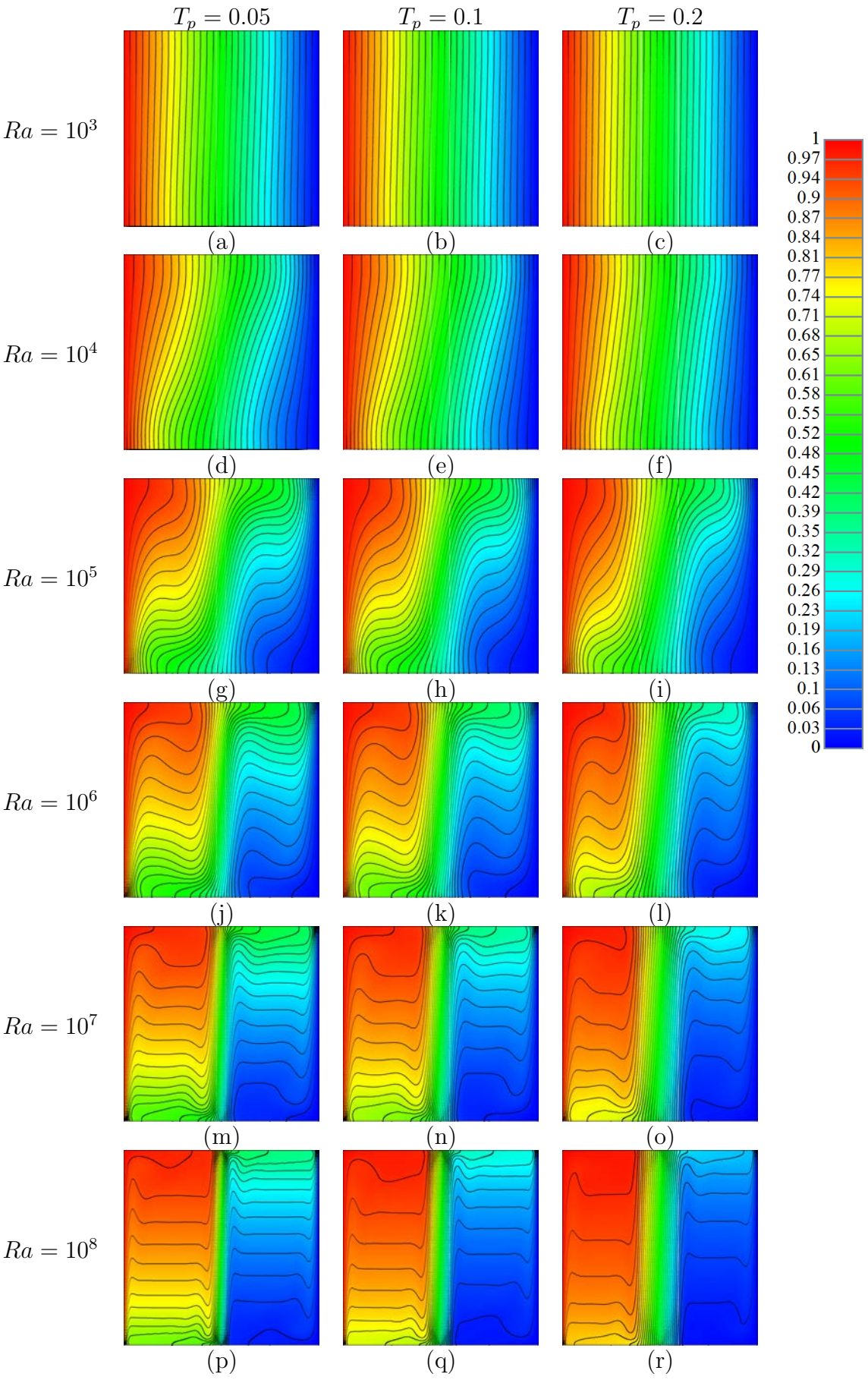

Figure 5.3: Temperature contours at $k_r = 1$ and $X_p = 0.5$ for different Ra values ($10^3 \leq Ra \leq 10^8$) and T_p ($T_p = 0.05$, 0.1 and 0.2).

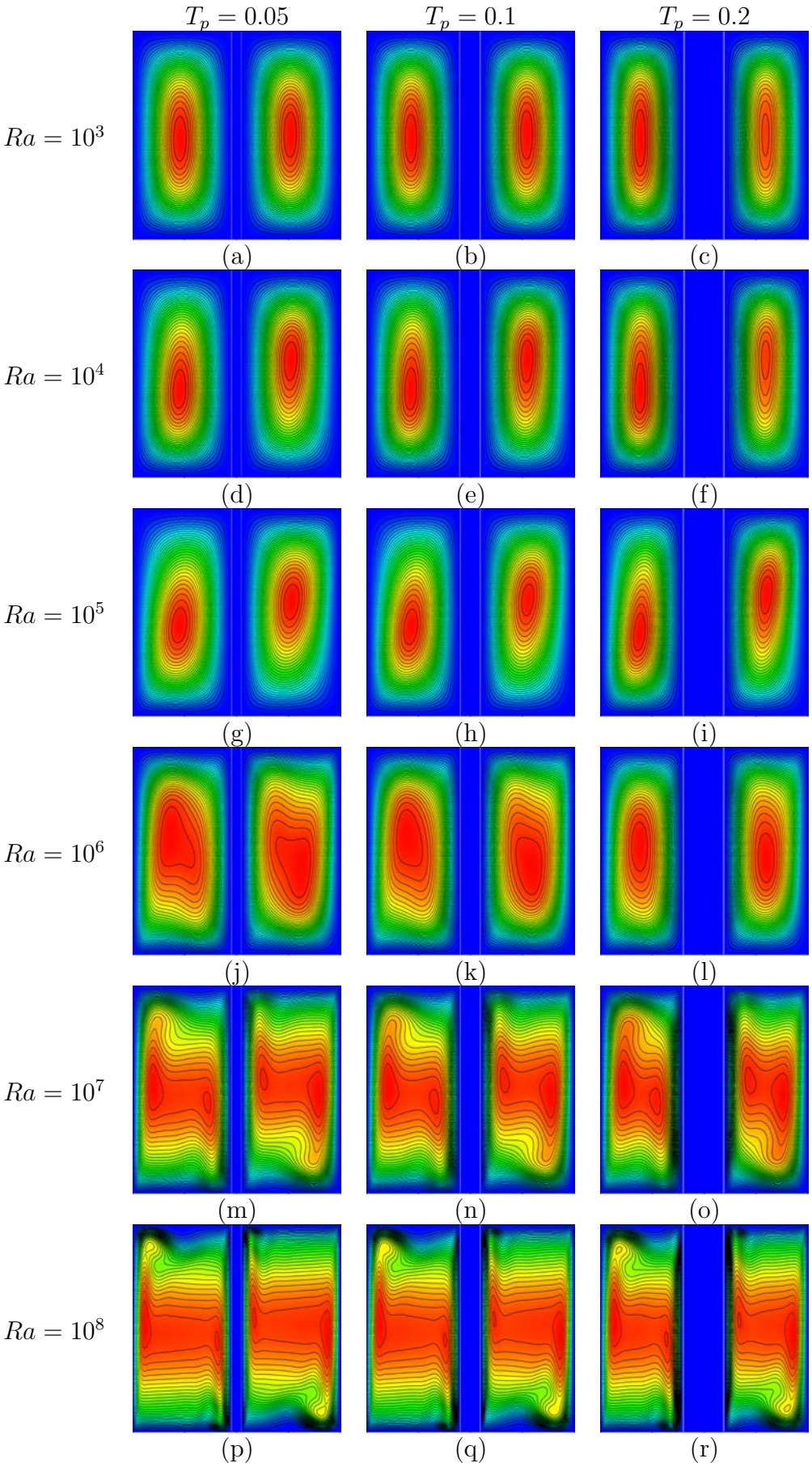

Figure 5.4: Stream function contours at $k_r = 1$ and $X_p = 0.5$ for different Ra values ($10^3 \leq Ra \leq 10^8$) and T_p ($T_p = 0.05$, 0.1 and 0.2).

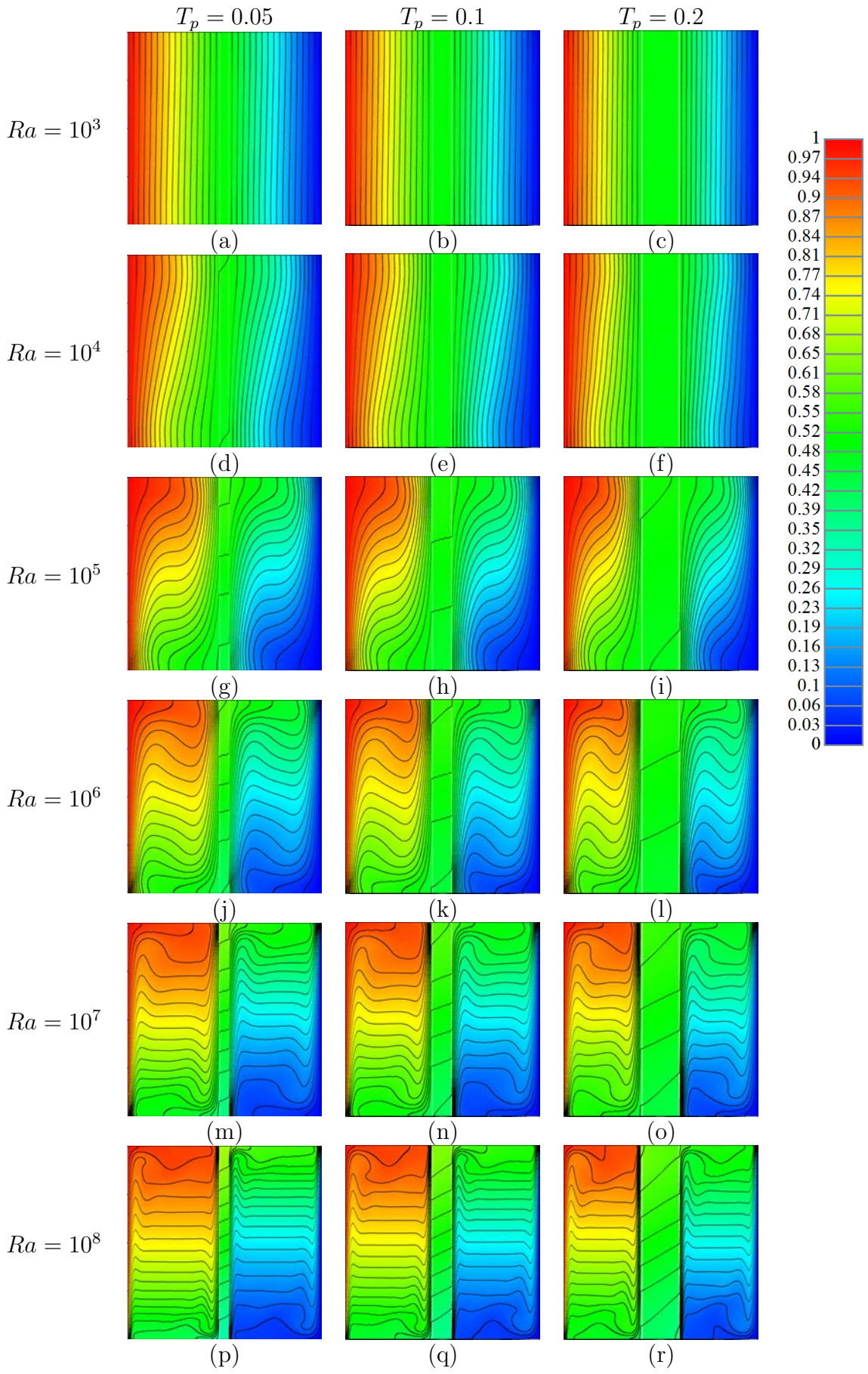

Figure 5.5: Temperature contours at $k_r = 100$ and $X_p = 0.5$ for different Ra values ($10^3 \leq Ra \leq 10^8$) and T_p ($T_p = 0.05$, 0.1 and 0.2).

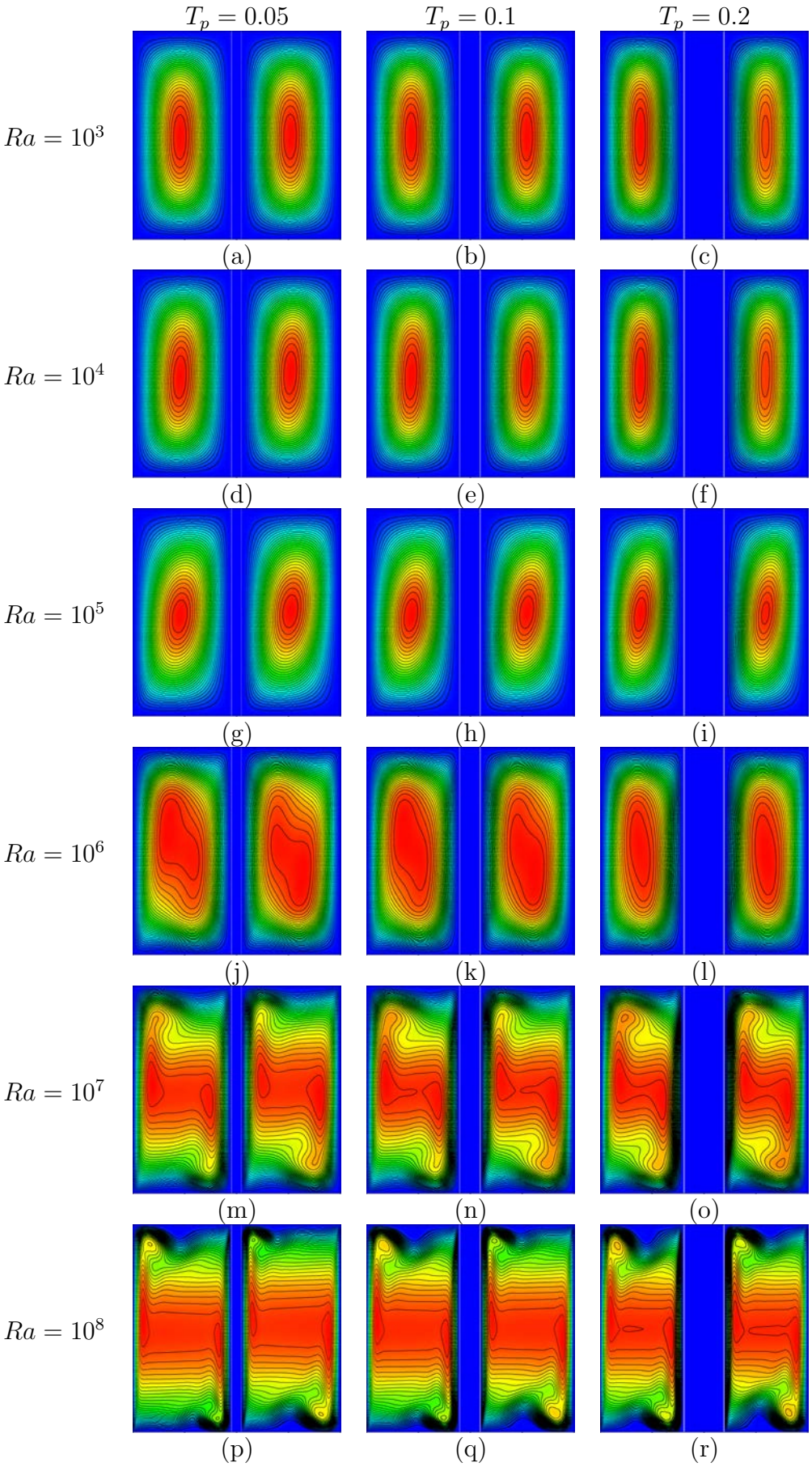

Figure 5.6: Stream function contours at $k_r = 100$ and $X_p = 0.5$ for different Ra values ($10^3 \leq Ra \leq 10^8$) and T_p ($T_p = 0.05$, 0.1 and 0.2).

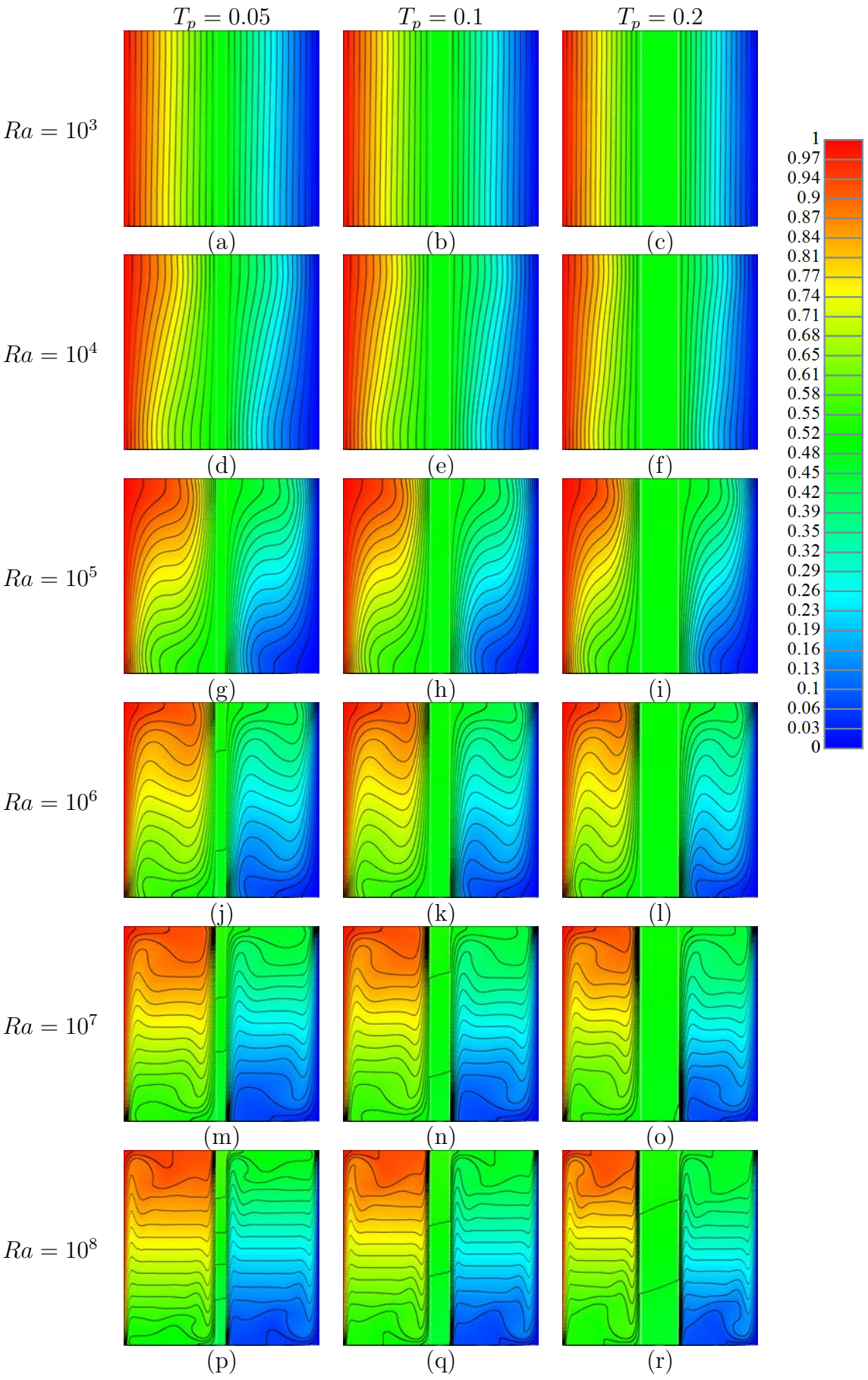

Figure 5.7: Temperature contours at $k_r = 500$ and $X_p = 0.5$ for different Ra values ($10^3 \leq Ra \leq 10^8$) and T_p ($T_p = 0.05$, 0.1 and 0.2).

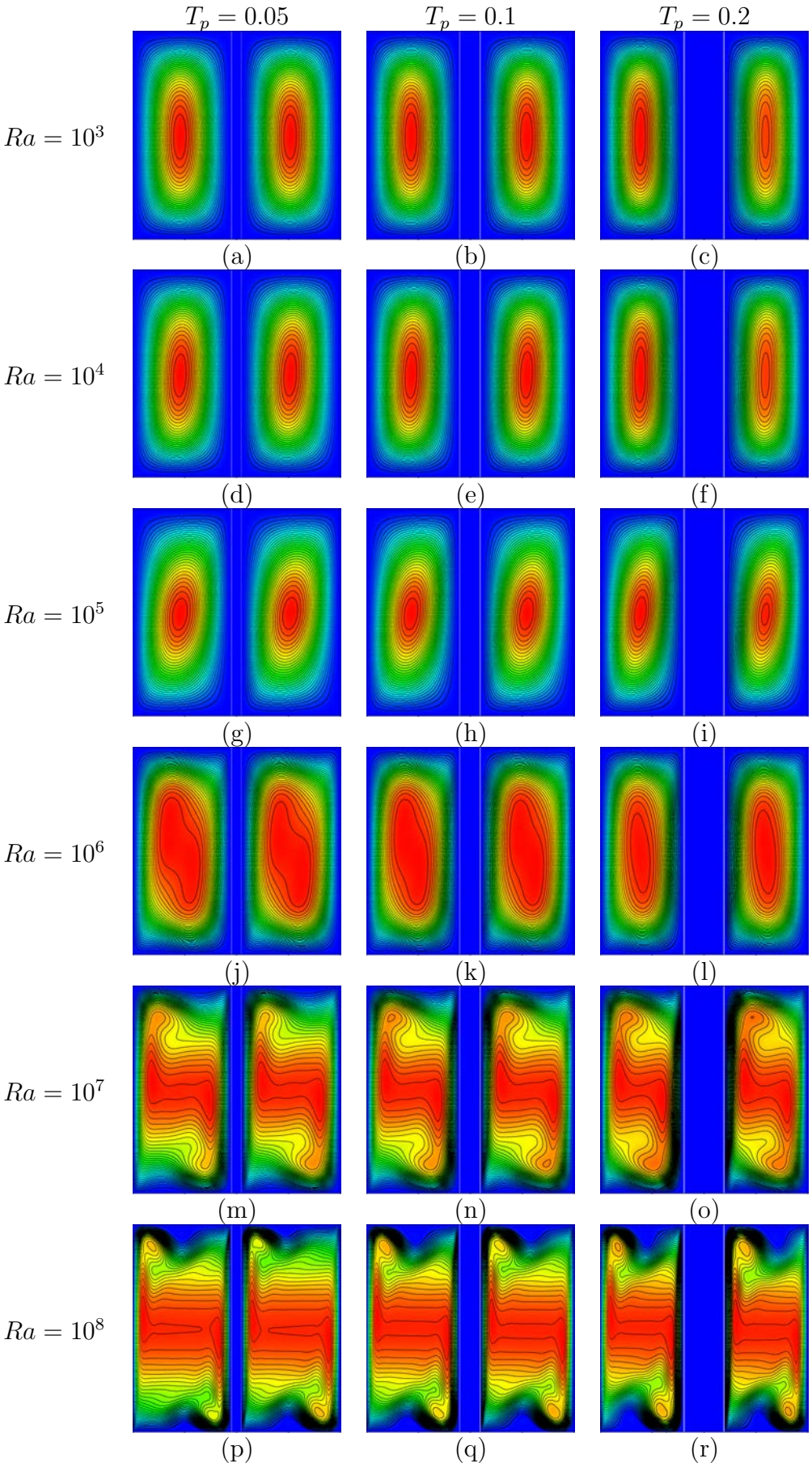

Figure 5.8: Stream function contours at $k_r = 500$ and $X_p = 0.5$ for different Ra values ($10^3 \leq Ra \leq 10^8$) and T_p ($T_p = 0.05$, 0.1 and 0.2).

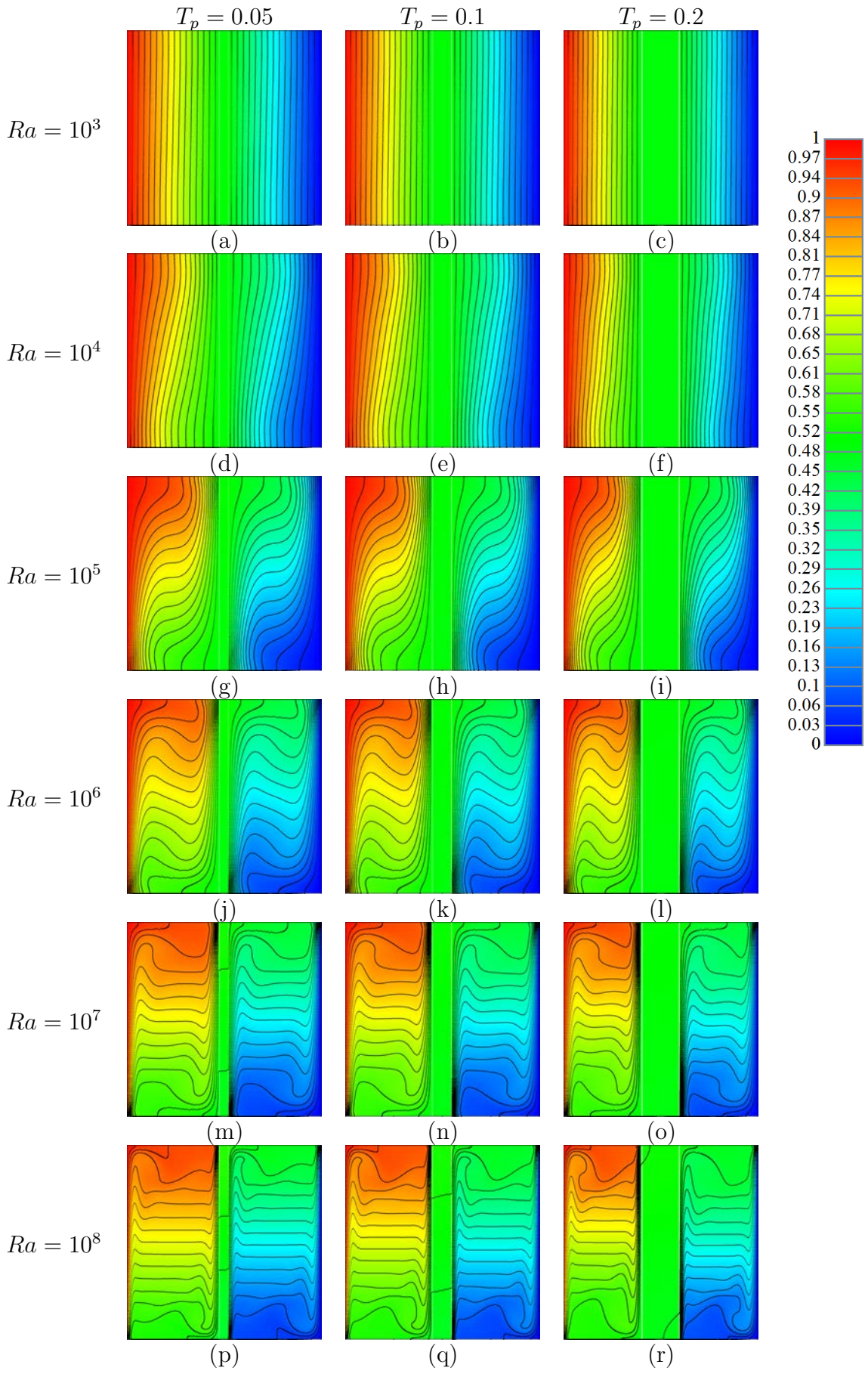

Figure 5.9: Temperature contours at $k_r = 1000$ and $X_p = 0.5$ for different Ra values ($10^3 \leq Ra \leq 10^8$) and T_p ($T_p = 0.05$, 0.1 and 0.2).

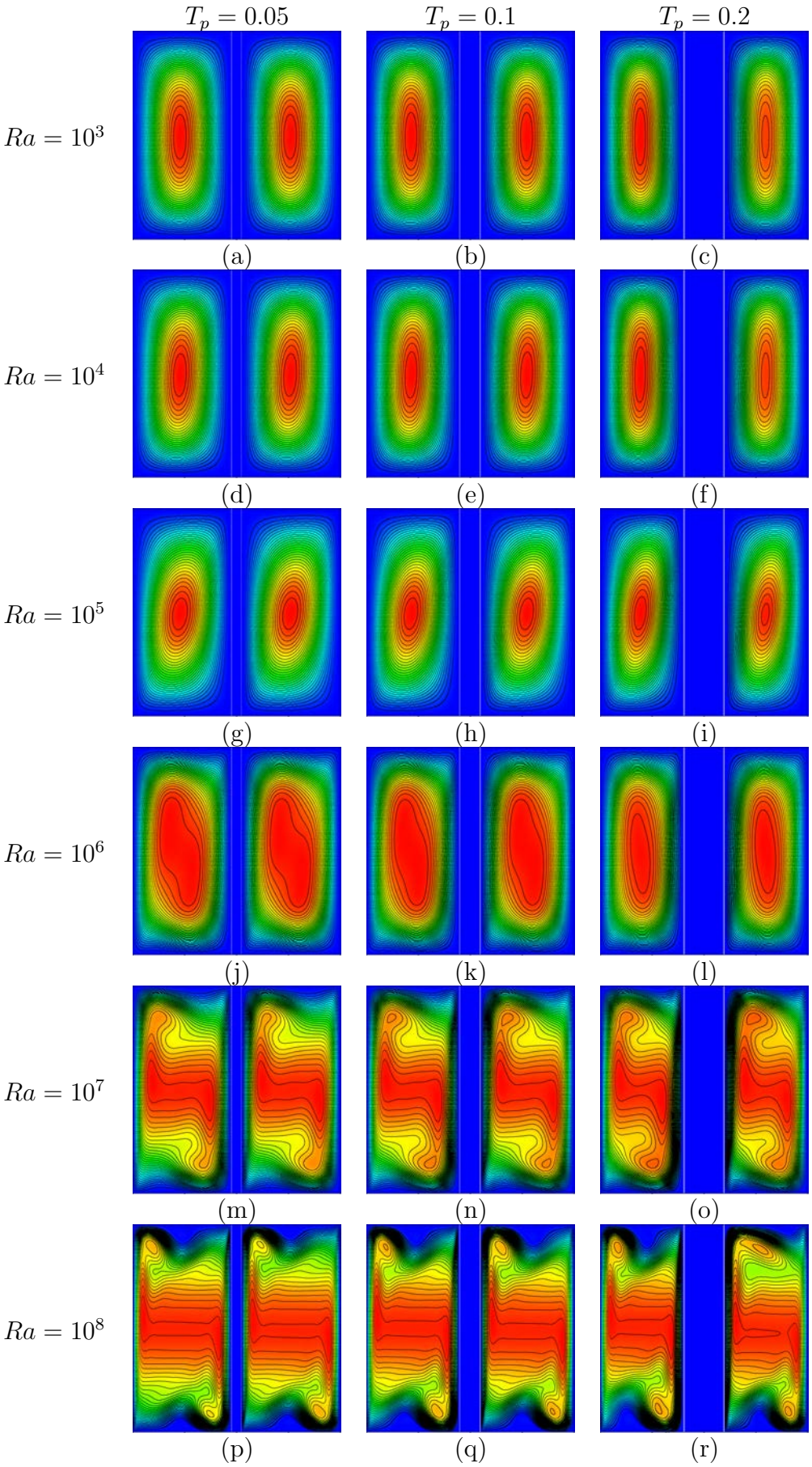

Figure 5.10: Stream function contours at $k_r = 1000$ and $X_p = 0.5$ for different Ra values ($10^3 \leq Ra \leq 10^8$) and T_p ($T_p = 0.05$, 0.1 and 0.2).

Flow in the half-cavity with the inverse S-shape pattern can be grouped into two streams similar to the classification by Ravi *et al.* [295] for the non-partitioned cavity. One stream has flow close to walls with the sudden expansion and the other flows around the central region without reaching the walls. The dividing border between those two streams is a streamline where the recirculating loop at the top-left corner region touches the recirculating loop in the central region or lower section. Figure 5.12 schematically illustrates the dividing stream function. Due to the asymmetrical flow pattern in the half-cavity, the corner with the stronger flow (top-left corner) is considered for the position of dividing streamline.

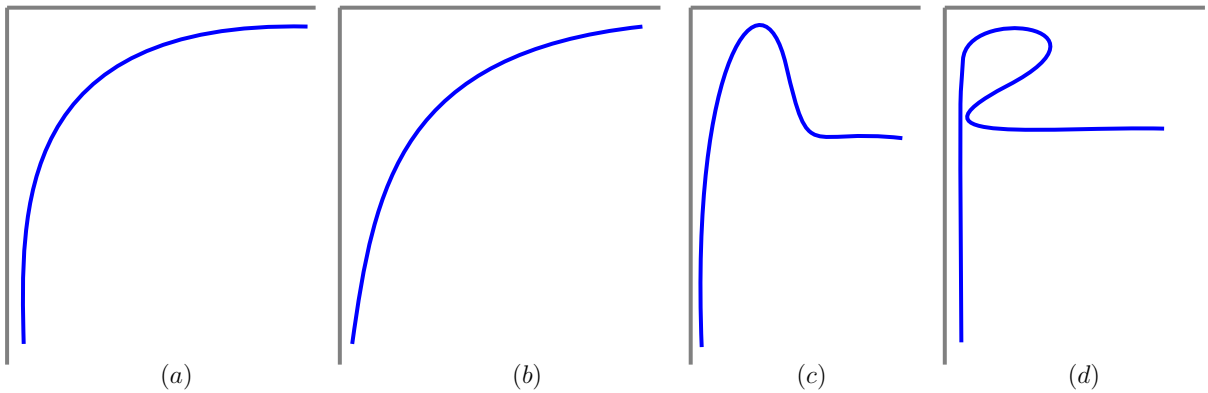

Figure 5.11: A schematic of the typical flow pattern in the upper left corner region of the rectangular cavity.

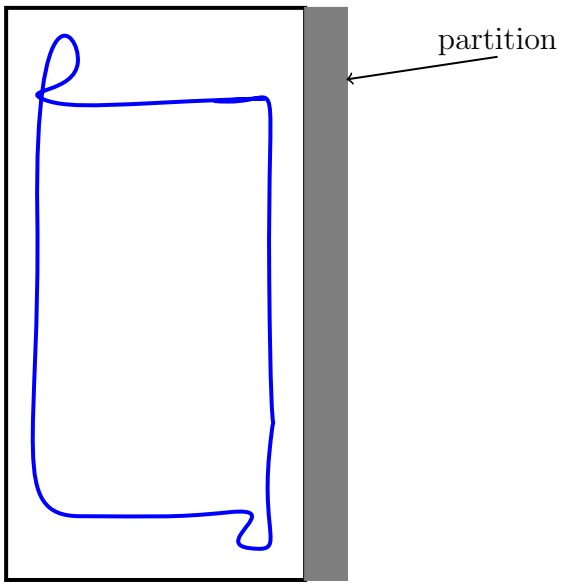

Figure 5.12: Dividing stream function in the left half-cavity.

The effect of the partition thickness can be seen in figures of temperature contours (*i.e.*, figures 5.1, 5.3, 5.5, 5.7 and 5.9) and stream function (*i.e.*, figures 5.2, 5.4, 5.6, 5.8 and 5.10). The partition thickness mainly influences temperature and stream function contours in the cavity by altering the fluid-filled area. Cavities with thinner partitions have wider half-cavities than the ones with thick partitions. Stronger convection in the wider half-cavities causes shifting from a single-cell flow pattern to a multiple cell flow pattern. This behaviour can be seen in figures 5.2(m, n and o) as the cavity with the thickest partition (*i.e.*, 5.2(o)) has a single-cell flow pattern and gradually by decreasing the partition thickness (*i.e.*, 5.2(n)) new vortex eyes appear. By further decreasing the partition thickness (*i.e.*, 5.2(m)) the created vortex eyes are completely separated and move to the vicinity of walls. After viewing the temperature contours within the partition for $k_r > 1$, it is seen that if there is a temperature difference between the top and the bottom of the partition, the thinner partition shows a bigger temperature difference which can be observed by the number of isotherms in that area. As the thickness increases the isotherms in the partition decreases. For instance, the number of isotherms in the partition is 8 in figure 5.5(m), 6 in figure 5.5(n), and 4 figure 5.5(o).

Thermal conductivity ratio (k_r) is the other parameter presented in the temperature contour figures (*i.e.*, figures 5.1, 5.3, 5.5, 5.7 and 5.9) and stream function figures (*i.e.*, figures 5.2, 5.4, 5.6, 5.8 and 5.10). The small thermal conductivity ratio of 0.1 implies high thermal resistance of the partition. As mentioned earlier, at the fluid-solid interface, the condition $k_s(\frac{\partial\theta}{\partial x})_s = k_f(\frac{\partial\theta}{\partial x})_f$ is satisfied, hence the isotherms in the vicinity of the fluid-solid interface are directly related to the thermal conductivities, and the increase of k_s pushes isotherms to become closer to a horizontal line whereas reducing k_s moves isotherm orientation to be closer to a vertical line. Figure 5.1 shows that the heat conduction from the left half-cavity to the right half-cavity through the partition is very low and all the heated fluids in the left half-cavity and cooled fluid in the right half-cavity are mainly trapped in each side. Isotherms in the partition for all cases in figure 5.1 are almost vertical. As Ra increases (from the top to the bottom in figure 5.1) the number of isotherms in the fluid-filled section of the cavity decreases and the isotherms in the partition increase. This implies that the main temperature gradient is in the partition, and the temperature difference between the left and the right sides of the partition

gets larger. Similar behavior can be seen for the T_p effect, as the partition thickness increases (from the left to the right in figure 5.1), the number of isotherms in the fluid-filled region of the cavity decreases. This trend continues as figure 5.1 (r) shows that only one isotherm is in each half-cavity and the rest of 28 isotherms are in the partition. By considering an equal thermal conductivity for the fluid and the partition, temperature contour figures drastically change. For the conduction-dominated case ($Ra = 10^3$), isotherms are vertical and uniformly spread in the whole cavity and no significant difference can be seen when partition thickness changes. As Ra increases the angle of isotherms in the fluid-filled and the partition area increases (*i.e.*, figure $5.3(d), (e)$ and (f)). Interestingly, by further increasing Ra isotherms in the fluid-filled area are continuously connected to the isotherms in the partition without any breaking point. This observation is expected due to the equal thermal conductivity of the fluid and the partition which does not create a different temperature gradient before and after the fluid-solid interface.

Increasing thermal conductivity of the partition ($k_r = 100$) causes a decrease in the thermal resistance of the partition which can be seen by the equal temperature on both sides of the partition as shown in figure 5.5 $(a-c)$. By increasing Ra and decreasing the partition thickness, some isotherms can be observed in the partition area. The angle of these isotherms is higher (from the vertical sidewalls) than the ones observed for the case $k_r = 1$. This angle gradually increases by increasing k_r to 1000. The number of partitions without any isotherms increases by decreasing Ra and increasing k_r. This behavior shows a trivial thermal resistance of the partition which can be considered as a thermal independence of each half-cavity. In other words, the partition can be evaluated as an isothermal wall in these cases. Eventually, it is possible to define the equivalent non-partitioned cavity to investigate each half-cavity. The new equivalent non-partitioned cavity has different conditions. The corresponding Ra, modified Ra (Ra^*), is defined as $Ra^* = Ra \times \frac{\Delta T^*}{T_h - T_c}$, where ΔT^* is the temperature difference between the sidewall and the partition. The height of the new equivalent non-partitioned cavity is larger than the length and the aspect ratio is $A = \frac{H}{L-(X_p-\frac{T_p}{2})}$.

Studying the stream function figures reveals that as k_r increases flow pattern in each half-cavity becomes vertically stretched (*e.g.*, $Ra = 10^6$ cases in figures 5.2, 5.4, 5.6, 5.8 and 5.10). With vertical stretching, the core of the flow pattern becomes more centered. The reason behind

this phenomenon can be explained by the temperature contour figures (*e.g.*, $Ra = 10^6$ cases in figures 5.1, 5.3, 5.5, 5.7 and 5.9). The cases with smaller k_r has a hotter or cooler half-cavity than the cases with larger k_r and as k_r increases temperature contour figures show less heated or cooled half-cavity. Also, the temperature difference at the top and the bottom of half-cavities is lower for small k_r than the ones with large k_r. Therefore, the horizontal discharges at the top and the bottom of the cases with large k_r are faster than that in the small k_r cases.

B. Vertical and horizontal velocity distributions

Figures 5.13, 5.15, 5.17, 5.19 and 5.21 present the vertical velocity contours and figures 5.14, 5.16, 5.18, 5.20 and 5.22 show the horizontal velocity at the fully developed stage obtained numerically for $T_p = 0.05$, 0.1, and 0.2, each at $X_p = 0.5$ and at $Ra = 10^3$, 10^4, 10^5, 10^6, 10^7 and 10^8, respectively. Due to different maximum and minimum values for each contour figure, the corresponding maximum and minimum value have been presented for each figure (*i.e.*, $maximum : minimum$).

By increasing Ra the vertical velocity boundary layers close to the sidewalls and the horizontal velocity boundary layers close to the top and bottom walls become thinner for all cases presented in the velocity contour figures. It can also be seen that the length of walls covered by the vertical velocity boundary layer increases as Ra increases. For the case of $Ra = 10^3$, velocity contours show a symmetrical pattern (with horizontal line symmetry) in each half-cavity. Increasing Ra to 10^4 and more causes stronger horizontal flow in the half-cavity and the symmetry becomes rotational. Vertical velocity boundary layers on sidewalls and the partition have a strong interaction with each other up to $Ra = 10^6$. As the partition thickness increases this interaction increases due to the decrease of the size of the half-cavity. Smaller k_r shows thicker velocity boundary layers and consequently the boundary layer interaction for those cases is higher (*e.g.*, $Ra = 10^6$ in figure 5.13(j) vs. $Ra = 10^6$ in figure 5.21(j)). Therefore, the boundary-layer thickness extracted from the cases with boundary layer interaction may not have the same trend of boundary-layer thickness of other cases without interaction.

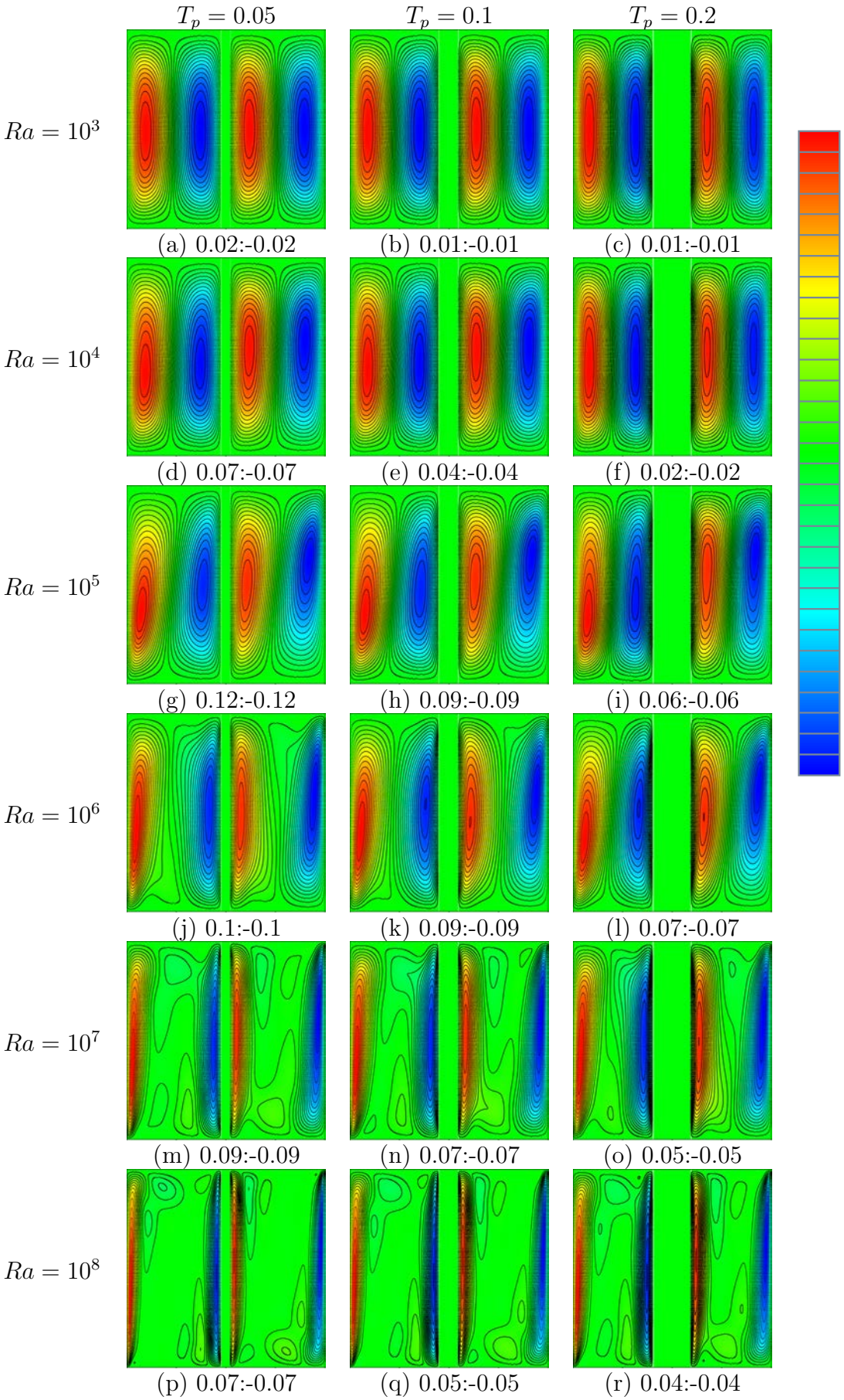

(a) 0.02:-0.02 (b) 0.01:-0.01 (c) 0.01:-0.01

(d) 0.07:-0.07 (e) 0.04:-0.04 (f) 0.02:-0.02

(g) 0.12:-0.12 (h) 0.09:-0.09 (i) 0.06:-0.06

(j) 0.1:-0.1 (k) 0.09:-0.09 (l) 0.07:-0.07

(m) 0.09:-0.09 (n) 0.07:-0.07 (o) 0.05:-0.05

(p) 0.07:-0.07 (q) 0.05:-0.05 (r) 0.04:-0.04

Figure 5.13: Vertical velocity contours at $k_r = 0.1$ and $X_p = 0.5$ for different Ra values ($10^3 \leq Ra \leq 10^8$) and T_p ($T_p = 0.05$, 0.1 and 0.2).

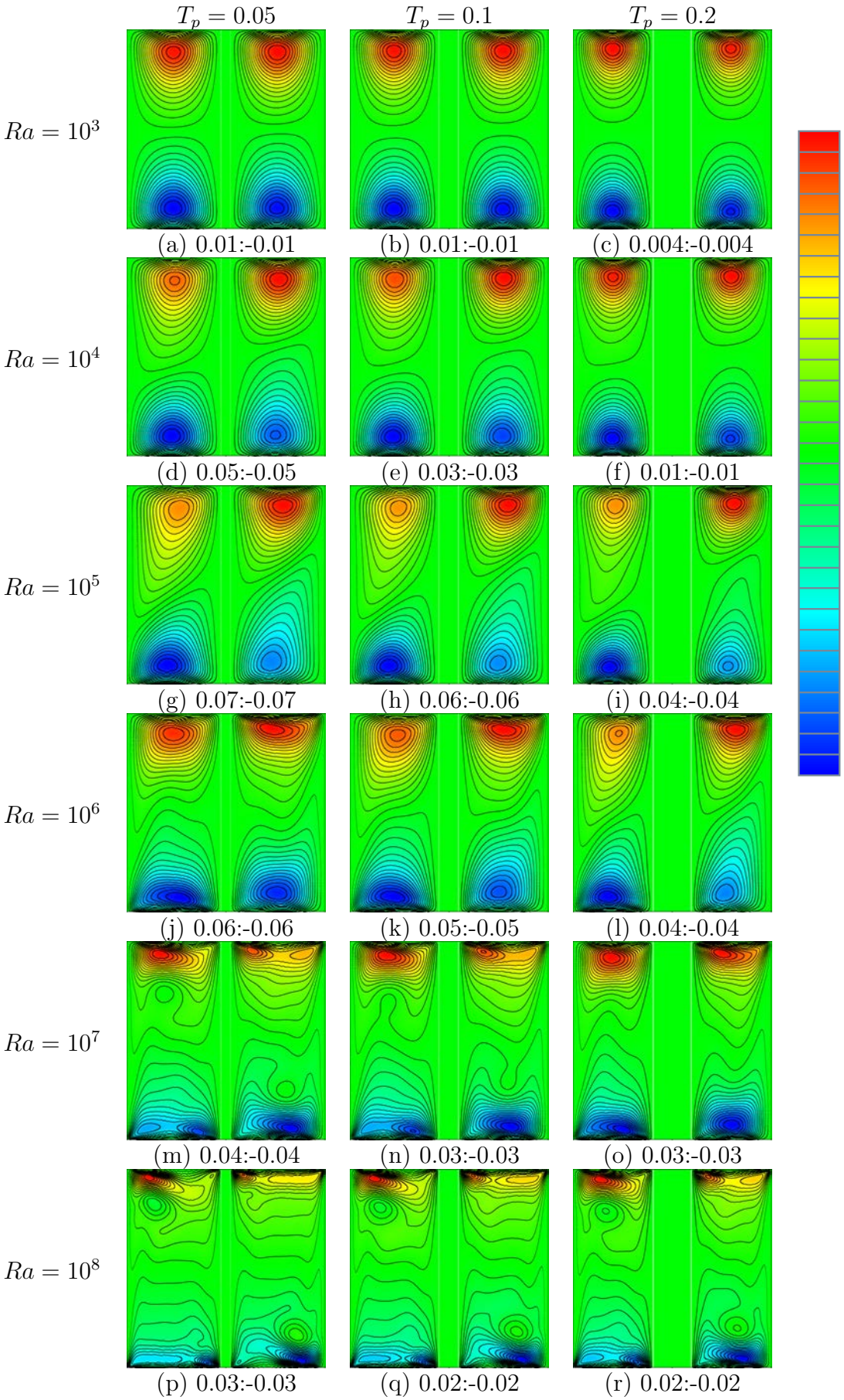

(a) 0.01:-0.01 (b) 0.01:-0.01 (c) 0.004:-0.004

(d) 0.05:-0.05 (e) 0.03:-0.03 (f) 0.01:-0.01

(g) 0.07:-0.07 (h) 0.06:-0.06 (i) 0.04:-0.04

(j) 0.06:-0.06 (k) 0.05:-0.05 (l) 0.04:-0.04

(m) 0.04:-0.04 (n) 0.03:-0.03 (o) 0.03:-0.03

(p) 0.03:-0.03 (q) 0.02:-0.02 (r) 0.02:-0.02

Figure 5.14: Horizontal velocity contours at $k_r = 0.1$ and $X_p = 0.5$ for different Ra values ($10^3 \leq Ra \leq 10^8$) and T_p ($T_p = 0.05$, 0.1 and 0.2).

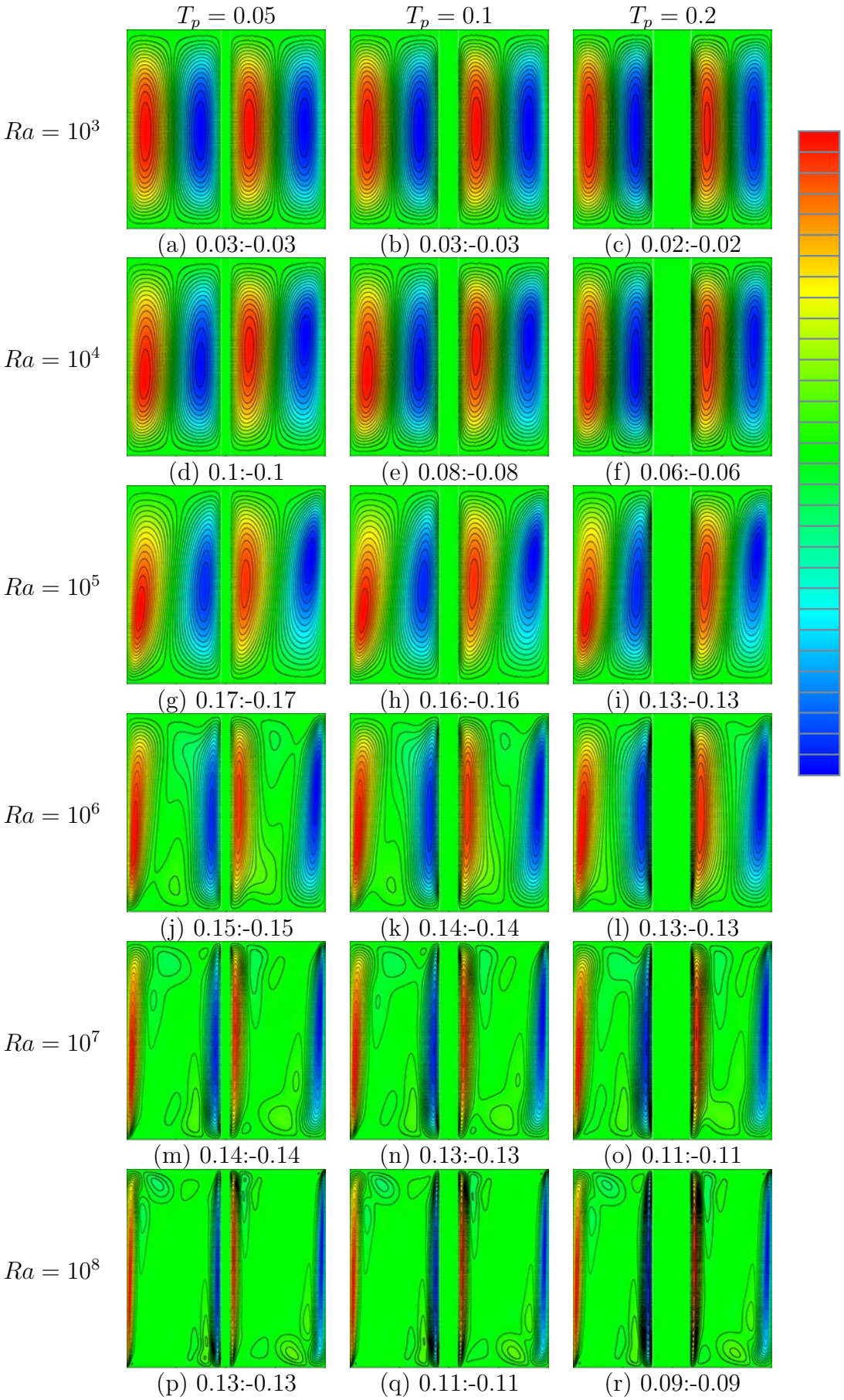

Figure 5.15: Vertical velocity contours at $k_r = 1$ and $X_p = 0.5$ for different Ra values ($10^3 \leq Ra \leq 10^8$) and T_p ($T_p = 0.05$, 0.1 and 0.2).

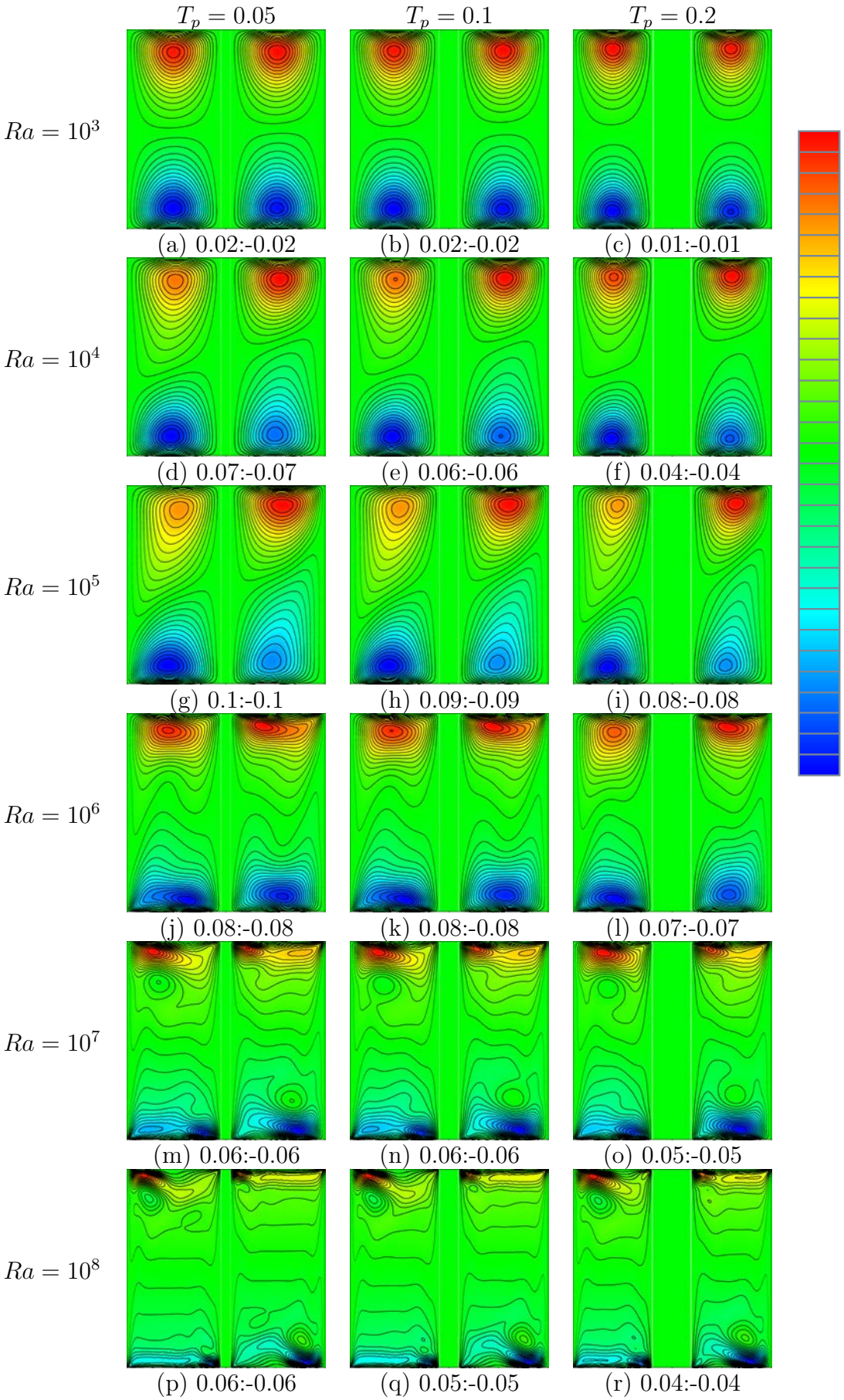

(a) 0.02:-0.02 (b) 0.02:-0.02 (c) 0.01:-0.01

(d) 0.07:-0.07 (e) 0.06:-0.06 (f) 0.04:-0.04

(g) 0.1:-0.1 (h) 0.09:-0.09 (i) 0.08:-0.08

(j) 0.08:-0.08 (k) 0.08:-0.08 (l) 0.07:-0.07

(m) 0.06:-0.06 (n) 0.06:-0.06 (o) 0.05:-0.05

(p) 0.06:-0.06 (q) 0.05:-0.05 (r) 0.04:-0.04

Figure 5.16: Horizontal velocity contours at $k_r = 1$ and $X_p = 0.5$ for different Ra values ($10^3 \leq Ra \leq 10^8$) and T_p ($T_p = 0.05$, 0.1 and 0.2).

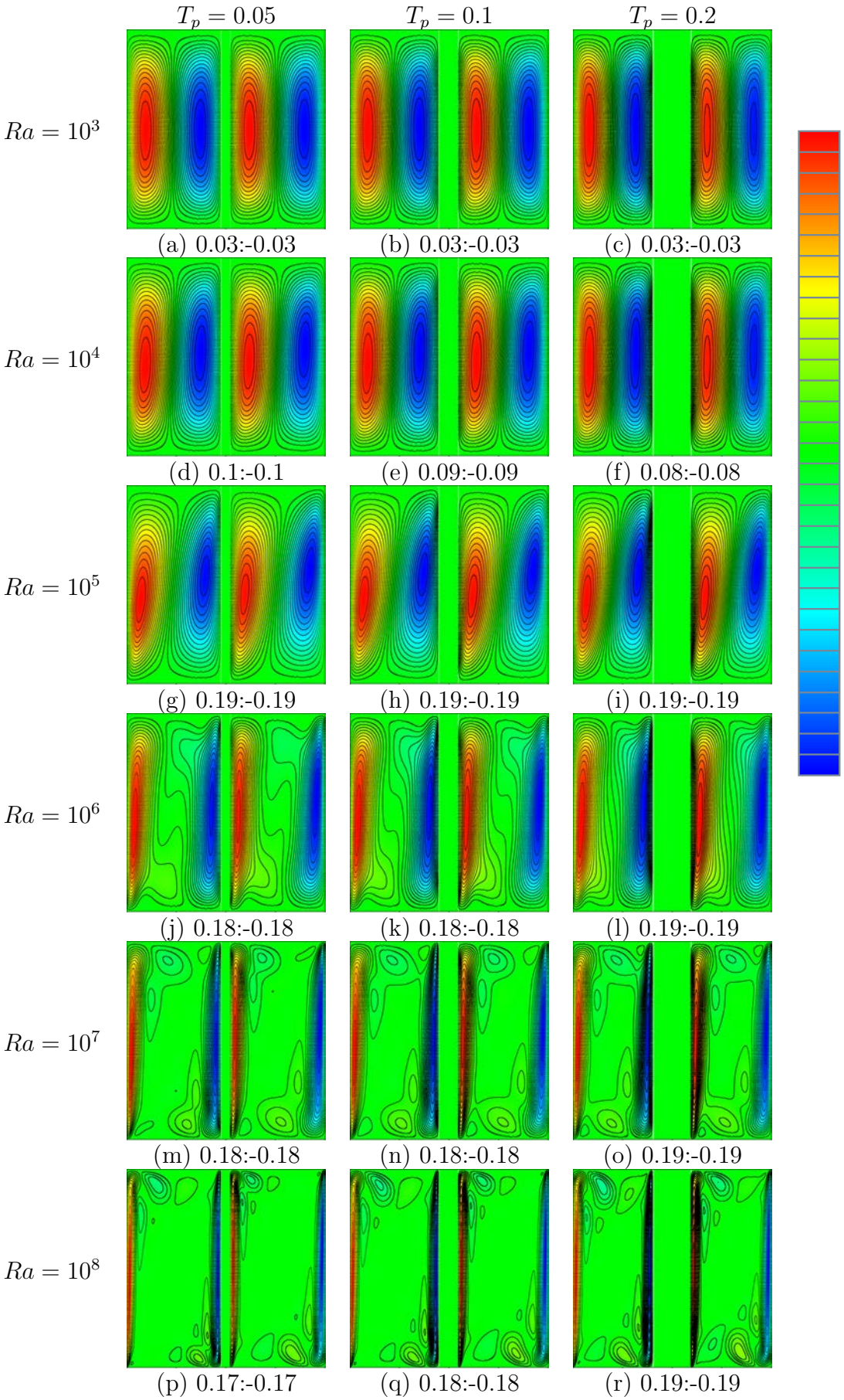

(a) 0.03:-0.03 (b) 0.03:-0.03 (c) 0.03:-0.03

(d) 0.1:-0.1 (e) 0.09:-0.09 (f) 0.08:-0.08

(g) 0.19:-0.19 (h) 0.19:-0.19 (i) 0.19:-0.19

(j) 0.18:-0.18 (k) 0.18:-0.18 (l) 0.19:-0.19

(m) 0.18:-0.18 (n) 0.18:-0.18 (o) 0.19:-0.19

(p) 0.17:-0.17 (q) 0.18:-0.18 (r) 0.19:-0.19

Figure 5.17: Vertical velocity contours at $k_r = 100$ and $X_p = 0.5$ for different Ra values ($10^3 \leq Ra \leq 10^8$) and T_p ($T_p = 0.05$, 0.1 and 0.2).

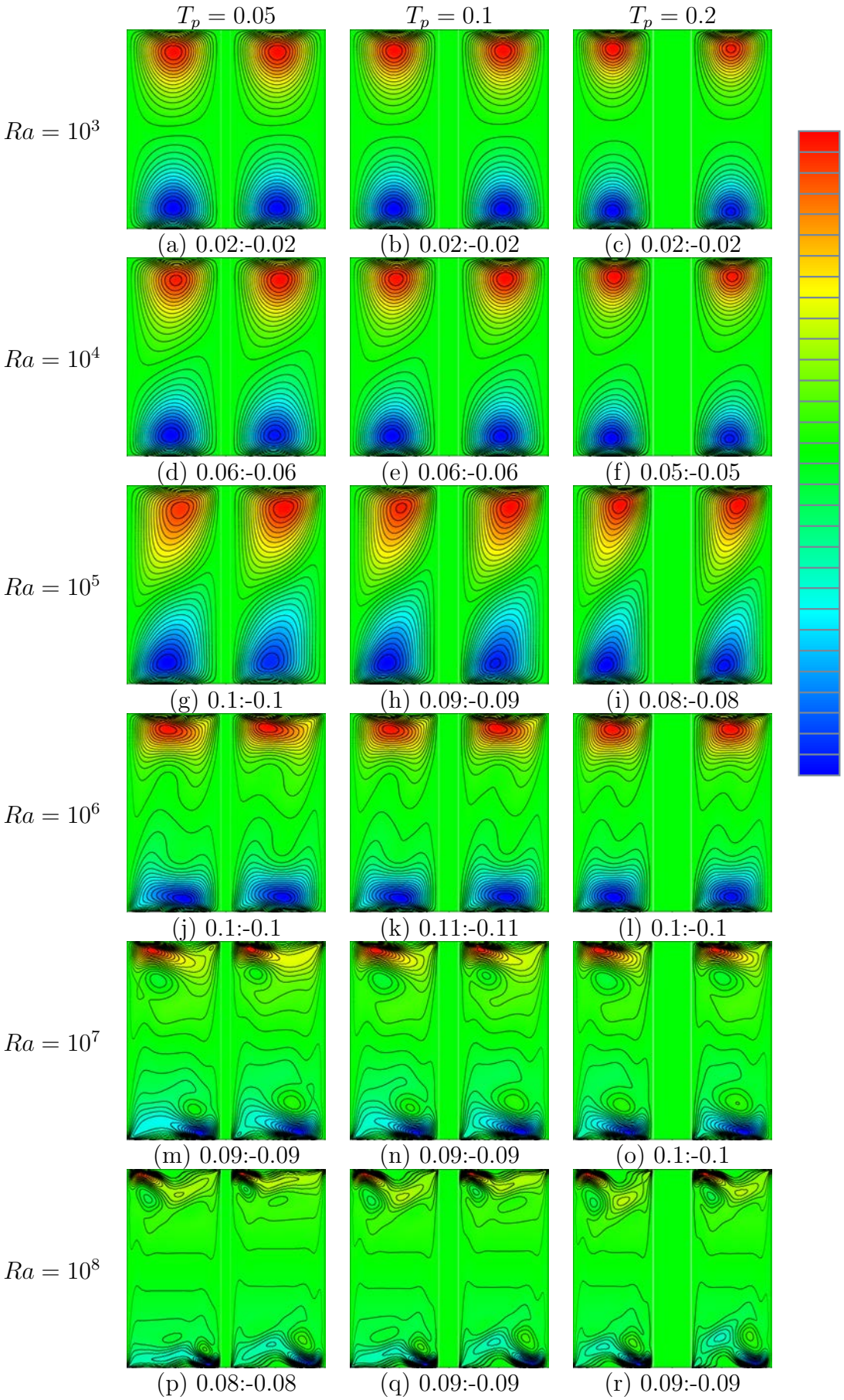

Figure 5.18: Horizontal velocity contours at $k_r = 100$ and $X_p = 0.5$ for different Ra values ($10^3 \leq Ra \leq 10^8$) and T_p ($T_p = 0.05$, 0.1 and 0.2).

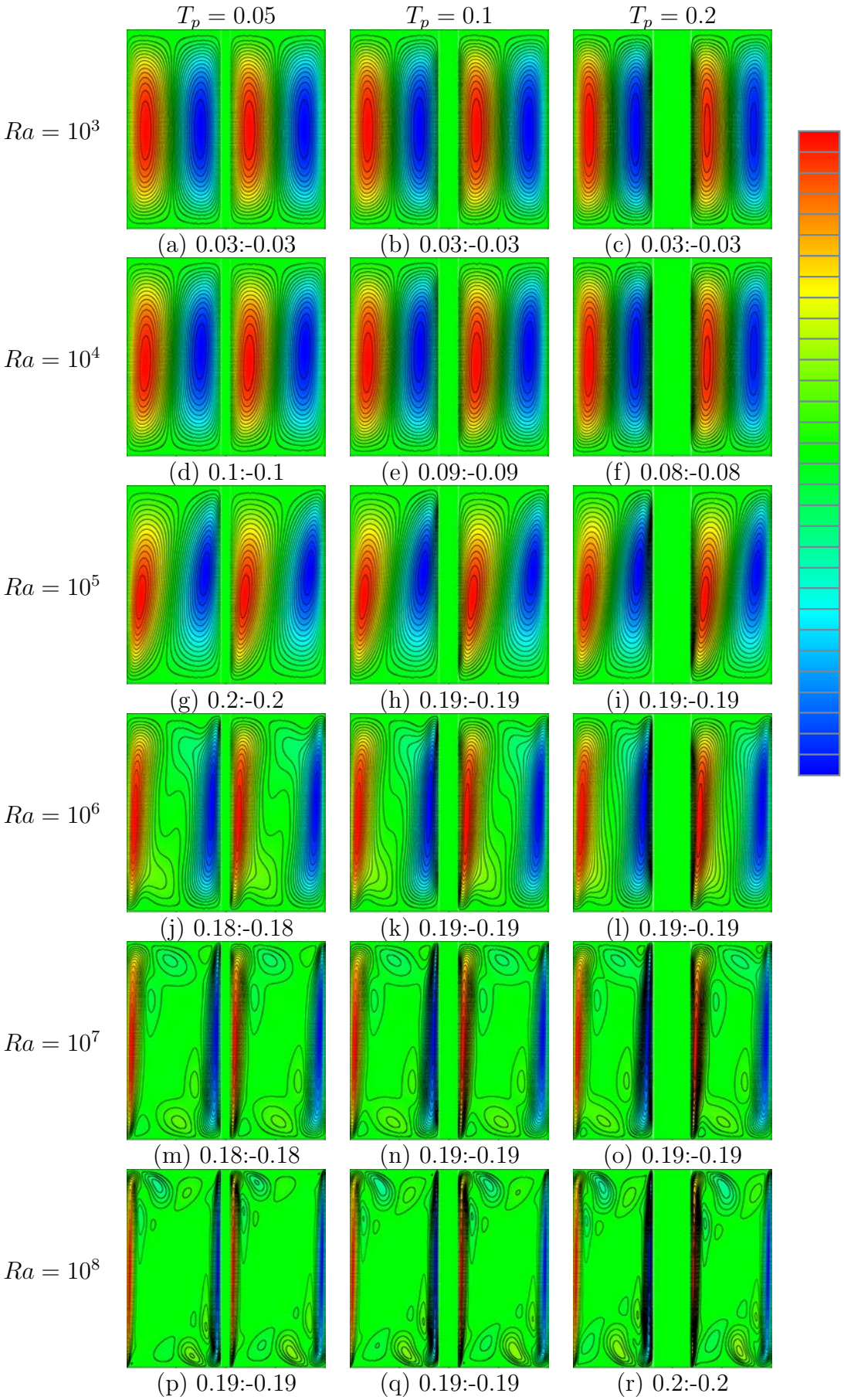

(a) 0.03:-0.03 (b) 0.03:-0.03 (c) 0.03:-0.03

(d) 0.1:-0.1 (e) 0.09:-0.09 (f) 0.08:-0.08

(g) 0.2:-0.2 (h) 0.19:-0.19 (i) 0.19:-0.19

(j) 0.18:-0.18 (k) 0.19:-0.19 (l) 0.19:-0.19

(m) 0.18:-0.18 (n) 0.19:-0.19 (o) 0.19:-0.19

(p) 0.19:-0.19 (q) 0.19:-0.19 (r) 0.2:-0.2

Figure 5.19: Vertical velocity contours at $k_r = 500$ and $X_p = 0.5$ for different Ra values ($10^3 \leq Ra \leq 10^8$) and T_p ($T_p = 0.05$, 0.1 and 0.2).

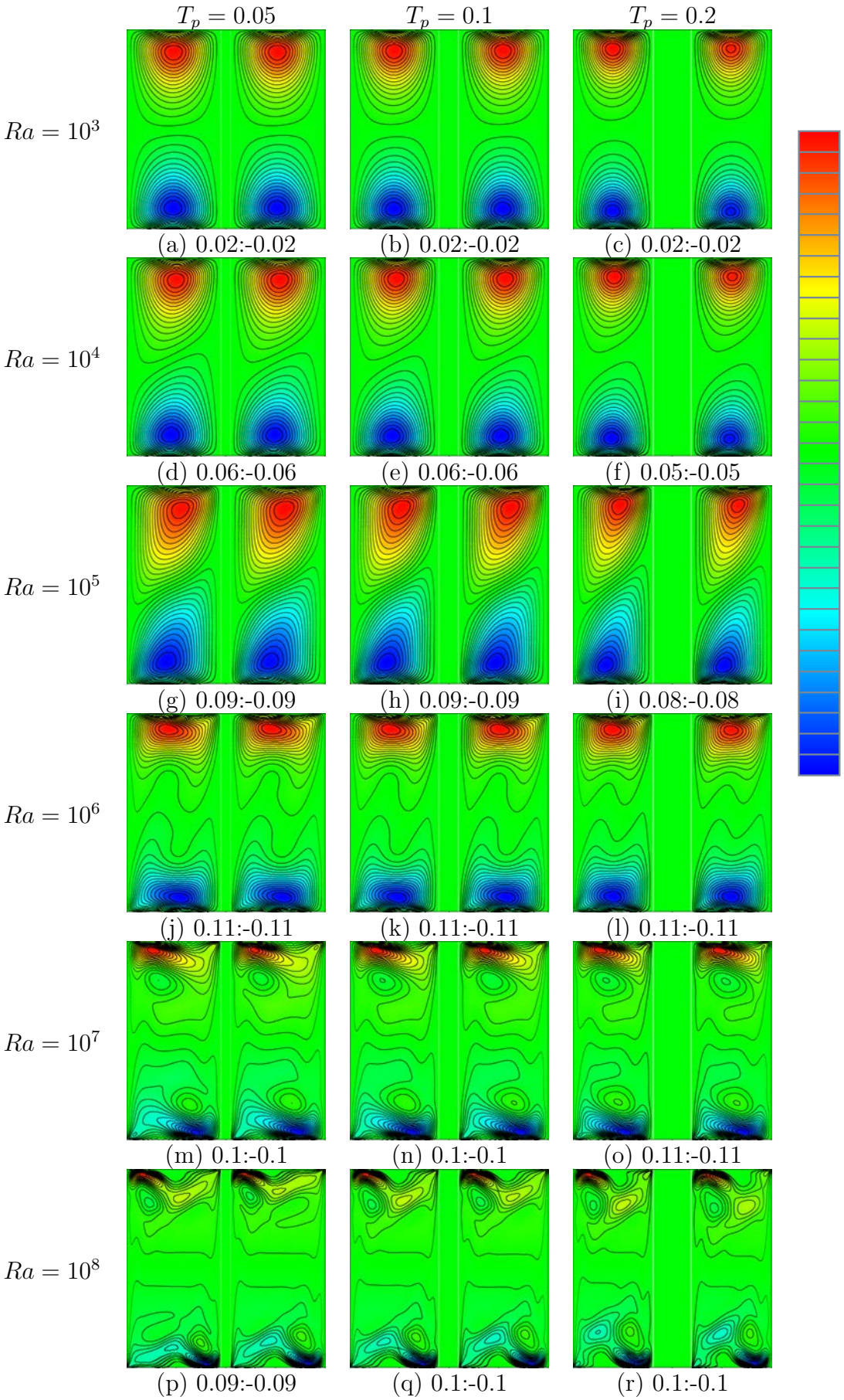

Figure 5.20: Horizontal velocity contours at $k_r = 500$ and $X_p = 0.5$ for different Ra values ($10^3 \leq Ra \leq 10^8$) and T_p ($T_p = 0.05$, 0.1 and 0.2).

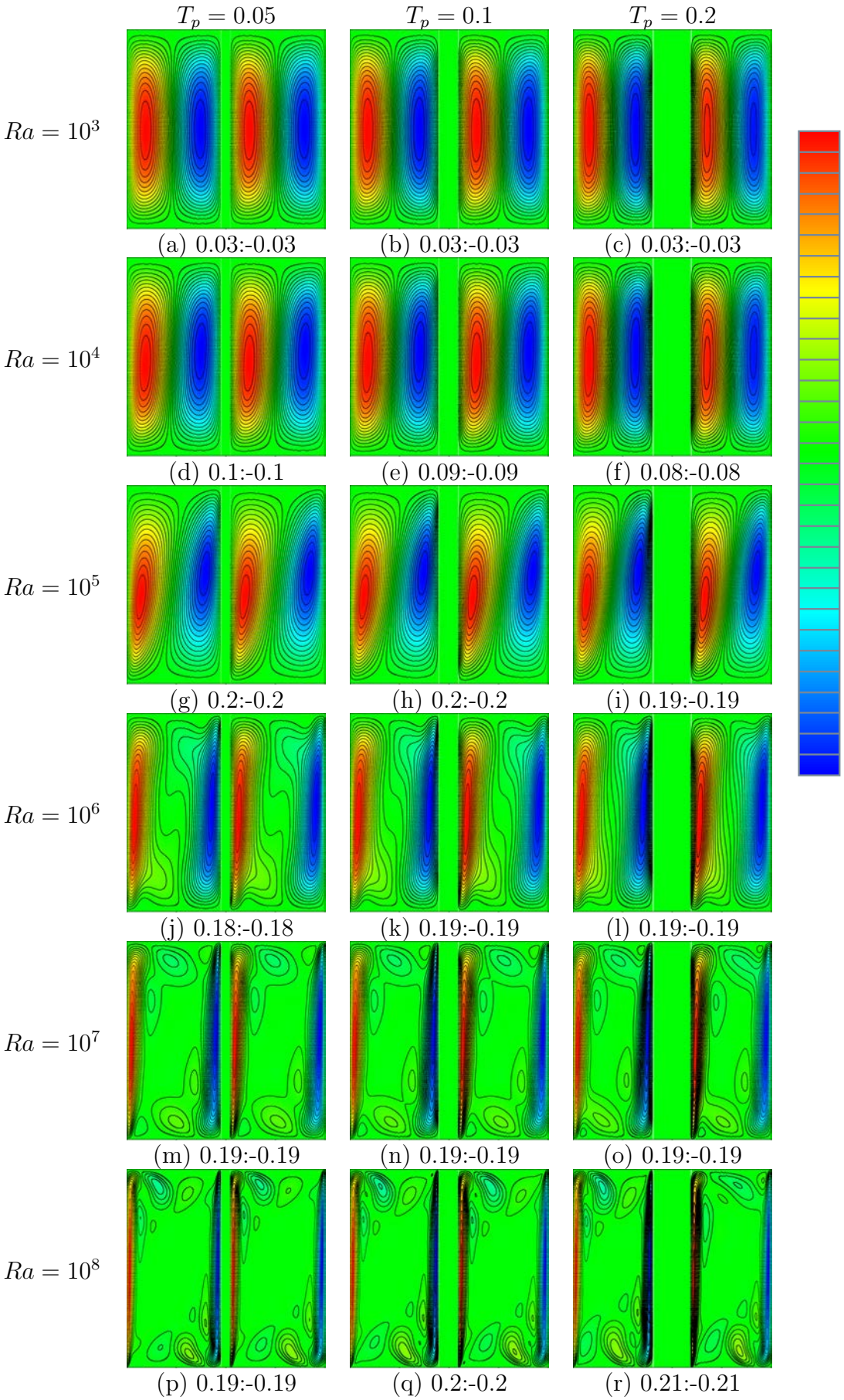

(a) 0.03:-0.03 (b) 0.03:-0.03 (c) 0.03:-0.03

(d) 0.1:-0.1 (e) 0.09:-0.09 (f) 0.08:-0.08

(g) 0.2:-0.2 (h) 0.2:-0.2 (i) 0.19:-0.19

(j) 0.18:-0.18 (k) 0.19:-0.19 (l) 0.19:-0.19

(m) 0.19:-0.19 (n) 0.19:-0.19 (o) 0.19:-0.19

(p) 0.19:-0.19 (q) 0.2:-0.2 (r) 0.21:-0.21

Figure 5.21: Vertical velocity contours at $k_r = 1000$ and $X_p = 0.5$ for different Ra values ($10^3 \leq Ra \leq 10^8$) and T_p ($T_p = 0.05$, 0.1 and 0.2).

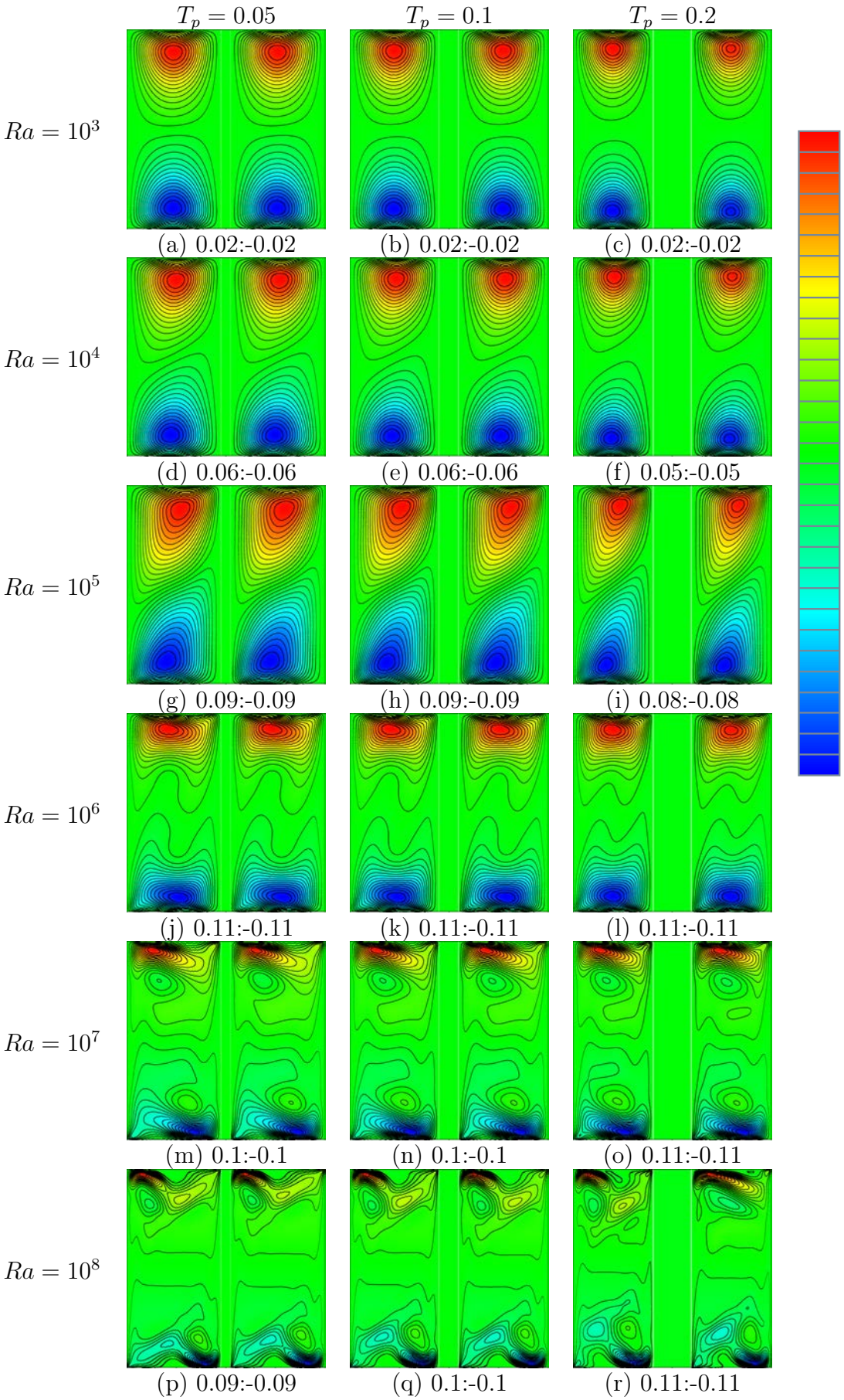

Figure 5.22: Horizontal velocity contours at $k_r = 1000$ and $X_p = 0.5$ for different Ra values ($10^3 \leq Ra \leq 10^8$) and T_p ($T_p = 0.05$, 0.1 and 0.2).

Interestingly, the flow jumping close to the corner observed in the stream function figures can be seen in horizontal velocity contours. It can be seen that there is an area of high horizontal velocity close to the corner. This high-velocity area becomes closer to the corner by increasing Ra (*e.g.*, top-left corner in figure 5.22(p)).

Figure 5.23 shows horizontal temperature profiles at the mid-height of the cavity ($y = 0.5$) for different values of Ra (10^3, 10^4, 10^5, 10^6, 10^7 and 10^8), k_r (0.1, 1, 100, 500 and 1000) and T_p (0.05, 0.1, and 0.2).

The horizontal temperature profiles presented for $Ra = 10^3$ and 10^4 are straight lines due to conduction-dominated heat transfer and the stratification showed for the higher Ra ($10^5 \leq Ra \leq 10^8$) do not exist. Regarding the effect of Ra and T_p on the horizontal temperature profile, two different behaviours can be seen for $0.1 \leq k_r \leq 1$ and $100 \leq k_r \leq 1000$. As figure 5.23(a) and (b) show, larger Ra and T_p show higher temperatures at the middle of the cavity. $k_r = 100$ is a turning point for the T_p effect where T_p shows decreasing effect on the temperature of the stratified region. For this range of k_r ($100 \leq k_r \leq 1000$), the Ra variation shows a little effect on the middle half-cavity temperature. $k_r = 100$ is also the starting point for the presence of the horizontal temperature profile inside the partition. It can also be seen that the shape of the temperature profile in the half-cavity is completely asymmetric for low k_r and as k_r rises the asymmetry diminishes. This means that thermal behavior of the sidewall and the partition becomes similar when the symmetry is achieved. Moreover, the temperature of the stratified region reduces with increasing k_r which is apparently due to the increased thermal conductivity of the partition.

5.2.2 Quantitative analysis of flow and heat transfer behaviour

To study the effects of the partition thickness and the thermal conductivity ratio, it is necessary to make use of a relation which is based on the scaling analysis of heat transfer through the partition wall. A wall function was suggested by Lock and Ko [242] to quantify the thermal resistance of a conducting partition and have criteria for thermal behaviour of the partition by

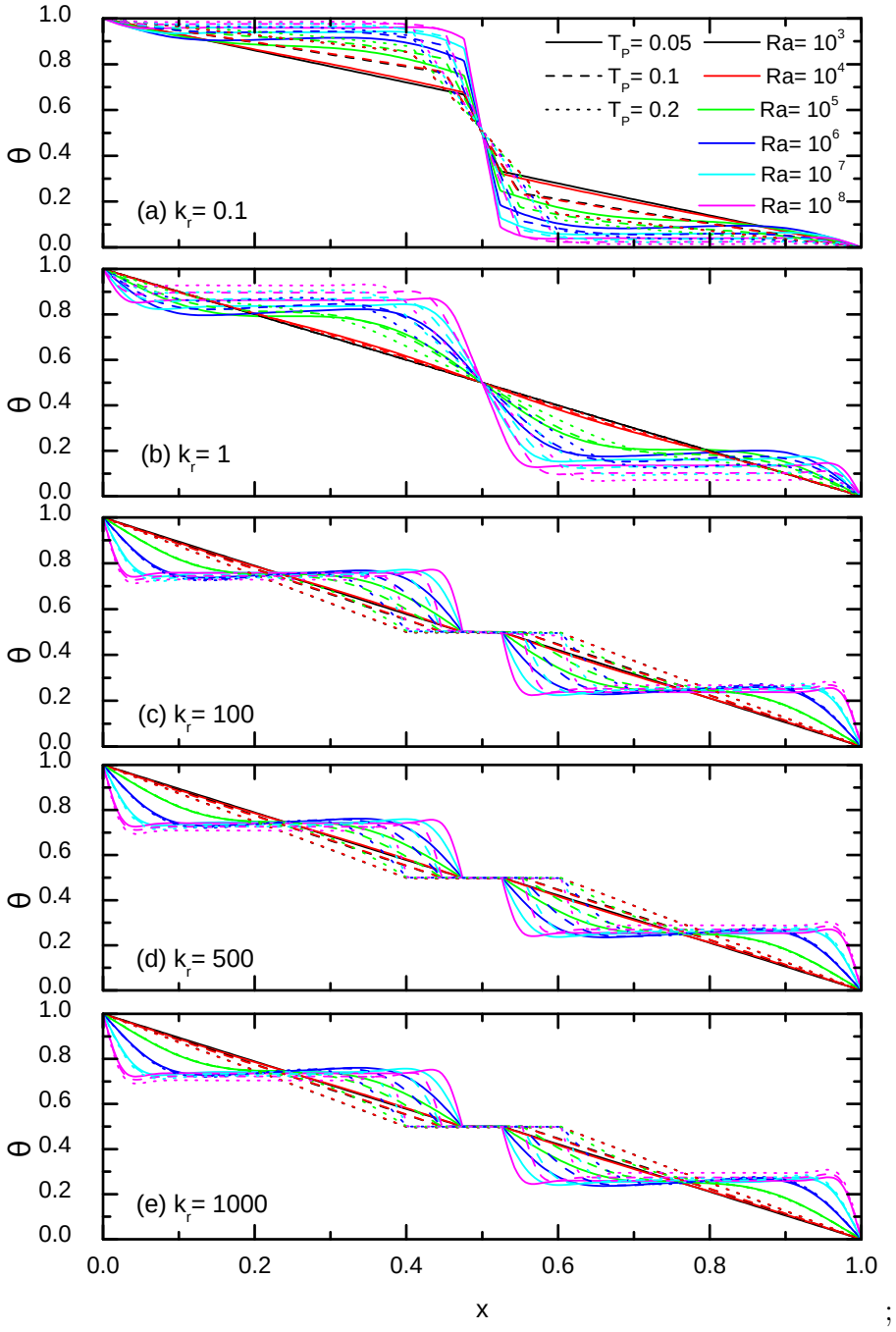

Figure 5.23: Horizontal temperature profiles at the mid-height ($y = 0.5$) for different values of Ra (10^3, 10^4, 10^5, 10^6, 10^7 and 10^8), k_r (0.1, 1, 100, 500 and 1000) and T_p (0.05, 0.1, and 0.2).

including Tp, Ra, k_r and Pr,

$$\chi = \frac{T_p}{k_r} Ra^{1/4} (\frac{Pr}{1+Pr})^{1/4}, \tag{5.1}$$

where χ is a dimensionless thermal resistance parameter for a partition.

At the steady state the heat flux passing through the partition (q_p'') is expected to be equal to the heat flux leaving the left half-cavity or entering right half-cavity (q_f'').

$$q_f'' = k_f \frac{\Delta\theta_f}{\delta_T} = q_p'' = k_s \frac{\theta_{D,x}}{T_p}, \tag{5.2}$$

where $\Delta\theta_f$ and $\theta_{D,x}$ are temperature differences between the partition temperature and the bulk temperature of fluid and between the temperatures on the left and right sides of the partition, respectively.

For large k_r cases, the number of isotherms in the partition is very low or none (see, figure 5.9). These cases also show an important point regarding the temperature gradient of the partition area where the temperature of the left and right side of the partition is almost equal. This low temperature difference leads to a negligible heat flux through the partition (see, equation (5.2)). In other words, this situation shows the adiabatic boundary condition of almost zero temperature gradient in the x direction at the partition. Considering $Ra = \frac{g\beta H^4 q''}{\alpha\nu k_f}$, these observations cause a low χ ($\chi \simeq 0$). The low thermal resistance parameter of the partition due to large k_r shows that the partition can be considered as an isothermal wall and the heat transfer characteristics are similar to those of a non-partitioned cavity case and consequently the scaling relations of an isothermal wall for a non-partitioned cavity can be used. The thermal boundary layer and the average Nusselt number scaling relations for an isothermal wall are as follows,

$$\delta_T \quad or \quad Nu \sim Ra^{1/4}. \tag{5.3}$$

This condition can also exist when the partition thickness is very small. A thinner partition causes a lower temperature difference between the left and right sides of the partition which intensifies isothermal behavior of the partition.

As already observed in the temperature contour figures, k_r influences the temperature gradient

in the partition. Smaller k_r induces the higher temperature gradient in the partition. Therefore, the temperature difference between the left and right side of the partition is dependent on both k_r and T_p. As a consequence, it is impossible to make a decision based on only one of these parameters (*i.e.*, T_p and k_r).

Meyer *et al.* [296] studied the effect of a conducting partition on natural convection in an inclined rectangular cavity and reported that to minimize the total heat transfer rate at $1 \leq k_r \leq 20$, the partition thickness should be less than 0.01.

By increasing the value of χ, the thermal behavior of the partition shifts from an isothermal wall like to an isoflux wall type. In this situation the partition has uniform heat flux and the thermal resistance parameter role becomes important. The scaling relations extracted for an isoflux wall in a non-partitioned cavity are more appropriate for the higher χ and the thermal boundary layer and the average Nusselt number scaling relations are as follows,

$$\delta_T \quad or \quad Nu \sim Ra^{1/5}. \tag{5.4}$$

The χ parameter range for this study is from 2.25×10^{-4}, which is for $k_r = 1000$, $T_p = 0.05$, $Pr = 0.71$ and $Ra = 10^3$, to 160.54, which is for $k_r = 0.1$, $T_p = 0.2$, $Pr = 0.71$ and $Ra = 10^8$.

To demonstrate the effect on the average Nusselt number (Nu_{Ave}), figure 5.25 presents Nu_{Ave} for a range of Ra values, partition thickness (T_p) and thermal conductivity ratio (k_r). As Ra increases Nu_{Ave} increases in all cases presented in the figure. Also, it can be seen that the difference between Nu_{Ave} of consecutive Ra values increases as Ra increases. The overall trend of Nu_{Ave} in this figure shows that k_r increases for low Ra and attains a plateau earlier than higher Ra. For instance, $Ra = 10^3$ and 10^4 cases level off at $k_r = 1$, $Ra = 10^5$ from $k_r = 100$ and $Ra = 10^6$ from $k_r = 500$. These results are in agreement with those obtained by Kahveci [5]. Figure 5.24 shows the results presented by Kahveci [5] (data extracted by *WebPlotDigitizer* [297]) and this study for $10^4 \leq Ra \leq 10^6$ and $1 \leq k_r \leq 1000$, $T_p = 0.1$ and $X_p = 0.5$.

The effect of the partition thickness is notable for the range of k_r and Ra investigated in this

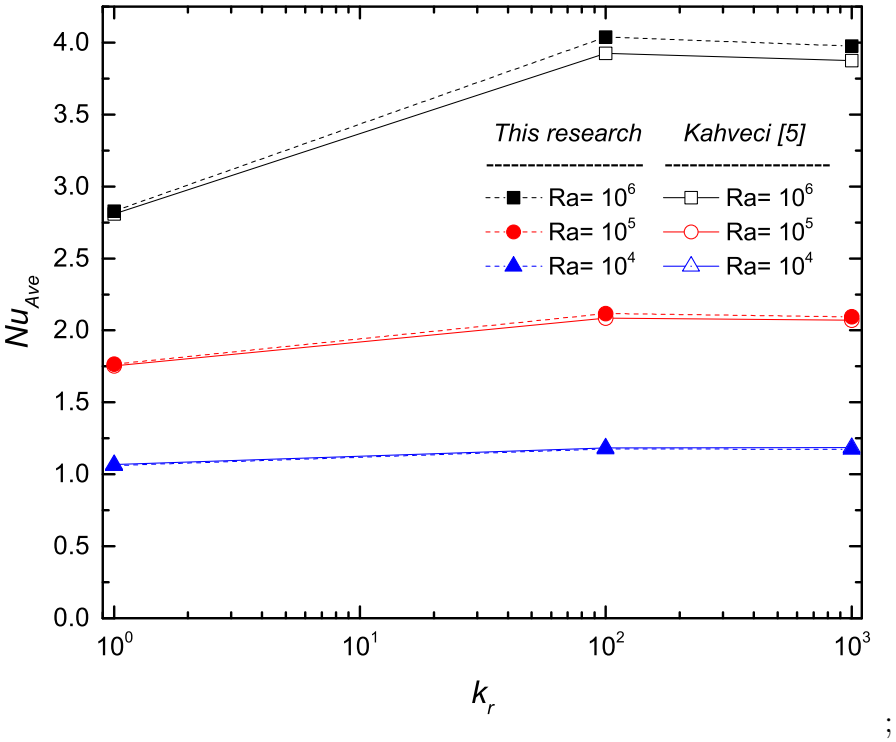

;

Figure 5.24: Average Nusselt number on the hot wall for a partitioned cavity with different partition thermal conductivity ratio ($1 \leq k_r \leq 1000$), $T_p = 0.1$ and $X_p = 0.5$ for $10^4 \leq Ra \leq 10^6$.

work. The first observation is that the effect of T_p is trivial for lower Ra cases than higher cases. As k_r increases to 1, T_p shows a significant effect on Nu_{Ave} for $10^5 \leq Ra \leq 10^8$ with thinner partition showing higher Nu_{Ave} (the expansion of lines from $k_r = 0.1$ to 1 at $10^5 \leq Ra \leq 10^8$). T_p has almost no effect on Nu_{Ave} in the range $10^3 \leq Ra \leq 10^4$ which can also be seen in figures 5.3. Interestingly, at $k_r = 100$, the increasing trend of Nu_{Ave} stops, indicating the presence of a maximum value of Nu_{Ave} between $1 < k_r \leq 100$. Increasing the value of k_r to 100 shows another remarkable behavior regarding the effect of the partition thickness. The influence of T_p on Nu_{Ave} is almost zero at $k_r = 100$. To explain this observation, it is necessary to review equation (5.1). As the equation shows, T_p and k_r have the opposite effects on the thermal resistance parameter of the partition. Therefore, it is expected to reach a point where k_r nullifies the effect of T_p. In this case, at $k_r = 100$, the increased thermal conductivity of the partition overcomes the thermal damping effect of the partition thickness. By further increasing k_r to 500 and 1000, the effect of k_r intensifies gradually (mainly for $10^6 \leq Ra \leq 10^8$) and the thicker partition with a larger k_r has higher Nu_{Ave} than the thinner partition.

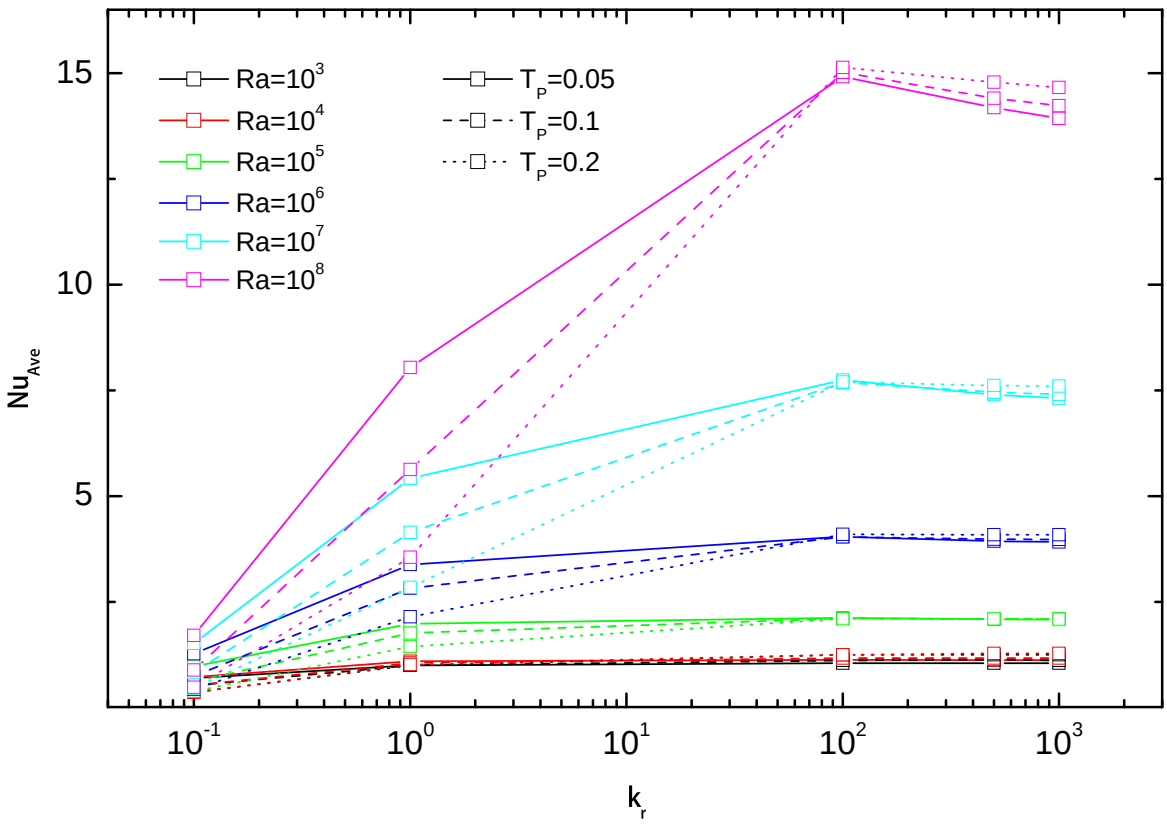

Figure 5.25: Average Nusselt number on the hot wall for a partitioned cavity with different partition thicknesses and thermal conductivity ratios for $10^3 \leq Ra \leq 10^8$.

Based on figure 5.25, the overall behaviour of Nu_{Ave} as k_r varies is illustrated schematically in figure 5.26. This schematic representation includes three main regions. The first region covers the low k_r range and according to equation (5.1) the value of χ is relatively high. By increasing k_r (*i.e.*, increase k_s with constant k_f), Nu_{Ave} rises and the horizontal temperature gradient in the partition gradually decreases (*i.e.*, $\frac{\partial \theta}{\partial x}$). This effect can be explained by using equation (5.2). To keep valid the constant heat flux in the cavity, the horizontal temperature gradient in the partition must decease. Eventually, this means that $\theta_{D,x}$ should decrease. In this region, the vertical temperature gradient in the partition is negligible. Finally this increasing trend of Nu_{Ave} reaches to a peak point and the horizontal temperature gradient in the partition becomes almost zero (*i.e.*, $\frac{\partial \theta}{\partial x} \approx 0$) which means the partition wall becomes horizontally isothermal. This region is named the thermal resistance region. Further increasing in k_r results in intensifying the vertical temperature gradient in the partition (*i.e.*, $\frac{\partial \theta}{\partial y}$). A stronger vertical temperature gradient than the horizontal one leads to characterizing the partition by the

vertical temperature gradient. Increasing k_r causes the partition to become vertically isothermal and eventually decreases Nu_{Ave}. This means that the temperature difference between the top and the bottom of the partition decreases which reduces heat flux in the partition and consequently decrease Nu_{Ave}. This decreasing trend of Nu_{Ave} continues until the vertical temperature gradient becomes negligible. This region is called the thermal transient region. Finally after the thermal transient region, by further increasing k_r, the vertical and horizontal temperature gradients in the partition become negligible (*i.e.*, $\frac{\partial\theta}{\partial x} \approx 0$ and $\frac{\partial\theta}{\partial y} \approx 0$). It is obvious that in this situation the partition becomes isothermal. In other words, increasing k_r dose not alter Nu_{Ave} and the heat transfer rate remains constant. By reaching this point, it can be appropriate to consider each half-cavity as a separate cavity with constant temperature on the sidewalls. This region is named as the isothermal region.

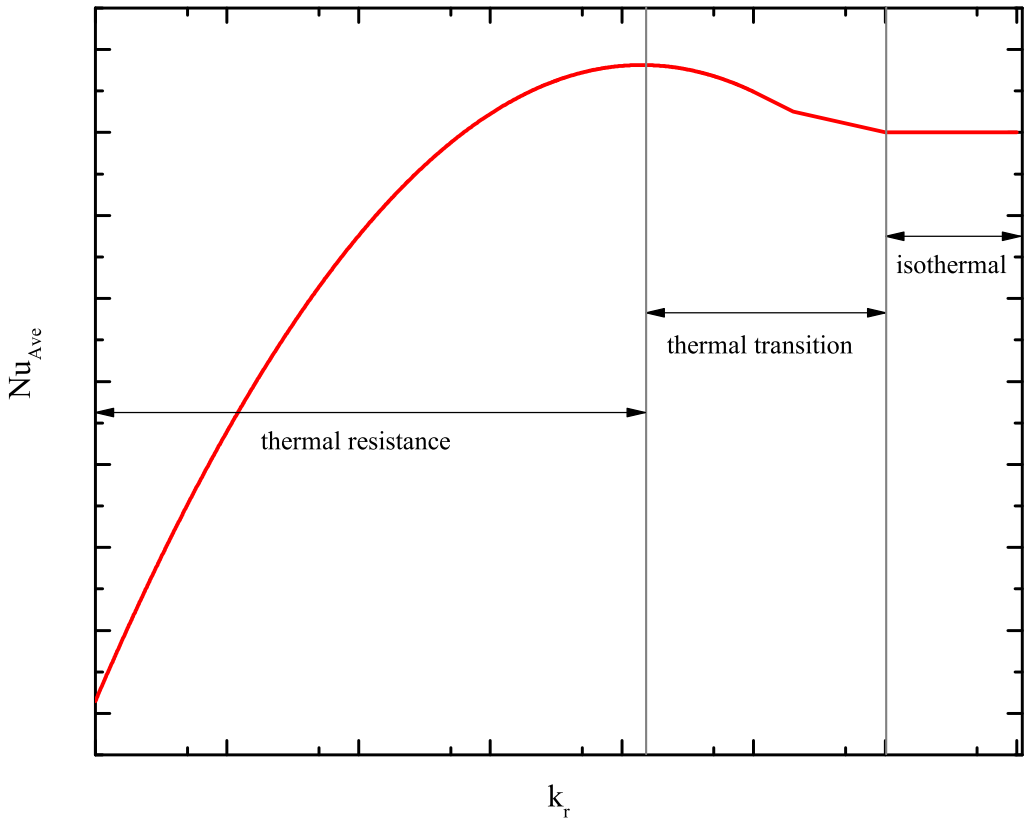

Figure 5.26: Schematic representation of Nu_{Ave} behaviour as k_r changes.

Figure 5.27 shows the vertical profiles of the local Nusselt number (Nu_{Local}) along the hot sidewall for $T_p = 0.05$, 0.1, and 0.2, $k_r = 0.1$, 1, 100, 500 and 1000, each at $X_p = 0.5$ and $Ra = 10^3$, 10^4, 10^5, 10^6, 10^7 and 10^8. Due to the symmetry in cases with $X_p = 0.5$, profiles just

for one sidewall (*i.e.*, hot sidewall) is presented. It is seen that Nu_{Local} decreases along most of the hot sidewall and there is a peak in the profiles which is close to the leading edge and becomes more pronounced at higher Rayleigh values. As expected, the leading edge of the hot sidewall is washed by the cooled fluid from the bottom side of the partition. Consequently, the local Nusselt number around the leading edge area is higher. Also, it is clear that by increasing the Rayleigh value, the peak point in the vertical profile of Nu_{Local} gets closer to the end of the wall, apparently due to a thinner boundary layer. As fluid moves up the hot sidewall, the temperature of the fluid increases and therefore, the local Nusselt number gradually decreases.

The Nu_{Local} is strongly dependent on Ra and as Ra increases, Nu_{Local} rises. Also, as a result of stronger convection of at Ra cases, the non-uniformity of Nu_{Local} graphs increases. Figure 5.27 also shows the dependency between T_p and Nu_{Local}. As T_p increases the overall trend especially for the peak point shows decreasing behavior. Moreover, the effect of T_p on Nu_{Local} is more noticeable at higher Ra cases than the lower ones. This observed effect of the partition thickness was also reported by others, such as Kahveci [5] and Oztop *et al.* [235] who observed that partition thickness had a weak or negligible effect on the rate of heat transfer at low Ra values.

The effect of k_r on Nu_{Local} is also presented in figure 5.27. As expected, the low Ra cases ($Ra = 10^3$ and 10^4) show little variation by changing the value of k_r. The main area affected by k_r variation on Nu_{Local} is on the leading edge and the tailing edge does not show significant changes. The reason for this difference on the leading and tailing edge is that the temperature gradient on the leading edge is mainly affected by the cooled fluid due to the right half-cavity on which thermal conductivity ratio has a direct impact. However, on the tailing edge, the temperature gradient is mainly influenced by the thermal stratification and the effect of the thermal conductivity ratio is weak.

Nu_{Local} of the cases with $k_r = 0.1$ (solid line) have the lowest value and as k_r increases to 1 (dashed line) and 100 (dotted line), Nu_{Local} values grows. The same thermal behaviour of Nu_{Ave} observed for $k_r = 100$ as be seen for Nu_{Local} of the hot sidewall where further increasing of k_r ($k_r = 500$ dashed dote line and $k_r = 1000$ dashed dote dote line) decreases the Nu_{Local}.

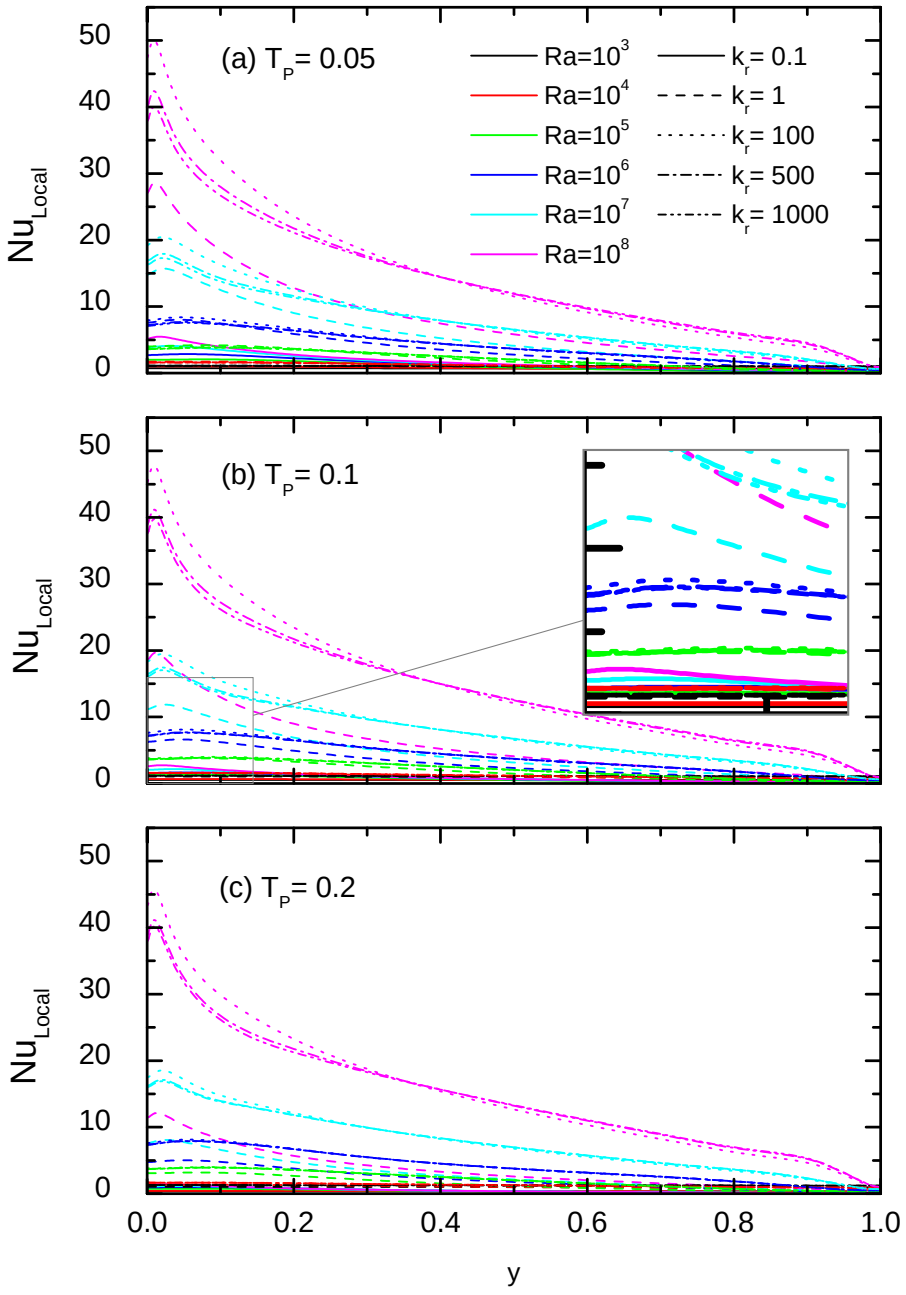

Figure 5.27: The vertical profiles of the local Nusselt number on the hot sidewall for different values of Ra (10^3, 10^4, 10^5, 10^6, 10^7 and 10^8), k_r (0.1, 1, 100, 500 and 1000) and T_p (0.05, 0.1, and 0.2).

As discussed earlier, altering the contributing parameters (T_p, X_p, k_r and Ra) can change the thermal behavior of the partition from being an isothermal wall to an isoflux wall. To investigate this possibility, figure 5.28 presents vertical profiles of Nu_{Local} on the left side of partition ($x = X_p - 0.5T_p$) for different values of Ra (10^3, 10^4, 10^5, 10^6, 10^7 and 10^8), k_r (0.1, 1, 100, 500 and 1000) and T_p (0.05, 0.1, and 0.2).

As expected, Ra has a considerable increasing effect on Nu_{Local} of the partition similar to that of Nu_{Ave} and Nu_{Local} of the sidewall for all cases. The profiles of Nu_{Local} in figure 5.28 can be roughly classified into two groups of non-uniform lines with significant peak points and uniform lines without notable peaks. The uniform lines of Nu_{Local} clearly represent an isoflux behavior on the partition and the non-uniform lines show more isothermal wall features. With this arrangement, it can be seen that as Ra increases the Nu_{Local} profiles become more non-uniform with a sharper jump on the top side of the partition. In other words, a rise in Ra intensifies the isothermal behavior of the partition. On the other hand, reducing Ra causes more uniform Nu_{Local} profiles which is a sign of uniform heat flux on the partition. The smallest value of k_r ($k_r = 0.1$) for all cases shows the lowest Nu_{Local} profiles in comparison with other k_r values selected in this work. Interestingly, the Nu_{Local} profiles of $k_r = 0.1$ shows uniform profiles even for high Ra values which have distinctive peak points. This observation can also be seen for $k_r = 1$ in which the Nu_{Local} profiles are always higher than the case of $k_r = 0.1$ but still the local heat transfer profiles are uniform. By further increasing k_r ($k_r = 100$), the Nu_{Local} profiles become more non-uniform and as Ra increases the non-uniformity increases. It can be noticed that the Nu_{Local} profiles rise from $k_r = 0.1$ to 100 and decrease from $k_r = 100$ to 1000 specifically on the lower half of the partition. However, on the upper side of the partition (in the vicinity of peak points), the effect of k_r on the Nu_{Local} profiles is different. The Nu_{Local} profiles on the top shows that k_r has a direct increasing effect on them. This outcome reveals that higher temperature gradient intensifies the effect of k_r on the upper side of the partition and by gradually decreasing the temperature gradient the influence of k_r weakens. Because the area of the low temperature gradient on the lower side of the partition is large (around two-thirds), the overall heat transfer rate (Nu_{Ave}) is dominated by the k_r behaviour of this section which is shown in figure 5.25.

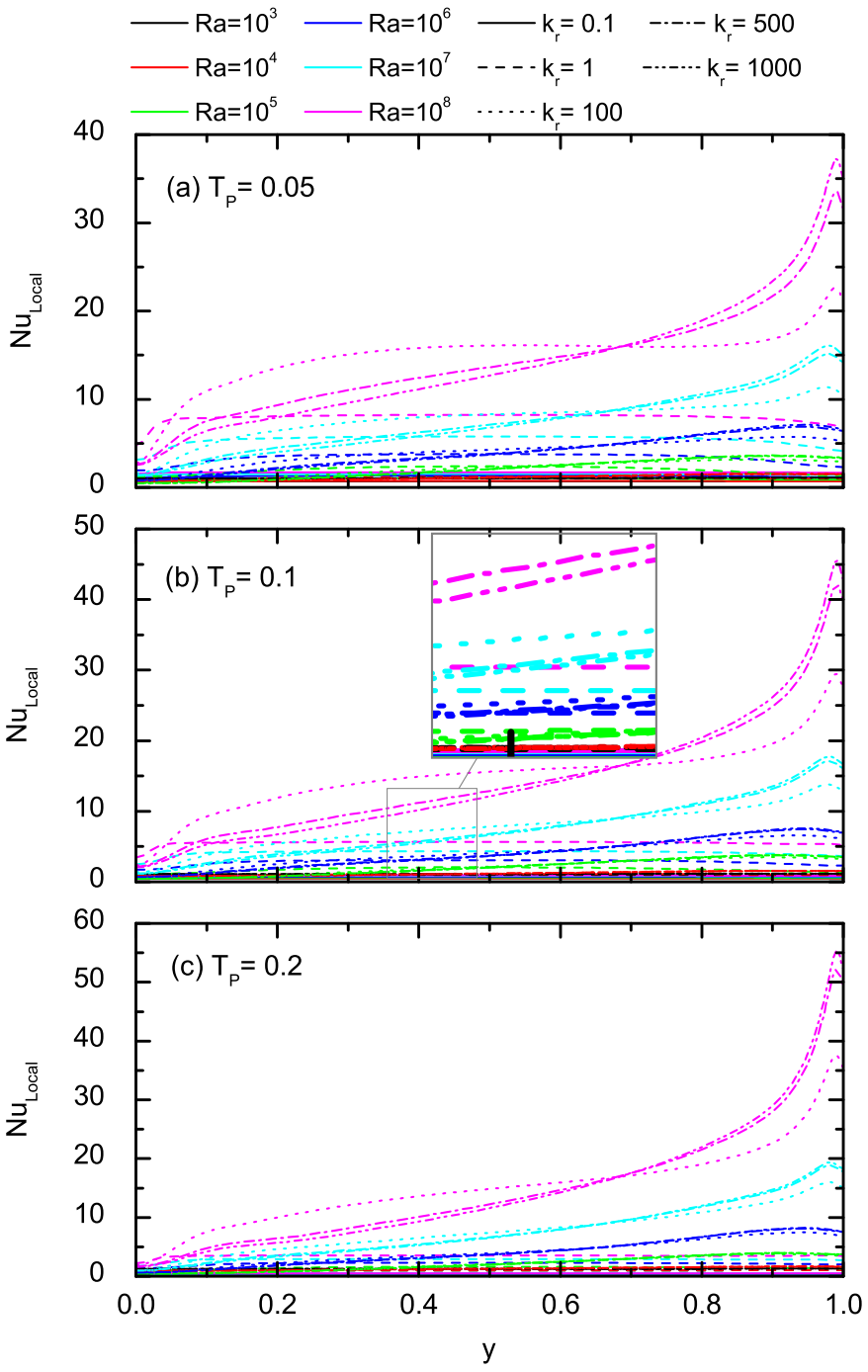

Figure 5.28: The vertical profiles of the local Nusselt number on the left side of partition ($x = X_p - 0.5T_p$) for different values of Ra (10^3, 10^4, 10^5, 10^6, 10^7 and 10^8), k_r (0.1, 1, 100, 500 and 1000) and T_p (0.05, 0.1, and 0.2).

Comparing figures 5.27 and 5.28 identifies interesting thermal specification of the partition. Although the peak point for Nu_{Local} of the hot sidewall is observed at the bottom of the sidewall, for the left side of the partition, a peak can be found at the top side of the partition. Therefore, partition plays a similar role of the cold sidewall for the cases with non-uniform profiles. As k_r increases this similarity increases. Observing this thermal behavior on the partition leads to a conclusion that it is possible to separate each half-cavity and find an equivalent non-partitioned cavity with the same temperature and flow pattern. This assumption has also been made by Anderson and Bejan [298]. Studying the peak points in those figures illuminates another interesting aspect, that is the effect of T_p on the partition is opposite to that on the sidewalls. As T_p increases, the value of Nu_{Local} at the peak points increases. This thermal aspect also observed in figure 5.25.

Figure 5.29 shows the vertical temperature distribution on the left side of the partition ($x = X_p - 0.5T_p$) (left column) and the horizontal temperature drop of the left ($x = X_p - 0.5T_p$) to the right ($x = X_p + 0.5T_p$) sides of the partition ($\theta_{D,x}$) (right column) for various Ra (10^3, 10^4, 10^5, 10^6, 10^7 and 10^8), k_r (0.1, 1, 100, 500 and 1000) and T_p (0.05, 0.1, and 0.2) at $X_p = 0.5$.

As temperature contour figures show, the upper part is in contact with the heated fluid from the hot sidewall, while the lower section receives cooled fluid from the right sidewall. Therefore, for all cases of the vertical temperature profiles, the upper part has a higher temperature than the lower section. The profiles of $Ra = 10^3$ show almost horizontal lines which imply there is not any convection heat transfer phenomenon to cause a temperature gradient. As Ra increases the value of the temperature profiles increases. This difference is larger when k_r reduces. Small thermal conductivity ratio is a sign of low thermal conductivity of the partition and the consequence of this trapping heat by the partition which causes high overall temperature and can be seen in figure 5.29. As K_r increases (increasing thermal conductivity of the partition), the partition allows more heat generated on the left half-cavity to pass to the right one and the temperature of the partition gradually decreases. The gradual decreasing trend of the vertical temperature profile is to mid-temperature of the cavity ($\theta = 0.5$). The higher k_r is, the closer the vertical temperature profile of the partition to $\theta = 0.5$. Although the profiles presented for $k_r = 0.1$ and 1 are away from the $\theta = 0.5$ line, for $100 \leq k_r$, profiles have a

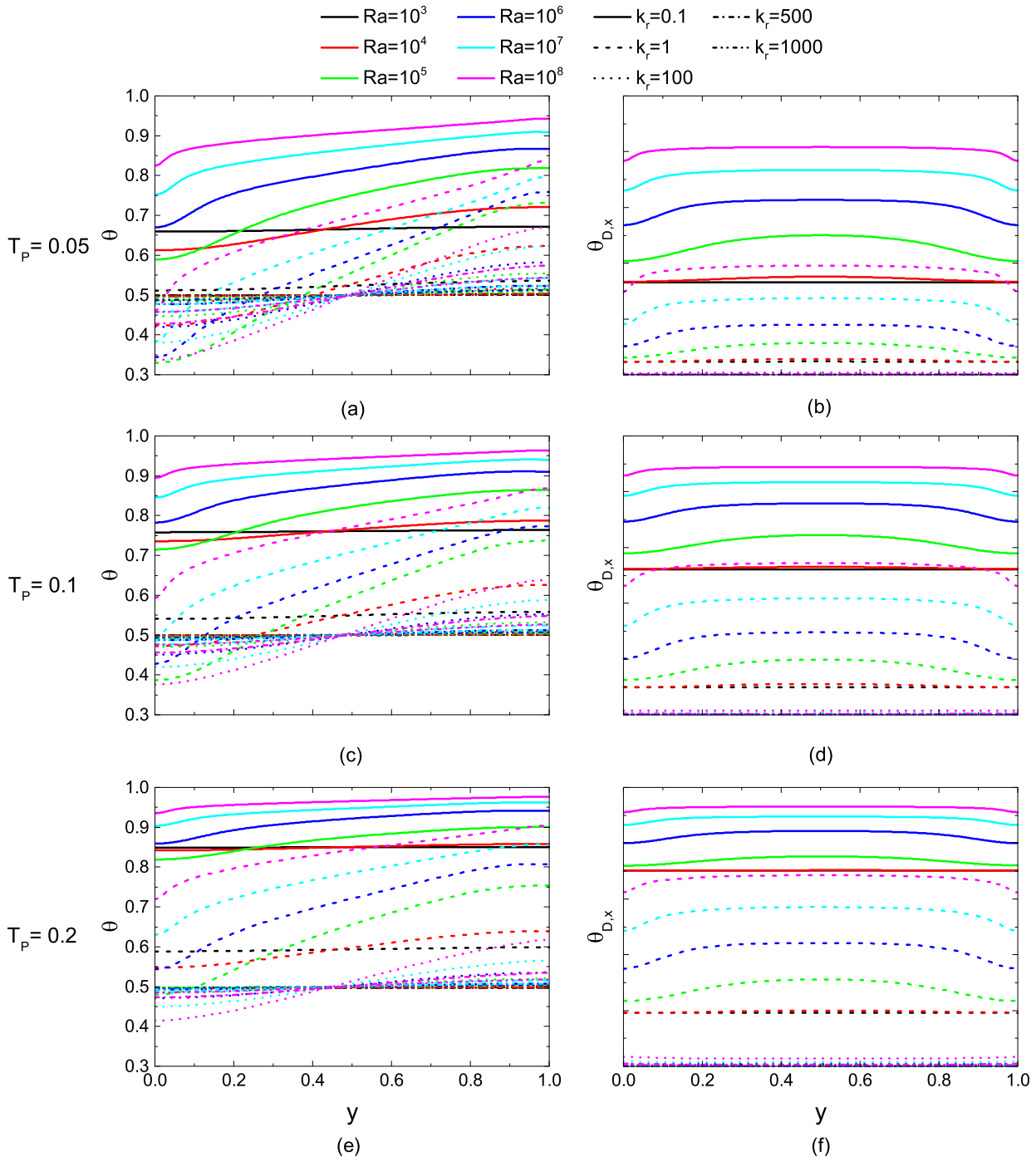

Figure 5.29: Vertical temperature profiles on the left side of partition ($x = X_p - 0.5T_p$) and horizontal temperature drops ($\theta_{D,x}$) for different values of Ra (10^3, 10^4, 10^5, 10^6, 10^7 and 10^8), k_r (0.1, 1, 100, 500 and 1000), $X_p = 0.5$ and T_p (0.05, 0.1, and 0.2).

point of intersection with $\theta = 0.5$ line at almost the mid-height of the partition ($y = 0.5$). Figure 5.29 also shows the effect of partition thickness on the vertical temperature profiles of the partition. As T_p increases, the heat resistance aspect of the partition increases. Therefore, the temperature of trapped heated fluid on the left half-cavity should be higher, leading to higher vertical temperature profiles of the partition for thicker partitions. Interestingly, the temperature difference between the top and the bottom of the vertical temperature profiles of the partition for thicker partitions is lower than thinner ones. This means that the vertical temperature profiles of the partition become closer to the horizontal line. This tendency shows that the cavities with thicker partitions have weaker convection which can be explained by the decreased area filled with fluid.

The second parameter presented in figure 5.29 is the horizontal temperature drop on the partition ($\theta_{D,x}$) which is defined as the temperature difference between the left and the right sides of the partition. The overall shape of $\theta_{D,x}$ graphs show mainly the horizontal line except at the two ends (probably due to the impingement of intrusion on the partition wall). This implies the symmetry of the vertical temperature profiles on the left and right sides of the partition for $X_p = 0.5$. Also, it can be seen that as Ra increases $\theta_{D,x}$ rises and the horizontal area of profiles becomes wider. The case of $k_r = 0.1$ has the highest $\theta_{D,x}$ and as k_r increases $\theta_{D,x}$ becomes smaller as for $100 \leq k_r$, $\theta_{D,x}$ is very close to zero. Regarding the effect of T_p, it is clear that T_p has an increasing effect on $\theta_{D,x}$ and the horizontal area of $\theta_{D,x}$ graphs get wider as T_p increases.

As figure 5.29 illustrates, $\theta_{D,x}$ for large k_r, $\theta_{D,x}$ is very low and the profile cannot be identified by using a linear scale on the y axis. Therefore, the graphs for $\theta_{D,x}$ of figure 5.29$(b), (d)$ and (f) are represented in figure 5.30 in log scale for y axis.

Figure 5.30 shows that for all cases of T_p by decreasing Ra and increasing k_r, $\theta_{D,x}$ reduces. Also, as T_p increases $\theta_{D,x}$ rises. This behavior is clear for the lowest $\theta_{D,x}$ profile for instance (*i.e.*, the case at $k_r = 1000$ and $Ra = 10^3$) as at $T_p = 0.05$ the value of $\theta_{D,x}$ is 5×10^{-5}, at $T_p = 0.1$, $\theta_{D,x} = 1.2 \times 10^{-4}$, and at $T_p = 0.2$, $\theta_{D,x} = 2.5 \times 10^{-4}$. An interesting observation regarding the $\theta_{D,x}$ profile is that for all T_p values the $\theta_{D,x}$ profiles of the cases $k_r = 1$ and 500 has the most non-uniform profiles with fewer flat areas. There is not any clear relation between

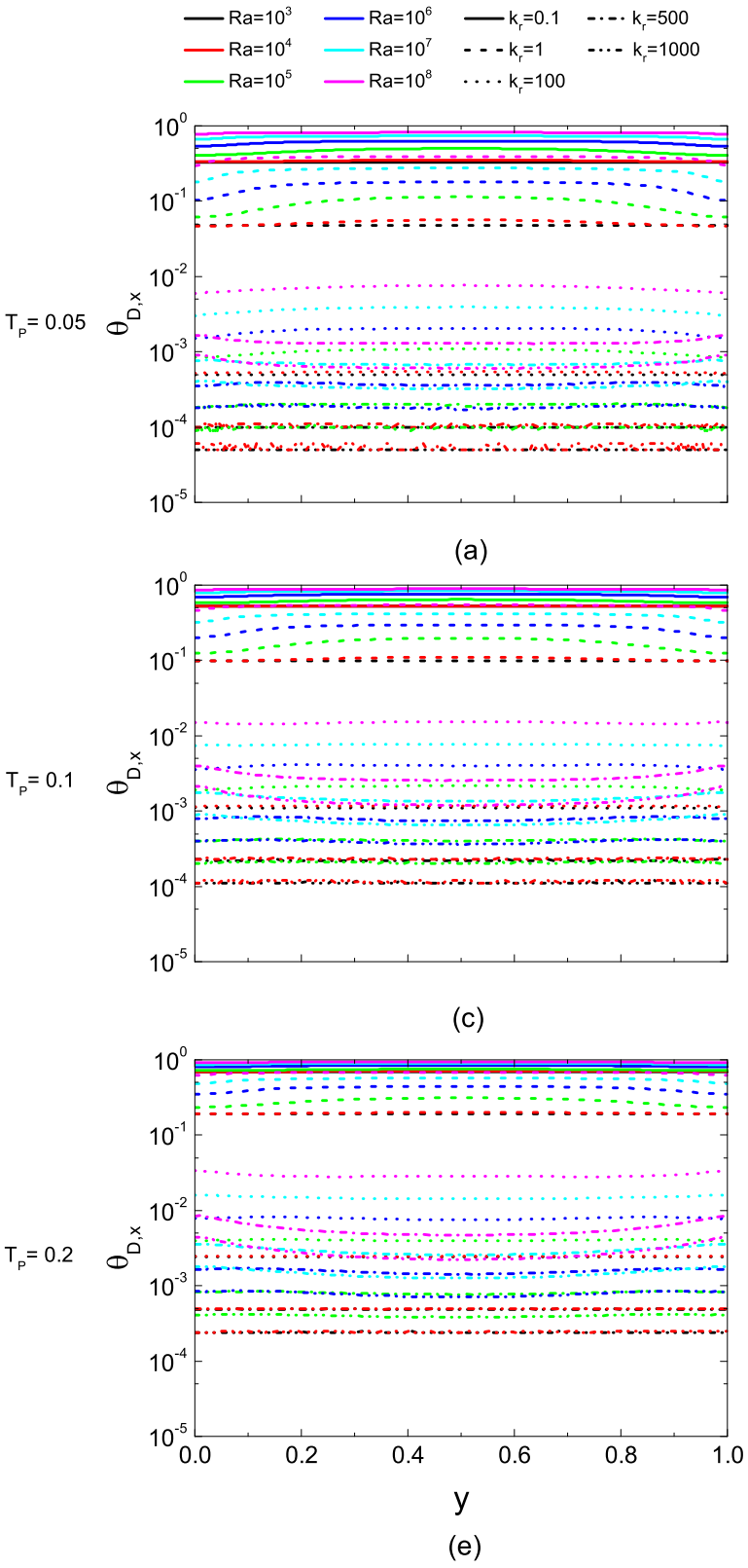

Figure 5.30: Horizontal temperature drop ($\theta_{D,x}$) for different values of Ra (10^3, 10^4, 10^5, 10^6, 10^7 and 10^8), k_r (0.1, 1, 100, 500 and 1000), $X_p = 0.5$ and T_p (0.05, 0.1, and 0.2).

the profile shape of $\theta_{D,x}$ and Ra as generally low and high Ra cases show a more uniform shape.

The observed effect of k_r on $\theta_{D,x}$ or the temperature profiles can also be extracted from the equations (5.1) and (5.2). As it is explained earlier, the heat flux of the partition and the fluid-filled area of the cavity is equal at the steady state. Increasing k_r means that for the constant k_f, k_s should be increased. By considering equation (5.2), to keep the equality of heat flux, $\frac{\Delta T_p}{T_p}$ should decrease. In essence, increasing k_r leads to a reduction in $\theta_{D,x}$ which is found in figure 5.29. This dropping of $\theta_{D,x}$ value (by increasing k_r) can finally reach to a point where the temperature of the left and right side of the partition becomes almost equal. The equality of the temperatures of the left and right side of the partition ($\theta_{D,x} \cong 0$) indicates that the partition is horizontally isothermal. Moreover, due to the adiabatic condition on the top and bottom walls ($\frac{\partial \theta}{\partial y} = 0$) and the fact that $H >> T_p$, the horizontal heat flux of the partition should be much higher than the vertical heat flux and can be expressed as follows,

$$k_s \frac{\partial \theta}{\partial x} >> k_s \frac{\partial \theta}{\partial y}. \tag{5.5}$$

This outcome reveals that for the cases with high k_r, the one-dimensional conduction in the partition (horizontal) could be an appropriate assumption to simplify the analytical studies and may cause a small error in the final calculations.

After investigating the sides of the partition in contact with the fluid, it is necessary to study the thermal behavior inside the partition. Figure 5.31 illustrates the vertical temperature profiles at the middle of the partition ($x = X_p$) for different values of Ra (10^3, 10^4, 10^5, 10^6, 10^7 and 10^8), k_r (0.1, 1, 100, 500 and 1000) and T_p (0.05, 0.1, and 0.2). Surprisingly, the vertical profiles at the middle of the partition do not show the same trends observed for the vertical profiles of the left or right sides of the partition. There is not any clear increasing or decreasing trend for various Ra or k_r values. The profile of the case $k_r = 1$ and $Ra = 10^5$ shows the highest slop and consequently the highest temperature at the upper side or the lowest at the bottom of the partition. The profiles for $Ra = 10^3$ shows the closest to the horizontal line. As T_p increases the overall slop of the temperature profiles decreases. Clearly to have a better understanding

of the vertical thermal behavior of the partition, it is essential to define a new parameter. To satisfy this need the vertical temperature drop ($\theta_{D,y}$) is defined as the temperature difference between the top and bottom of partition at $x = X_p$. Figure 5.32 presents the steady state value of $\theta_{D,y}$ for different values of Ra (10^3, 10^4, 10^5, 10^6, 10^7 and 10^8), k_r (0.1, 1, 100, 500 and 1000) and T_p (0.05, 0.1, and 0.2).

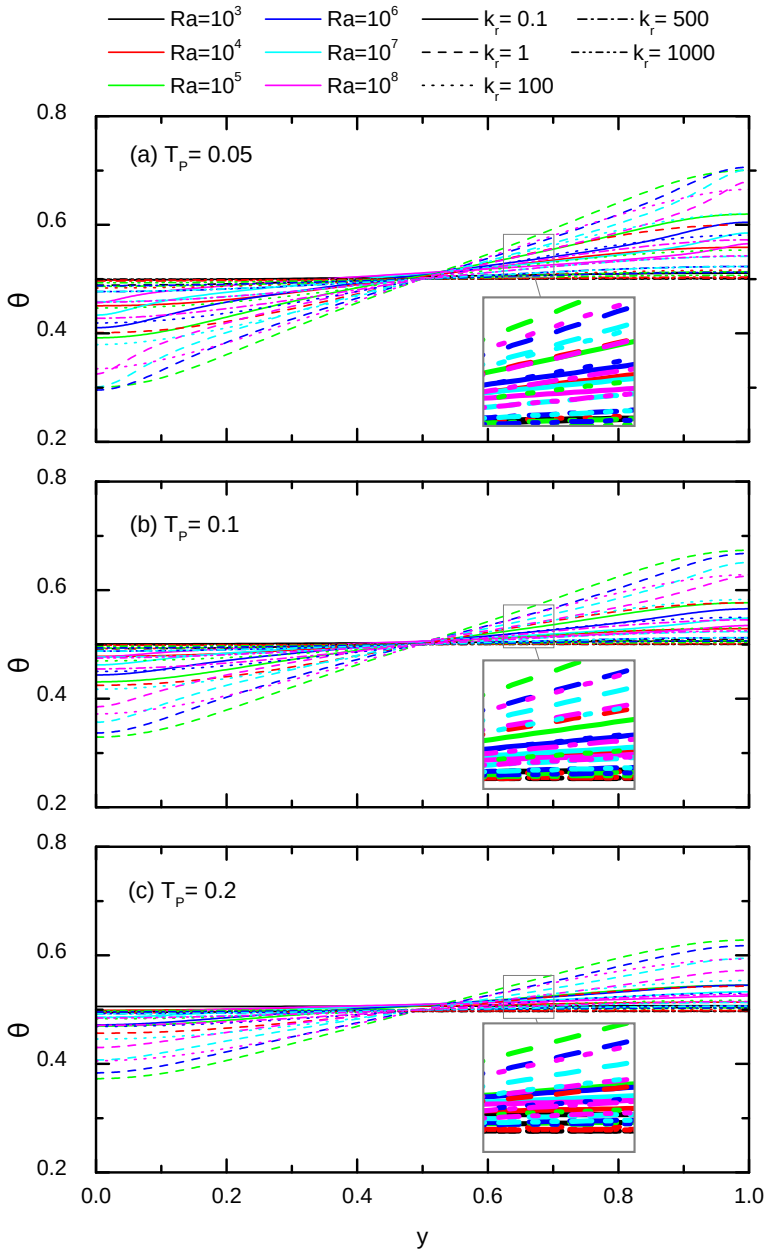

Figure 5.31: Vertical temperature profiles on the middle of the centrally positioned partition for different values of Ra (10^3, 10^4, 10^5, 10^6, 10^7 and 10^8), k_r (0.1, 1, 100, 500 and 1000) and T_p (0.05, 0.1, and 0.2).

The lines presented in figure 5.32 can be categorized into two types. Type one is the lines with

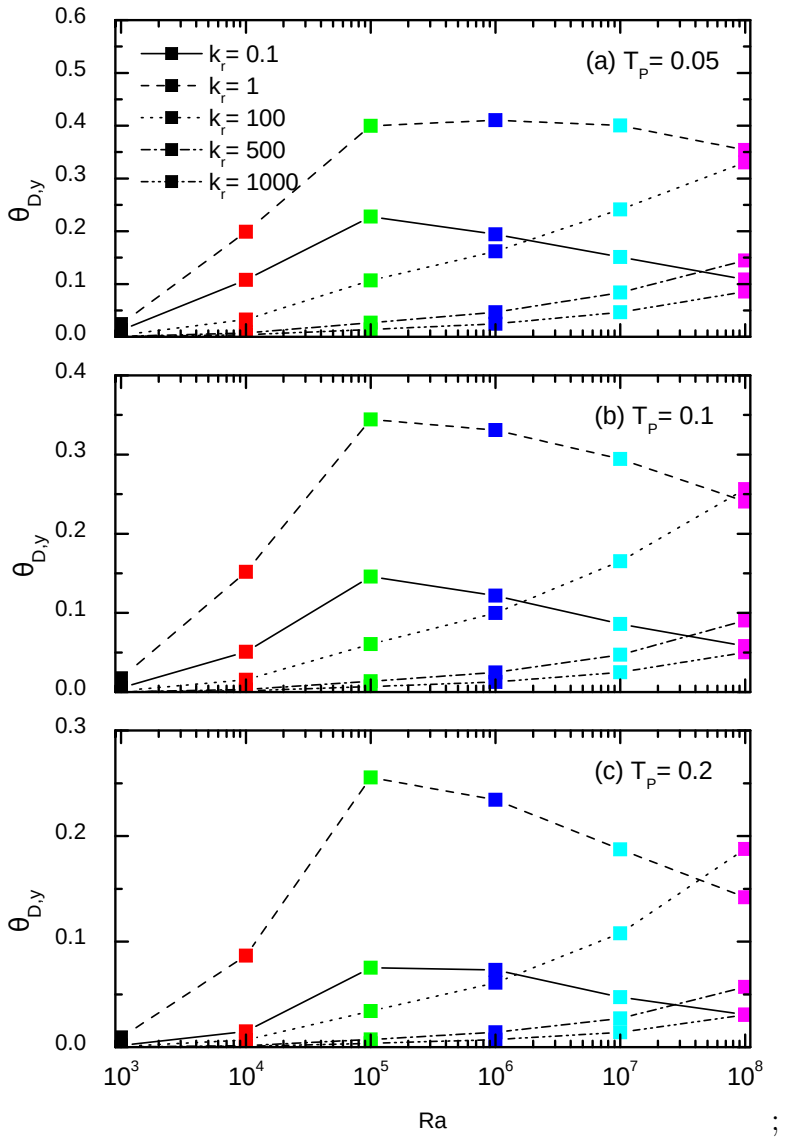

Figure 5.32: Vertical temperature drop ($\theta_{D,y}$) at the middle of the partition for different values of Ra (10^3, 10^4, 10^5, 10^6, 10^7 and 10^8), k_r (0.1, 1, 100, 500 and 1000) and T_p (0.05, 0.1, and 0.2).

an increase and decrease trend and a subsequent peak point ($k_r \leq 1$) and type two includes the lines with just increasing trend ($100 \leq k_r \leq 1000$). The cases of $k_r = 1$ show the highest $\theta_{D,y}$ for $10^3 \leq Ra \leq 10^7$. At $Ra = 10^8$, $\theta_{D,y}$ of the case $k_r = 1$ is affected by the partition thickness and as T_p rises the value of $\theta_{D,y}$ decreases even to less than the case $k_r = 100$ (*i.e.*, figure 5.32(c)). The vertical temperature drop lines ($\theta_{D,y}$) of type one show a sharp increase up to $Ra = 10^5$ and then a gradual decrease except for the case of $k_r = 1$ with $T_p = 0.05$ in which $\theta_{D,y}$ is almost a plateau over the range of $10^5 \leq Ra \leq 10^7$ and after that steadily decreases when Ra is increased to $Ra = 10^8$. Type two includes the cases of $\theta_{D,y}$ with high k_r ($100 \leq k_r \leq 1000$) and shows a gradual and steady increase in $\theta_{D,y}$ as Ra increase. As k_r and T_p increases the value of $\theta_{D,y}$ reduces.

5.3 Off-centre partition

5.3.1 Qualitative analysis of flow and heat transfer behaviour

A. Isotherms and streamlines

Figures 5.33, 5.35, 5.37, 5.39 and 5.41 present the temperature contours and figures 5.34, 5.36, 5.38, 5.40 and 5.42 show streamlines at the fully developed stage obtained numerically for $T_p = 0.05$, 0.1, and 0.2, $k_r = 0.1$, 1, 100, 500 and 1000, each at $X_p = 0.25$ and at $Ra = 10^3$, 10^4, 10^5, 10^6, 10^7 and 10^8, respectively.

By placing the partition off-centre the symmetry existed in the half-cavities of the cavities with the centrally positioned partition losses. As a consequence, the flow patterns in the left and right half-cavities are different.

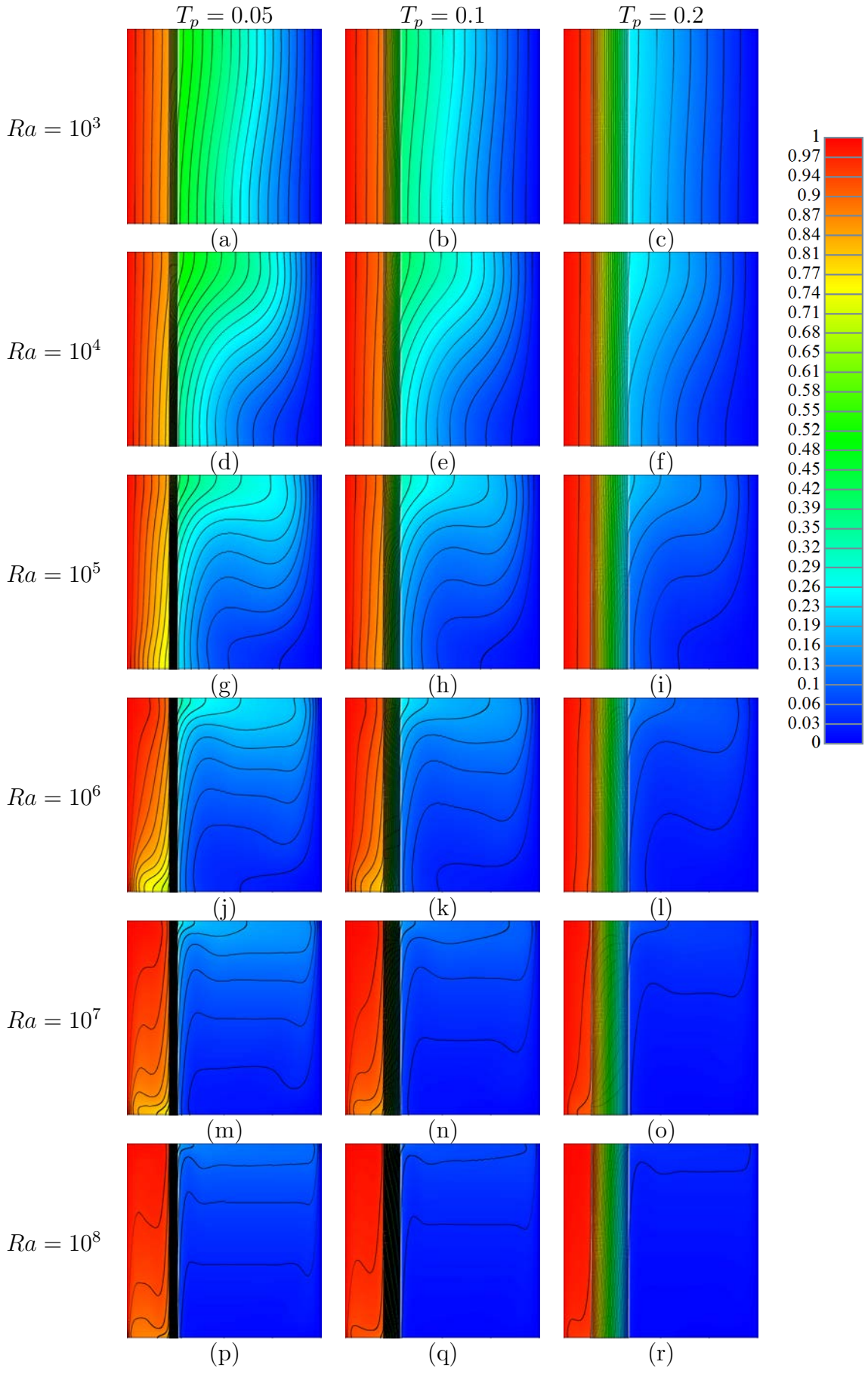

Figure 5.33: Temperature contours at $k_r = 0.1$ and $X_p = 0.25$ for different Ra values ($10^3 \leq Ra \leq 10^8$) and T_p ($T_p = 0.05$, 0.1 and 0.2).

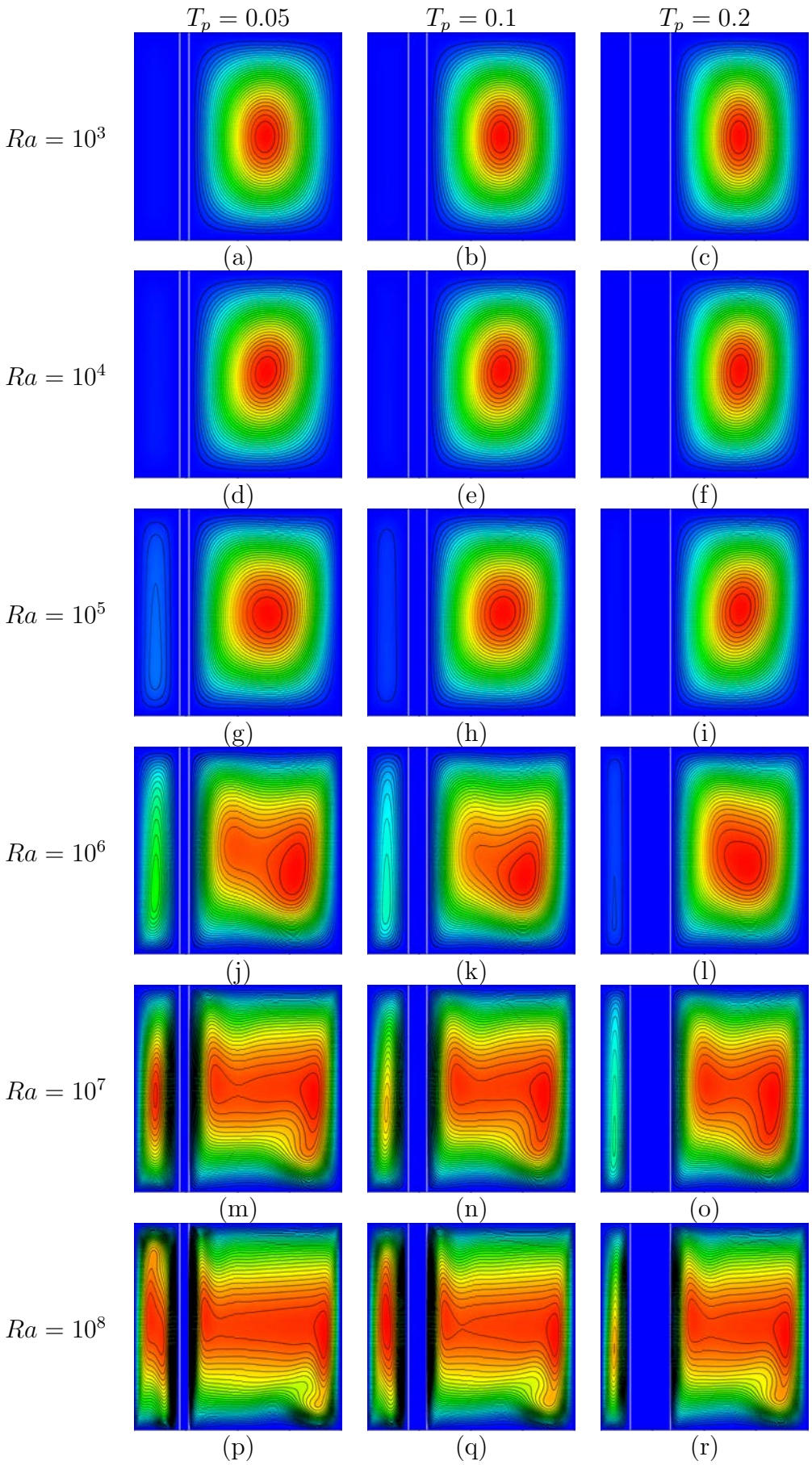

Figure 5.34: Stream function contours at $k_r = 0.1$ and $X_p = 0.25$ for different Ra values ($10^3 \leq Ra \leq 10^8$) and T_p ($T_p = 0.05$, 0.1 and 0.2).

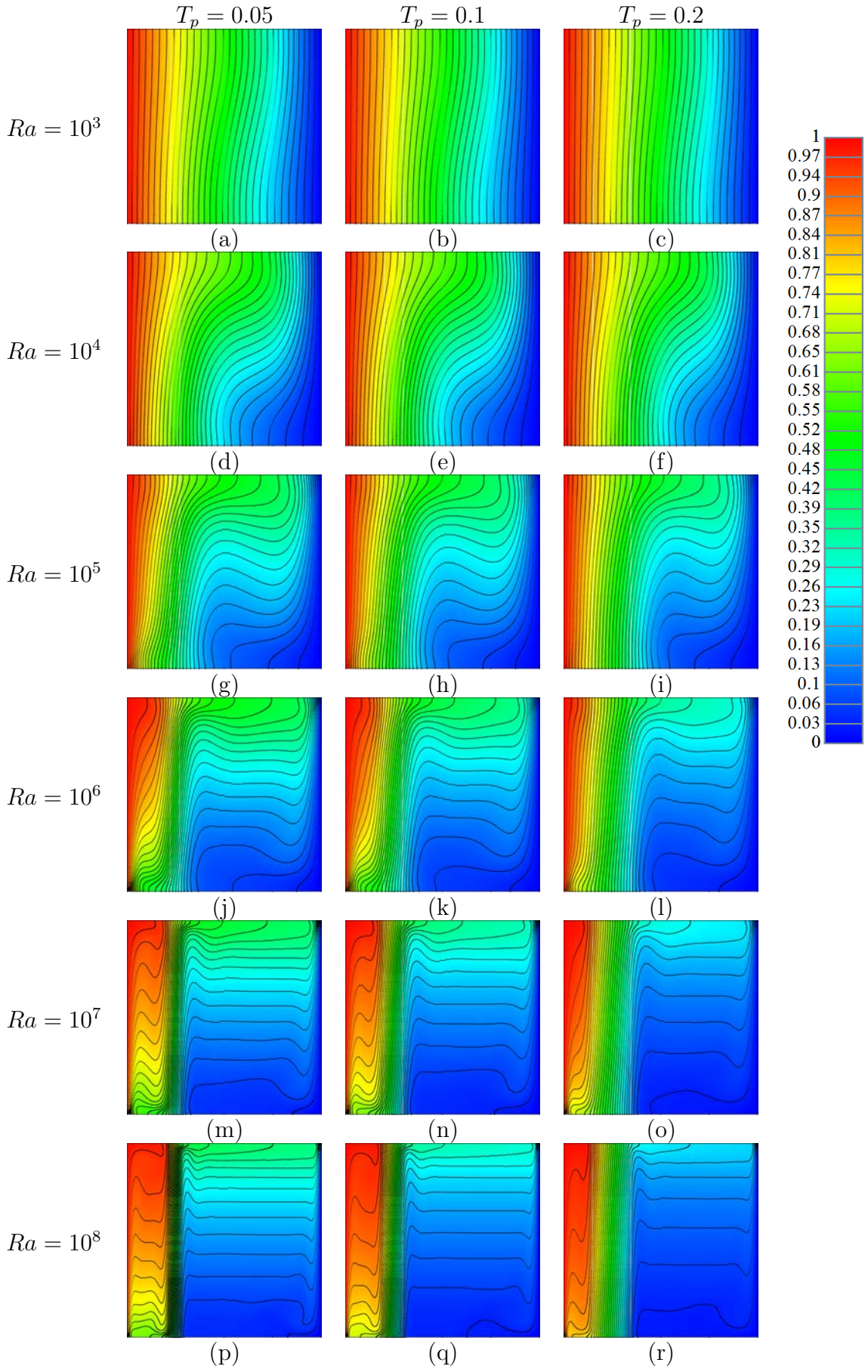

Figure 5.35: Temperature contours at $k_r = 1$ and $X_p = 0.25$ for different Ra values ($10^3 \leq Ra \leq 10^8$) and T_p ($T_p = 0.05$, 0.1 and 0.2).

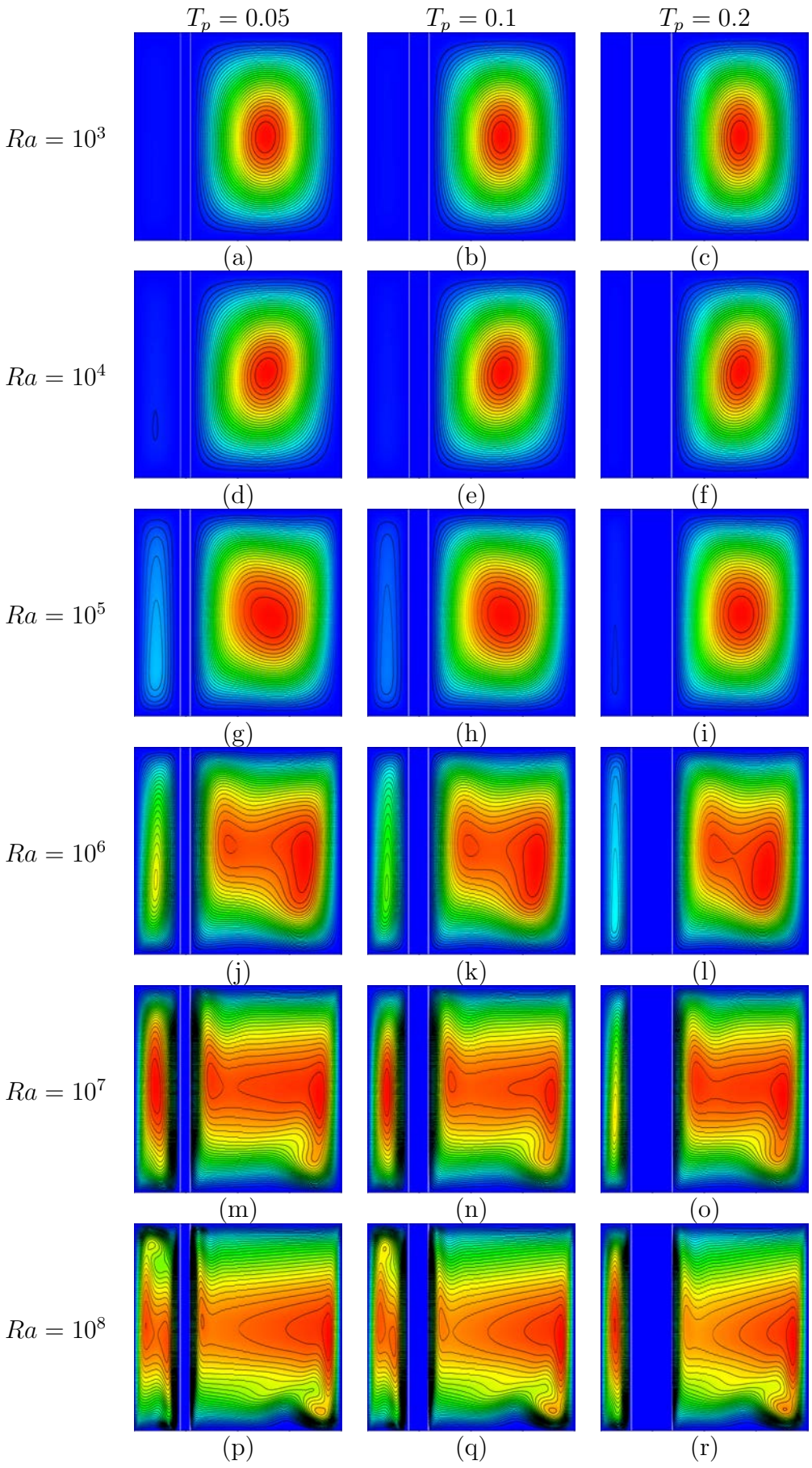

Figure 5.36: Stream function contours at $k_r = 1$ and $X_p = 0.25$ for different Ra values ($10^3 \leq Ra \leq 10^8$) and T_p ($T_p = 0.05$, 0.1 and 0.2).

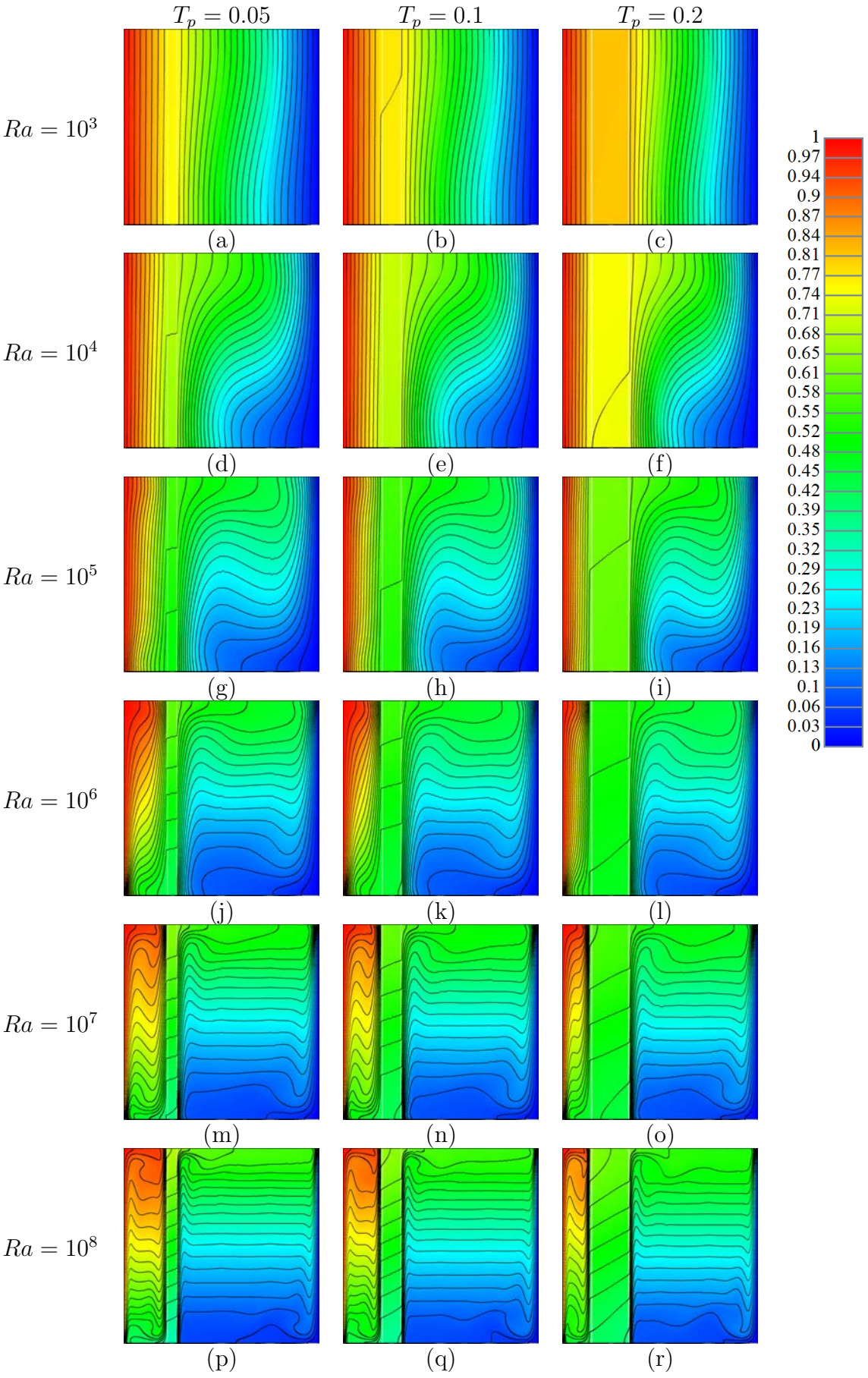

Figure 5.37: Temperature contours at $k_r = 100$ and $X_p = 0.25$ for different Ra values ($10^3 \leq Ra \leq 10^8$) and T_p ($T_p = 0.05$, 0.1 and 0.2).

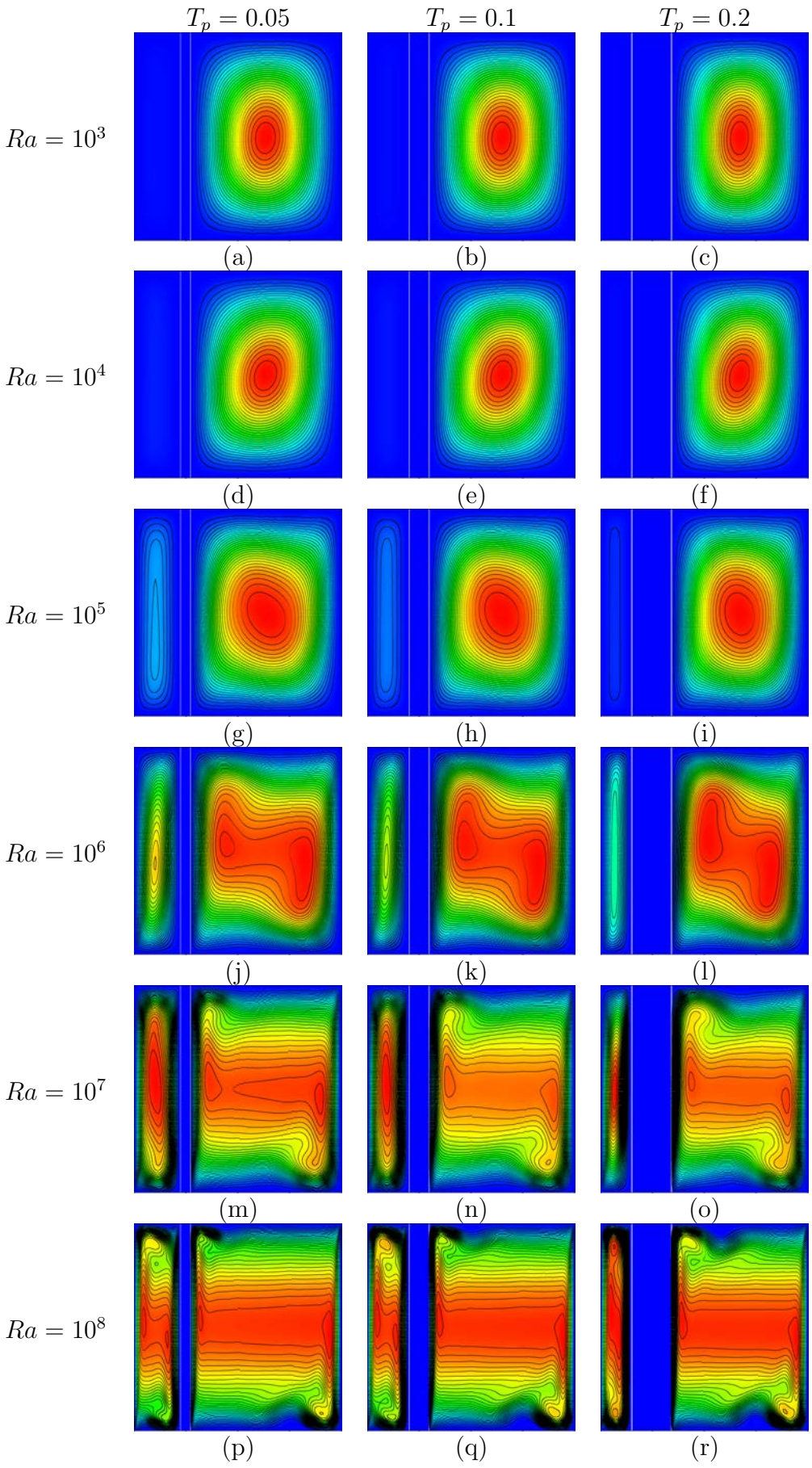

Figure 5.38: Stream function contours at $k_r = 100$ and $X_p = 0.25$ for different Ra values ($10^3 \leq Ra \leq 10^8$) and T_p ($T_p = 0.05$, 0.1 and 0.2).

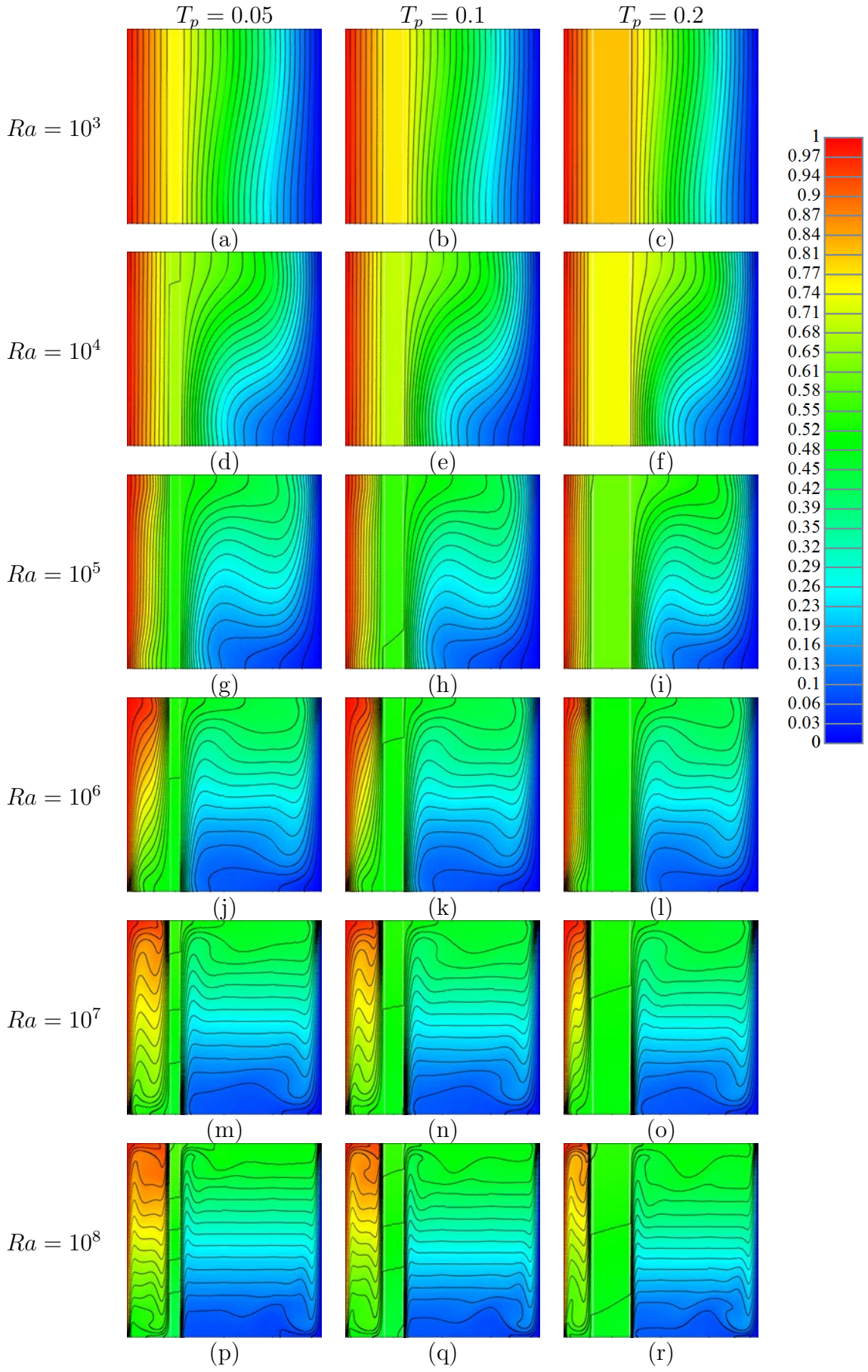

Figure 5.39: Temperature contours at $k_r = 500$ and $X_p = 0.25$ for different Ra values ($10^3 \leq Ra \leq 10^8$) and T_p ($T_p = 0.05$, 0.1 and 0.2).

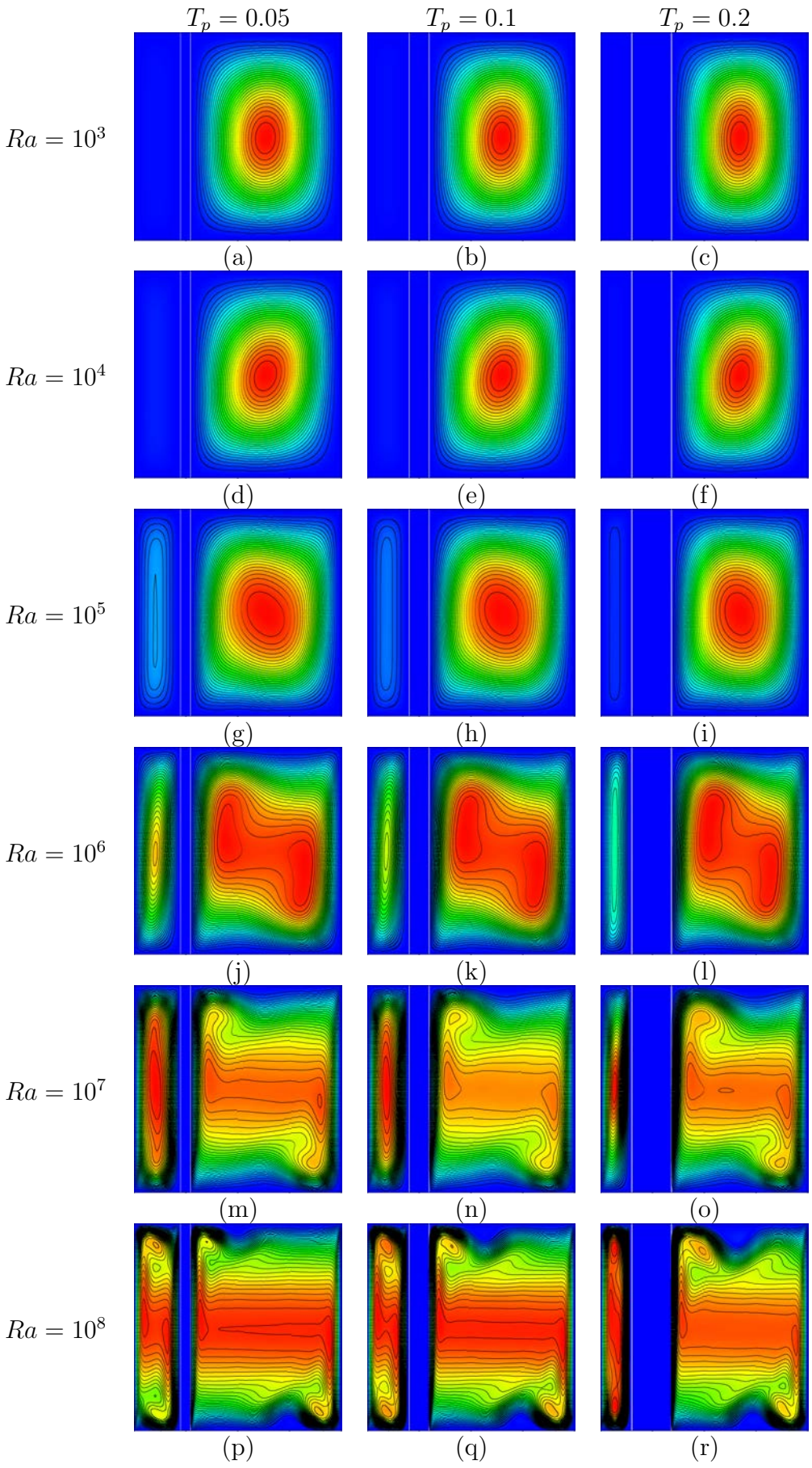

Figure 5.40: Stream function contours at $k_r = 500$ and $X_p = 0.25$ for different Ra values ($10^3 \leq Ra \leq 10^8$) and T_p ($T_p = 0.05$, 0.1 and 0.2).

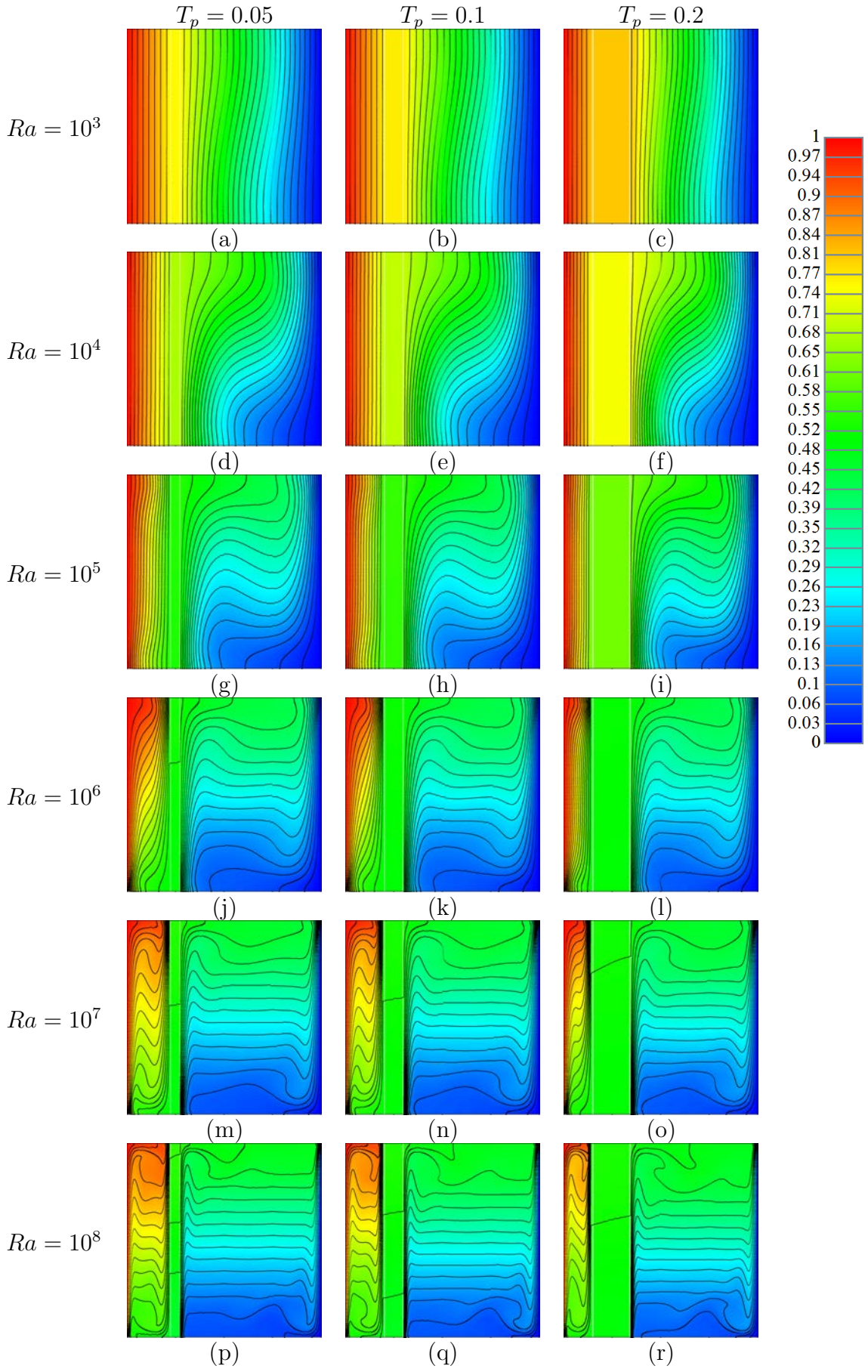

Figure 5.41: Temperature contours at $k_r = 1000$ and $X_p = 0.25$ for different Ra values ($10^3 \leq Ra \leq 10^8$) and T_p ($T_p = 0.05$, 0.1 and 0.2).

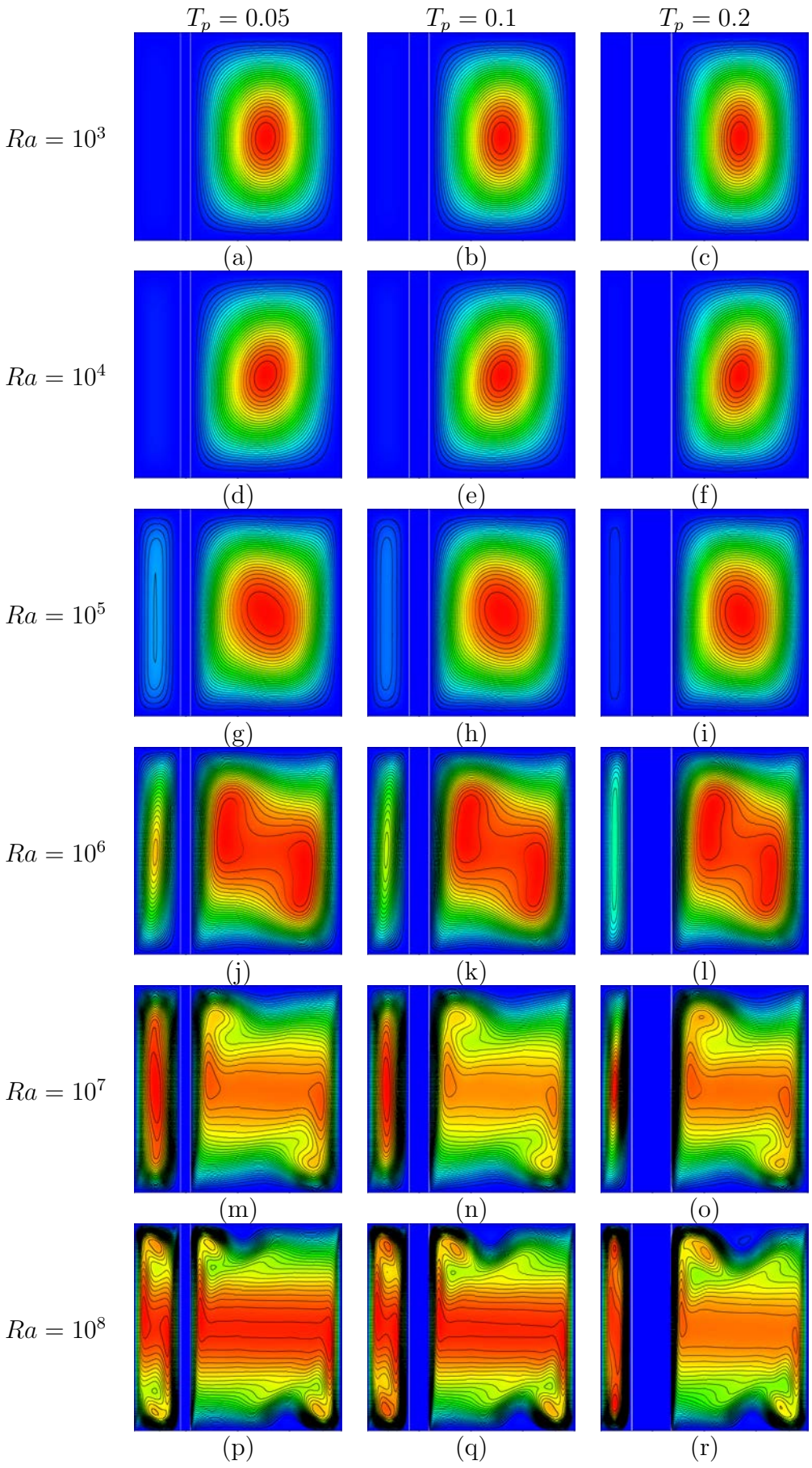

Figure 5.42: Stream function contours at $k_r = 1000$ and $X_p = 0.25$ for different Ra values ($10^3 \leq Ra \leq 10^8$) and T_p ($T_p = 0.05$, 0.1 and 0.2).

The general flow mechanism in the off-centre partitioned cavity is similar to the centrally-placed case, as described above, but with some distinct differences. Fluid close to the sidewall is heated/cooled and rises/falls along the sidewalls, eventually creating horizontal intrusions which carry heated/cooled fluid across the horizontal top/bottom walls to the partition. The impingement of the hot/cold intrusion to the partition results in the heat transfer, via conduction, from the left side of the partition to the right side.

For the case of the off-centre partition considered here (*i.e.*, a partition close to the hot sidewall), the conduction heat transfer in the left half-cavity is stronger than the right side, which is different from the centrally-placed partition case. This feature is clearly shown in the temperature and stream function as the left half-cavity has less angled isotherms or weaker circulation than that in the right half-cavity. For instance, figure 5.33(g) (at $Ra = 10^5$ and $T_p = 0.05$) shows that the left half cavity has almost vertical (or slightly angled) isotherms while in the right half-cavity isotherms in the middle of the half-cavity are almost horizontal which is an indication of stronger convection and the presence of a thermal stratification process. The stream function contours of the same case (figure 5.34(g)) also reveal that the circulation in the left half-cavity is much weaker than that in the right one. The reason is that by moving the partition to the left side, the area occupied by the fluid in the right half-cavity is increased. Therefore, it is expected that there is stronger convection in the wider cavity (*i.e.*, the right half-cavity) than the narrow one. A comparison between the results for the $X_p = 0.25$ case and the $X_p = 0.5$ case confirms this different flow and heat transfer behavior.

Investigation of cavities with low Ra values shows that for $X_p = 0.5$ generally $Ra = 10^3$ and 10^4 cases have slightly angled or almost vertical and uniformly spaced isotherms which are a sign of conduction domination. This type of isotherms for the case of $X_p = 0.25$ is observed at different Ra values for each half-cavities. For the left half-cavity in the $X_p = 0.25$ case, conduction domination can be identified at $Ra = 10^3$, 10^4 and 10^5 while for the right half-cavity it is only at $Ra = 10^3$.

The isotherms for the case of $Ra = 10^3$ show that the conduction in the left half-cavity is followed by conduction in the partition, and both regions have vertical isotherms. However,

the number of isotherms in those regions are dependent on T_p and k_r. As k_r increases the number of isotherms in the partition decreases and figure 5.33 shows denser isotherms in the partition for $k_r = 1$ with the isotherms' density equal to the fluid-filled area. By further increasing k_r ($k_r \geq 100$), the number of isotherms decreases. T_p also controls the number of isotherms through changing the width of the left half-cavity. A thicker partition shows a larger number of isotherm in the partition.

Another interesting observation regarding the temperature gradient in the partition is that for the cases of $Ra = 10^3$ and 10^4, the overall temperature in the partition is closer to the hot side, while for the higher Ra cases this temperature gradient is around the mid-temperature of the cavity. As an example, the comparison of temperatures in the partition of figure 5.37(c) and (o) shows such a difference.

The lack of circulation in the left half-cavity (lack of stream function contours) can be seen for almost all cases of $Ra = 10^3$ and 10^4 as shown in figures 5.34 to 5.42($a - f$). As Ra increases, convection intensifies and circulation gradually forms in the left half-cavity.

From the stream function contours in the right half-cavity (*i.e.*, the wide half-cavity), it can be seen that the flow pattern is very similar to the pattern observed in the centrally positioned partitioned cavities. The thinner half-cavity, due to the dominance of conduction, has less stream function contours in comparison with the right half-cavity. This weak convection flow in the left half-cavity is more clear for $10^3 \leq Ra \leq 10^4$. As Ra increases, the convective flow becomes strong enough and the flow pattern can be seen in the left half-cavity. Another difference between the centrally positioned and off-centre partition cases is at the occurring stage of multiple vortex eyes. Off-centre partition cases show that the multiple vortex eyes formation in the right half-cavity happens at lower Ra values than the cases of the centrally placed partition case because of the wider half-cavity which intensifies convective heat transfer phenomenon. For instance, by comparing figures 5.34(j) and 5.2(j), it can be seen that the multiple vortex eyes formation happens at $Ra = 10^6$ and 10^7, respectively.

As discussed earlier, the partition thickness alters the size of the half-cavities which leads to change in the temperature and stream function contours in the cavity. The influence of

partition thickness in the cavity can be seen qualitatively in figures of temperature contours (*i.e.*, figures 5.33, 5.35, 5.37, 5.39 and 5.41) and stream function contours (*i.e.*, figures 5.34, 5.36, 5.38, 5.40 and 5.42).

Cavities with thinner partitions have wider half-cavities. Therefore, for the cases of the off-center partition, increasing partition thickness applies further restriction for the fluid in the left half cavity and leads to a weaker flow circulation. This can be seen in figure 5.42(g) to (i). For instance, for the case of $T_p = 0.2$, there is one streamline in the left half-cavity and this number increases as the partition thickness decreases. Stronger convection in the wider half-cavities causes shifting from a single-cell flow pattern to a multiple cell one. This behavior can be seen in figures 5.34(j, k and l) as the cavity with the thickest partition (*i.e.*, figure 5.34(l)) has a single-cell flow pattern and gradually by decreasing the partition thickness (*i.e.*, figure 5.34(k)) new vortex eyes are gradually formed. By further decreasing the partition thickness (*i.e.*, figure 5.34(j)) the formed vortex eyes gradually move into the vicinity of walls.

Comparing figures 5.1 and 5.33 depicts an interesting difference in temperature contours between the centrally-positioned and the off-centre partitioned cavities. The temperature range of the partition is generally around the mid-temperature (*i.e.*, $\theta = 0.5$). The only exception can be observed for the low Ra cases of the off-centre partitioned cavities. For example, the overall temperature of the partition of the case of $Ra = 10^3$, $k_r = 100$, $X_p = 0.25$ and $T_p = 0.05$ is $\theta = 0.74$. This observation is attributed to the presence of a thick thermal boundary layer at the hot sidewall which includes the area partition is placed. Therefore, the temperature of the partition at low Ra cases is highly influenced by the sidewall thermal boundary-layer. As the thickness of partition increases to $T_p = 0.1$ and 0.2 the overall temperature increases to $\theta = 0.80$ and 0.83, respectively. By increasing Ra, convection in the left half-cavity intensifies and consequently, the thermal boundary layer thickness on the hot sidewall reduces. The thickness of the thermal boundary layer becomes smaller than the width of the left half-cavity (*i.e.*, $X_p - \frac{T_p}{2}$) and the direct thermal effect on the partition is no longer exists. This condition can be seen in higher Ra cases where the temperature of the partition is about $\theta = 0.5$.

Another interesting point is the difference in stratification. Comparing the temperature con-

tours of the centre and off-centre partitioned cavities shows that the formation of the horizontal isotherm in the centre of the half-cavities generally happens at $Ra = 10^7$ for the centrally-positioned cavity. However, those type of isotherms in the left and right half-cavities in the off-centre partitioned cavity forms at $Ra = 10^8$ and $Ra = 10^6$, respectively. This means that a wider half-cavity (*i.e.*, the right half-cavity) has the stratification at lower Ra values and a narrower half-cavity has it at higher Ra cases. This can clearly be seen in figures 5.5 and 5.37.

For the case of $Ra = 10^3$ and $k_r = 1$, due to the equal thermal conductivity of the partition and the fluid, no significant difference should be seen between different partition thickness. By comparing such cases in off-centre and centrally placed partitioned cavities, it can be found that isotherms on the left side of cavities are very similar and there is a small difference (slightly more angled) for the right side which is due to slightly stronger convective flow in the right half-cavity for the off-centre partition case.

As k_r increases the thermal conductivity of the partition rises and the angle of isotherms in the partition becomes closer to zero (the horizontal line). This behavior can be seen in the off-centre placed partitioned cavity. Interestingly as Ra increases the temperature gradient in the partition for the off-centre and centre partitioned cavities becomes more similar. A good example of this similarity can be found in figures 5.5 and 5.37 for the cases of $Ra = 10^8$ (*i.e.*, the sub-figures p, q and r). It is clear that the number and angle of isotherms present in the partition area are similar in both figures. For the highest k_r, the temperature of the partition on both sides is constant (isothermal wall). This character is also observed in the centrally-positioned partitioned cavities. Therefore, it is possible to draw the same conclusion and separate each half-cavities and define an equivalent non-partitioned cavity for each half-cavity.

B. Vertical and horizontal velocity distributions

Figures 5.43, 5.45, 5.47, 5.49 and 5.51 present the vertical velocity contours and figures 5.44, 5.46, 5.48, 5.50 and 5.52 show the horizontal velocity at the fully developed stage obtained numerically for $T_p = 0.05$, 0.1, and 0.2, each at $X_p = 0.5$ and at $Ra = 10^3$, 10^4, 10^5, 10^6, 10^7 and 10^8, respectively.

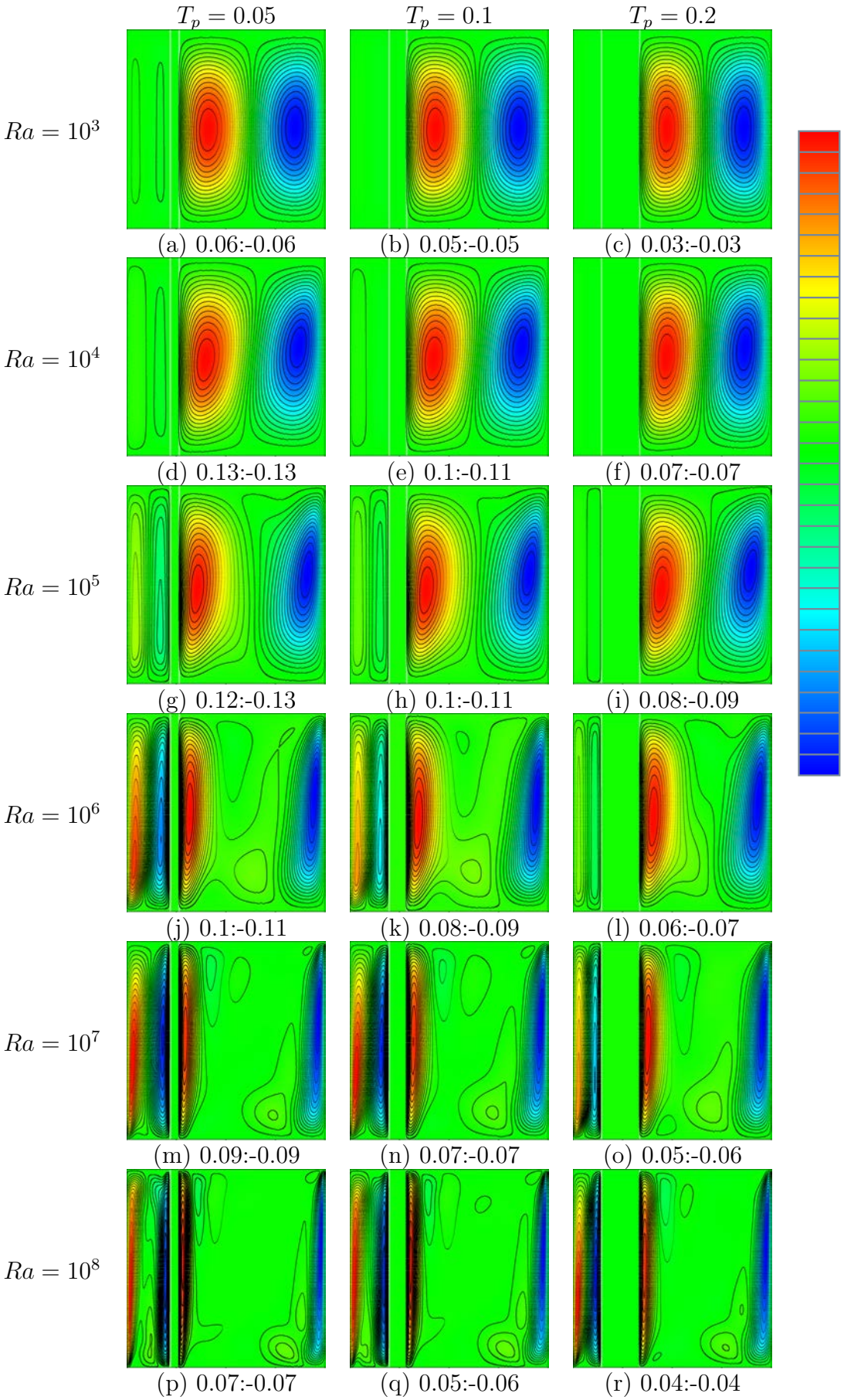

(a) 0.06:-0.06 (b) 0.05:-0.05 (c) 0.03:-0.03

(d) 0.13:-0.13 (e) 0.1:-0.11 (f) 0.07:-0.07

(g) 0.12:-0.13 (h) 0.1:-0.11 (i) 0.08:-0.09

(j) 0.1:-0.11 (k) 0.08:-0.09 (l) 0.06:-0.07

(m) 0.09:-0.09 (n) 0.07:-0.07 (o) 0.05:-0.06

(p) 0.07:-0.07 (q) 0.05:-0.06 (r) 0.04:-0.04

Figure 5.43: Vertical velocity contours at $k_r = 0.1$ and $X_p = 0.25$ for different Ra values ($10^3 \leq Ra \leq 10^8$) and T_p ($T_p = 0.05$, 0.1 and 0.2).

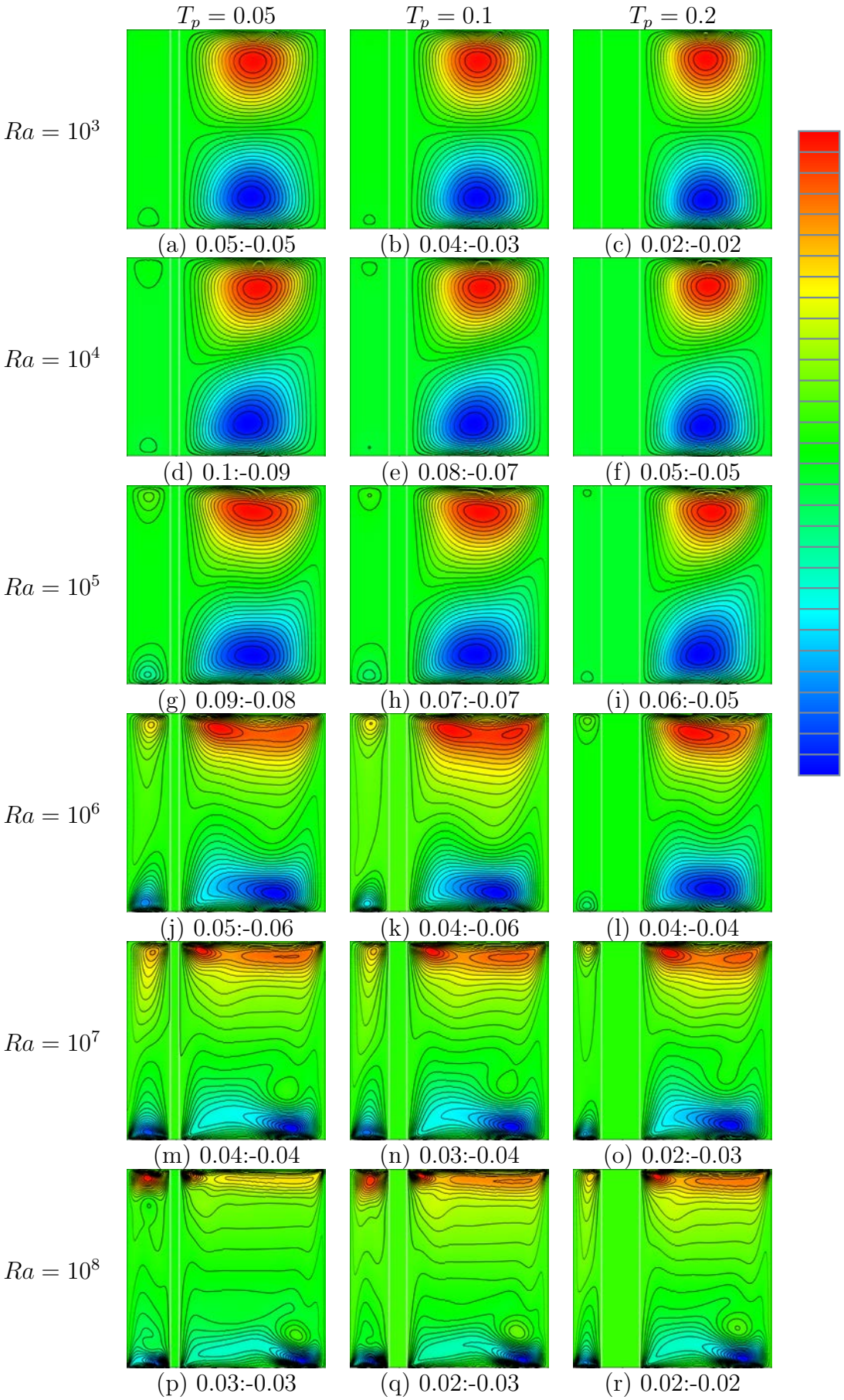

Figure 5.44: Horizontal velocity contours at $k_r = 0.1$ and $X_p = 0.25$ for different Ra values ($10^3 \leq Ra \leq 10^8$) and T_p ($T_p = 0.05$, 0.1 and 0.2).

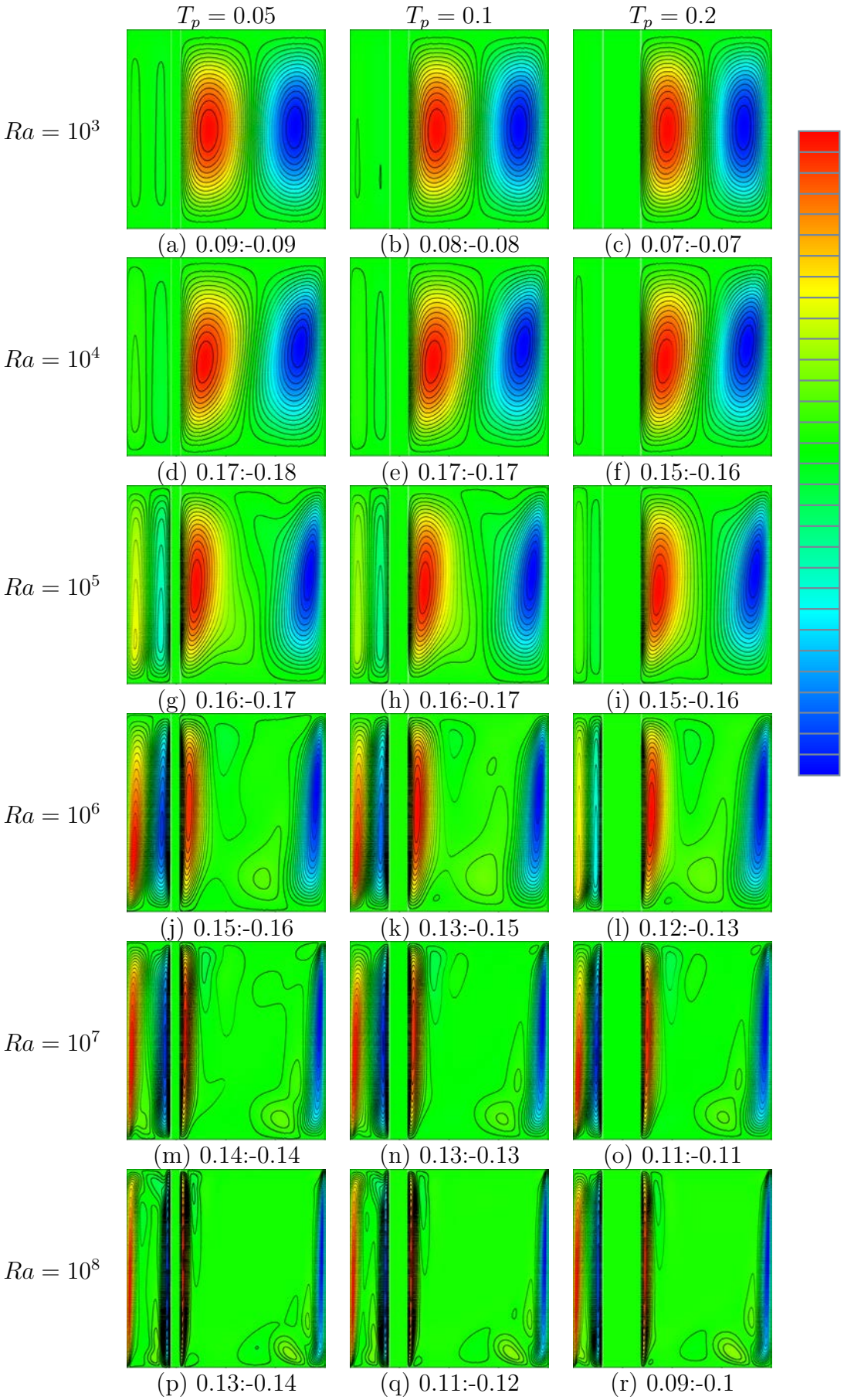

(a) 0.09:-0.09 (b) 0.08:-0.08 (c) 0.07:-0.07

(d) 0.17:-0.18 (e) 0.17:-0.17 (f) 0.15:-0.16

(g) 0.16:-0.17 (h) 0.16:-0.17 (i) 0.15:-0.16

(j) 0.15:-0.16 (k) 0.13:-0.15 (l) 0.12:-0.13

(m) 0.14:-0.14 (n) 0.13:-0.13 (o) 0.11:-0.11

(p) 0.13:-0.14 (q) 0.11:-0.12 (r) 0.09:-0.1

Figure 5.45: Vertical velocity contours at $k_r = 1$ and $X_p = 0.25$ for different Ra values ($10^3 \leq Ra \leq 10^8$) and T_p ($T_p = 0.05$, 0.1 and 0.2).

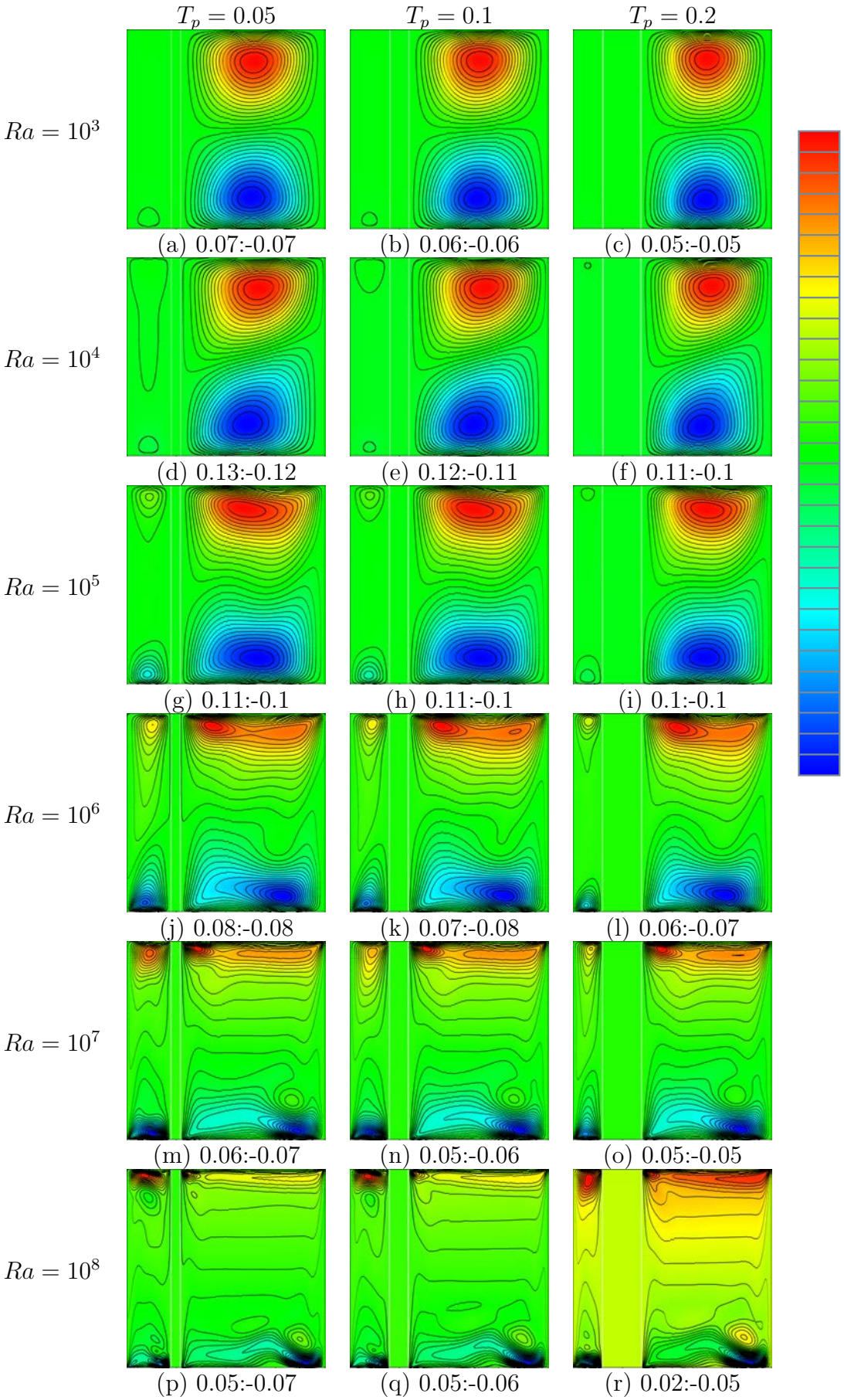

Figure 5.46: Horizontal velocity contours at $k_r = 1$ and $X_p = 0.25$ for different Ra values ($10^3 \leq Ra \leq 10^8$) and T_p ($T_p = 0.05$, 0.1 and 0.2).

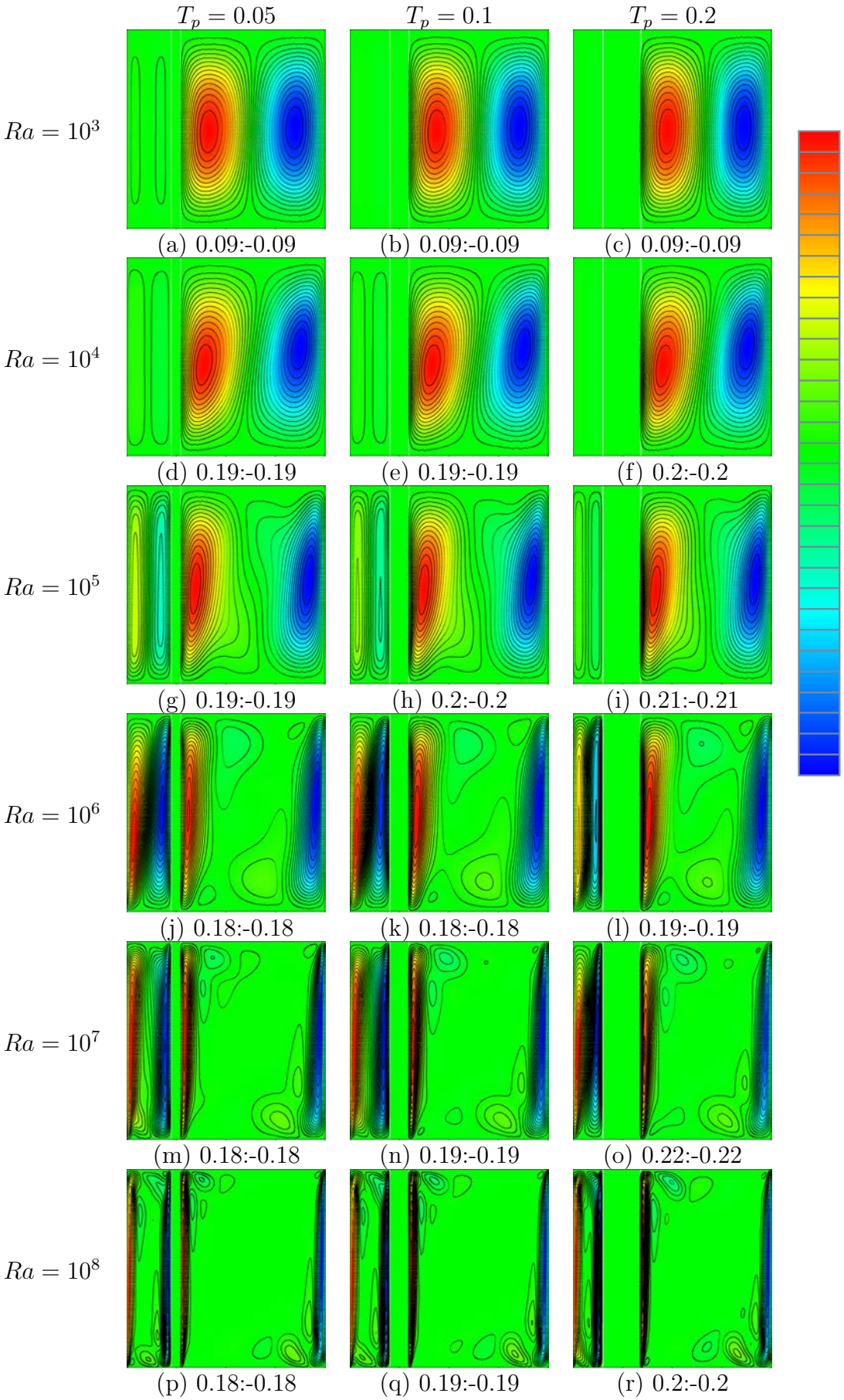

(a) 0.09:-0.09 (b) 0.09:-0.09 (c) 0.09:-0.09

(d) 0.19:-0.19 (e) 0.19:-0.19 (f) 0.2:-0.2

(g) 0.19:-0.19 (h) 0.2:-0.2 (i) 0.21:-0.21

(j) 0.18:-0.18 (k) 0.18:-0.18 (l) 0.19:-0.19

(m) 0.18:-0.18 (n) 0.19:-0.19 (o) 0.22:-0.22

(p) 0.18:-0.18 (q) 0.19:-0.19 (r) 0.2:-0.2

Figure 5.47: Vertical velocity contours at $k_r = 100$ and $X_p = 0.25$ for different Ra values ($10^3 \leq Ra \leq 10^8$) and T_p ($T_p = 0.05$, 0.1 and 0.2).

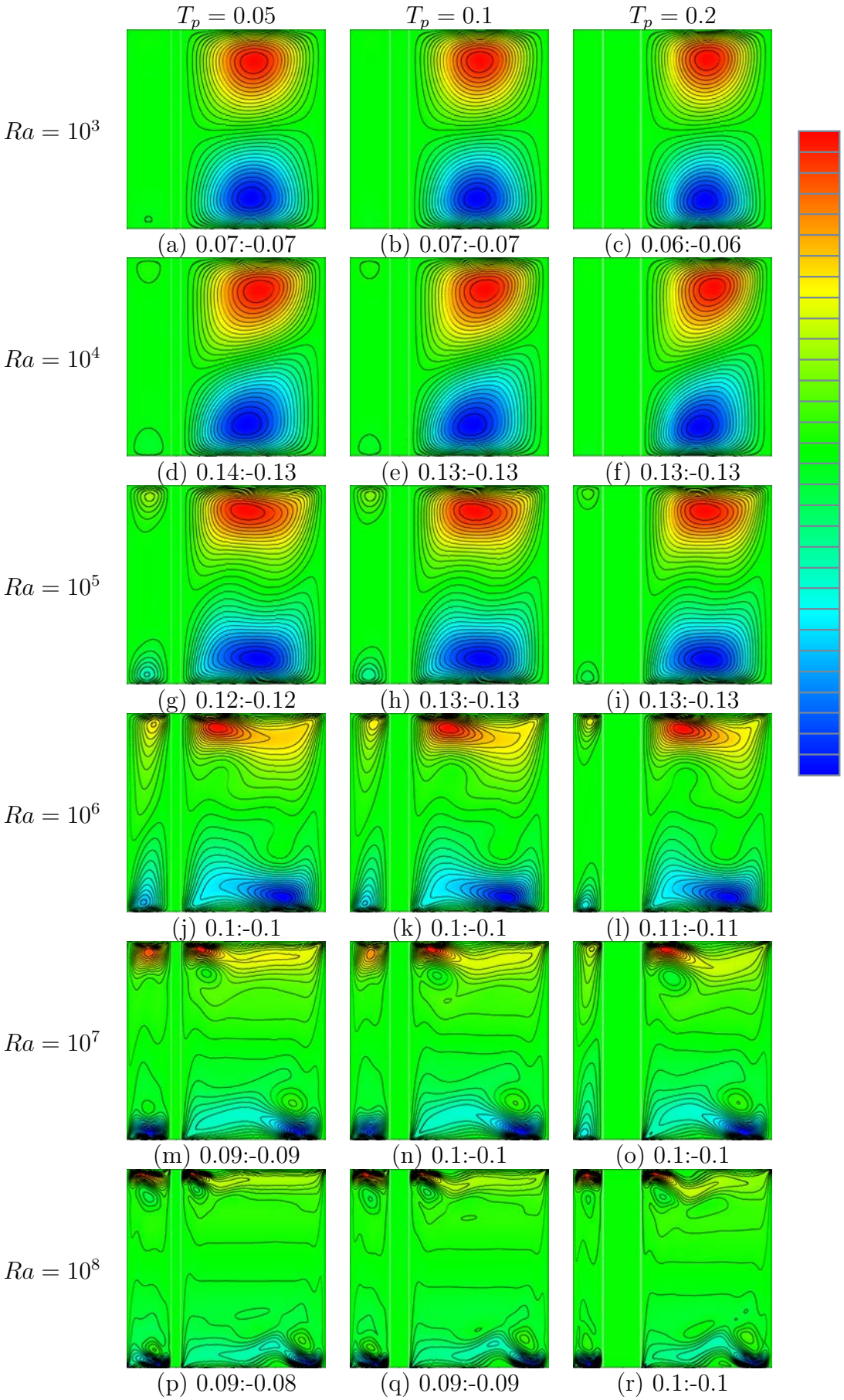

Figure 5.48: Horizontal velocity contours at $k_r = 100$ and $X_p = 0.25$ for different Ra values ($10^3 \leq Ra \leq 10^8$) and T_p ($T_p = 0.05$, 0.1 and 0.2).

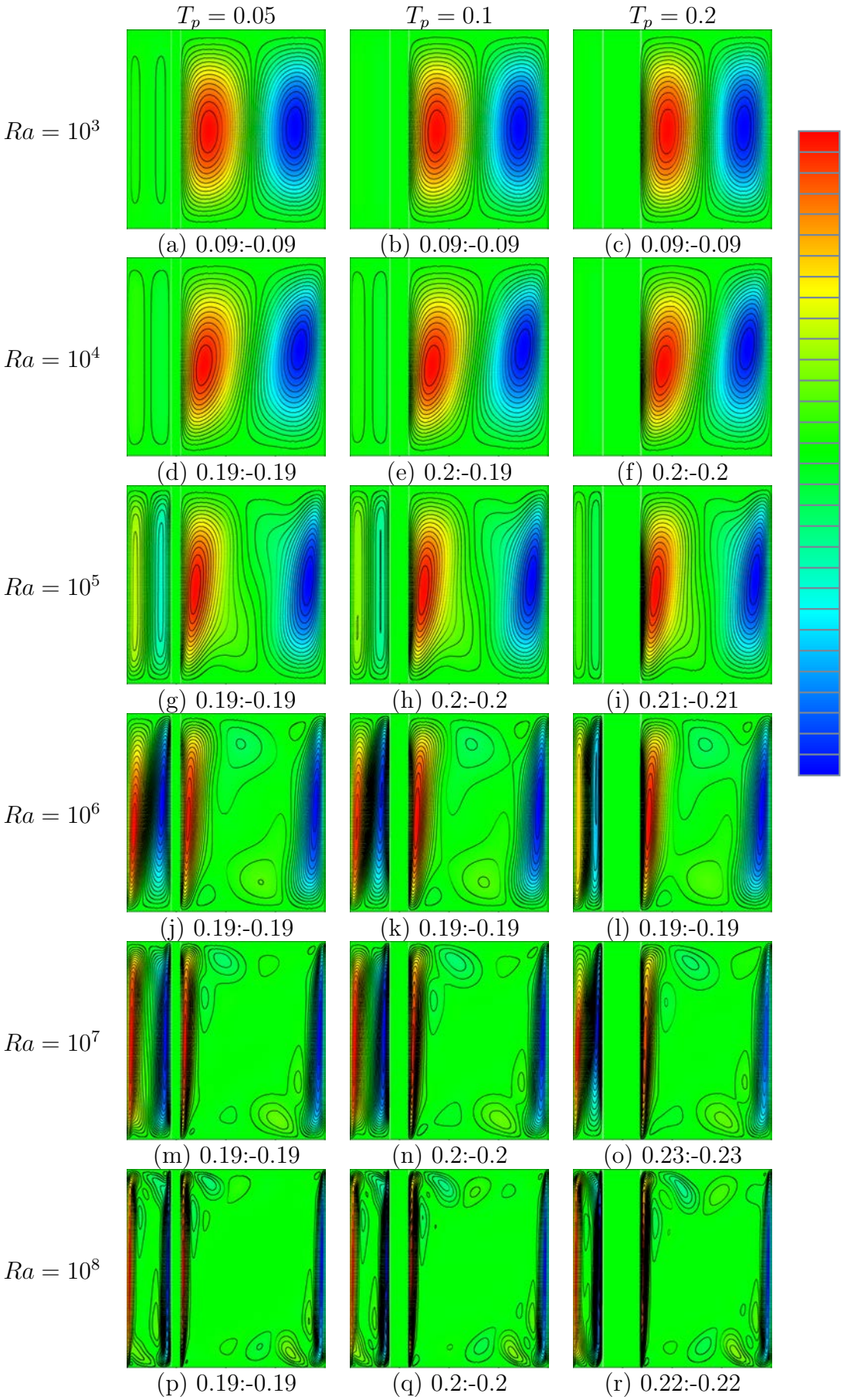

(a) 0.09:-0.09 (b) 0.09:-0.09 (c) 0.09:-0.09

(d) 0.19:-0.19 (e) 0.2:-0.19 (f) 0.2:-0.2

(g) 0.19:-0.19 (h) 0.2:-0.2 (i) 0.21:-0.21

(j) 0.19:-0.19 (k) 0.19:-0.19 (l) 0.19:-0.19

(m) 0.19:-0.19 (n) 0.2:-0.2 (o) 0.23:-0.23

(p) 0.19:-0.19 (q) 0.2:-0.2 (r) 0.22:-0.22

Figure 5.49: Vertical velocity contours at $k_r = 500$ and $X_p = 0.25$ for different Ra values ($10^3 \leq Ra \leq 10^8$) and T_p ($T_p = 0.05$, 0.1 and 0.2).

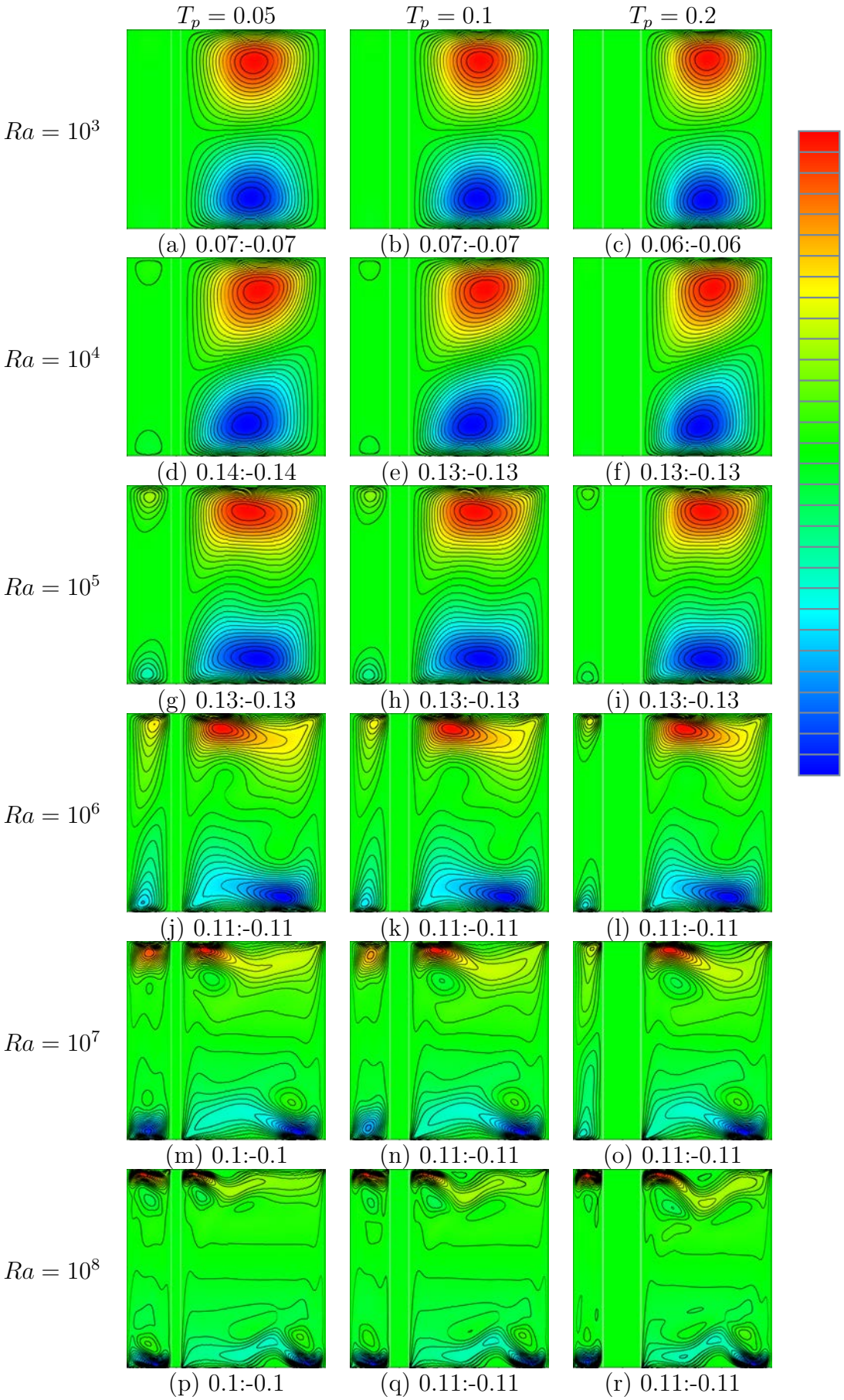

Figure 5.50: Horizontal velocity contours at $k_r = 500$ and $X_p = 0.5$ for different Ra values ($10^3 \leq Ra \leq 10^8$) and T_p ($T_p = 0.05$, 0.1 and 0.2).

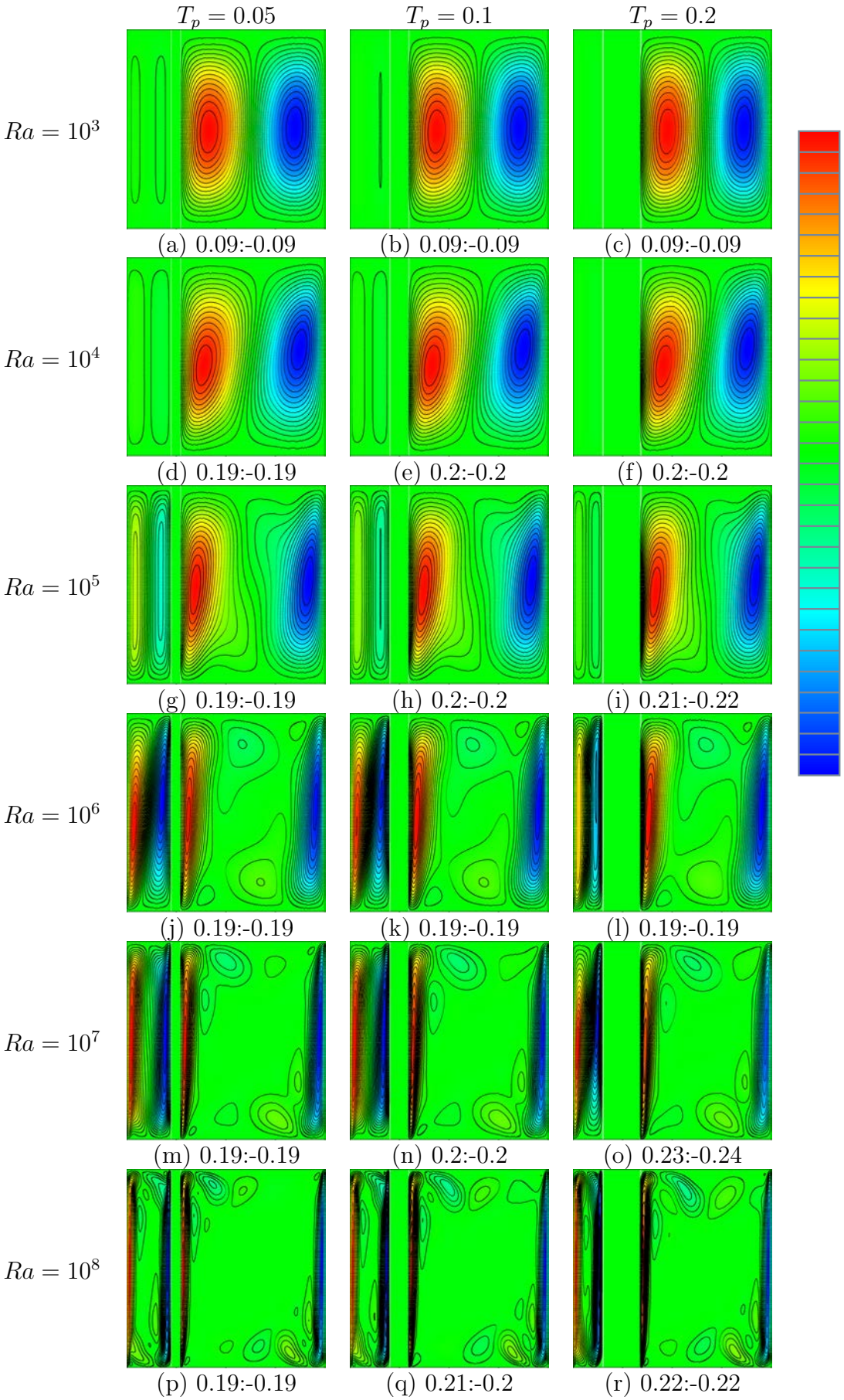

(a) 0.09:-0.09 (b) 0.09:-0.09 (c) 0.09:-0.09

(d) 0.19:-0.19 (e) 0.2:-0.2 (f) 0.2:-0.2

(g) 0.19:-0.19 (h) 0.2:-0.2 (i) 0.21:-0.22

(j) 0.19:-0.19 (k) 0.19:-0.19 (l) 0.19:-0.19

(m) 0.19:-0.19 (n) 0.2:-0.2 (o) 0.23:-0.24

(p) 0.19:-0.19 (q) 0.21:-0.2 (r) 0.22:-0.22

Figure 5.51: Vertical velocity contours at $k_r = 1000$ and $X_p = 0.25$ for different Ra values ($10^3 \leq Ra \leq 10^8$) and T_p ($T_p = 0.05$, 0.1 and 0.2).

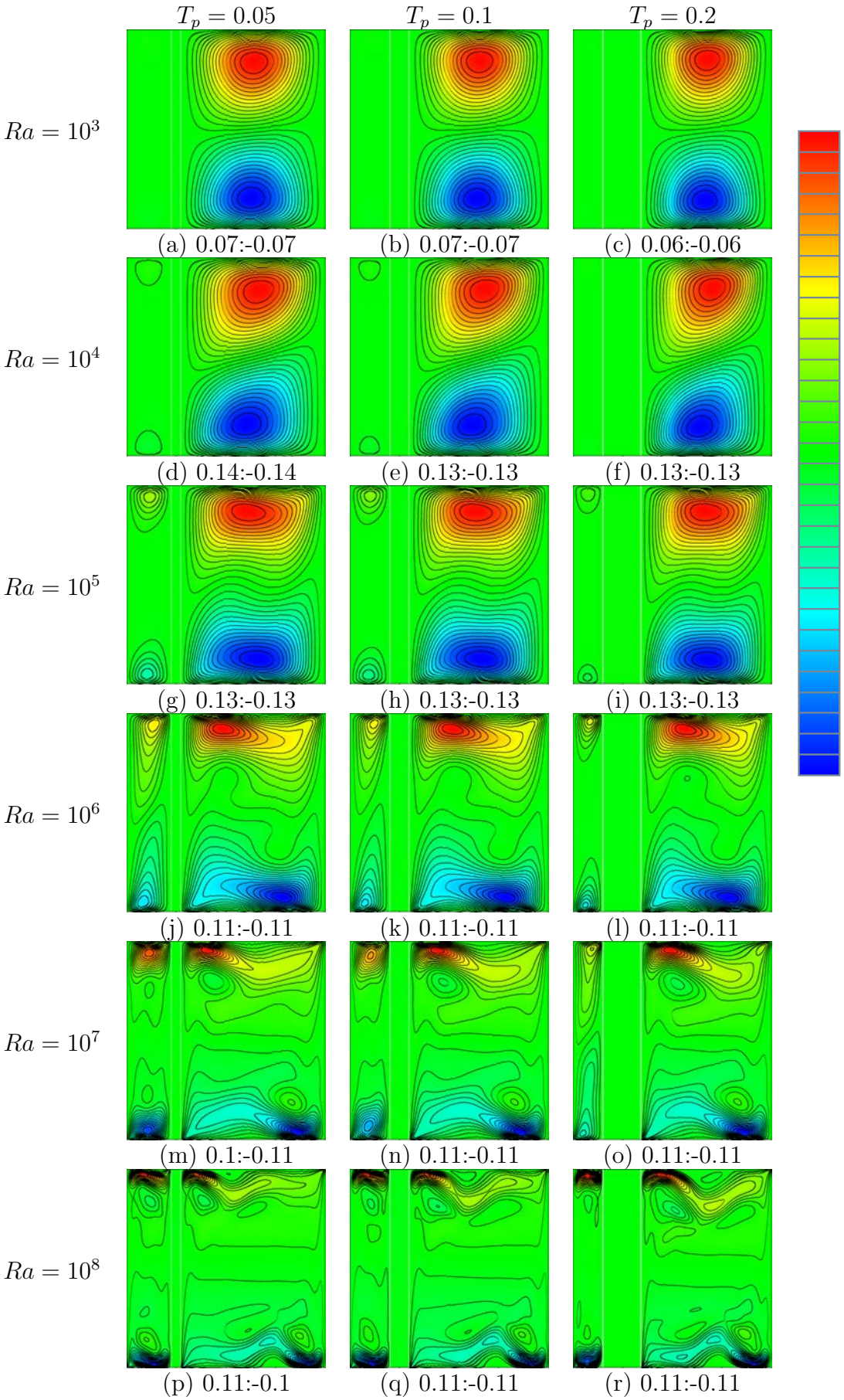

Figure 5.52: Horizontal velocity contours at $k_r = 1000$ and $X_p = 0.25$ for different Ra values ($10^3 \leq Ra \leq 10^8$) and T_p ($T_p = 0.05$, 0.1 and 0.2).

As expected, to move the partition to the left side ($X_p = 0.25$) has a significant effect on the vertical and horizontal velocities. Flow motion in the thinner left half-cavity is much less than the thicker right half-cavity up to $Ra = 10^5$. However, as Ra increases the difference between the maximum and minimum velocities of both sides become smaller. The thinner half-cavity shows very small or no vertical and horizontal velocities at low Ra cases due to the dominance of conduction which can be seen by the vertical isotherms in the temperature contour figures. By increasing Ra the vertical and horizontal boundary layers become thinner for all cases presented in the velocity contour figures. This observation is not applicable for low Ra cases as their velocity boundary layers are so thick and the inner area of the half-cavity does not provide enough room for the full growth of a boundary layer. The horizontal velocity contour figures show that the side vertical boundary layers of the right half-cavity have no interaction at $10^6 \leq Ra \leq 10^8$ and this condition for the left half-cavity is identified at $Ra = 10^8$. Due to the presence of a vertical partition in the cavity, the distance between the top and bottom walls has not altered, therefore the horizontal velocity boundary layers in the left and right half-cavities have an almost same point (*i.e.*, $Ra = 10^7$) for losing the interaction between the boundary layers.

Figure 5.53 shows the horizontal temperature profiles at the mid-height of the cavity ($y = 0.5$) of the case $X_p = 0.25$ for different values of Ra (10^3, 10^4, 10^5, 10^6, 10^7 and 10^8), k_r (0.1, 1, 100, 500 and 1000) and T_p (0.05, 0.1, and 0.2).

The horizontal temperature profiles presented for $10^3 \leq Ra \leq 10^5$ are straight lines in the left half-cavity due to the conduction-dominated heat transfer. Therefore, the reason for the uniform isotherm distribution for those low Ra cases in the left half-cavity is obvious from this figure. At this range of Ra values, the angle of the horizontal temperature profile in the left half-cavity gradually changes and becomes steeper as Ra increases. For the case of $k_r = 0.1$, as T_p increases the horizontal temperature profile rises, indicating a hotter left half cavity. Results for $k_r = 1$ illustrates an interesting behavior, as T_p shows no significant effect on the horizontal temperature profile of $Ra = 10^3$. As Ra increases the effect of T_p becomes stronger and a thicker partition cause a higher horizontal temperature profile. Further increasing k_r has a remarkable effect on the horizontal temperature profile. As figures 5.53($c - e$) depicts, the growth in the

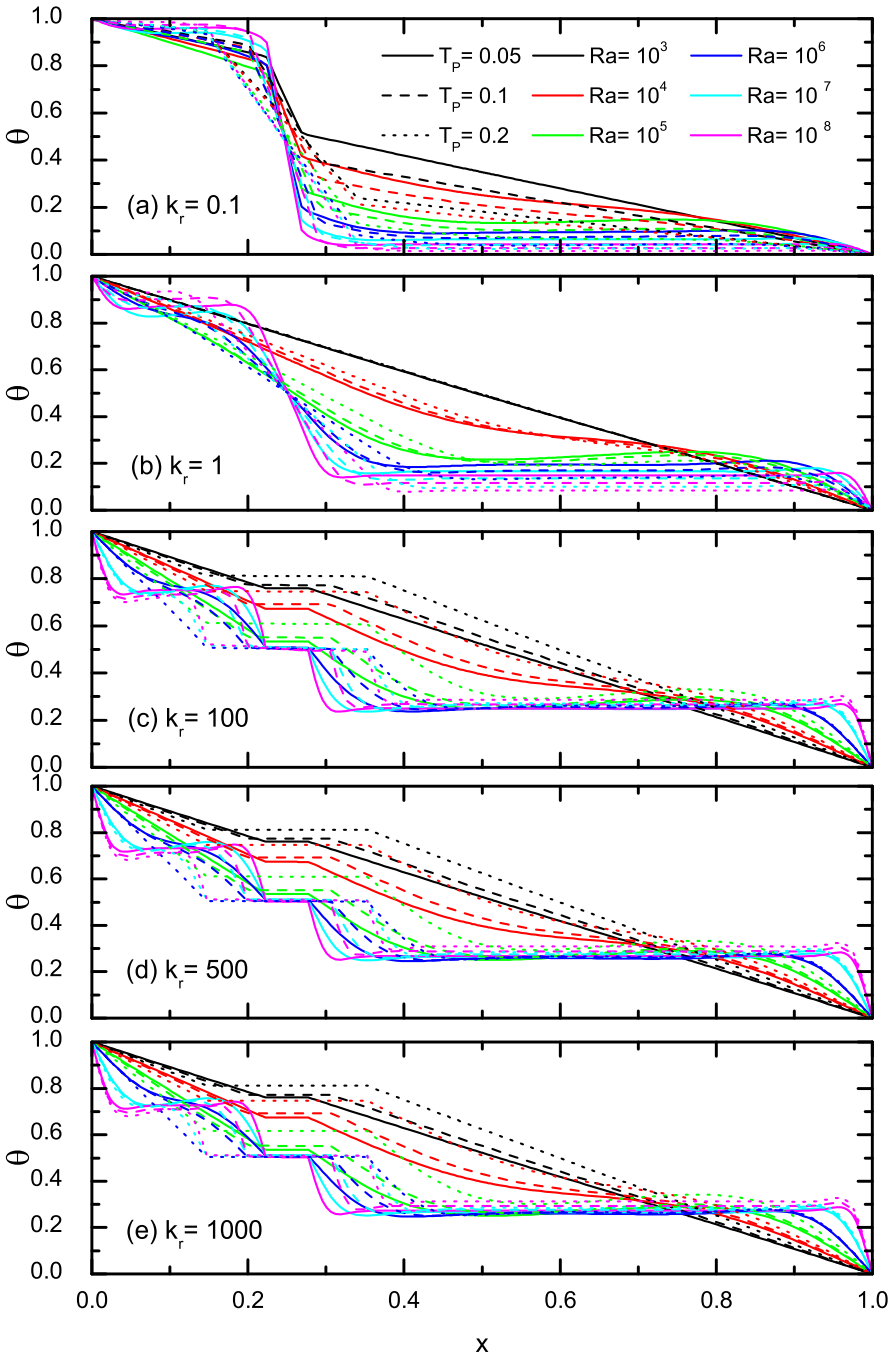

Figure 5.53: Horizontal temperature profiles at the mid-height ($y = 0.5$) of the case $X_p = 0.25$ for different values of Ra (10^3, 10^4, 10^5, 10^6, 10^7 and 10^8), k_r (0.1, 1, 100, 500 and 1000) and T_p (0.05, 0.1, and 0.2).

partition thickness causes the reduction in the horizontal temperature profile and eventually a cooler left half-cavity.

By studying the right half-cavity it is found that the case of $Ra = 10^3$ has a straight line of the horizontal temperature profile for the whole half-cavity and the rest of the horizontal temperature profiles are showing signs of convection heat transfer and finally stratification process at the high Ra cases. The horizontal temperature profiles of $k_r = 0.1$ shows that unlike the left half-cavity, T_p has a decreasing effect on the horizontal temperature profile and lead to cooler right half-cavity for all Ra values. Increasing Ra at this k_r causes the reduction in the horizontal temperature profiles. The case $k_r = 1$ is interesting as for $10^4 \leq Ra \leq 10^6$, the effect of increasing T_p is not clear and close to the partition it is shown that the horizontal temperature profile increases and close to the cold sidewall it decreases. Again increasing Ra decreases the horizontal temperature profile. For higher k_r, any increase in T_p results in a hotter right half-cavity and the increase of Ra decreases the horizontal temperature profile up to $Ra = 10^6$ and then increases (*e.g.*, figures 5.53$(c - e)$). Moreover, the temperature distribution in the partition shows that over $10^3 \leq Ra \leq 10^6$ with the increase of Ra the temperature of the partition decreases. However, the horizontal temperature profile becomes almost invariant for $10^6 \leq Ra \leq 10^8$ in the partition.

It can also be seen that the shape of the temperature profile in the half-cavity is completely asymmetric for low k_r and as k_r increases the asymmetry diminishes. This symmetry means that the thermal behavior of the sidewalls and the partition becomes similar. Moreover, the temperature of the stratified region reduces with increasing k_r which is clearly due to the increased thermal conductivity of the partition.

5.3.2 Quantitative analysis of flow and heat transfer behaviour

The effect of Ra, T_p and k_r on the average Nusselt number (Nu_{Ave}) is shown in figure 5.54 for a range of these parameters. It can be seen that as Ra increases Nu_{Ave} increases in all cases and the difference between Nu_{Ave} of the consecutive Ra values increases as well. The overall trend of Nu_{Ave} in this figure shows that by increasing k_r, Nu_{Ave} increases and reaches a peak

point and then stays invariant. These are also observed for the centrally-positioned partition case, as illustrated in figure 5.26.

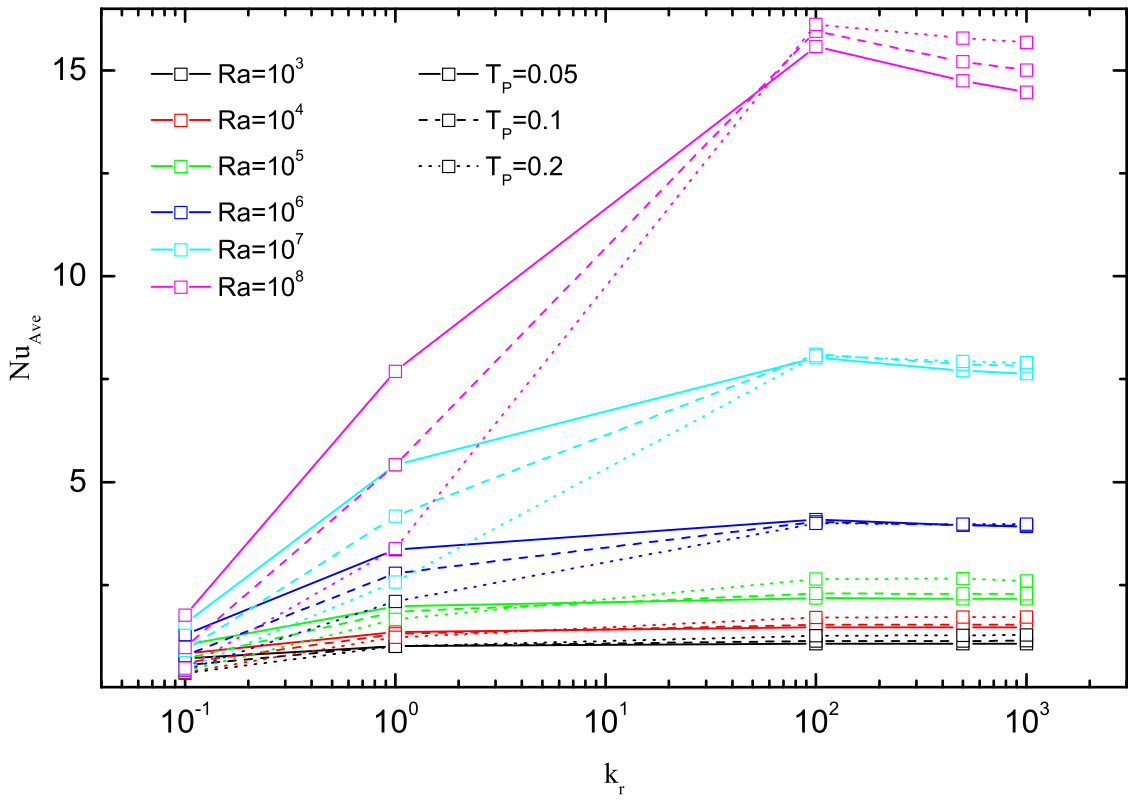

Figure 5.54: Average Nusselt number on the hot wall for an off-centre partitioned cavity with different partition thicknesses and thermal conductivity ratios for $10^3 \leq Ra \leq 10^8$.

The effect of the partition thickness on Nu_{Ave} for low Ra values is less than that for high Ra values. By increasing k_r from 0.1 to 1, the effect of T_p on Nu_{Ave} escalates and a thicker partition has a smaller value of Nu_{Ave}. Further increasing k_r alters the effect of T_p and as can be seen in the figure at high k_r values thicker partitions have larger Nu_{Ave}. However, unlike the centrally-placed partition cases, the value of k_r with such changes happening is different for different Ra values. This value for $Ra = 10^3$, 10^4 and 10^5 is $1 \leq k_r \leq 10$, for $Ra = 10^6$ and 10^7 is $k_r = 100$ and for $Ra = 10^8$ is $10 \leq k_r \leq 100$. Interestingly, the peak point of Nu_{Ave} at $k_r = 100$ is similar to that in the case of $X_p = 0.5$.

Over the range of $10^3 \leq Ra \leq 10^5$, as k_r increases from 10 to 1000, the effect of T_p gradually becomes significant especially for the case of $T_p = 0.2$. The reason for this is that for those Ra values, convection in the left half-cavity is not strong enough and increasing the partition

thickness basically converts a partitioned cavity with two half-cavities to one cavity with a heat conducting left side. Decreasing the partition thickness for those cases results in forming stronger convective heat transfer in the left half-cavity in which it can decrease Nu_{Ave} in comparison with the thicker partition with high thermal conductivity (see, figures 5.41, 5.42, 5.51 and 5.52$(a-i)$).

Figure 5.55 shows the vertical distribution of the local Nusselt number (Nu_{Local}) along the sidewalls for $T_p = 0.05$, 0.1, and 0.2, $k_r = 0.1$, 1, 100, 500 and 1000, each at $X_p = 0.25$ and at $Ra = 10^3$, 10^4, 10^5, 10^6, 10^7 and 10^8. Due to the asymmetry caused by placing the partition off-centre ($X_p = 0.25$), the profiles for both sidewalls are presented. It is seen that Nu_{Local} decreases along most of the hot sidewall but on the contrary, increases along most of the cold sidewall. Similar to the centrally-positioned partition cases there is a peak in the profile near the leading edges on both sidewalls. The effect of Ra, T_p and k_r on Nu_{Local} is the same as that in the centrally placed partition case.

Comparing Nu_{Local} profiles for the left and right sidewalls shows that the symmetry observed in the cases of $X_p = 0.5$ does not exist. The main area of non-similarity between the profiles of the sidewalls is in the vicinity of the leading edges. For example on the hot sidewall the peak point of Nu_{Local} of case $Ra = 10^8$, $T_p = 0.05$ and $k_r = 100$ (at the peak point of $Nu_{Local} = 55$) is higher than the point on the cold sidewall (at the peak point of $Nu_{Local} = 51$). This difference for various Ra values and T_p is different as on the hot sidewall the peak point of Nu_{Local} of the case $Ra = 10^8$, $T_p = 0.2$ and $k_r = 100$ (at the peak point of $Nu_{Local} = 45$) is lower than the point on the cold sidewall (at the peak point of $Nu_{Local} = 48$). There are some cases of Nu_{Local} profiles in which the difference between the hot sidewall and cold side wall is negligible. An example in this case can be seen in figure 5.55 for $Ra = 10^8$, $T_p = 0.05$ and $k_r = 1$ in which the value of the maximum Nu_{Local} for both hot and cold sidewalls is 29. A closer look at Nu_{Local} profiles of a centrally positioned and off-centre partitioned cavity (*i.e.*, figures 5.55 and 5.28) shows that the profiles presented for the cold sidewall are very similar (or even identical in some cases) to the ones illustrated for the centrally-positioned partitioned cavity. This is expected as the temperature and flow pattern in the wider half-cavity is much closer to the half-cavities of the centrally placed partition case than the thin half-cavity which has less convective flow.

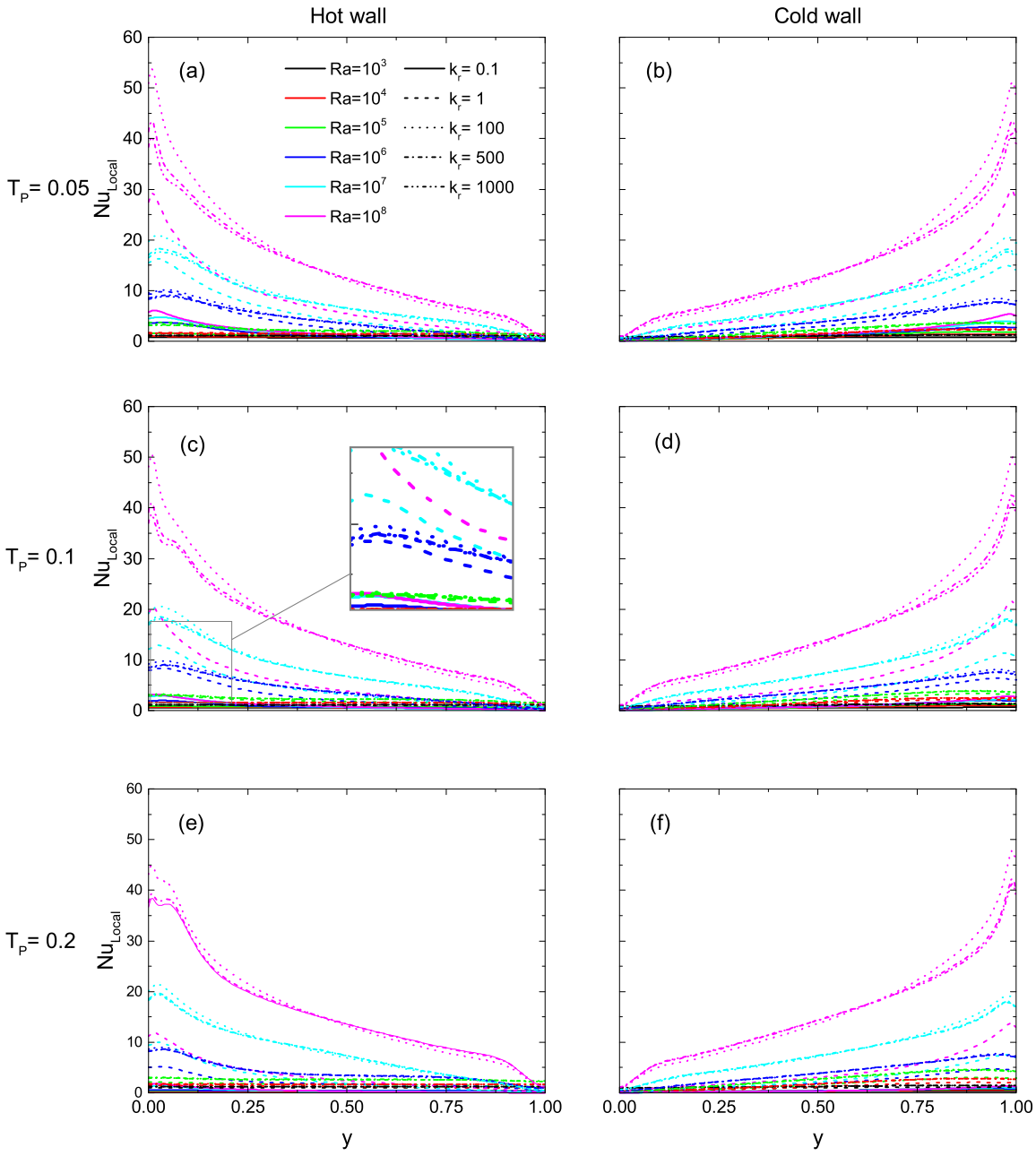

Figure 5.55: The vertical profiles of the local Nusselt number on the hot and cold sidewalls of the case $X_p = 0.25$ for different values of Ra (10^3, 10^4, 10^5, 10^6, 10^7 and 10^8), k_r (0.1, 1, 100, 500 and 1000) and T_p (0.05, 0.1, and 0.2).

To investigate the heat transfer rate on the partition, figure 5.56 presents the vertical profiles of Nu_{Local} on the left and right sides of partition (*i.e.*, $x = X_p - 0.5T_p$ and $x = X_p + 0.5T_p$) of the case $X_p = 0.25$ for different values of Ra (10^3, 10^4, 10^5, 10^6, 10^7 and 10^8), k_r (0.1, 1, 100, 500 and 1000) and T_p (0.05, 0.1, and 0.2).

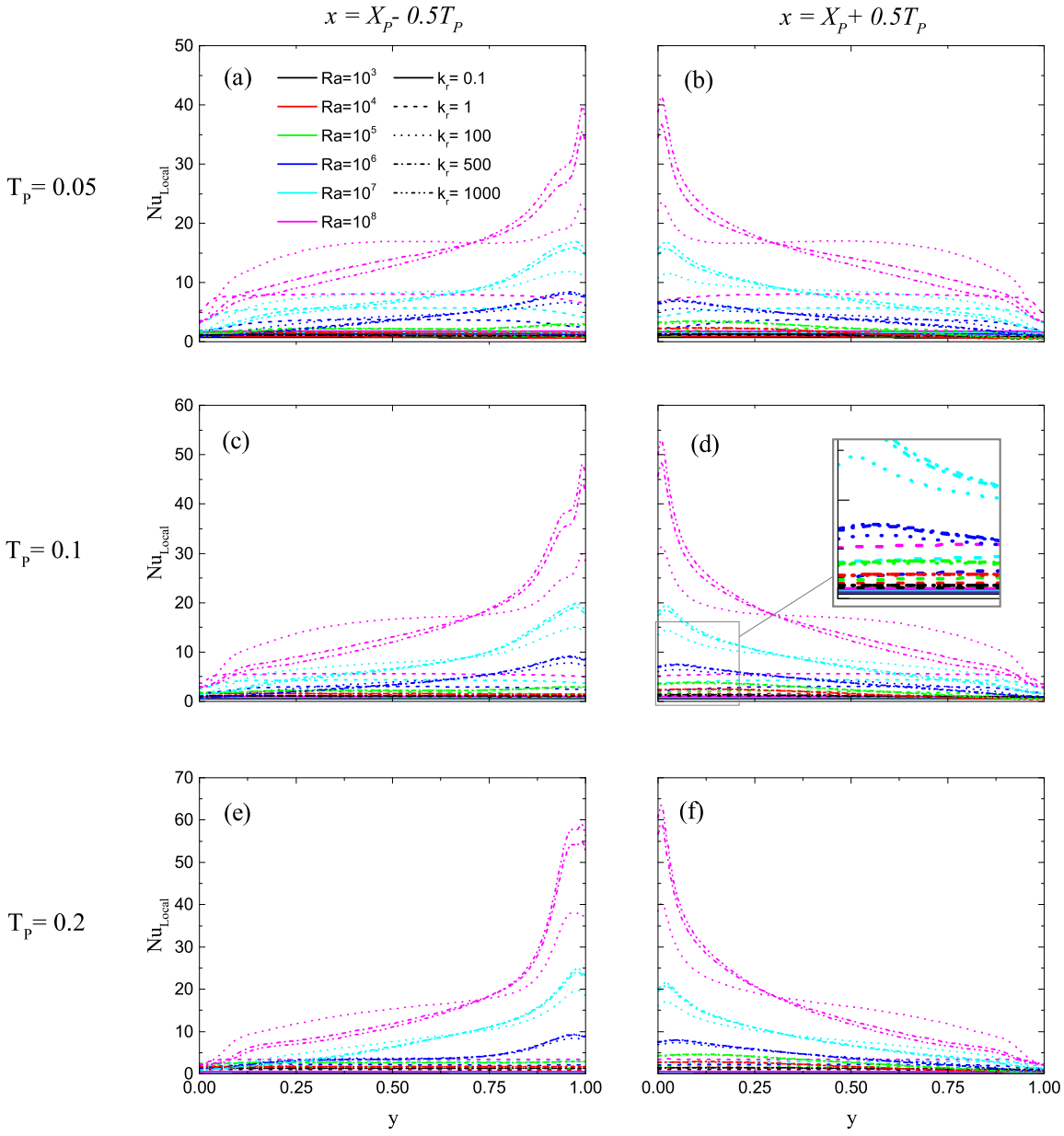

Figure 5.56: The vertical profiles of the local Nusselt number on the both sides of the partition of the case $X_p = 0.25$ for different values of Ra (10^3, 10^4, 10^5, 10^6, 10^7 and 10^8), k_r (0.1, 1, 100, 500 and 1000) and T_p (0.05, 0.1, and 0.2).

Nu_{Local} of the partition, similar to Nu_{Ave} and Nu_{Local} of the sidewalls, is strongly affected by Ra. As Ra increases Nu_{Local} rises. The profiles of Nu_{Local} in the centrally-positioned cavity

is roughly classified into two groups of non-uniform lines with a significant peak point and uniform lines without a notable peak. The same classification can be used for profiles of the off-centre case illustrated in figure 5.56.

As uniform lines of Nu_{Local} represent an isoflux wall like behavior on the partition and the non-uniform lines shows more isothermal wall features, the Nu_{Local} profiles at high Ra cases (*i.e.*, $Ra = 10^6$, 10^7 and 10^8) which are non-uniform with a sharp jump on the leading edge can be considered to have the isothermal wall like behavior. On the other hand, low Ra cases which have more uniform Nu_{Local} profiles can be identified to become isoflux (*i.e.*, $Ra = 10^3$, 10^4 and 10^5). The effects of investigated parameters (*i.e.*, T_p, k_r and Ra) are similar to those discussed in the centrally-positioned partitioned cavity.

Comparing figures 5.55 and 5.56 identifies interesting thermal specification of the partition. Although the peak point for Nu_{Local} of the hot sidewall is observed at the bottom of the sidewall, for the left side of the partition, the peak can be found at the top side of the partition. Therefore, partition plays a similar role of the cold sidewall for the cases with non-uniform profiles. As k_r increases this similarity increases. Observing this thermal behavior on the partition is another sign which leads to a conclusion that it is possible to separate each half-cavity and find an equivalent non-partitioned cavity with the same temperature and flow pattern.

Studying the peak points in those figures illuminates another interesting aspect which is the effect of T_p on the partition and is the opposite of the sidewalls. As T_p increases, the value of Nu_{Local} at the peak points increases. This feature is also observed in figure 5.55. Moreover, it can be seen that unlike that in figures 5.55, the maximum Nu_{Local} in figure 5.56 increases as k_r increases. This observation is due to the direct effect of k_r on the temperature gradient of the partition which can also be seen in temperature contours figures.

From the profiles of Nu_{Local} on the left and right sides of the partition can be seen that the same asymmetry observed for the Nu_{Ave} profiles exists. The main area of the difference between the profiles is in the vicinity of the leading edge before Nu_{Local} reaches the peak point. Due to the thin half-cavity, the temperature gradient in the left half-cavity is different from that in the right half-cavity. For the case of $Ra = 10^8$, as T_p increases this difference increases and

the distinct peak points becomes less pronounced. Comparing figures 5.56 and 5.28 shows that there is a trend similarity between Nu_{Local} profiles of the centrally-positioned partitioned cavity and those from the right side of the partition (*i.e.*, $x = X_p + 0.5T_p$). The value of Nu_{Local} of those compared cases should be different as the place of data gathering line is totally different. The value of Nu_{Local} at the peak point of figure 5.56 for the case $Ra = 10^8$, $T_p = 0.05$ and $k_r = 1000$ is 42; however, this value for the same case of the centrally-positioned cavity is about 37.

Figure 5.57 shows the vertical temperature distribution on the left (left column) and right (right column) sides of the partition (*i.e.*, $x = X_p - 0.5T_p$ and $x = X_p + 0.5T_p$) of the case $X_p = 0.25$ for various Ra (10^3, 10^4, 10^5, 10^6, 10^7 and 10^8), k_r (0.1, 1, 100, 500 and 1000) and T_p (0.05 , 0.1, and 0.2) at $X_p = 0.5$. From these figures, it is found that, similar to the case of $X_p = 0.5$, the upper part of the left side of the partition is in contact with the heat fluid from the hot sidewall, while the lower section receives cooled fluid of the right sidewall. Therefore, for all cases of the vertical temperature profiles, the upper part has a higher temperature than the lower section at $x = X_p - 0.5T_p$. On the other hand, it is the opposite for the vertical temperature profiles at $x = X_p + 0.5T_p$.

A significant difference can be seen between the vertical temperature profiles of the left and right sides of the partition. The profiles at $x = X_p - 0.5T_p$ covers a thinner range of temperature than that at $x = X_p + 0.5T_p$. For example, the temperature range covered by the profiles for the case $T_p = 0.05$ at $x = X_p - 0.5T_p$ (*i.e.*, figure 5.57(a)) is almost $0.3 - 0.9$, however, for the same situation on the right side of the partition (*i.e.*, figure 5.57(b)) this range is wider, from almost 0.1 to 0.8. Another interesting observation is the effect of T_p for the profiles of both sides of the partition. As T_p increases the temperature range covered by the profiles on the left side of the partition reduces but on the contrary increase of T_p for the right side has an increasing effect. Moreover, studying of the temperature profiles at $x = X_p - 0.5T_p$ and $x = X_p + 0.5T_p$ reveals that there is a symmetry for high Ra cases and as Ra decreases this symmetry decreases. For example, the profile of the case of $Ra = 10^8$, $T_p = 0.05$ and $k_r = 0.1$ for the left and right sides of the partition have the same trend (rotational symmetry) and range (for left side of partition $0.8 \leq \theta \leq 0.92$ and for the right side of the partition $0.08 \leq \theta \leq 0.2$). The reason for this

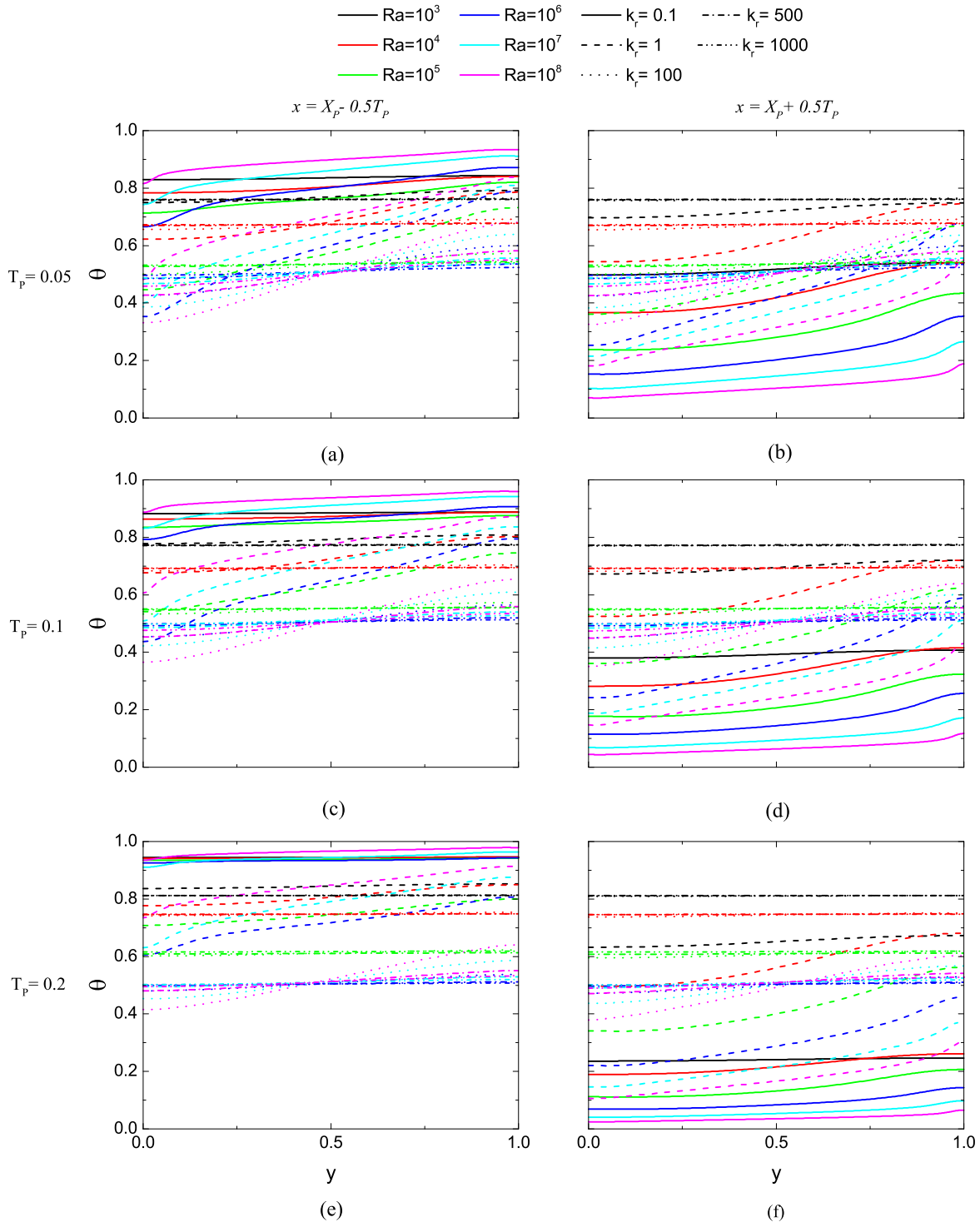

Figure 5.57: Vertical temperature profiles on both sides of the partition of the case $X_p = 0.25$ for different values of Ra (10^3, 10^4, 10^5, 10^6, 10^7 and 10^8), k_r (0.1, 1, 100, 500 and 1000) and T_p (0.05, 0.1, and 0.2).

symmetry is establishing convective flow in the thin half-cavity which decreases the thickness of the sidewall thermal boundary layer. By comparing figures 5.57 and 5.29 it can be seen that the profiles extracted for low Ra cases (*i.e.*, $10^3 \leq Ra \leq 10^5$) is higher than those depicted in figure 5.29 and increasing T_p increases its value. This observation is a sign for a hotter partition in the off-centre partition.

Figure 5.58 shows the horizontal temperature drop on the partition ($\theta_{D,x}$) of the case $X_p = 0.25$ for various Ra (10^3, 10^4, 10^5, 10^6, 10^7 and 10^8), k_r (0.1, 1, 100, 500 and 1000) and T_p (0.05, 0.1, and 0.2) at $X_p = 0.5$. In this figure $\theta_{D,x}$ is represented in two different scales of y axis in order to illustrate the profile shapes (figure 5.58$(a), (c)$ and (e)) and the values for the high k_r cases (figure 5.58$(b), (d)$ and (f)). As expected, due to the asymmetry existing in the cavity, $\theta_{D,x}$ profiles for low Ra (*i.e.*, $10^3 \leq Ra \leq 10^5$) is angled. However, for the centrally-positioned partition case, those profiles are completely symmetrical. Interestingly, as Ra increases over the range of $10^6 \leq Ra \leq 10^8$ and the convection in the left half-cavity intensifies, $\theta_{D,x}$ profiles become more symmetrical and horizontal. By increasing Ra, $\theta_{D,x}$ increases for all cases of T_p and k_r and higher Ra values have wider horizontal sections.

The $k_r = 0.1$ case has the highest $\theta_{D,x}$ and as k_r increases $\theta_{D,x}$ reduces and, similar to the centrally-positioned case the profiles of $\theta_{D,x}$ for $k_r \geq 100$ is very close to zero and can be seen as one line in the left column figures. The logarithmic scale y axis figures (right column figures) show that clearly as k_r further increases $\theta_{D,x}$ becomes smaller and closer to zero. The same increasing effect of T_p on $\theta_{D,x}$ found in the centrally positioned partition case occurs here as well. As T_p increases the flat section of the $\theta_{D,x}$ profiles also increases.

After investigating the sides of partition in contact of the fluid, it is necessary to study the thermal behaviour inside the partition. Figure 5.59 illustrates the vertical temperature profiles at the middle of the partition ($x = X_p$) of the case $X_p = 0.25$ for different values of Ra (10^3, 10^4, 10^5, 10^6, 10^7 and 10^8), k_r (0.1, 1, 100, 500 and 1000) and T_p (0.05, 0.1, and 0.2). It can be seen that the vertical temperature profiles at the middle of the partition have different shapes and can be divided into two separate groups. The first group is the profiles of the low Ra values ($10^3 \leq Ra \leq 10^5$) which have small convection heat transfer in the left half-cavity. Those cases

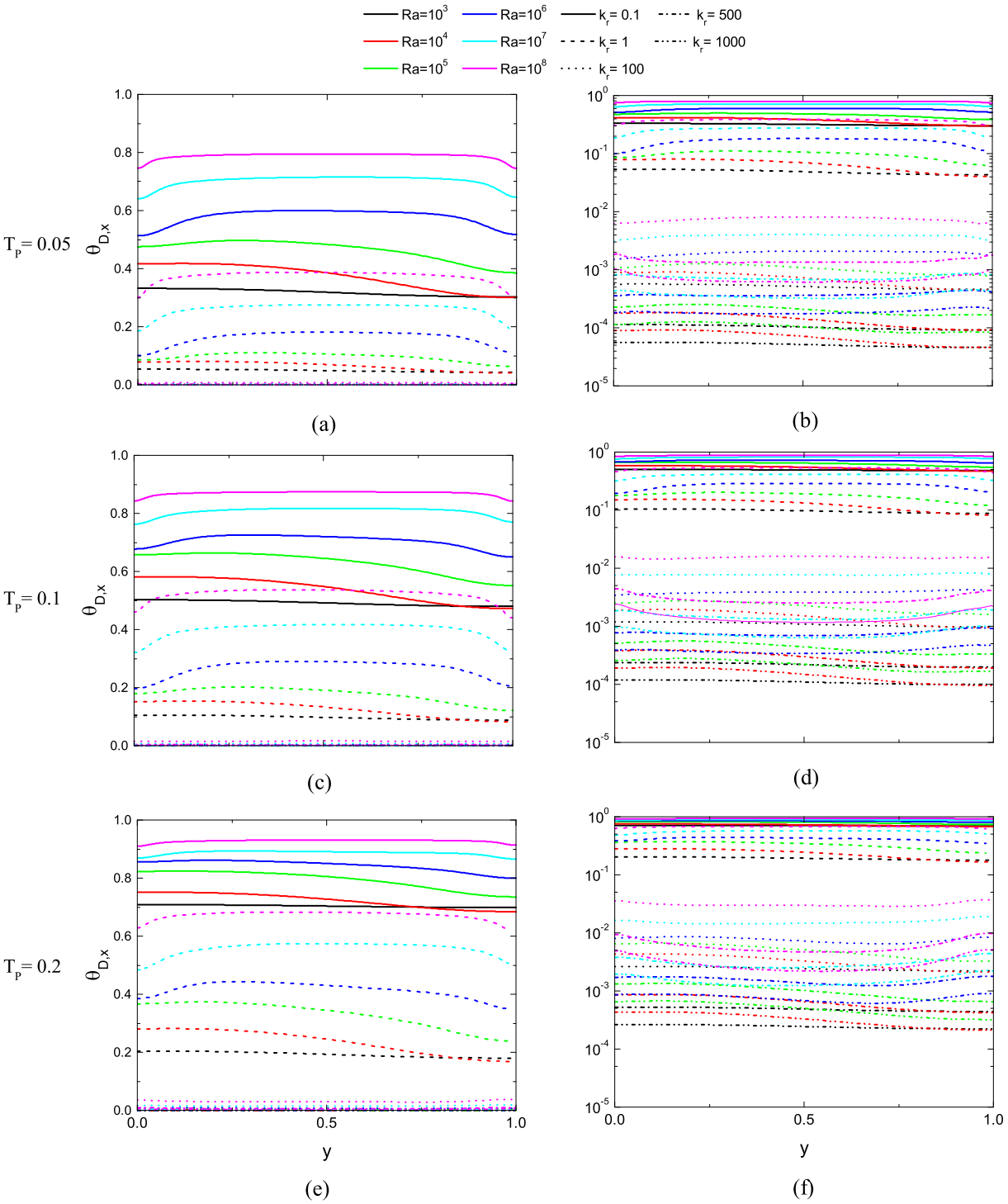

Figure 5.58: Horizontal temperature drop on the partition of the case $X_p = 0.25$ for different values of Ra (10^3, 10^4, 10^5, 10^6, 10^7 and 10^8), k_r (0.1, 1, 100, 500 and 1000) and T_p (0.05, 0.1, and 0.2).

show high temperature profiles above the mid-temperature of the cavity (*i.e.*, $\theta = 0.5$) at the middle of the partition. The profiles of this group rise by increasing k_r and T_p. The second group is the cases with large convection formed in the left half-cavity. The profiles of the second group are centered at $\theta = 0.5$ and $y = 0.5$, similar to the cases of $X_p = 0.5$. Increasing k_r from 0.1 to 1 increases the profiles' slopes. Further increasing k_r ($k_r \geq 100$) reduces the slopes and profiles become very close to horizontal lines. As T_p increases the overall slopes of the temperature profiles decrease.

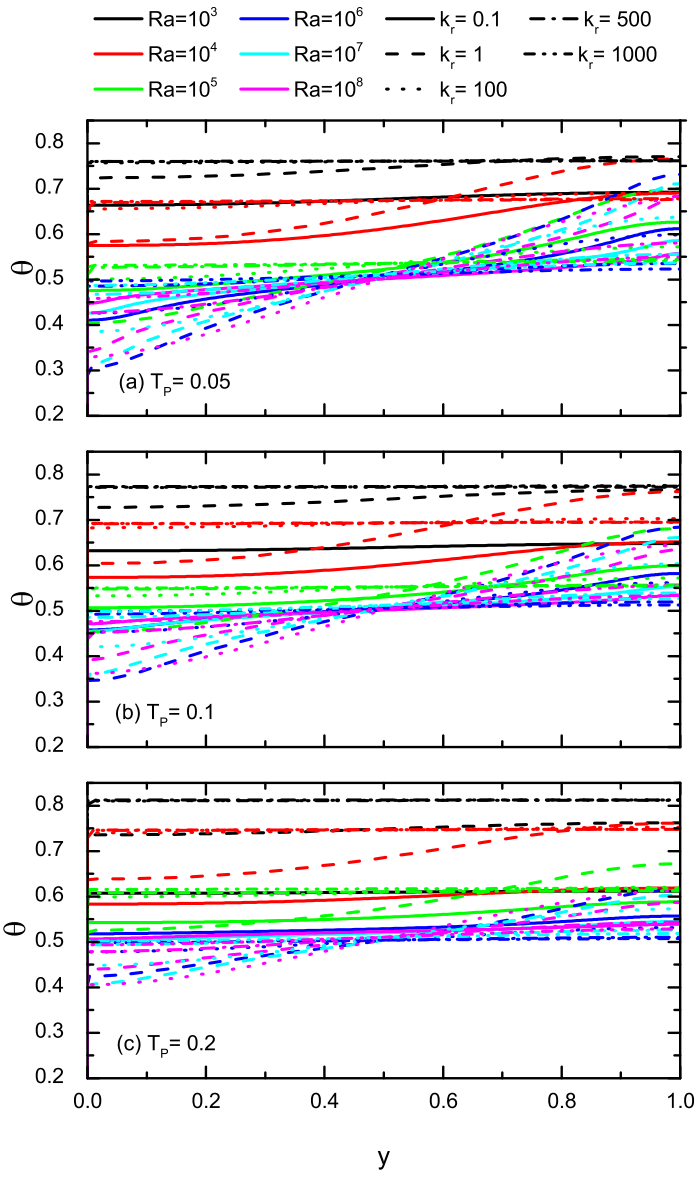

Figure 5.59: Vertical temperature profiles at the middle of the partition ($x = X_p$) of the case $X_p = 0.25$ for different values of Ra (10^3, 10^4, 10^5, 10^6, 10^7 and 10^8), k_r (0.1, 1, 100, 500 and 1000) and T_p (0.05, 0.1, and 0.2).

Figure 5.60 presents the steady-state value of $\theta_{D,y}$ of the case $X_p = 0.25$ for different values of Ra (10^3, 10^4, 10^5, 10^6, 10^7 and 10^8), k_r (0.1, 1, 100, 500 and 1000) and T_p (0.05, 0.1, and 0.2). The same two types of graphs observed for the case $X_p = 0.5$ can be seen in this figure. The graphs of $k_r = 0.1$ and 1 have a peak point for all T_p cases. Unlike the centrally-placed partition cases, the peak points for those graphs happen at higher Ra values ($Ra = 10^6$). For the case of $T_p = 0.2$ this peak point is at $Ra = 10^7$.

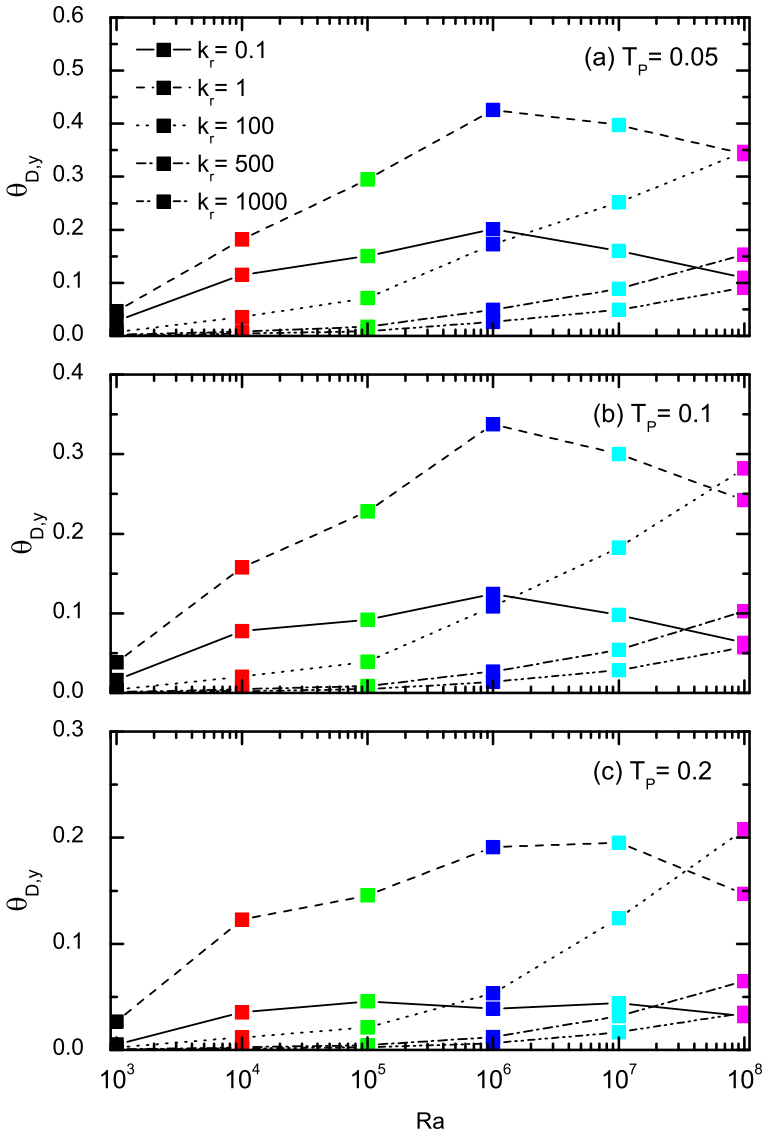

Figure 5.60: Vertical temperature drop at the middle of partition of the case $X_p = 0.25$ for different values of Ra (10^3, 10^4, 10^5, 10^6, 10^7 and 10^8), k_r (0.1, 1, 100, 500 and 1000) and T_p (0.05, 0.1, and 0.2).

The cases of $k_r = 1$ show the highest $\theta_{D,y}$ for $10^3 \leq Ra \leq 10^7$. At $Ra = 10^8$, $\theta_{D,y}$ of the case $k_r = 1$ is affected by the partition thickness and as T_p increases the value of $\theta_{D,y}$ decreases,

even to less than the case of $k_r = 100$ (*i.e.*, figure 5.60(c)).

The second type of graphs includes the cases of $\theta_{D,y}$ with high k_r ($100 \leq k_r \leq 1000$) and shows gradual and steady increase in $\theta_{D,y}$ as Ra increase. As k_r and T_p increases the value of $\theta_{D,y}$ reduces.

5.4 Empirical correlations for the average Nusselt number

A number of empirical correlations were developed for the average Nusselt number in a partitioned cavity with air as working fluid, as reported in previous studies. By assuming an isothermal partition, Duxbury [299] proposed the following correlation for a partitioned cavity,

$$Nu_{Ave} = 0.339A^{-0.25}Ra^{0.25}(N+1)^{-1.25}, \tag{5.6}$$

where N is the number of partitions inside the cavity and $A = H/L$ is the aspect ratio of the cavity. A similar correlation was proposed by Nishimura *et al.* [270], as shown below, but by assuming a thin partition,

$$Nu_{Ave} = 0.297A^{-0.25}Ra^{0.25}(N+1)^{-1} \quad \text{for} \quad A \geq 1, \tag{5.7}$$

while Cuckovic-Dzodzo *et al.* [269] gave the following correlation based on their experimental results over the range of $38000 < Ra < 369000$ but with glycerol as the working medium,

$$Nu_{Ave} = 0.201Ra^{0.276}(N+1)^{-1.4}. \tag{5.8}$$

Similarly, Anderson and Bejan [298] obtained the following correlation from their experimental and numerical study using water as the working medium,

$$Nu_{Ave} = 0.167Ra^{0.25}(N+1)^{-0.61}, \tag{5.9}$$

while more recently, Kahveci [5] developed the following correlation which incorporates the effects of some partition parameters with air as the working medium,

$$Nu_{Ave} = (0.115 + 0.006r_k - 0.023r_k^2)Ra^{0.25}X_p^{-0.044}, \tag{5.10}$$

where $r_k = k_f/k_s$ $(= 1/k_r)$ is the ratio of the thermal conductivity of fluid with respect to that of partition.

These empirical correlations are summarized in Table 5.1. It can be seen that the partition parameters have only been included in the correlation of Kahveci [5], which includes the effects of the partition position and the thermal conductivity ratio, but only considered low Rayleigh values.

Table 5.1: Characteristics of the correlations presented in some previous studies.

Study	**Parameters**	*Ra* **range**	**Assumptions**	**Fluid**
Duxbury [299]	*Ra*, *A* and *N*	less than 10^6	Isothermal partition	air
Nishimura *et al.* [270]	*Ra*, *A* and *N*	10^6 - 10^8	Thin partition	air and water
Cuckovic-Dzodzo *et al.* [269]	*Ra* and *N*	38000 - 369000	-	glycerol
Kahveci [5]	r_k, *Ra* and X_p	10^4 - 10^6	-	air
Anderson and Bejan [298]	*Ra* and *N*	10^9 - 10^{10}	-	water

With the numerically obtained results presented in figure 5.61, the following general correlation formula was selected for the curve fitting in this study,

$$Nu_{Ave} = aRa^bT_P^ck_r^dX_P^e, \tag{5.11}$$

where a, b, c, d and e are the parameters to be found which give the best correlation formula fitting. The initial curve fitting attempts showed that the X_p is a statistically insignificant parameter and including or excluding of this parameter does not have any effect on the final fitted curve. Therefore, X_p was removed from the general correlation formula. The non-linear curve fitting is obtained using the iterative procedure of the Levenberg-Marquardt algorithm [300, 301]. The following correlation shows the best fit for the numerical data for the

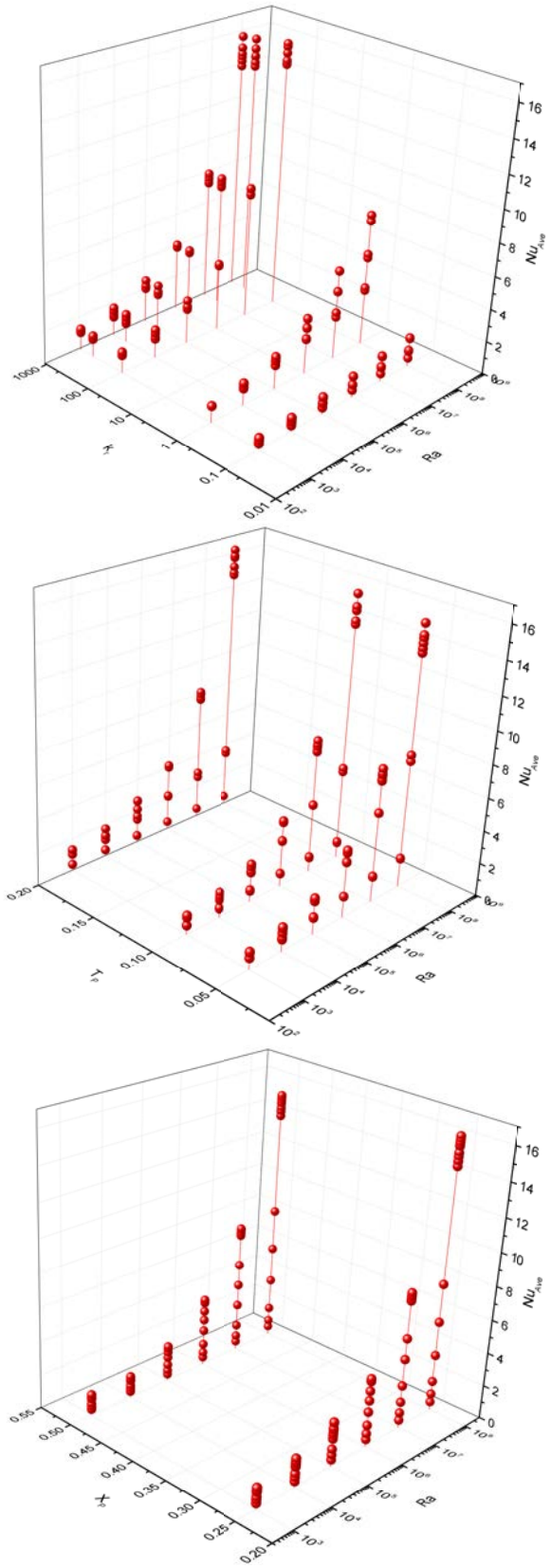

Figure 5.61: Average Nusselt number for three values of T_p ($T_p = 0.05$, 0.1, and 0.2), two values of X_p ($X_p = 0.25$ and 0.5), five values of k_r ($k_r = 0.1, 1, 100, 500$ and 1000) and six values of Ra ($Ra = 10^3, 10^4, 10^5, 10^6, 10^7$ and 10^8).

whole range of Ra studied for this work,

$$Nu_{Ave} = 0.0456 Ra^{0.2637} T_P^{-0.0054} k_r^{0.1454}, \quad \text{for } 10^3 \leq Ra \leq 10^8. \tag{5.12}$$

The presented correlation (equation (5.12)) obtained after performing 43 iterations with reduced $Chi - square$ value of 1.57 and $R - square$ value of 0.91. The comparison of the empirical correlations developed by the current study for the average Nusselt number with some other available correlations with different working fluids is depicted in figure 5.62 for the case $X_p = 0.5$, $r_k = 0.01$ (*i.e.*, $k_r = 100$), $N = 1$ and $T_p = 0.05$.

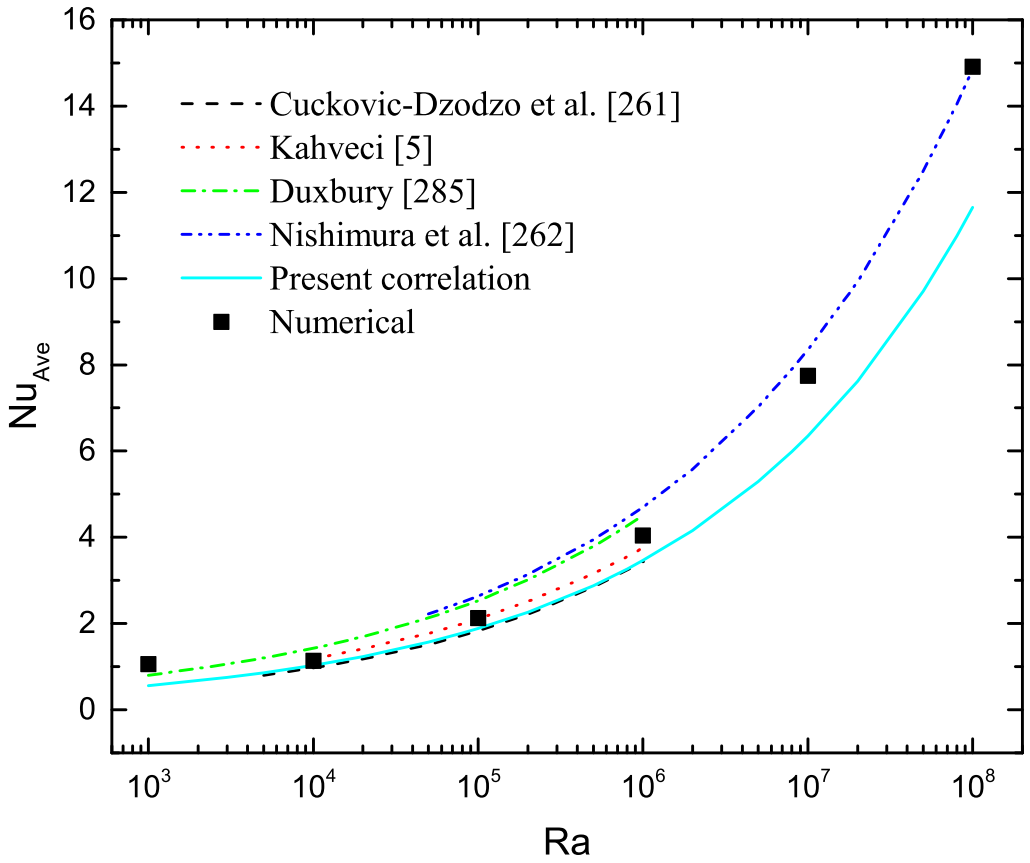

Figure 5.62: Comparison of the correlations for the average Nusselt number obtained in the current study with some others available over the Rayleigh number range considered for the case of $X_p = 0.5$, $r_k = 0.01 (i.e., k_r = 100)$, $N = 1$ and $T_p = 0.05$.

Chapter 6

Transient natural convection heat transfer in a partitioned cavity

6.1 Centrally positioned partition

The transient Nu_{Ave} at the hot wall can be characterized by four regimes, as illustrated in figure 6.1. This figure illustrates transient Nu_{Ave} at the hot wall for the case of $X_p = 0.5$,$Ra = 10^8$, $k_r = 1000$ and $T_p = 0.2$ as an example. At the conduction regime, the fluid is isothermal and motionless as the cavity undergoes the increasing temperature step and the heat transfer mode is pure conduction. At this regime, $\tau \leq 5$, the conduction heat transfer starts to establish thermal boundary layers around the sidewalls and grow with time. Nu_{Ave} reaches a local minimum value, $Nu_{Ave} = 20$, and then begins to increase up to $Nu_{Ave} = 22$ before reaching a value that is almost maintained during a quasi-steady period. At the identified local minimum Nu_{Ave}, the thermal boundary-layer thickness is the maximum and decreases when the major fluid motion begins. As expected, at the conduction regime, Nu_{Ave} at the partition is zero and convective heat transfer has not started to thermally active the partition and its temperature is still in the initial condition (*i.e.*, $\theta = 0.5$). By developing fluid motion, Nu_{Ave} increases to its quasi-steady value (*i.e.* $20 \leq Nu_{Ave} \leq 22$ at $5 \leq \tau < 11$) and thermal and viscous boundary layers are fully developed. At this regime, intrusions create a temperature difference in the

partition and gradually Nu_{Ave} of the partition increases to $Nu_{Ave} = 5$. By comparing the quasi-steady regime of the Nu_{Ave} graph for the sidewall and the partition, it can be seen that fluctuations on the partition case are much more than the sidewall one which is the indication of unsteadiness created by the striking intrusion on the partition. Interestingly, the conduction and the quasi-steady regimes show similar length for the case presented in the figure 6.1. As time elapses, the bulk temperature in the cavity significantly rises. The increasing bulk temperature causes a reduction in the temperature difference and the driving force for heat transfer, which result in decaying Nu_{Ave}. This regime takes longer period of time than the two previous introduced regimes as the stratification process is gradual and time consuming phenomenon. The decaying regime starts from $\tau = 11$ and ends at $\tau = 150$ which is about 23 time longer period than the previous regimes. While the overall temperature difference of the fluid occupied area decreases, due to the presence of pure conduction in the partition, the process of forming temperature gradient continues and penetrates more in the partition. Therefore, at the decaying regime, Nu_{Ave} of the partition shows an increasing trend. Some fluctuations still can be observed in this regime for the partition which gradually decay by increasing Nu_{Ave} and intensifying the stratification process. Both Nu_{Ave} graphs of the sidewall and the partition at the end of decaying regime reach the same value of $Nu_{Ave} \approx 14$. The final regime is steady-state where the value of Nu_{Ave} reaches a constant value after the decaying regime of the hot wall and increasing trend at the partition. Therefore, the four distinct regimes of Nu_{Ave} at the hot wall are conduction, quasi-steady, decaying and steady-state.

As the total rate of heat transfer across the cavity is of significant importance for numerous industrial applications, the transient responses of the average Nusselt number at the heated sidewall and the left side of the partition ($x = X_p - 0.5T_p$) of the case $X_p = 0.5$ for different values of Ra (10^3, 10^4, 10^5, 10^6, 10^7 and 10^8), k_r (0.1, 1, 100, 500 and 1000) and T_p (0.05, 0.1, and 0.2) are illustrated in figure 6.2. Nu_{Ave} value of the hot wall is large at the beginning of the process due to high temperature gradients near the isothermal hot wall (*i.e.*, the conduction regime). This value decreases and reaches the quasi-steady value. Higher Ra values have more distinct regimes than lower Ra cases in which the difference between Nu_{Ave} of different regimes are smaller and consequently, there is a smoother transition between regimes. Nu_{Ave} for the

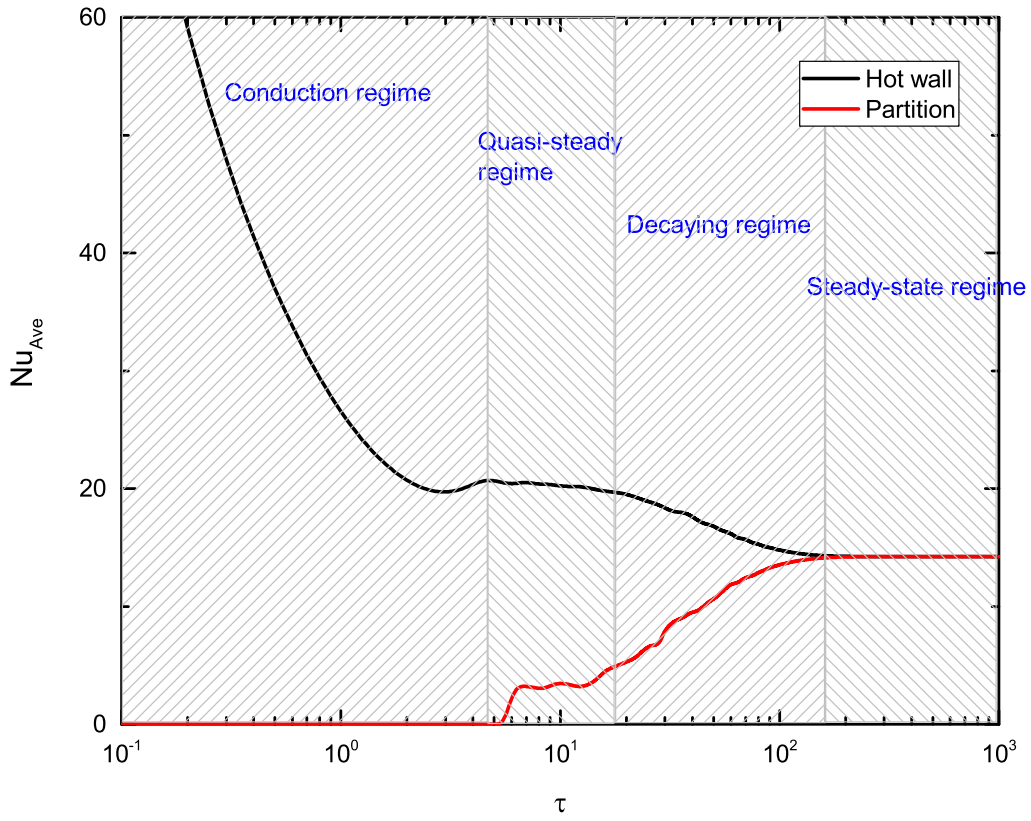

Figure 6.1: Regimes of transient Nu_{Ave} at the hot wall for the case of $X_p = 0.5$,$Ra = 10^8$, $k_r = 1000$ and $T_p = 0.2$.

partition is zero for all cases at the early stages (*i.e.*, the conduction regime) and gradually increases by reaching intrusion to the partition in the cavity (*i.e.*, the quasi-steady regime) and this increasing trend continues until the steady-state where Nu_{Ave} of the side wall and the partition becomes equal. All higher Ra value cases have larger Nu_{Ave} than the lower Ra cases and the time to reach the steady-state increases as Ra increases.

Nu_{Ave} of the hot wall for all cases of T_p are equal at the conduction regime. Over the quasi-steady regime, as partition becomes thermally active, the effect of T_p intensifies and it is observed that Nu_{Ave} curves of each T_p gradually change. As k_r increases Nu_{Ave} increases. As observed earlier, the effect of T_p on Nu_{Ave} for low and high k_r is different. For $k_r \leq 1$, T_p has a decreasing effect on Nu_{Ave} and for $1 < k_r$, rising T_p causes an increase in Nu_{Ave}.

Typical temperature contours at different time steps ranging from $\tau = 3$ to $\tau = 550$ are shown in figures 6.3 and 6.4 for the case of $k_r = 0.1$ and 1000, $T_p = 0.1$, $Ra = 10^8$ and $X_p = 0.5$. Initially, the fluid in the cavity is at a uniform temperature (*i.e.*, $\theta = 0.5$) and motionless (*i.e.*,

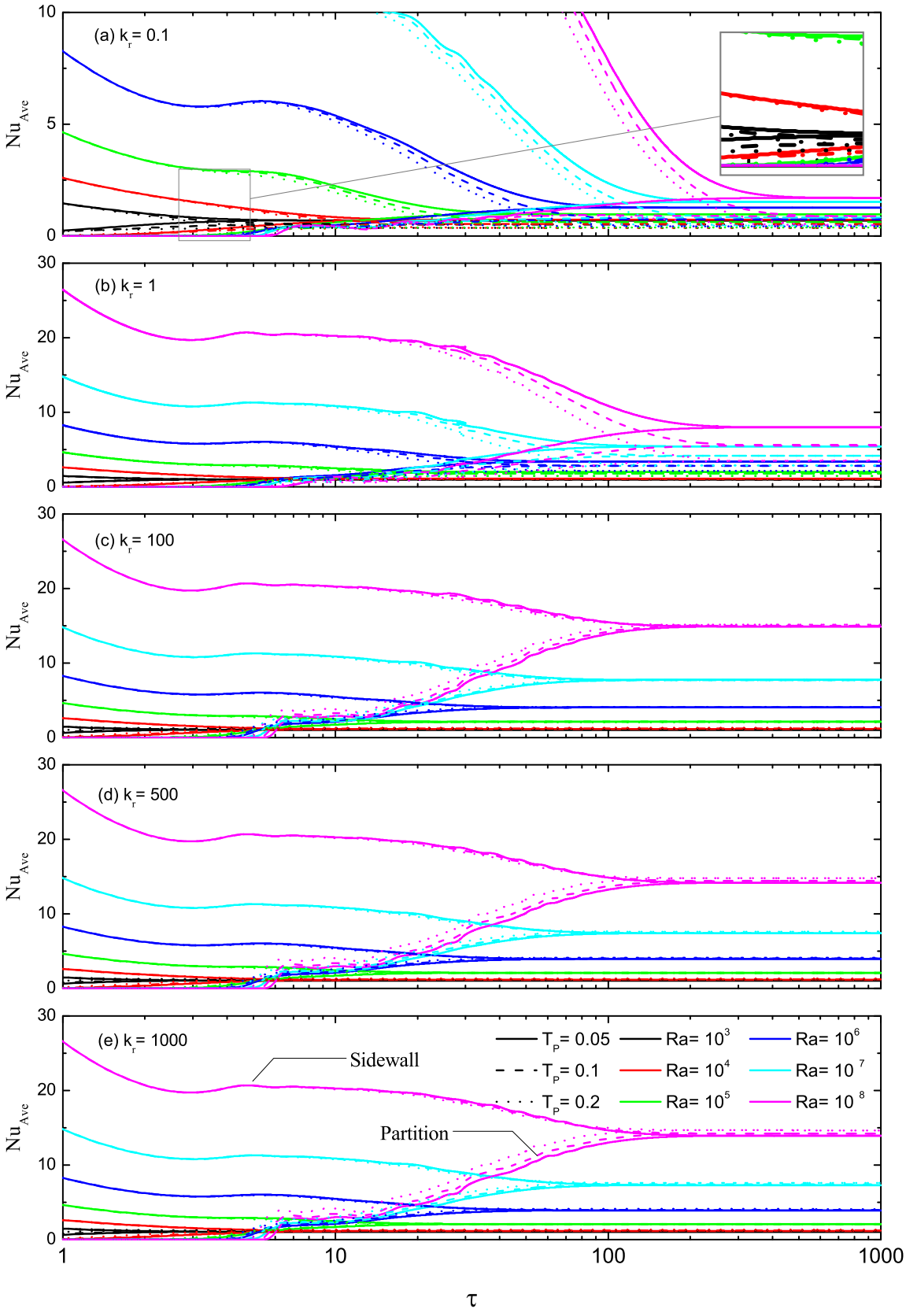

Figure 6.2: Time series of average Nusselt number on the hot sidewall and the partition ($x = X_p - 0.5T_p$) of the case $X_p = 0.5$ for different values of Ra (10^3, 10^4, 10^5, 10^6, 10^7 and 10^8), k_r (0.1, 1, 100, 500 and 1000) and T_p (0.05, 0.1, and 0.2).

$u = v = 0.0$). The sidewalls are suddenly deferentially heated at $\tau \geq 0$. Consequently, a sharp temperature gradient is created in the proximity of the isothermal sidewalls. The fluid in the central region of each half-cavity and the partition are still at the initial uniform temperature. Therefore, due to the initial development, the fluid close to the left/right sidewall starts to heat up/cool down. For $\tau = 3$ (*i.e.*, the conduction regime), the isotherms are mainly adjacent to sidewalls and at the tailing edge, the heated/cooled intrusion forms and starts to move horizontally due to the presence of the top adiabatic wall and the remaining portion of the fluid inside the half-cavities is stagnant. As the fluid moves horizontally, a horizontal boundary layer is established. Further increasing to $\tau = 5$ (*i.e.*, the quasi-steady regime) the intrusion develops more and reaches to the vicinity of the partition. There is not any difference between temperature contours of the cases $k_r = 0.1$ and 1000 as the partition is not completely active and does not have any influence on the heat transfer in the cavity up to this stage. When $\tau = 8$ (*i.e.*, quasi-steady regime), the intrusion reaches the partition and it is reflected back toward the half-cavity center. Temperature contours of the cases $k_r = 0.1$ and 1000 are different at this time. Due to the presence of the partition, the heated intrusion in the left half-cavity flows downward along the partition and the cooled intrusion in the right half-cavity moves upward attached to the right side of the partition. At the end of the quasi-steady period, the bulk temperature in the cavity is beginning to rise significantly. The local temperature difference across the half-cavity is beginning to decrease from the top down. The reduction in the driving force coincides with the start of heat transfer to decay at the hot wall. Owing to the intensified convective motions, the temperature field in the cores of both half-cavities begins to be stratified. The effect of thermal conductivity of the partition is clearer as time passes. For instance, at $\tau = 70$ (*i.e.*, decaying regime) for the case with low thermal conductivity partition (*i.e.*, $k_r = 0.1$), isotherms in the partition are almost vertical showing high thermal resistance of the partition which leads to trapping all the heated and cooled fluids on the left and right half-cavities and can be seen in figure 6.3(h). As a result of this high thermal resistance, the main temperature gradient happens in the partition area and this character can be identified by the presence of the majority of isotherms in the partition. On the other hand, the cavity with high thermal conductivity partition (*i.e.*, $k_r = 1000$) shows almost horizontal isotherms

in the partition which is a sign of low thermal resistance.

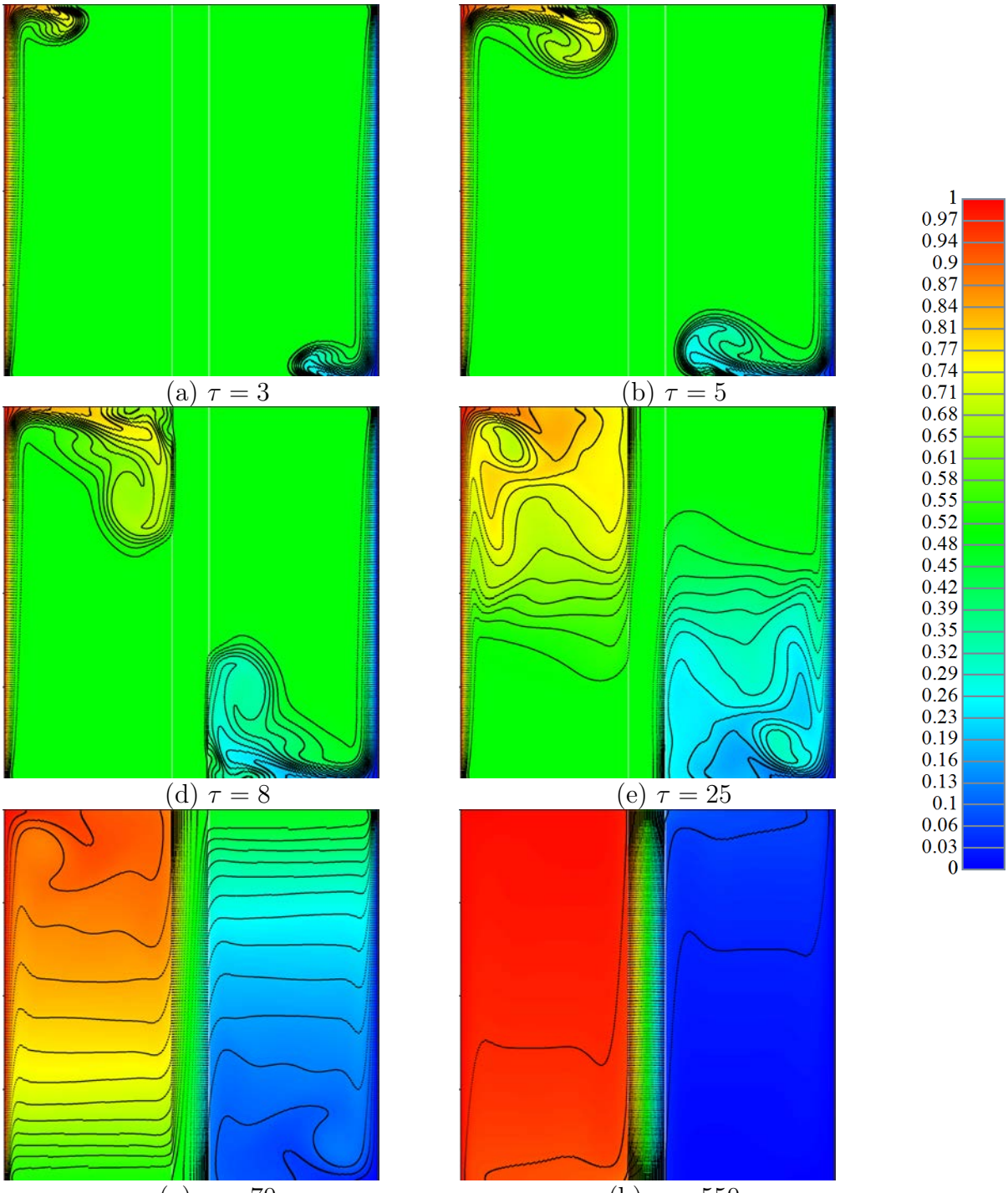

(a) $\tau = 3$ (b) $\tau = 5$

(d) $\tau = 8$ (e) $\tau = 25$

(g) $\tau = 70$ (h) $\tau = 550$

Figure 6.3: Temperature contours of the case $k_r = 0.1$, $T_p = 0.1$, $Ra = 10^8$ and $X_p = 0.5$ at different times.

The time series of θ of the case $X_p = 0.5$ at $x = 0.05$ and $y = 0.5$ for different values of Ra (10^3, 10^4, 10^5, 10^6, 10^7 and 10^8), k_r (0.1, 1, 100, 500 and 1000) and T_p (0.05, 0.1, and 0.2) are illustrated in figure 6.5. It can be seen that low Ra cases have a higher local temperature

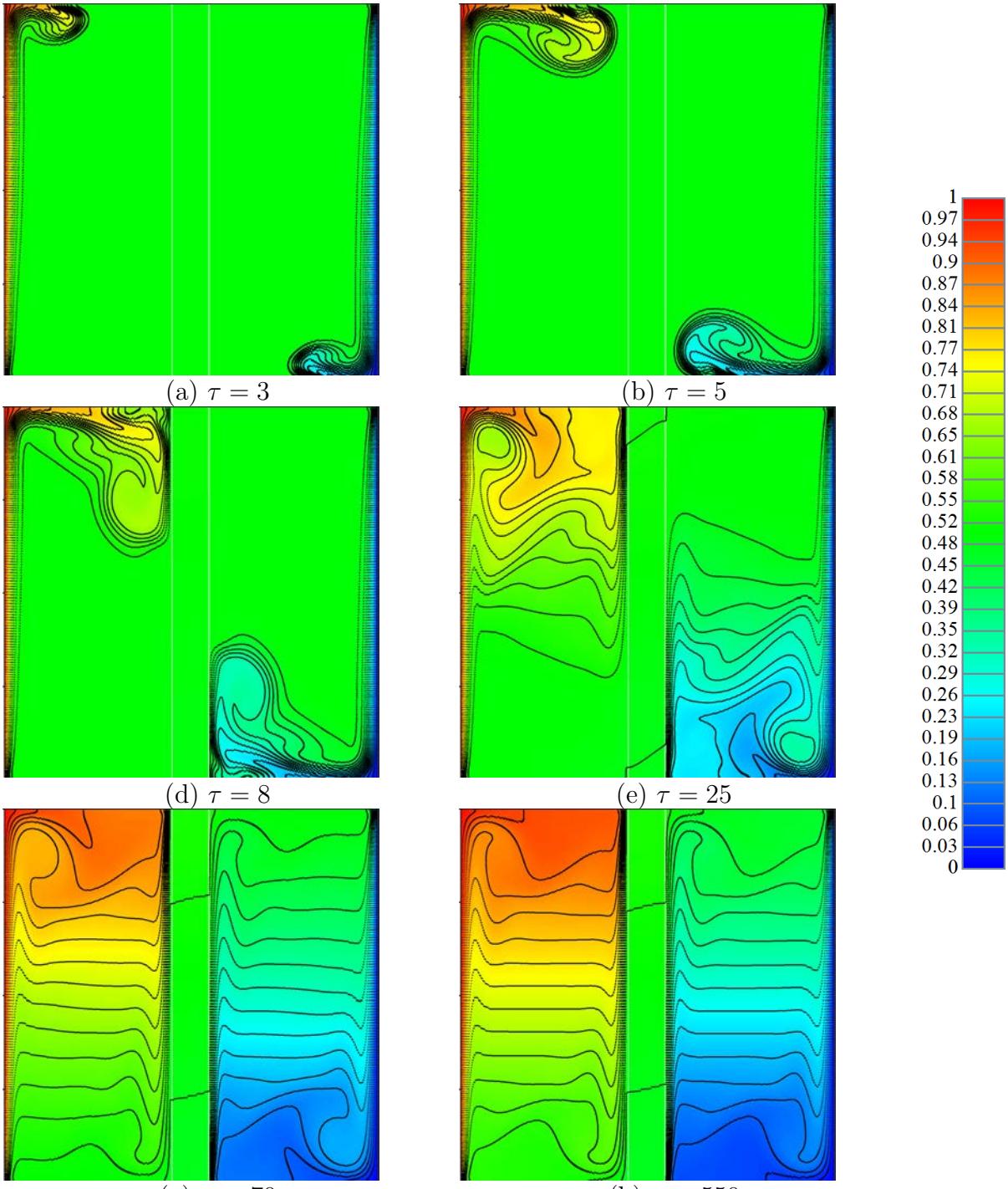

(a) $\tau = 3$ (b) $\tau = 5$

(d) $\tau = 8$ (e) $\tau = 25$

(g) $\tau = 70$ (h) $\tau = 550$

Figure 6.4: Temperature contours of the case $k_r = 1000$, $T_p = 0.1$, $Ra = 10^8$ and $X_p = 0.5$ at different times.

at the selected point than high Ra cases which have thinner thermal boundary layers at the walls. Therefore, the temperature difference is mainly applied by the stratified fluid in the half-cavity rather than the sidewall boundary layers and consequently; longer time is necessary to form the thermal stratification in the half-cavities. By increasing Ra to 10^7 and 10^8, the time

series of temperature show fluctuations which gradually decay as reaching the steady state. Interestingly, the characterized regimes for Nu_{Ave} can be justified as in the case presented in figure 6.1. For instance, the cavity bulk temperature only begins to rise significantly at the end of the quasi-steady period and continues to increase during the decay period. For $k_r \leq 1$, increasing T_p increases the local temperature and for $1 < k_r$, increasing T_p causes a reduction in the temperature value and this T_p effect starts at the quasi-steady regime.

Some assumptions, like constant partition temperature (*e.g.*, [29,30]), constant heat flux (*e.g.*, [31]), and a power-law temperature distribution (*e.g.*, [32]), can help to overcome the difficulty of this problem. To investigate the constant partition temperature assumption (lumped conduction analysis), the horizontal temperature drop parameter ($\theta_{D,x}$) is defined as the temperature difference between the left and right side of the partition. Time series of $\theta_{D,x}$ at $y = 0.5$ of the case $X_p = 0.5$ for different values of Ra (10^3, 10^4, 10^5, 10^6, 10^7 and 10^8), k_r (0.1, 1, 100, 500 and 1000) and T_p (0.05, 0.1, and 0.2) are illustrated in figure 6.6. This figure shows that the time parameter is an important variable for $\theta_{D,x}$ as in spite of steady-state values, at some stages, horizontal temperature drop of higher Ra values are lower than the lower Ra cases (*e.g.*, figure 6.6, $\tau = 30$). The transient $\theta_{D,x}$ graph mainly shows an increasing trend in all Ra cases and the maximum $\theta_{D,x}$ is the steady-state value. Increasing Ra increases $\theta_{D,x}$ of the same partition thickness. Partition thickness has a considerable effect on $\theta_{D,x}$ as a thicker partition shows higher $\theta_{D,x}$ for all cases of Ra and k_r values. The effect of T_p on $\theta_{D,x}$ can be seen in figure 6.6(e) as $\theta_{D,x}$ of $Ra = 10^7$ and $T_p = 0.2$ is higher than that of the case of $Ra = 10^8$ and $T_p = 0.1$. k_r also has a significant effect on $\theta_{D,x}$. For the case $k_r = 0.1$, the overall steady-state value of $\theta_{D,x}$ is between 0.3 and 0.9. At $k_r = 1$, the $\theta_{D,x}$ range decreases to $0.05 - 0.7$ and beyond $k_r = 1$, this range decreases to $0 - 0.03$, $0 - 0.005$ and $0 - 0.0022$ for $k_r = 100$, $k_r = 500$ and $k_r = 1000$, respectively. Therefore, increasing k_r dramatically reduces $\theta_{D,x}$.

To get more insights into the transient heat transfer behavior inside the partition wall, the total vertical temperature drop, $\theta_{D,y}$, is introduced, which is defined as the temperature difference between the top and bottom of the partition wall at a specific horizontal location (x) within the partition wall. The time series of $\theta_{D,y}$ at the middle of the partition wall (*i.e.*, at $x = 0.5$) are presented in figure 6.7 for different Ra, k_r and T_p values.

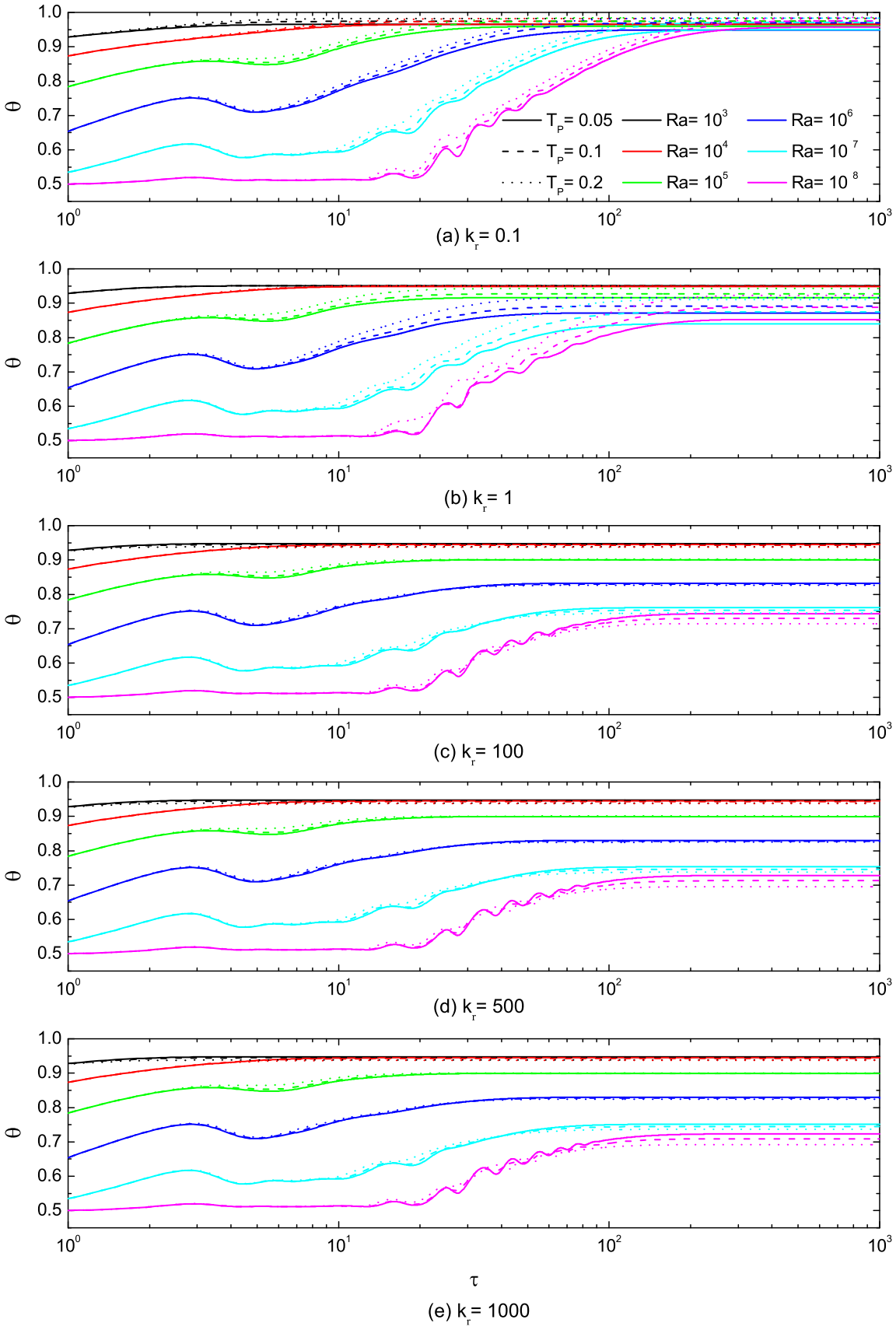

Figure 6.5: Time series of θ of the case $X_p = 0.5$ at $x = 0.05$ and $y = 0.5$ for different values of Ra (10^3, 10^4, 10^5, 10^6, 10^7 and 10^8), k_r (0.1, 1, 100, 500 and 1000) and T_p (0.05, 0.1, and 0.2).

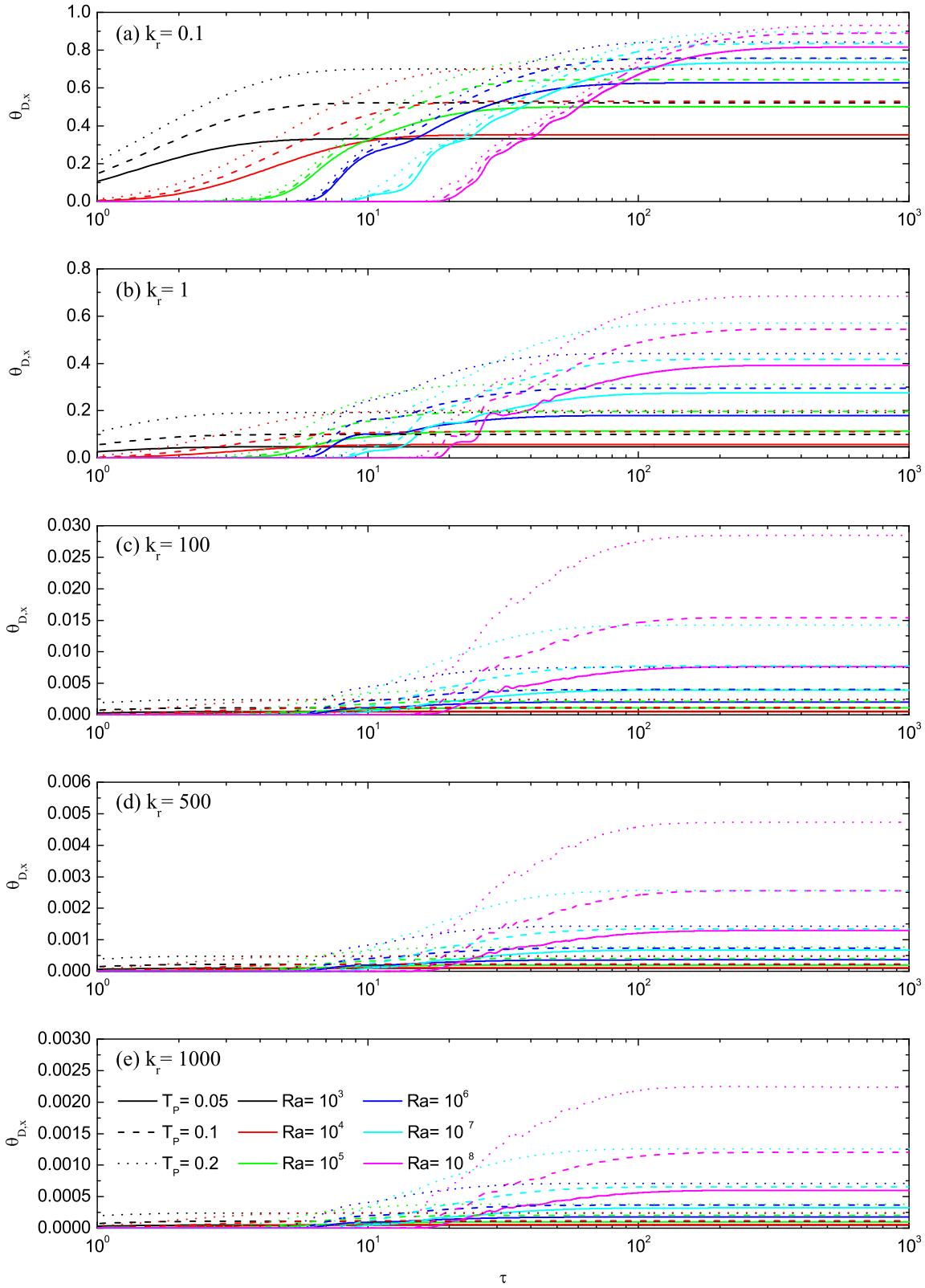

Figure 6.6: Time series of $\theta_{D,x}$ at $y = 0.5$ of the case $X_p = 0.5$ for different values of Ra (10^3, 10^4, 10^5, 10^6, 10^7 and 10^8), k_r (0.1, 1, 100, 500 and 1000) and T_p (0.05, 0.1, and 0.2).

It is seen that $\theta_{D,y}$ at $Ra = 10^3$ is much lower than the initial temperature difference between the two cavity sidewalls as well as than those at other Ra values, demonstrating the essentially pure conduction heat transfer nature of this case.

For other Ra values, the $\theta_{D,y}$ curves are highly k_r dependent. For $k_r = 0.1$, for all Ra cases (except $Ra = 10^3$), $\theta_{D,y}$ increases until attains the maximum value and then decreases to reach a constant steady-state value. The lower the Ra value, the earlier the maximum value and steady-state value can be reached.

For $k_r = 1$, for low Ra values (no more than 10^6), $\theta_{D,y}$ has a steady and smooth increase from the initial value of $\theta_{D,y} = 0$ to a constant value at the steady state, which increases monotonically with Ra, and the rate of increase increases substantially when Ra increases. When Ra is beyond 10^6, there are fluctuations present throughout the time series, which are apparently caused by traveling waves. For these high Ra cases, $\theta_{D,y}$ increases until it attains a maximum value, but gradually decreases subsequently, before it reaches a constant steady-state value, which decreases with Ra.

For $k_r > 1$, $\theta_{D,y}$ has a steady and smooth increase from the initial value of $\theta_{D,y} = 0$ to a constant value at the steady state, which increases monotonically with Ra, and the rate of increase increases substantially when Ra increases.

To investigate further the flow properties in a partitioned cavity, the position of u_{max} at the top half of the left half-cavity ($0 \leq x \leq X_p$ and $0.5 \leq y \leq 1$) and v_{max} at the left half of the left half-cavity ($0 \leq x \leq 0.25$ and $0 \leq y \leq 1$) by passing time for different values of Ra (10^3, 10^4, 10^5, 10^6, 10^7 and 10^8), k_r (0.1, 1, 100, 500 and 1000) and T_p (0.05, 0.1, and 0.2) are illustrated in figure 6.8. The sweeping direction to find position is from the left to the right and from the bottom to the top. Therefore, the corresponding position of an area with the maximum amount will be the first swept position from the left and the bottom. In all cases, the position of u_{max} in the cavity moves from the vicinity of the left corner in the left half-cavity towards the partition sloping inward. As Ra increases the position of u_{max} becomes closer to the top wall and their slopes become closer to the horizontal line. When the cavity approximately reaches the steady state, it can be seen more repeated points around the steady region.

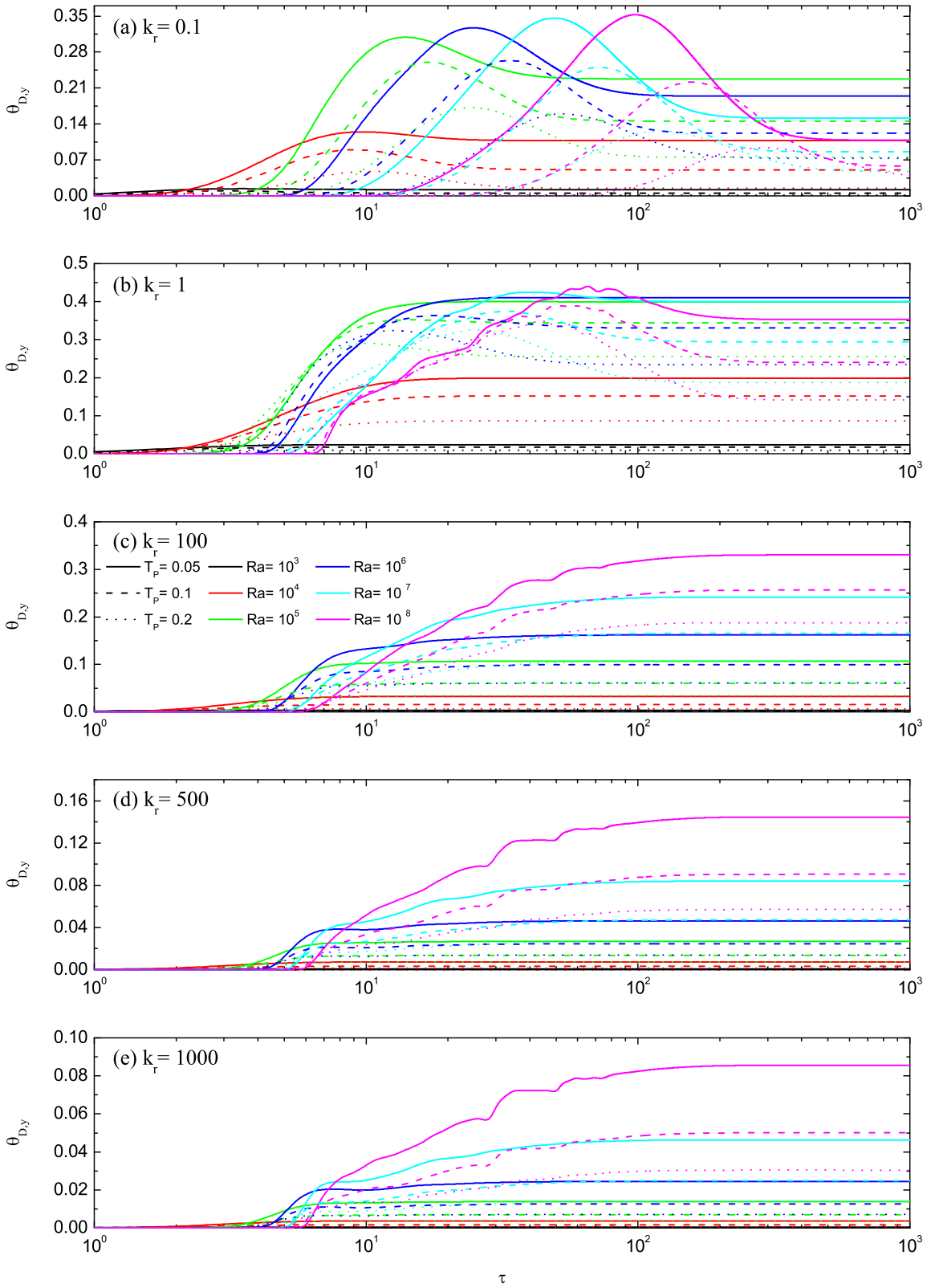

Figure 6.7: Time series of $\theta_{D,y}$ of the case $X_p = 0.5$ for different values of Ra (10^3, 10^4, 10^5, 10^6, 10^7 and 10^8), k_r (0.1, 1, 100, 500 and 1000) and T_p (0.05, 0.1, and 0.2).

For the v_{max} cases (*i.e.*, figure 6.8(b), (d), (f), (h) and (j)), low Ra cases (*i.e.*, $Ra = 10^3$ and 10^4) show almost straight lines from the left side to the right side. However, as Ra value increases (*i.e.*, $Ra > 10^4$), the position of v_{max} gradually rises from the mid-height towards the top wall and then sharply moves downward. The lower Ra is, the farther the position of v_{max} moves from the left sidewall. The initial rise of the position of v_{max} is sharper and higher as Ra increases. Therefore, the steady-state position for v_{max} is closer to the left sidewall for the high Ra values than the low cases. T_p and k_r do not show a significant effect on the position of u_{max} and v_{max}.

The position of the maximum stream function at the left half-cavity by passing time for different values of Ra (10^3, 10^4, 10^5, 10^6, 10^7 and 10^8), k_r (0.1, 1, 100, 500 and 1000) and T_p (0.05, 0.1, and 0.2) is presented in figure 6.9. For $Ra = 10^3$, the position of the maximum stream function starts at the mid-height and moves to the centre of the half-cavity. The distribution of those points is an almost horizontal line like. As Ra increases, the trace of the maximum stream function shows a gradual upward and then downward move trend. Higher Ra values have sharper upward movements and gradually the position becomes closer to the top wall. The trace of the maximum stream function for different T_p is identical, especially at early stages; however, as time passes, the difference between those graphs enlarges.

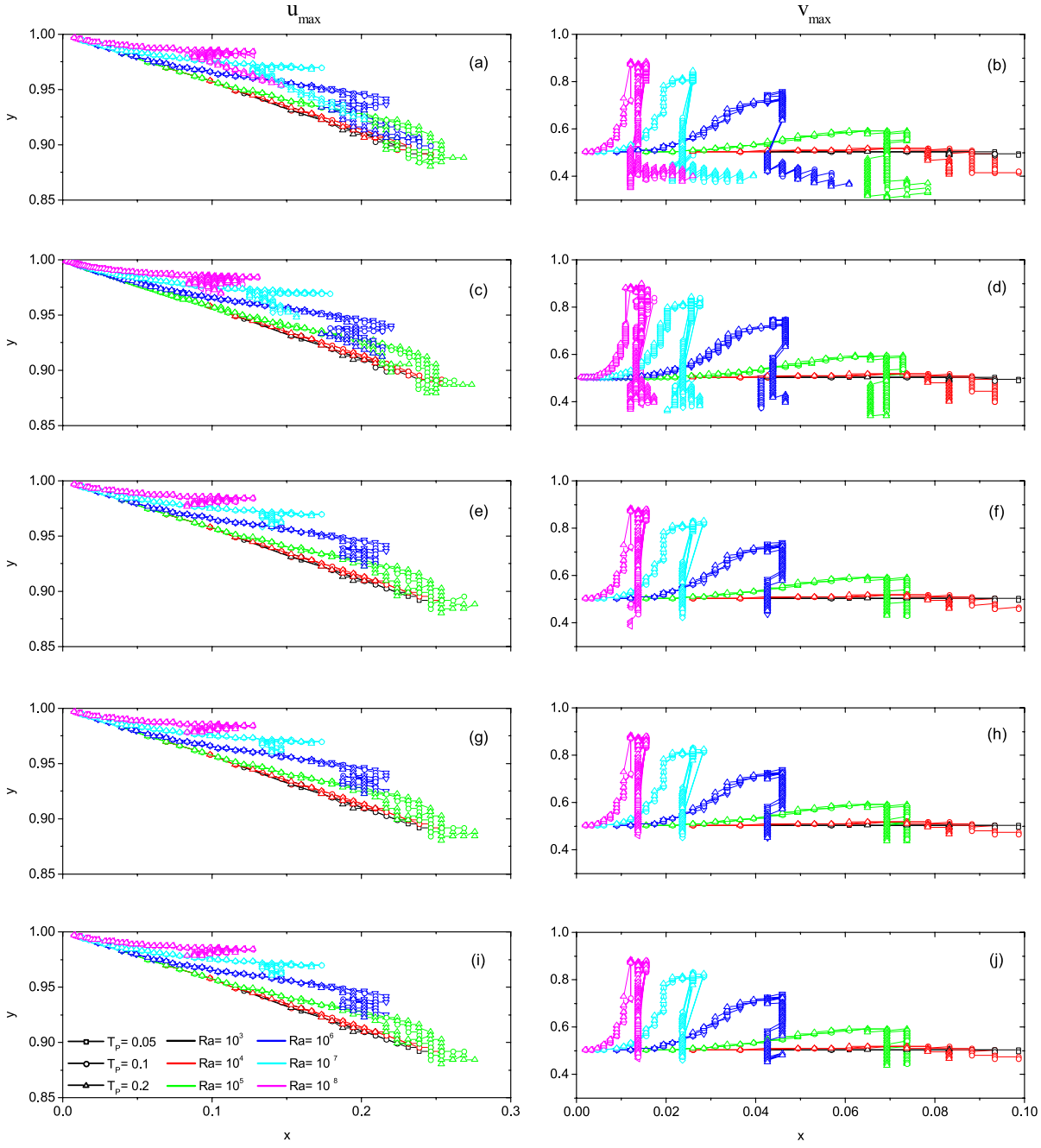

Figure 6.8: Position of u_{max} at the top half of the left half-cavity ($0 \leq x \leq X_p$ and $0.5 \leq y \leq 1$) and v_{max} at the left half of the left half-cavity ($0 \leq x \leq 0.25$ and $0 \leq y \leq 1$) by passing time for different values of Ra (10^3, 10^4, 10^5, 10^6, 10^7 and 10^8), k_r ($0.1(a,b)$, $1(c,d)$, $100(e,f)$, $500(g,h)$ and $1000(i,j)$) and T_p (0.05, 0.1, and 0.2).

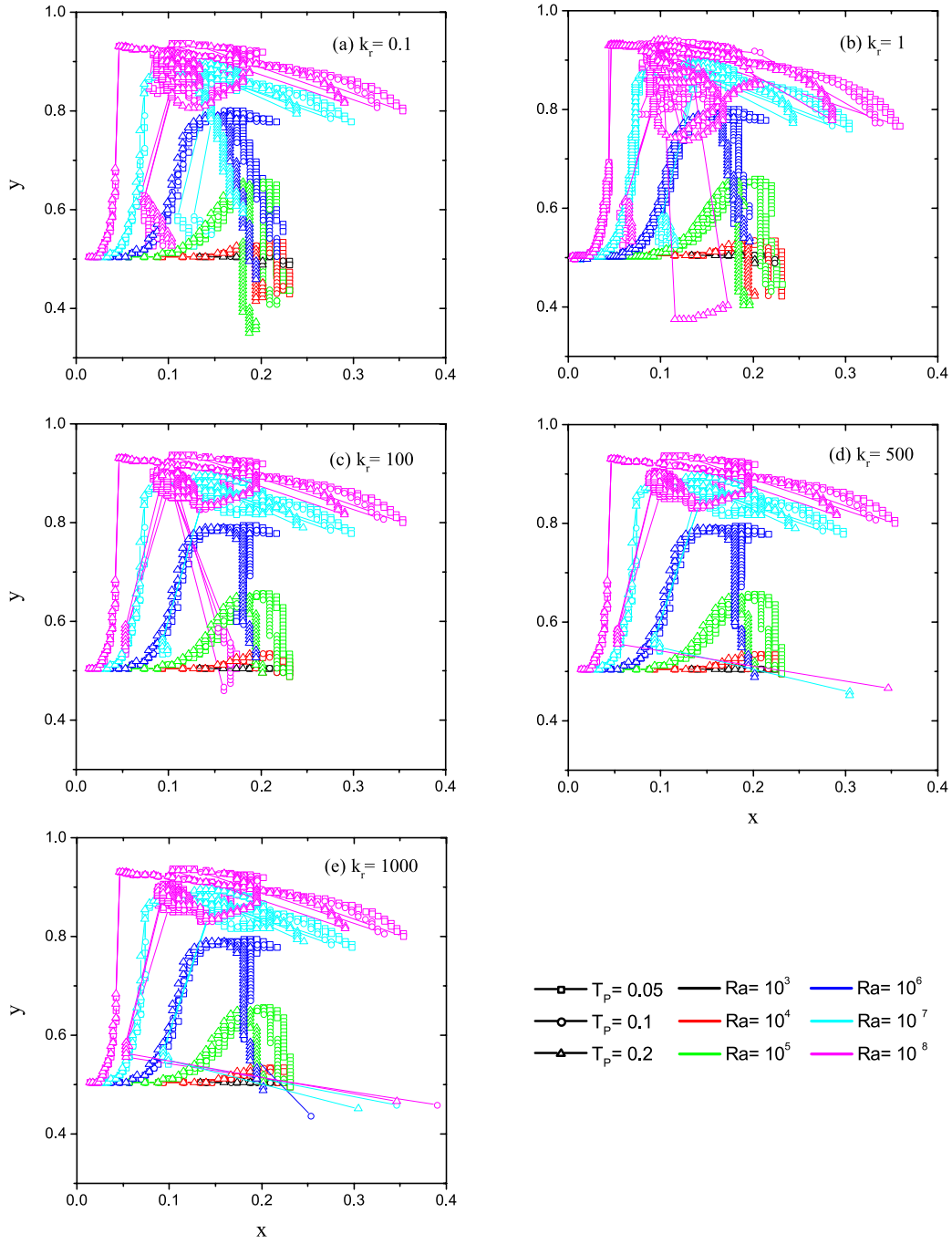

Figure 6.9: Position of the maximum stream function at the left half-cavity by passing time for different values of Ra (10^3, 10^4, 10^5, 10^6, 10^7 and 10^8), k_r (0.1, 1, 100, 500 and 1000) and T_p (0.05, 0.1, and 0.2).

6.2 Off-centre partition

The main regimes of transient Nu_{Ave} at the hot and cold sidewalls for a cavity with an off-centre partition are illustrated in figure 6.10. The figure presents the time series of Nu_{Ave} for the case of $X_p = 0.25$, $Ra = 10^8$, $k_r = 1000$ and $T_p = 0.2$ at the hot and cold sidewalls as well as the partition which is similar to the case selected for figure 6.1. To simplify the characterized regimes, the main regimes of the cold and hot sidewalls are named in blue and red colors, respectively (*i.e.*, $R_1 - R_4$ for the cold sidewall and $R_1 - R_5$ for the hot sidewall). At the conduction regime (*i.e.*, R_1 and R_1) the fluid is isothermal and motionless as the cavity undergoes the increasing temperature step and the heat transfer mode is pure conduction. At this regime, the conduction heat transfer starts to establish thermal boundary layers around the sidewalls which grow with time. Nu_{Ave} reaches a local minimum value and then begins to increase before reaching a value that is almost maintained during a quasi-steady period. The conduction regime of the cold and hot sidewalls are identical, similar to the centrally-positioned partition case. The reason for this similarity is that during the conduction regime sidewalls are thermally active and fluid in the vicinity of the sidewalls experience temperature change and the partition (either at the center or off-centre) is inactive. Therefore, this regime duration is directly affected by the position of the partition and closer the partition is to the sidewall, shorter the conduction regime is. At the identified local minimum Nu_{Ave}, the thermal boundary-layer thickness maximum decreases when the major fluid motion begins. As expected, at the conduction regime, Nu_{Ave} at the partition is zero and convective heat transfer has not started to thermally active the partition and its temperature is still at the initial one (*i.e.*, $\theta = 0.5$). By developing fluid motion, Nu_{Ave} increases to its quasi-steady value and thermal and viscous boundary layers are fully developed (*i.e.*, R_2 and R_2). It can be seen that the quasi-steady regime for the sidewall next to the wider half-cavity (*i.e.*, cold sidewall) is much longer than the other sidewall. This observation is expected as thermal and viscous boundary layers develop much faster at the thinner half-cavity (*i.e.*, left half-cavity) than the wider one (*i.e.*, right half-cavity).

Intrusions create a temperature difference on the partition and gradually Nu_{Ave} of the partition increases. As time passes, the bulk temperature in the cavity significantly rises. The increasing bulk temperature causes a reduction in the temperature difference and the driving force for heat transfer, which results in decaying Nu_{Ave}. The decaying regime for the hot sidewall (*i.e.*, R_3) starts earlier than the cold sidewall after a short quasi-steady regime (*i.e.*, R_2). While the overall temperature difference of the fluid occupied area decreases, due to the presence of pure conduction in the partition, the process of forming a temperature gradient continues and penetrates more in the partition. The stratification and filling process in the left half-cavity progress to a point that the temperature gradient of the partition and the left sidewall becomes equal and is directly affected by the hot isothermal wall. Consequently, a regime of identical Nu_{Ave} is identified after the decaying regime for the hot sidewall case (*i.e.*, R_4). This regime is called the filling regime. The final regime is the steady state (*i.e.*, R_4 and R_5) at which the value of Nu_{Ave} reaches a constant value after the decaying regime of the cold wall and increasing trend at the partition and the hot sidewall. Therefore, the five distinct regimes of Nu_{Ave} at the hot sidewall are conduction, quasi-steady, decaying, filling and steady state while the cold sidewall showed four regimes of conduction, quasi-steady, decaying and steady-state.

For observing quantitatively natural convection flows and to describe heat transfer through the cavity, the average Nusselt number at the heated and cooled sidewalls and the left side of the partition ($x = X_p - 0.5T_p$) of the case $X_p = 0.25$ for different values of Ra (10^3, 10^4, 10^5, 10^6, 10^7 and 10^8), k_r (0.1, 1, 100, 500 and 1000) and T_p (0.05, 0.1, and 0.2) is illustrated in figures 6.11-6.13.

As presented in figure 6.10, the general trend for the time series of the average Nusselt number starts with the conduction regime. By increasing Ra, the duration of this regime increases. The end of this regime also can be identified by the initiation of Nu_{Ave} of the partition. The value of Nu_{Ave} decreases to reach the quasi-steady regime (*i.e.*, R_2). Higher Ra cases show longer quasi-steady regimes and comparing the line in the cold and hot sidewalls shows that this regime at the hot sidewall is very short. The duration of the quasi-steady regime in the case of $Ra = 10^8$, $T_p = 0.05$ and $k_r = 100$ of the hot and cold sidewalls are $\tau = 1$ and $\tau = 7$, respectively. The quasi-steady regime ends with starting the decaying regime (*i.e.*, R_3 or R_3).

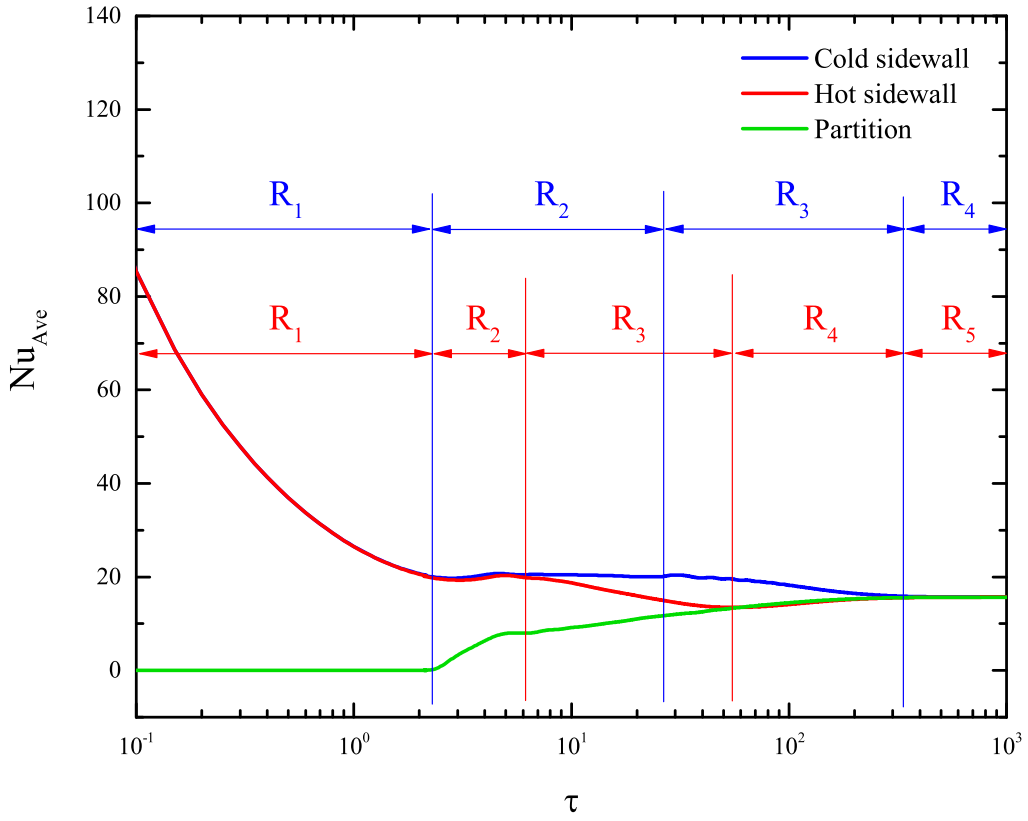

Figure 6.10: Regimes of transient Nu_{Ave} at the hot and cold sidewalls for the case $X_p = 0.25$,$Ra = 10^8$, $k_r = 1000$ and $T_p = 0.2$.

For the cold sidewall, Nu_{Ave} gradually falls during this period till reaching the steady-state (*i.e.*, R_4). Similar to the centrally-positioned partitioned case, the line for the cold sidewall shows some oscillations at high Ra values which gradually damp as reaching the steady-state. On the other hand, the line for the hot sidewall is smooth or the fluctuations are trivial. The decreasing trends of Nu_{Ave} at the decaying regime for the hot and cold sidewalls are different. For all cases investigated, decreasing rate of this regime at the hot sidewall is higher than that at the cold sidewall. This sharp decrease at the hot sidewall necessitates an extra regime (*i.e.*, R_4) at which Nu_{Ave} increases to reach the steady-state value (*i.e.*, R_5). Higher Ra values have more distinct regimes than lower Ra cases at which the difference between Nu_{Ave} of different regimes are smaller and consequently, have a smoother transition between regimes.

Nu_{Ave} of the hot sidewall for all cases of T_p are equal at the conduction regime. Over the quasi-steady regime, as the partition becomes thermally active, the effect of T_p intensifies and it can be observed that Nu_{Ave} curves of each T_p gradually changes. As k_r increases Nu_{Ave} increases. Increasing k_r also weakens the fluctuations of decaying regimes as can be seen by

comparing figures 6.11(b) and (e). As observed earlier, the effects of T_p on Nu_{Ave} for low and high k_r are different. For $k_r \leq 1$, T_p has decreasing effect on Nu_{Ave} and for $1 < k_r$, rising T_p causes increase in Nu_{Ave}.

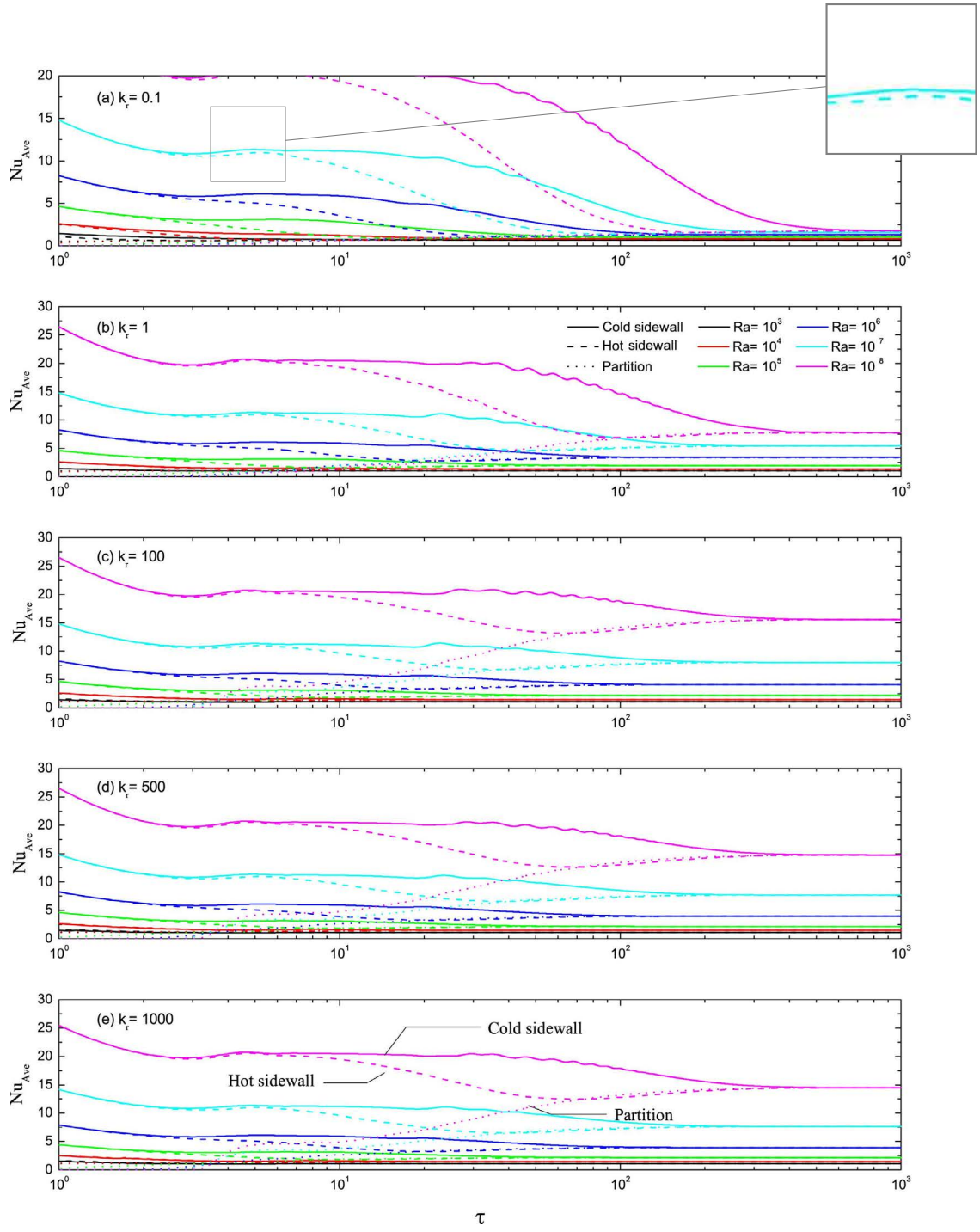

Figure 6.11: Time series of the average Nusselt number on the cold and hot sidewalls and the partition ($x = X_p - 0.5T_p$) for the case of $X_p = 0.25$ and $T_p = 0.05$ for different values of Ra (10^3, 10^4, 10^5, 10^6, 10^7 and 10^8), k_r (0.1, 1, 100, 500 and 1000).

To provide a direct perception of the transient evolving process of the conjugate natural con-

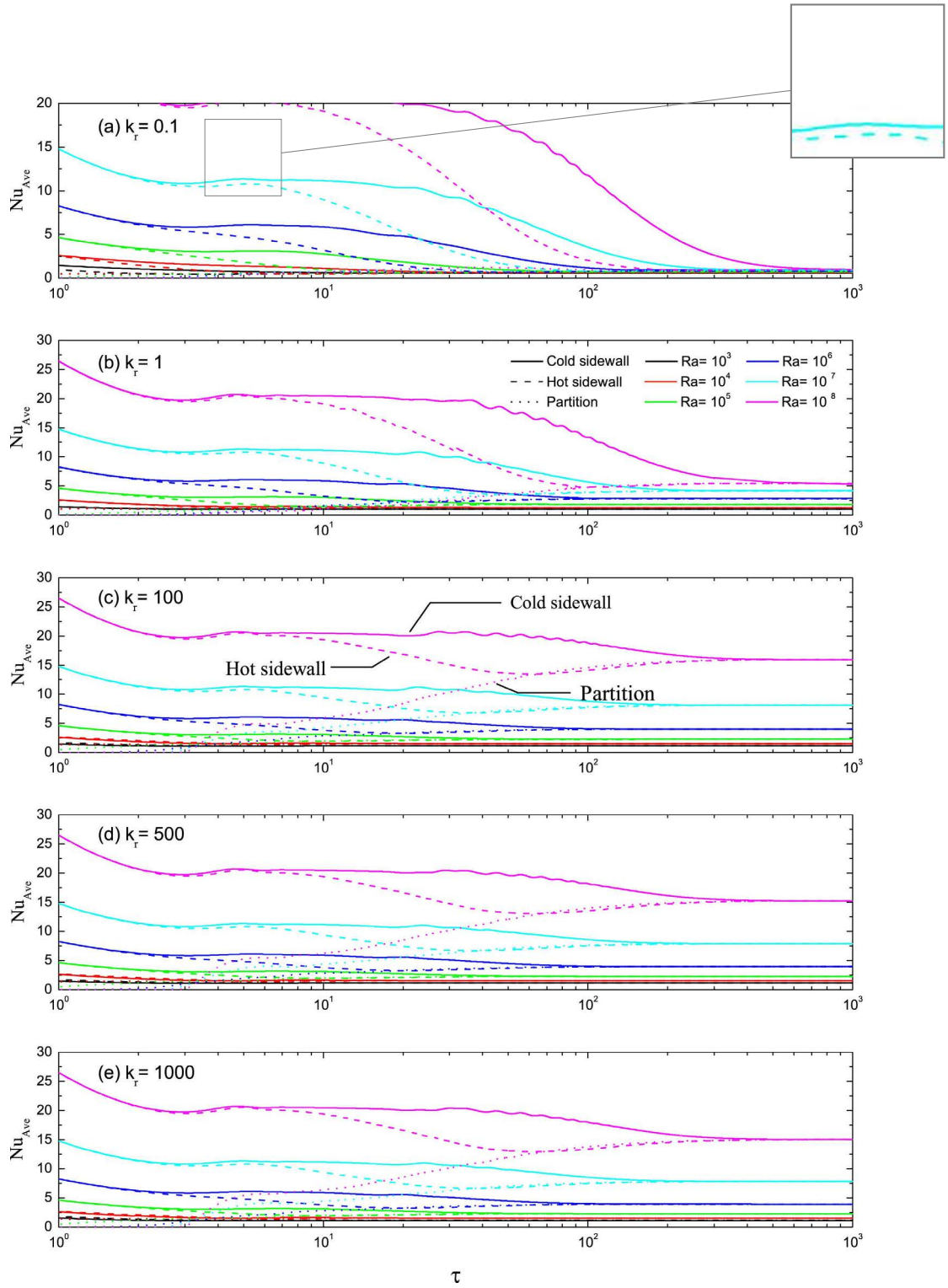

Figure 6.12: Time series of the average Nusselt number on the cold and hot sidewalls and the partition ($x = X_p - 0.5T_p$) for the case of $X_p = 0.25$ and $T_p = 0.1$ for different values of Ra (10^3, 10^4, 10^5, 10^6, 10^7 and 10^8), k_r (0.1, 1, 100, 500 and 1000).

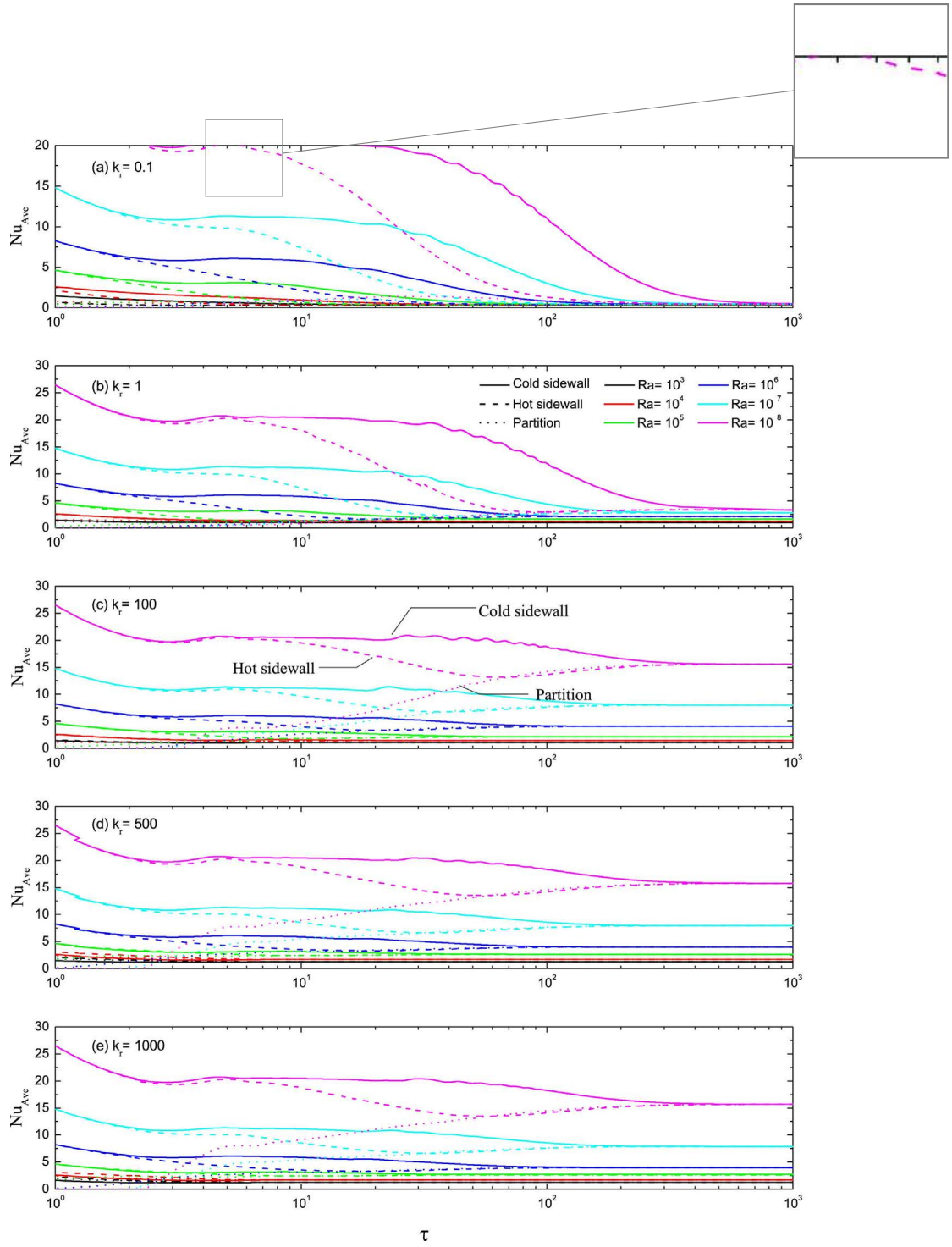

Figure 6.13: Time series of the average Nusselt number on the cold and hot sidewalls and the partition ($x = X_p - 0.5T_p$) for the case of $X_p = 0.25$ and $T_p = 0.2$ for different values of Ra (10^3, 10^4, 10^5, 10^6, 10^7 and 10^8), k_r (0.1, 1, 100, 500 and 1000).

vection flow, the snapshot of the transient temperature contours for the natural convection in a cavity with an off-centre partition (*i.e.*, $X_p = 0.25$) is presented in figures 6.14 and 6.15 for the case of $T_p = 0.1$, $Ra = 10^8$, $k_r = 0.1$ and $k_r = 1000$, as a sample. These figures present the temperature contours at six different times for the left and right half of the cavity. At the initial stage, a rising natural convection boundary layer forms on the left/right side wall, discharging heated/cooled fluid as an intrusion below/above the top/bottom wall. At this time (*i.e.*, $\tau = 3$) intrusions have not reached to the partition and no difference can be seen between figure 6.14(a) and 6.15(a). The fluid in the remainder of the domain is still at the initial temperature $\theta = 0.5$. At $\tau = 5$, the heated intrusions discharged by the rising natural convection boundary layers have impinged on the partition and are in the process of filling the left half-cavity with hotter fluid. The cooled intrusions discharged by the cold sidewall are at the mid-way and have not reached to the partition. At $\tau = 8$, the cooled intrusions reach the partition and the left half-cavity is already in the filling process started from $\tau = 5$. As the partition becomes thermally active, its properties become important. It is clear that there is a substantial difference at $\tau = 25$ between figure 6.14(e) and 6.15(e). The case with a low thermal conductivity partition (*i.e.*, figure 6.14(e)) shows that the temperature difference has small penetration inside the partition while the case with high thermal conductivity partition depicts several isothermal lines completely passed across the partition and the discharge of the heated intrusion at the top-left corner of the right half-cavity is noticeable. Figure 6.15(e) shows that two natural convection phenomena on both sides of the partition have coupled through the conduction inside the partition, and though three phenomena are tightly connected to each other and any change in one of them will affect the rest of them. The boundary layers created due to this coupling, the conjugate natural convection boundary layers (CNCBLs), at the mid-height will be asymmetrical for this case as the left and right half-cavities are at different stages of the filling process which is because of the off-centre partition. As time elapses, the filling process inside both half-cavities develops further and CNCBLs covers all length of the partition. It is worth mentioning that since the temperature difference across the partition is dependent on time and position, CNCBLs are time and position dependent too. At $\tau = 70$, figure 6.14(g) shows almost vertical isotherms inside the partition which is clear indication of the high ther-

mal resistance of the partition and little temperature exchange between two half-cavities. At this stage, the left half-cavity is about 90% filled with hot fluid while the right half-cavity is about 50% filled with cold fluid. On the other hand, figure 6.15(g) shows a totally different situation. The stratification level for both half-cavities is very similar as expected which is due to the very high thermal conductivity of the partition. Finally, by passing enough time, the cavity fully develops and reaches to the steady state. The steady-state case of the cavity with $k_r = 0.1$ shows that the half-cavities are filled with intrusions and the majority of isotherms are presented inside the partition. The partition plays the role of insulation wall and the hot and cold fluids are trapped in their half-cavities. However, for the case showing in figure 6.15(h) thermal interaction between both half-cavities is very significant and the effect of the left and right half-cavities on each other is clear as for both sides stratification range starts with $\theta = 0.5$.

The time series of θ of the case $X_p = 0.25$ at $x = 0.05$ and $y = 0.5$ for different values of Ra ($10^3, 10^4, 10^5, 10^6, 10^7$ and 10^8), k_r (0.1, 1, 100, 500 and 1000) and T_p (0.05, 0.1, and 0.2) are illustrated in figure 6.16. By comparing the temperature time series presented for the centrally positioned case (*i.e.*, figure 6.5) and the off-centre positioned case (*i.e.*, figure 6.16), it is seen that the general trends are very similar; however, the time series show a delay in the case $X_p = 0.5$. This delay can be evidently seen from the main temperature jump of $Ra = 10^8$ case which is around $\tau = 10$ while this point for the $X_p = 0.5$ is about $\tau = 11$. This delay clearly due to a wider right half-cavity which makes the stratification process longer. Another observed difference is the effect of T_p on the temperature time series. At the early stages the time series of the lower Ra cases (*i.e.*, $10^3 \leq Ra \leq 10^4$) show distinct separate lines; however, the time series presented in figure 6.5 do not show any significant effect of T_p. By increasing Ra to 10^7 and 10^8, the time series of temperature shows fluctuations in the case $X_p = 0.5$ which gradually decay when reaching the steady state. Those fluctuations are very smooth or not present in figure 6.16. This indicates that the thinner half-cavity has fewer instabilities than a wide half cavity. Interestingly, the characterized regimes for Nu_{Ave} can be justified as in the case presented in figure 6.10; for instance, the cavity bulk temperature only begins to rise significantly at the end of the quasi-steady period and continues to increase during the decay period. For $k_r \leq 1$, increasing T_p increases the local temperature and for $1 < k_r$, rising

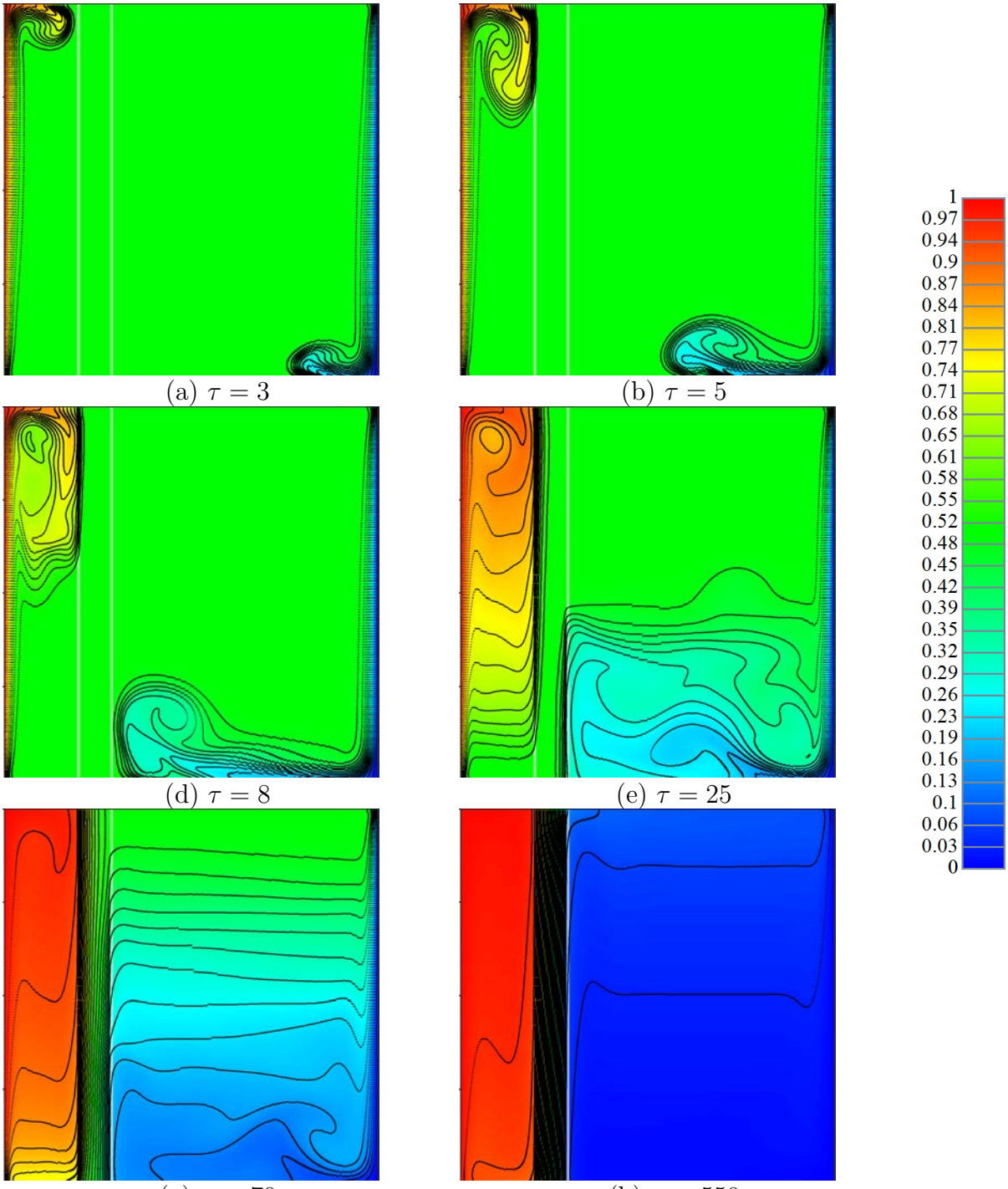

(a) $\tau = 3$ (b) $\tau = 5$

(d) $\tau = 8$ (e) $\tau = 25$

(g) $\tau = 70$ (h) $\tau = 550$

Figure 6.14: Temperature contours of the case $k_r = 0.1$, $T_p = 0.1$, $Ra = 10^8$ and $X_p = 0.25$ at different times.

T_p causes a reduction to the temperature value and this T_p effect starts at the quasi-steady regime.

Figure 6.17 presents the time series of $\theta_{D,x}$ at height $y = 0.5$ of the case $X_p = 0.25$ for different

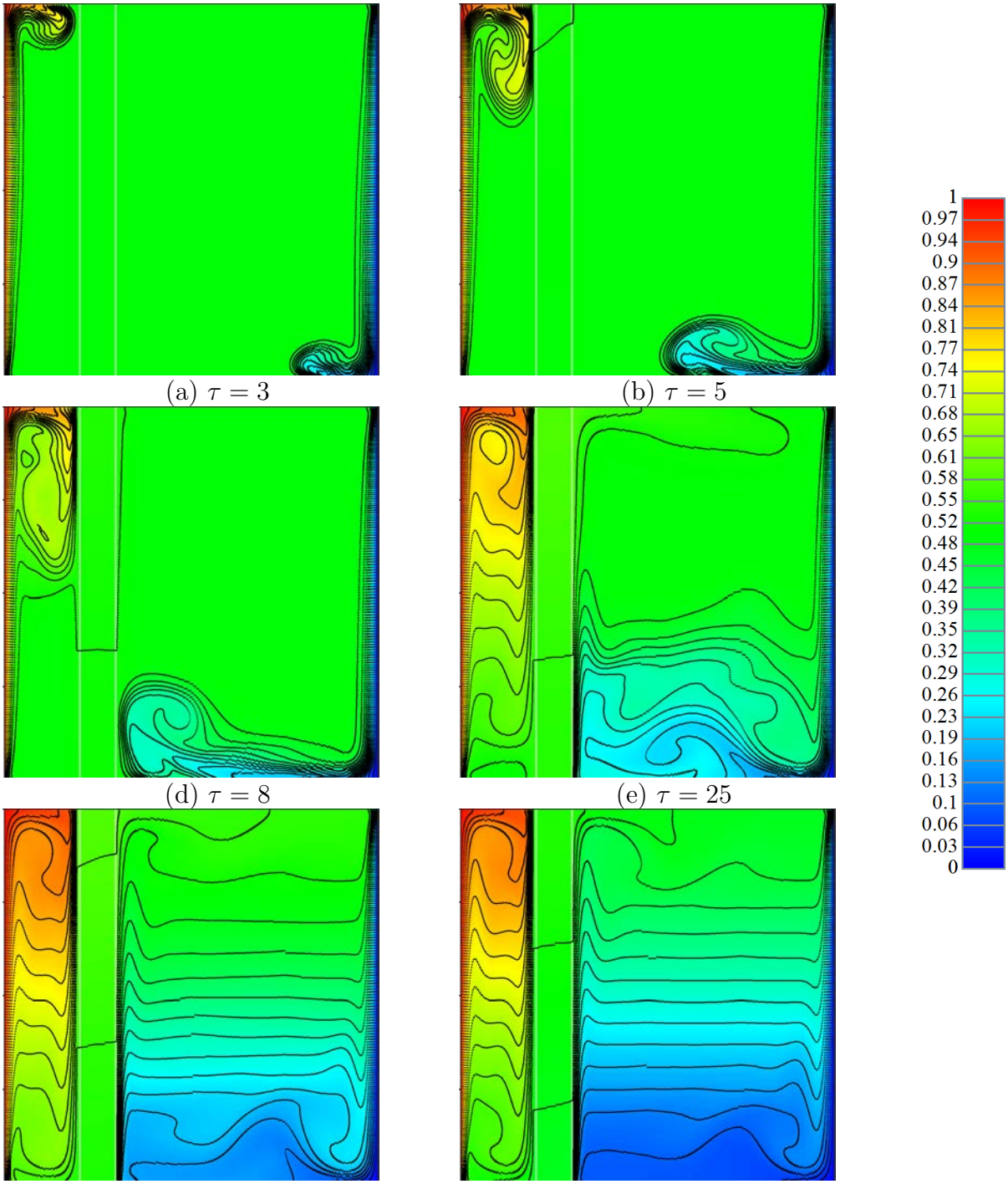

(a) $\tau = 3$ (b) $\tau = 5$

(d) $\tau = 8$ (e) $\tau = 25$

(g) $\tau = 70$ (h) $\tau = 550$

Figure 6.15: Temperature contours of the case $k_r = 1000$, $T_p = 0.1$, $Ra = 10^8$ and $X_p = 0.25$ at different times.

values of Ra (10^3, 10^4, 10^5, 10^6, 10^7 and 10^8), k_r (0.1, 1, 100, 500 and 1000) and T_p (0.05, 0.1, and 0.2). The transient $\theta_{D,x}$ graph shows a general increasing trend for all Ra, k_r and T_p cases. Similar to the centrally-positioned partition case the value of $\theta_{D,x}$ at the steady state increases as Ra and T_p increases and decreases as k_r increases. The comparison of figures 6.17 and 6.6

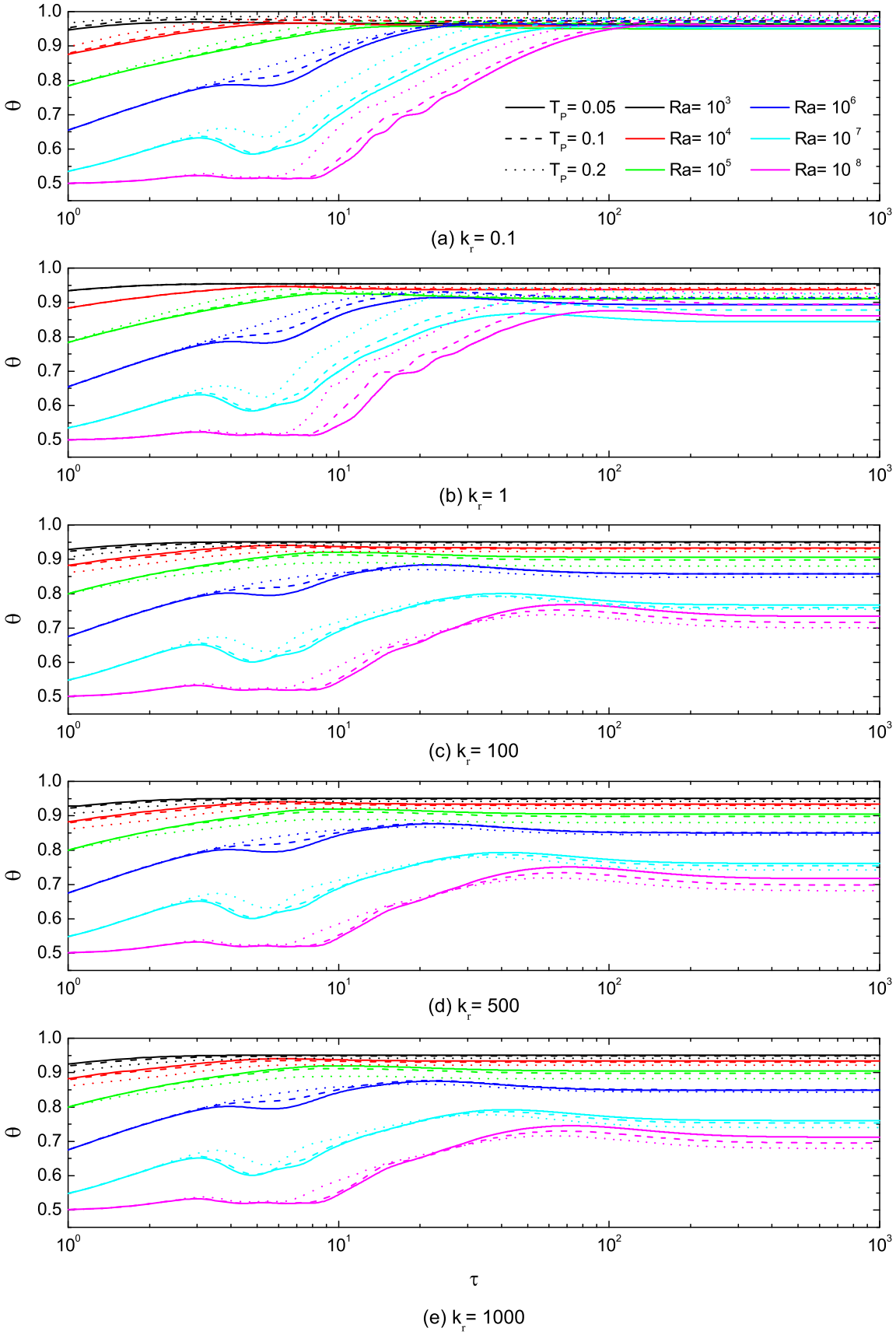

Figure 6.16: Time series of θ of the case $X_p = 0.25$ at $x = 0.05$ and $y = 0.5$ for different values of Ra (10^3, 10^4, 10^5, 10^6, 10^7 and 10^8), k_r (0.1, 1, 100, 500 and 1000) and T_p (0.05, 0.1, and 0.2).

identifies a delay at the first increasing point of $\theta_{D,x}$. The first increasing point of the case $Ra = 10^8$ and $k_r = 0.1$ is $\tau = 10$ for the off-centre partition case; however, this point for the centrally-positioned partition case has a delay and occurs at $\tau = 11$.

For the case $k_r = 0.1$, the overall steady-state value of $\theta_{D,x}$ is between 0.3 and 0.95. At $k_r = 1$, the $\theta_{D,x}$ range decreases to $0.05 - 0.7$ and beyond $k_r = 1$ (*i.e.*, $k_r > 1$), this range decreases to $0 - 0.03$, $0 - 0.005$ and $0 - 0.0022$ for $k_r = 100$, $k_r = 500$ and $k_r = 1000$, respectively. These ranges are very similar to the case of the centrally-positioned partition (*i.e.*, figure 6.6). Therefore, increasing k_r dramatically reduces $\theta_{D,x}$.

The time series of $\theta_{D,y}$ at the middle of the partition wall are presented in figure 6.18 for different Ra, k_r and T_p values. For the case of $k_r = 0.1$, figures 6.18 and 6.7 show a difference at the steady-values of $\theta_{D,y}$. The steady-state value of $\theta_{D,y}$ in a centrally-positioned partitioned cavity increases from $Ra = 10^3$ to 10^5 and decreases from 10^5 to 10^8. However, for the off-centre case, $Ra = 10^6$ shows the maximum steady-state value for $\theta_{D,y}$. The maximum $\theta_{D,y}$ of $Ra = 10^5$ is less pronounced and is slightly higher than its steady-state value as shown in figure 6.18 in comparison with the figure 6.7. For $k_r = 1$, just $Ra = 10^7$ and 10^8 cases have a maximum value higher than the steady-state result. For low Ra values ($10^6 \leq Ra$), $\theta_{D,y}$ has a steady and smooth increase from the initial value ($\theta_{D,y} = 0$) to a constant value at the steady state. Similar to the centrally-positioned partition case, at $k_r > 1$, $\theta_{D,y}$ has a steady and smooth increase from the initial value of $\theta_{D,y} = 0$ to a constant value at the steady state, which increases monotonically with Ra, and the rate of increase increases substantially with Ra.

To investigate further the flow behavior in an off-centre partitioned cavity, the position of u_{max} at the top half of both half-cavities ($0 \leq x \leq 1$ and $0.5 \leq y \leq 1$) and v_{max} at the left half of the left half-cavity ($0 \leq x \leq 0.5(X_p - 0.5T_p)$) and the left half of the right half-cavity ($X_p \leq y \leq 0.5 + X_p - 0.25T_p$) by passing time for different values of Ra (10^3, 10^4, 10^5, 10^6, 10^7 and 10^8), k_r (0.1, 1, 100, 500 and 1000) and T_p (0.05, 0.1, and 0.2) are illustrated in figures 6.19 and 6.20. The sweeping direction to find position is from the left to the right and from the bottom to the top. Therefore, the corresponding position of an area with the maximum amount

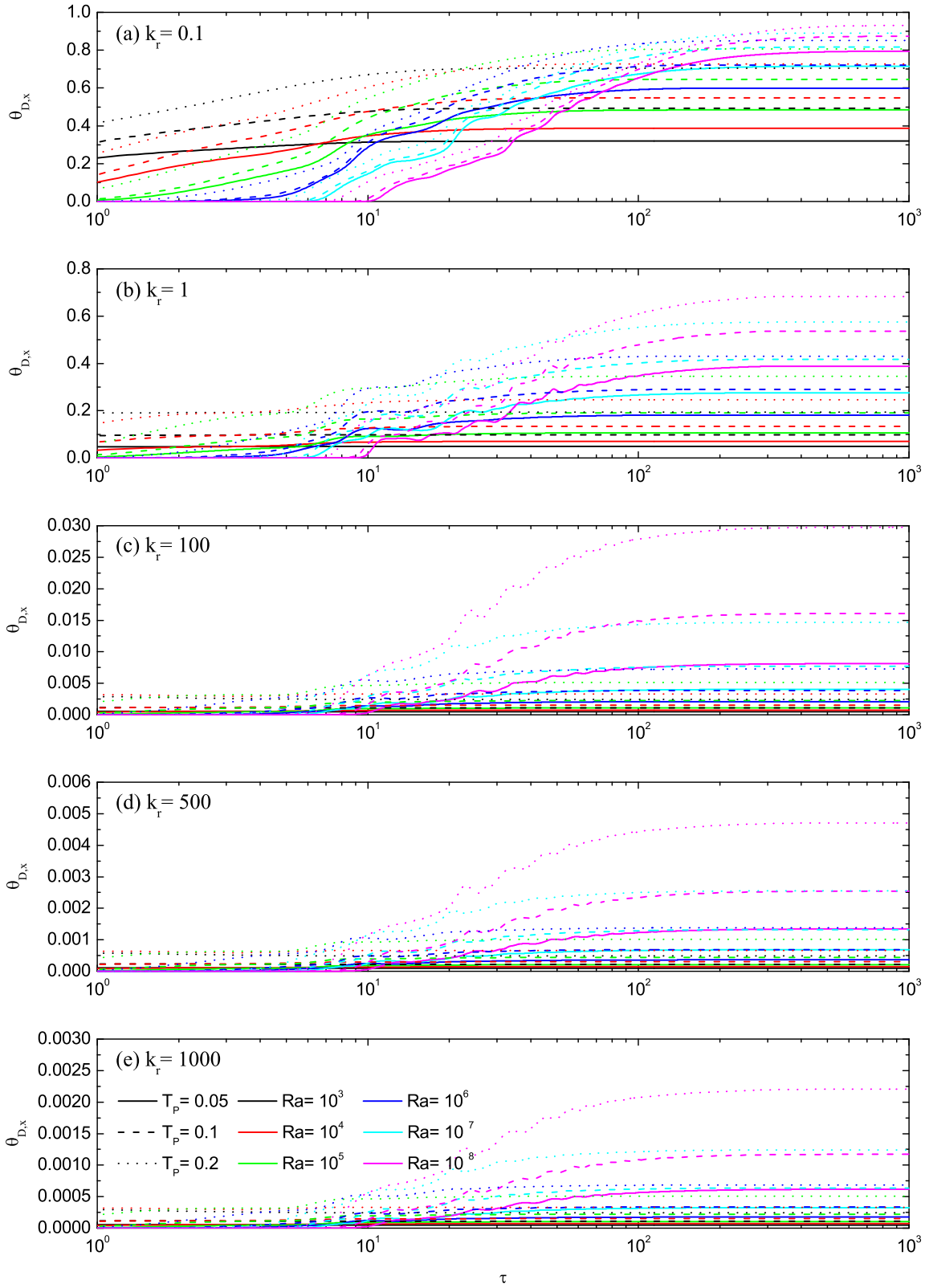

Figure 6.17: Time series of $\theta_{D,x}$ at $y = 0.5$ of the case $X_p = 0.25$ for different values of Ra (10^3, 10^4, 10^5, 10^6, 10^7 and 10^8), k_r (0.1, 1, 100, 500 and 1000) and T_p (0.05, 0.1, and 0.2).

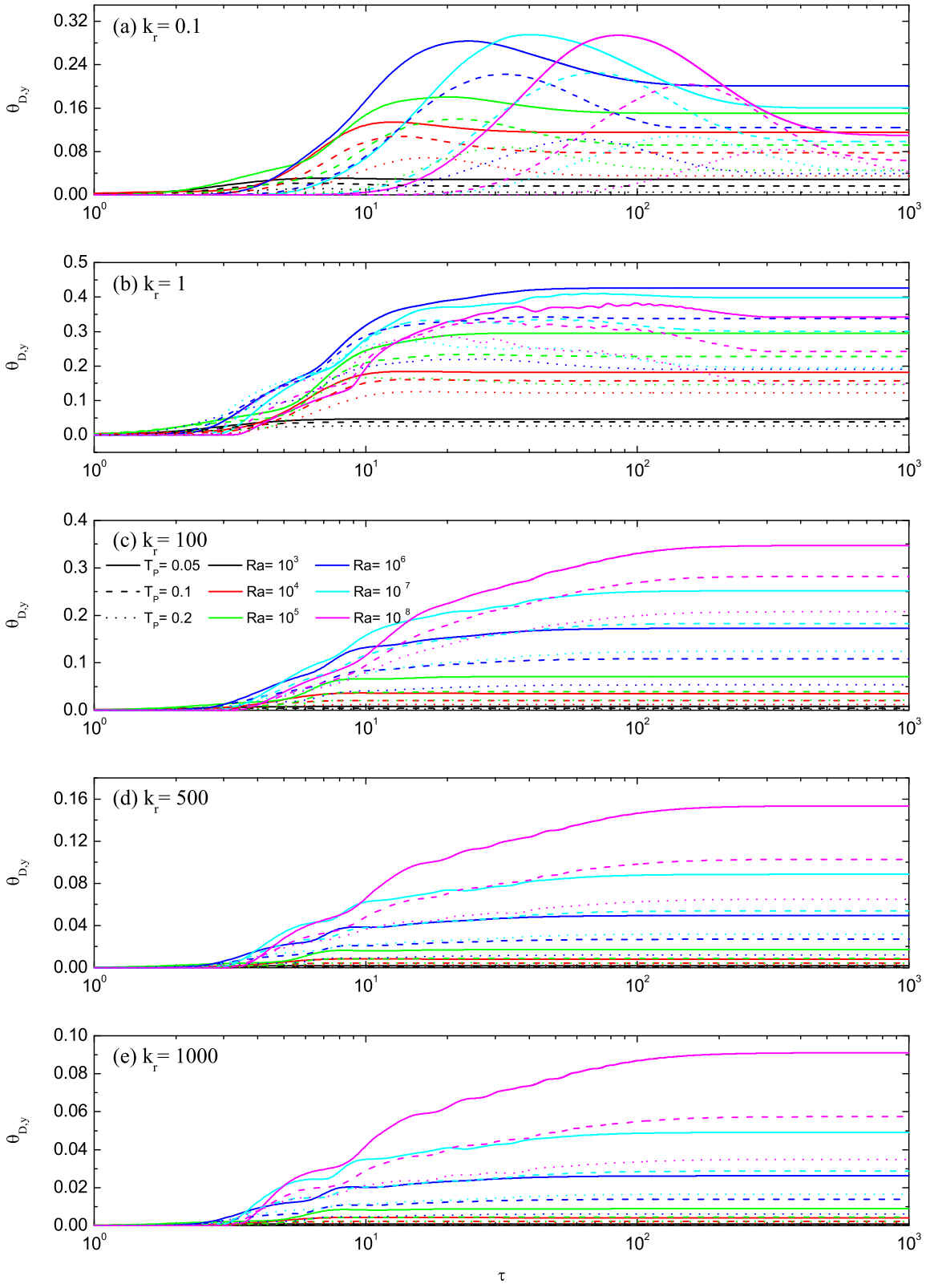

Figure 6.18: Time series of $\theta_{D,y}$ of the case $X_p = 0.25$ for different values of Ra (10^3, 10^4, 10^5, 10^6, 10^7 and 10^8), k_r (0.1, 1, 100, 500 and 1000) and T_p (0.05, 0.1, and 0.2).

will be the first swept position from the left and the bottom. In all cases, the position of u_{max} in the left half-cavity moves from the vicinity of the left corner of left half-cavity towards the partition sloping inward. This pattern is similar to the one observed in the centrally positioned partitioned case, but in this case as the half-cavity is thin, the captured points extended up to $x = 0.15$. With regard to the right half-cavity, this position starts from the right top corner and moves toward the partition. As Ra increases the position of u_{max} becomes closer to the top wall and their slopes get closer to a horizontal line. When the cavity approximately reaches the steady state, it can be seen more repeated points around the steady-state region. The u_{max} points occupy a wider area in the right half-cavity. As figure 6.19 shows, these points cover $0.3 < x \leq 1.0$ and $0.8 < y \leq 1.0$, respectively. Figure 6.19 also shows some points about the mid-height of the right half-cavity which are due to waves created in the transitional period. As k_r increases those momentary captured points appear just for high Ra values. Because of the sweeping range (*i.e.*, $0 \leq x \leq 1$ and $0.5 \leq y \leq 1$), the pattern of those points is not clear.

For the v_{max} cases (*i.e.*, figure 6.20), the results for low Ra values (*i.e.*, $Ra = 10^3$ and 10^4) show almost straight lines from the left side to the right at the right half-cavity. However, as Ra increases (*i.e.*, $Ra > 10^4$), the position of v_{max} starts from lower height and gradually rises until reach the vicinity of the partition and then sharply moves downward along the partition.

At low k_r (*i.e.*, $k_r = 0.1$), the position of v_{max} for high Ra values ($10^6 \leq Ra \leq 10^8$) directly starts from the vicinity of the partition and the gradual process of moving from the sidewall to the partition does not exist. As k_r increases the horizontal transition from the right side to the left gradually appears. The higher Ra value is, the closer the position of v_{max} is to the partition. The effect of T_p can be seen mainly for higher Ra values.

The position of v_{max} inside the left half-cavity is different from that in the right half-cavity. For all values of Ra, k_r and T_p this position moves vertically upward along the sidewall. The results in higher Ra cases show closer points to the left sidewall and T_p does not show a significant effect on the position of v_{max} as they all overlap each other.

Comparing the position of v_{max} figures for the case of the centrally-positioned and off-centre cases shows that the patterns in the right half-cavity of the case $X_p = 0.25$ and $X_p = 0.5$ have

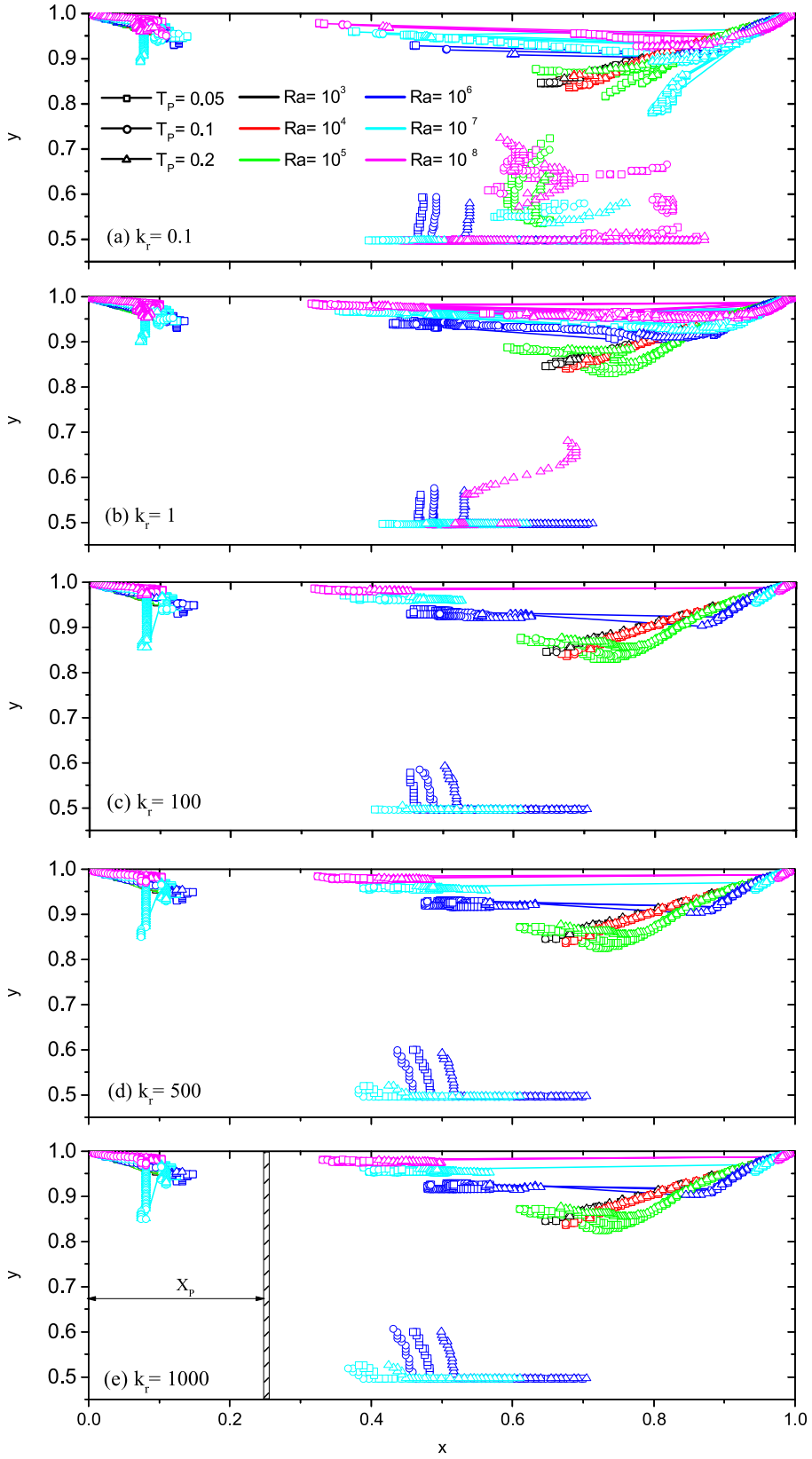

Figure 6.19: Position of u_{max} at the top half of cavity ($0 \leq x \leq 1$ and $0.5 \leq y \leq 1$) by passing time for different values of Ra (10^3, 10^4, 10^5, 10^6, 10^7 and 10^8), k_r (0.1, 1, 100, 500 and 1000) and T_p (0.05, 0.1, and 0.2).

the movement from the sidewall toward the partition but the rest of patterns are different. In regard to the pattern observed in the left half-cavity, the pattern is totally different from the case of $X_p = 0.5$.

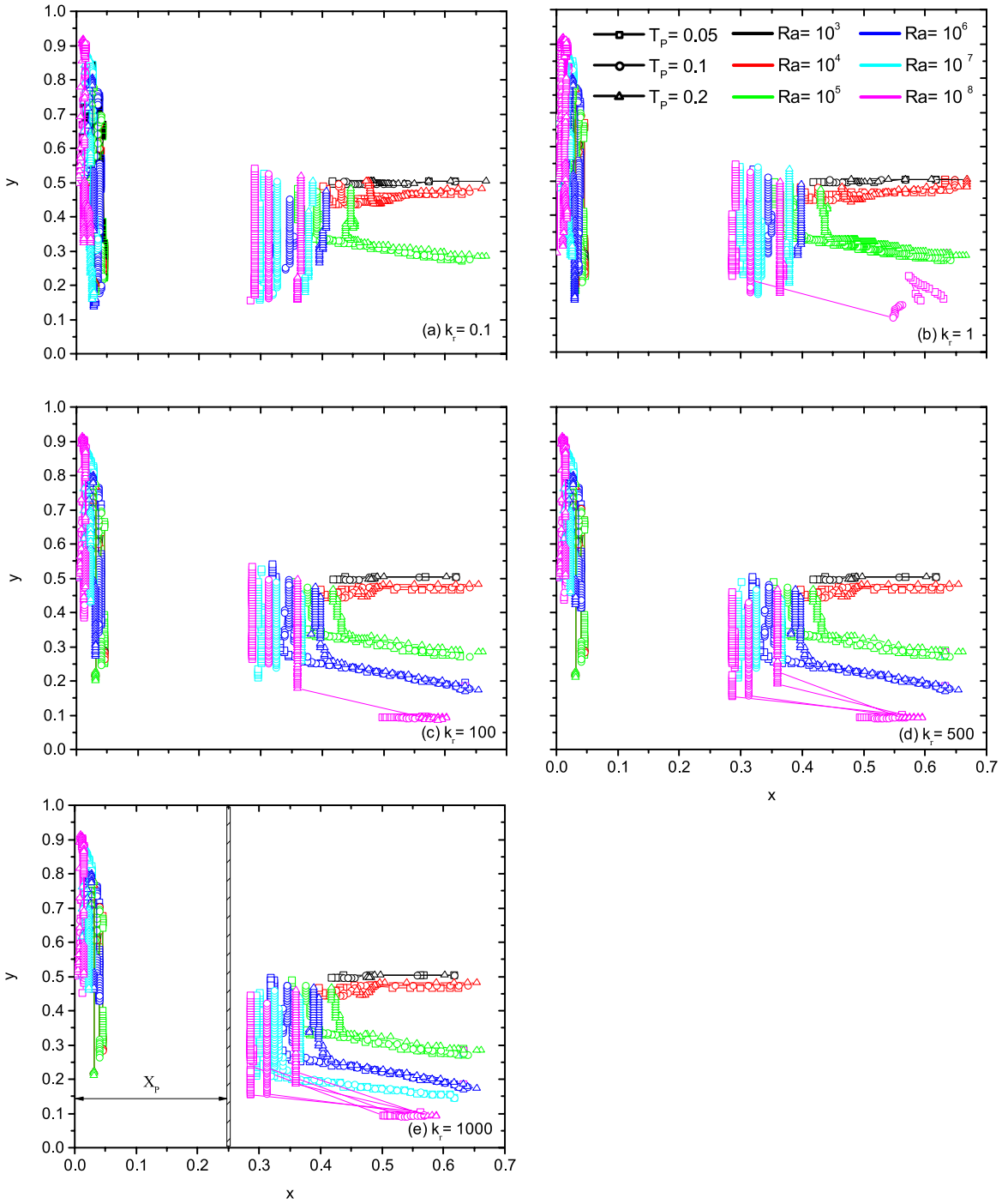

Figure 6.20: Position of v_{max} at the left half of the left half-cavity ($0 \leq x \leq 0.5(X_p - 0.5T_p)$) and the left half of the right half-cavity ($X_p \leq y \leq 0.5 + X_p - 0.25T_p$) by passing time for different values of Ra (10^3, 10^4, 10^5, 10^6, 10^7 and 10^8), k_r (0.1, 1, 100, 500 and 1000) and T_p (0.05, 0.1, and 0.2).

The position of the maximum stream function at the left and right half-cavities by passing

time for different values of Ra (10^3, 10^4, 10^5, 10^6, 10^7 and 10^8), k_r (0.1, 1, 100, 500 and 1000) and T_p (0.05, 0.1, and 0.2) is presented in figure 6.21. For the left half-cavity, the position of the maximum stream function starts at the mid-height of the cavity and then moves upward along the left sidewall to the vicinity of the left-top corner. The concentration of captured points close to the top-left corner is higher which indicates that the maximum stream function position stays in that area for a longer period of time. Also, the results for higher Ra values show higher jump and closer points to the top horizontal wall. Then gradually this position moves downward to the lower half of the left half-cavity. At this half-cavity, it is difficult to differentiate the effect of the partition thickness.

The position of the maximum stream function at the right half-cavity shows a similar behavior. For all cases, this position starts at the mid-height. As time passes the captured points move toward the middle of the half cavity. For low Ra value cases (*i.e.*, $Ra = 10^3$ and 10^4) this inward movement is almost horizontal. By increasing Ra the shape of the captured points becomes the shape of a sickle. The higher the Ra value is, the bigger the sickle shape is.

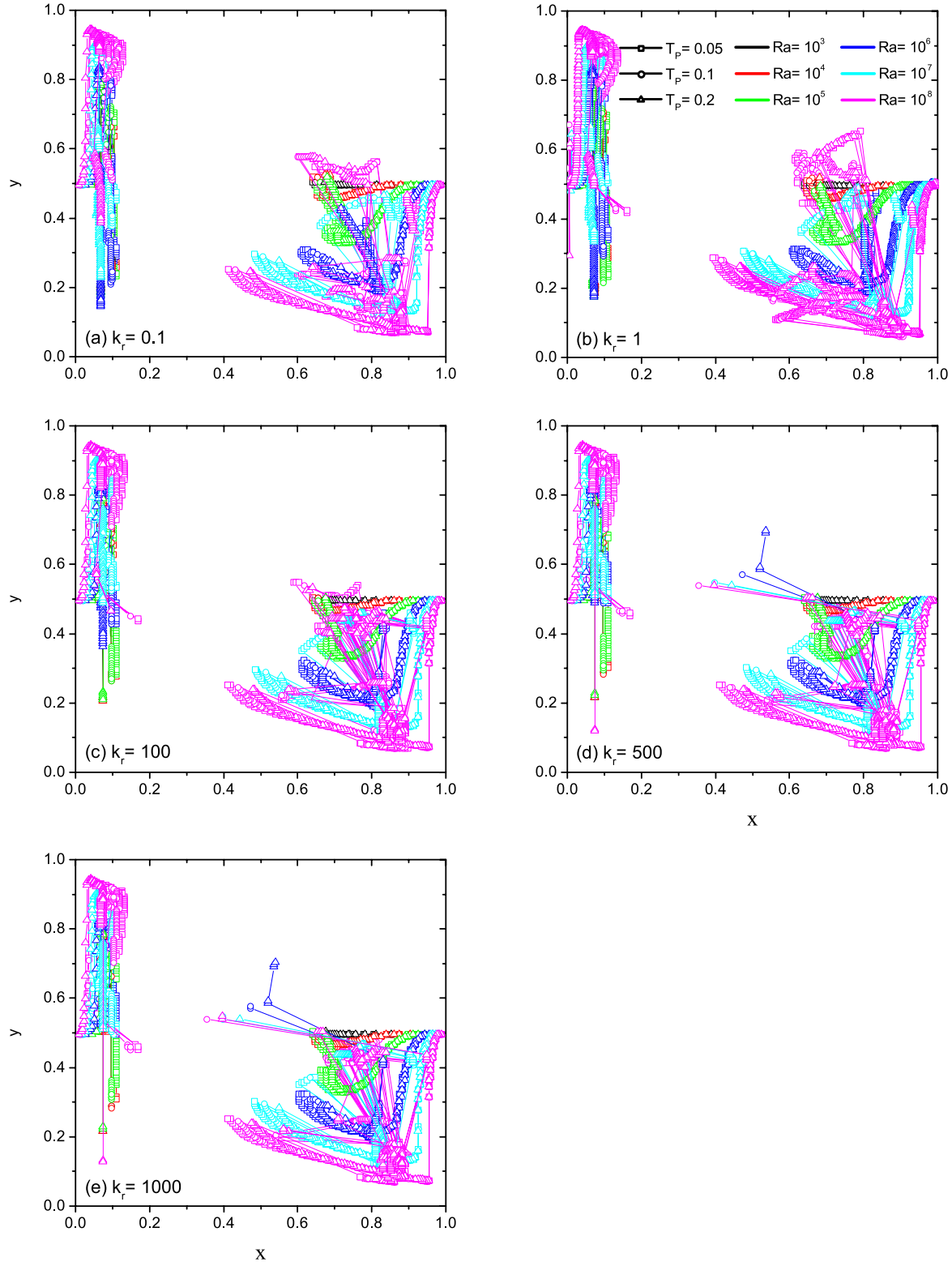

Figure 6.21: Position of the maximum stream function at the left and right half-cavities by passing time for different values of Ra (10^3, 10^4, 10^5, 10^6, 10^7 and 10^8), k_r (0.1, 1, 100, 500 and 1000) and T_p (0.05, 0.1, and 0.2).

Chapter 7

Conclusion

7.1 Summary of Thesis Outcomes

This study presents unsteady and laminar heat transfer characteristics of natural convection in a two-dimensional partitioned cavity. The fluid is considered through the incompressible fluid model under Boussinesq approximation. The governing equations for the flow (*i.e.*, the Navier-Stokes and temperature equations) were discretized using the finite volume method and solved by the SIMPLE algorithm. The QUICK scheme and the Adams-Bashforth scheme were employed for the advection and time integration and the second-order central difference scheme was used for all other terms. An in-house direct numerical simulation (DNS) code written in Visual *C#* was developed and used to solve the discretized governing equations. A non-unifom rectangular mesh was used, with coarser grids in the core regions and finer grids concentrated in the proximity of the partition and boundary walls of the cavity.

The major findings from this thesis may be summarized as follows:

- A computer code was written in Visual *C#* programming language. The code operates by solving the relevant conservation equations for heat, mass and momentum by means of a finite volume method. The main variables used throughout the code are velocities

and pressure and the SIMPLE algorithm is employed to solve for the velocity and pressure fields. Each equation can be solved by TDMA (as a default algorithm) or other methods. The developed code presented for steady/unsteady, compressible/incompressible and, turbulent/laminar flows in a Cartesian coordinate system. Nomenclature of the TEACH code (originated at the Imperial College) is mainly used in this code to increase readability. To improve further the readability of this code, the structure of code was designed to have separate and independent sections. Another code is written in visual $C\#$ to do the post-processing of data using already produced binary files by the main code. The code was verified and validated against the published results of partitioned (data from 2 studies) and non-partitioned (data from 14 studies) cavities.

- Empirical correlations (*i.e.*, $Nu_{Ave} = 0.0456\ Ra^{0.2637}\ T_P^{-0.0054}\ k_r^{0.1454}$, for $10^3 \leq Ra \leq 10^8$) have been developed for the average Nusselt number, which include the effects of Ra and partition thickness. The results show that the partition position parameter (*i.e.*, X_P) is a statistically insignificant parameter and including and excluding it does not have any effect on the final fitted curve.

- For high k_r cases, the number of isotherms in the partition is very low or do not exist. The low temperature difference in the partition leads to a negligible heat flux through the partition. This situation shows the adiabatic boundary condition of almost zero temperature gradient in the x direction at the partition. Considering $Ra = \frac{g\beta H^4 q''}{\alpha\nu k_f}$, these observations cause a low χ ($\chi \simeq 0$). The low thermal resistance parameter of the partition due to high k_r shows the partition can be considered as an isothermal wall and the heat transfer characteristics are similar to those of the non-partitioned cavity case and consequently, the scaling relations of isothermal of a non-partitioned cavity can be used. For this situation, the thermal boundary layer and average Nusselt number scaling relations for an isothermal wall can be used (*i.e.*, δ_T *or* $Nu \sim Ra^{1/4}$). This condition can also exist when the partition thickness is very small. Thinner partition causes a lower temperature difference between the left and right side of the partition which intensifies isothermal behavior of the partition.

- Low k_r cases induce a higher temperature gradient in the partition than the high k_r cases. Therefore, the temperature difference between the left and right side of the partition is dependent on both k_r and T_P. As a consequence, it is impossible to decide based on only one of these parameters (i.e. T_P and k_r) and both influence thermal characteristics of the cavity. By increasing the value of χ, the thermal behavior of the partition shifts from an isothermal wall like to an isoflux wall type. In this situation, the partition has uniform heat flux and the thermal resistance parameter role becomes important. The scaling relations extracted for isoflux wall (*i.e.*, δ_T *or* $Nu \sim Ra^{1/5}$) in a non-partitioned cavity are more appropriate for the higher χ.

- The overall behaviour of Nu_{Ave} as k_r varies was identified to have three distinctive regions. The first region covers low k_r range and the value of χ is relatively high. By increasing k_r (*i.e.*, increase k_P and constant k_f), Nu_{Ave} rises and the horizontal temperature gradient in the partition gradually decreases (*i.e.*, $\frac{\partial \theta}{\partial x}$). In this region, the vertical temperature gradient in the partition is negligible. The increasing trend of Nu_{Ave} reaches a peak point and the horizontal temperature gradient in the partition becomes almost zero (*i.e.*, $\frac{\partial \theta}{\partial x} \approx 0$) which means the partition wall becomes horizontally isothermal. This region is named the thermal resistance region. Further increasing in k_r results in intensifying the vertical temperature gradient in the partition (*i.e.*, $\frac{\partial \theta}{\partial y}$). A larger vertical temperature gradient than the horizontal one leads to characterizing the partition by the vertical temperature gradient. Increasing k_r causes the partition to become vertically isothermal and eventually decreases Nu_{Ave}. This region is called the thermal transient region. Finally after the thermal transient region, by further increasing k_r, the vertical and horizontal temperature gradients in the partition become negligible (*i.e.*, $\frac{\partial \theta}{\partial x} \approx 0$ and $\frac{\partial \theta}{\partial y} \approx 0$). It is obvious that in this situation the partition becomes isothermal. By reaching this point, it can be appropriate to consider each half-cavity as a separate cavity with constant temperature on the sidewalls. This region is named the isothermal region.

- The effect of T_P on Nu_{Ave} is trivial for lower Ra values than higher Ra value cases. T_P and k_r have opposite effects on the thermal resistance parameter of the partition. Therefore, there is a point where k_r nullifies the effect of T_P and the increased thermal conduc-

tivity of the partition overcomes the thermal damping effect of the partition thickness. This situation happens around $k_r = 100$ for both the centrally-positioned and off-centre partitioned cavities.

- The vertical thermal behavior of the partition was investigated by defining the $\theta_{D,y}$ parameter and is categorized into two types. Type one is the lines with an increase and decrease trend and a subsequent peak point ($k_r \leq 1$) and type two includes the lines with just increasing trend ($100 \leq k_r \leq 1000$).

- The transient Nu_{Ave} at the hot wall of a centrally-partitioned cavity is characterized by four regimes. At the conduction regime, the fluid is isothermal and motionless as the cavity undergoes the increasing temperature step and the heat transfer mode is pure conduction. Nu_{Ave} reaches a local minimum value and then begins to increase before reaching a value that is almost maintained during a quasi-steady period. As expected, at the conduction regime, Nu_{Ave} at the partition is zero and convective heat transfer has not started to thermally active the partition and its temperature is still at the initial condition (*i.e.*, $\theta = 0.5$). By developing fluid motion, Nu_{Ave} increases to its quasi-steady value and thermal and viscous boundary layers are fully developed. The increasing bulk temperature causes a reduction in the temperature difference and the driving force for heat transfer which result in decaying Nu_{Ave}. While the overall temperature difference of fluid occupied area decreases, due to the presence of pure conduction in the partition, the process of forming temperature gradient continues and penetrates more in the partition. The final regime is the steady state. Therefore, the four distinct regimes of Nu_{Ave} at the hot wall are conduction, quasi-steady, decaying and steady-state. For cavities with the off-centre partitions (in this study partition is close to the hot sidewall) this classification is different. The cold sidewall is characterized by the same four regimes presented for a centrally-partitioned cavity. For the hot sidewall, an extra regime, called the filling regime, is identified after the decaying region. Consequently, the five distinct regimes of Nu_{Ave} at the hot wall of an off-centre partitioned cavity are conduction, quasi-steady, decaying, filling and steady state.

7.2 Future Work

Important areas for further work are suggested by the results of this thesis:

- Implementing the Multigrid (MG) method in the numerical analysis and the program to decrease the computing time.
- Implementing the adaptive mesh refinement, or AMR, a method to obtain an accurate solution within certain sensitive regions.
- Investigation of turbulent flow in a partitioned cavity which should include Ra values beyond 10^9.
- Investigation of fluid properties (*i.e.*, Pr) in the whole partitioned cavity or inside each half-cavity. This variation of Pr can increase the range of industrial application of this study.
- Considering the effect of multi-layer partitions in a cavity. The thickness of partition, number of partitions, position of partition and fluid trapped inside partition layers are the parameters to study.
- Investigation of the cavity aspect ratio will be very useful. Adding this parameter will increase the range of application for this study.
- As one of the main applications of this study is electronic devices, it is suggested to add the effect of radiation heat transfer mode to increase the accuracy.
- This study can be very useful for pollution or sediment investigations by adding particle motion equations in the partitioned cavity.
- Due to the lack of experimental data, the experimental studying of flow and thermal characteristics of a partitioned cavity is essential.

Bibliography

[1] Ó. Andrjesdóttir. *Experimental characterization and optimization of a compact thermosyphon with enhanced boiling surface for power electronics cooling.* PhD thesis, Department of Mechanical and Process Engineering, 2012.

[2] Y. J. Choi. *A numerical study on a lumped-parameter model and a CFD code coupling for the analysis of the loss of coolant accident in a reactor containment.* PhD thesis, Thermal and Energy Systems, 2005.

[3] J. M. F. Oro, C. S. Morros, K. M. A. Díaz, and P. L. G. Ybarra. Numerical simulation of the fuel oil cooling process in a wrecked ship. *Journal of Fluids Engineering*, 128: 1390–1393, 2006.

[4] S. F. Corzo, S. Márquez Damián, D. Ramajo, and N. M. Nigro. Numerical simulation of natural convection phenomena. *Mecánica Computacional*, 30: 277–96, 2011.

[5] K. Kahveci. Numerical simulation of natural convection in a partitioned enclosure using pdq method. *International Journal of Numerical Methods for Heat & Fluid Flow*, 17: 439–456, 2007.

[6] S. K. Patra. *CFD analysis of electronics chip cooling.* PhD thesis, National Institute of Technology Rourkela, 2007.

[7] A. C. Yunus. Heat transfer: a practical approach. *MacGraw Hill, New York*, 2003.

[8] J. W. Park, J. H. Bae, and H. J. Song. Conjugate heat transfer analysis for in-vessel retention with external reactor vessel cooling. *Annals of Nuclear Energy*, 88: 57–67, 2016.

[9] A. K. Sharma, K. Velusamy, and C. Balaji. Conjugate transient natural convection in a cylindrical enclosure with internal volumetric heat generation. *Annals of Nuclear Energy*, 35: 1502–1514, 2008.

[10] A. Liaqat and A. C. Baytas. Numerical comparison of conjugate and non-conjugate natural convection for internally heated semi-circular pools. *International Journal of Heat and Fluid Flow*, 22: 650–656, 2001.

[11] A. Bentaib, N. Meynet, and A. Bleyer. Overview on hydrogen risk research and development activities: Methodology and open issues. *Nuclear Engineering and Technology*, 47: 26–32, 2015.

[12] J. Xiong, Y. Yang, and X. Cheng. CFD application to hydrogen risk analysis and par qualification. *Science and Technology of Nuclear Installations*, 2009, 2009.

[13] B. R. Sehgal. *Nuclear Safety in Light Water Reactors: Severe Accident Phenomenology*. Elsevier Science, 2011.

[14] M. A. Antar and H. Baig. Conjugate conduction-natural convection heat transfer in a hollow building block. *Applied Thermal Engineering*, 29: 3716–3720, 2009.

[15] A. Missoum, M. Elmir, A. Belkacem, M. Nabou, and B. Draoui. Numerical simulation of heat transfer through a double-walled facade building in arid zone. *Energy Procedia*, 36: 834–843, 2013.

[16] M. Gijón-Rivera, J. Serrano-Arellano, J. Xamán, and G. Álvarez. Effect of different building materials on conjugate heat and mass transfer. *Ingeniería Mecánica, Tecnología y Desarrollo*, 5: 395–404, 2016.

[17] C. Popa, D. Ospir, S. Fohanno, and C. Chereches. Numerical simulation of dynamical aspects of natural convection flow in a double-skin faade. *Energy and Buildings*, 50: 229–233, 2012.

[18] A. Ben-Nakhi and M. A. Mahmoud. Conjugate natural convection in the roof cavity of heavy construction building during summer. *Applied Thermal Engineering*, 27: 287–298, 2007.

[19] D. Angeli and A. Dama. Modelling natural ventilation in double skin facade. *Energy Procedia*, 78: 1537–1542, 2015.

[20] A. H. Lefebvre. *GAS Turbine Combustion, Second Edition*. Combustion: An International Series. Taylor & Francis, 1998.

[21] P. Wang, Y. Li, Z. Zou, and W. Zhang. Conjugate heat transfer investigation of cooled turbine using the preconditioned density-based algorithm. *Propulsion and Power Research*, 2: 56–69, 2013.

[22] R. Teertstra, J. R. Urbanski, and J. R. Culham. Conjugate heat transfer measurements for air-cooled electronics - a new experimental method. In *Ninteenth Annual IEEE Semiconductor Thermal Measurement and Management Symposium*, 195–201, March 2003.

[23] T. C. Hung and C. S. Fu. Conjugate heat transfer analysis for the passive enhancement of electronic cooling through geometric modification in a mixed convection domain. *Numerical Heat Transfer, Part A: Applications*, 35: 519–535, 1999.

[24] M. H. A. Piro and B. W. Leitch. Conjugate heat transfer simulations of advanced research reactor fuel. *Nuclear Engineering and Design*, 274: 30–43, 2014.

[25] S. E. Potter and C. P. Underwood. A modelling method for conjugate heat transfer and fluid flow in building spaces. *Building Services Engineering Research and Technology*, 25: 111–125, 2004.

[26] M. A. Antar. Thermal radiation role in conjugate heat transfer across a multiple-cavity building block. *Energy*, 35: 3508–3516, 2010.

[27] A. Dorfman and Z. Renner. Conjugate problems in convective heat transfer: Review. *Mathematical Problems in Engineering*, 2009, 2009.

[28] T. L. Perelman, R. S. Levitin, L. B. Cdalevich, and B. M. Khusid. Unsteady-state conjugated heat transfer between a semi-infinite surface and incoming flow of a compressible fluidi. reduction to the integral relation. *International Journal of Heat and Mass Transfer*, 15: 2551–2561, 1972.

[29] S. Ostrach. An analysis of laminar free-convection flow and heat transfer about a flat plate parallel to the direction of the generating body force. Technical report, NASA, National Advisory Committee for Aeronautics. Lewis Flight Propulsion Lab.; Cleveland, OH, United States, 1 1953.

[30] R. Anderson and A. Bejan. Heat transfer through single and double vertical walls in natural convection: theory and experiment. *International Journal of Heat and Mass Transfer*, 24: 1611–1620, 1981.

[31] E. M. Sparrow and J. L. Gregg. Laminar free convection from a vertical plate with uniform surface heat flux. *Journal of Heat Transfer*, 78: 435–440, 1956.

[32] B. Gebhart. *Heat Transfer*, chapter 8. McGrawHill, 2nd edition, 1971.

[33] T. Grosan and I. Pop. Temperature and internal heat generation in a porous medium. *Technische Mechanik*, 21: 313–318, 2001.

[34] S. Ostrach. Natural convection in enclosures. *Journal of Heat Transfer*, 110: 1175–1190, 1988.

[35] I. Catton. Natural convection in enclosures. In *Proceedings of the sixth international heat transfer conference*, volume 6, 13–31, 1978.

[36] A. Baïri, E. Zarco-Pernia, and J. M. G. De María. A review on natural convection in enclosures for engineering applications. the particular case of the parallelogrammic diode cavity. *Applied Thermal Engineering*, 63: 304–322, 2014.

[37] A. J. N. Khalifa. Natural convective heat transfer coefficient a review: I. isolated vertical and horizontal surfaces. *Energy Conversion and Management*, 42: 491–504, 2001.

[38] A. J. N. Khalifa. Natural convective heat transfer coefficient a review: Ii. surfaces in two- and three-dimensional enclosures. *Energy Conversion and Management*, 42: 505–517, 2001.

[39] R. J. Goldstein, W. E. Ibele, S. V. Patankar, T. W. Simon, T. H. Kuehn, P. J. Strykowski, K. K. Tamma, J. V. R. Heberlein, J. H. Davidson, J. Bischof, F. A. Kulacki, U. Kortshagen, S. Garrick, and V. Srinivasan. Heat transfera review of 2003 literature. *International Journal of Heat and Mass Transfer*, 49: 451–534, 2006.

[40] O. M. Kamiyo, D. Angeli, G. S. Barozzi, M. W. Collins, V. O. S. Olunloyo, and S. O. Talabi. A comprehensive review of natural convection in triangular enclosures. *Applied Mechanics Reviews*, 63: 060801, 2010.

[41] Q. Rubbab, D. Vieru, C. Fetecau, and C. Fetecau. Natural convection flow near a vertical plate that applies a shear stress to a viscous fluid. *PloS one*, 8: e78352, 2013.

[42] L. Prandtl. *Essentials of fluid dynamics*. Hafner Publishing Company, 1952.

[43] J. Tanny and J. Cohen. The mean temperature field of a buoyancyinduced boundary layer adjacent to a vertical plate immersed in a stratified medium. *International journal of heat and mass transfer*, 41: 2125–2130, 1998.

[44] K. T. Yang. Possible similarity solutions for laminar free convection on vertical plates and cylinders. *Journal of Applied Mechanics*, 27: 230–236, 1960.

[45] K. T. Yang, J. L. Novotny, and Y. S. Cheng. Laminar free convection from a nonisothermal plate immersed in a temperature stratified medium. *International journal of Heat and Mass transfer*, 15: 1097–1109, 1972.

[46] A. K. Kulkarni, H. R. Jacobs, and J. J. Hwang. Similarity solution for natural convection flow over an isothermal vertical wall immersed in thermally stratified medium. *International journal of heat and mass transfer*, 30: 691–698, 1987.

[47] R. A. W. M. Henkes and C. J. Hoogendoorn. Laminar natural convection boundary-layer flow along a heated vertical plate in a stratified environment. *International journal of heat and mass transfer*, 32: 147–155, 1989.

[48] J. Tao, P. Le Quéré, and S. Xin. Spatio-temporal instability of the natural-convection boundary layer in thermally stratified medium. *Journal of Fluid Mechanics*, 518: 363–379, 2004.

[49] Y. Jaluria and B. Gebhart. Stability and transition of buoyancy-induced flows in a stratified medium. *Journal of Fluid Mechanics*, 66: 593–612, 1974.

[50] R. Cheesewright. Natural convection from a plane, vertical surface in non-isothermal surroundings. *International journal of Heat and Mass transfer*, 10: 1847–1859, 1967.

[51] S. W. Armfield, J. C. Patterson, and W. Lin. Scaling investigation of the natural convection boundary layer on an evenly heated plate. *International Journal of Heat and Mass Transfer*, 50: 1592–1602, 2007.

[52] C. C. Chen and R. Eichhorn. Natural convection from a vertical surface to a thermally stratified fluid. *Journal of Heat Transfer*, 98: 446–451, 1976.

[53] B. J. Venkatachala and G. Nath. Nonsimilar laminar natural convection in a thermally stratified fluid. *International Journal of Heat and Mass Transfer*, 24: 1848–1850, 1981.

[54] D. Angirasa and J. Srinivasan. Natural convection heat transfer from an isothermal vertical surface to a stable thermally stratified fluid. *Journal of Heat Transfer*, 114: 917–923, 1992.

[55] C. L. Chang and Z. Y. Lee. Free convection on a vertical plate with uniform and constant heat flux in a thermally stratified micropolar fluid. *Mechanics Research Communications*, 35: 421–427, 2008.

[56] A. Shapiro and E. Fedorovich. Unsteady convectively driven flow along a vertical plate immersed in a stably stratified fluid. *Journal of Fluid Mechanics*, 498: 333–352, 2004.

[57] E. Fedorovich and A. Shapiro. Turbulent natural convection along a vertical plate immersed in a stably stratified fluid. *Journal of Fluid Mechanics*, 636: 41–57, 2009.

[58] W. Lin and S. W. Armfield. Unsteady natural convection on an evenly heated vertical plate for Prandtl number $\mathrm{Pr} < 1$. *Physical Review E*, 72: 066309, 2005.

[59] W. Lin and S. W. Armfield. Scalings for unsteady natural convection boundary layers on a vertical plate at time-dependent temperature. *International Journal of Thermal Sciences*, 111: 78–99, 2017.

[60] M. A. Hossain, S. Hussain, and D. A. S. Rees. Influence of fluctuating surface temperature and concentration on natural convection flow from a vertical flat plate. *Journal of Applied Mathematics and Mechanics (ZAMM) /Zeitschrift für Angewandte Mathematik und Mechanik*, 81: 699–709, 2001.

[61] M. D. Kelleher and K. T. Yang. Heat transfer response of laminar free-convection boundary layers along a vertical heated plate to surface-temperature oscillations. *Zeitschrift für Angewandte Mathematik und Physik (ZAMP)*, 19: 31–44, 1968.

[62] M. A. Hossain, S. K. Das, and I. Pop. Heat transfer response of mhd free convection flow along a vertical plate to surface temperature oscillations. *International journal of non-linear mechanics*, 33: 541–553, 1998.

[63] M. A. Hossain, S. K. Das, and D. A. S. Rees. Heat transfer response of free convection flow from a vertical heated plate to an oscillating surface heat flux. *Acta mechanica*, 126: 101–113, 1998.

[64] N. C. Roy and M. A. Hossain. Numerical solution of a steady natural convection flow from a vertical plate with the combined effects of streamwise temperature and species concentration variations. *Heat and Mass Transfer*, 46: 509–522, 2010.

[65] T. Aberra, S. W. Armfield, M. Behnia, and G. D. McBain. Boundary layer instability of the natural convection flow on a uniformly heated vertical plate. *International Journal of Heat and Mass Transfer*, 55: 6097–6108, 2012.

[66] A. V. Kuznetsov and D. A. Nield. Natural convective boundary-layer flow of a nanofluid past a vertical plate. *International Journal of Thermal Sciences*, 49: 243–247, 2010.

[67] A. V. Kuznetsov and D. A. Nield. Natural convective boundary-layer flow of a nanofluid past a vertical plate: A revised model. *International Journal of Thermal Sciences*, 77: 126–129, 2014.

[68] A. R. Teymourtash, D. R. Khonakdar, and M. R. Raveshi. Natural convection on a vertical plate with variable heat flux in supercritical fluids. *The Journal of Supercritical Fluids*, 74: 115–127, 2013.

[69] P. Le Quere, J. A. C. Humphrey, and F. S. Sherman. Numerical calculation of thermally driven two-dimensional unsteady laminar flow in cavities of rectangular cross section. *Numerical Heat Transfer*, 4: 249–283, 1981.

[70] A. A. Mohamad. Natural convection in open cavities and slots. *Numerical Heat Transfer, Part A: Applications*, 27: 705–716, 1995.

[71] M. Miyamoto, T. H. Kuehn, R. J. Goldstein, and Y. Katoh. Two-dimensional laminar natural convection heat transfer from a fully or partially open square cavity. *Numerical heat transfer*, 15: 411–430, 1989.

[72] K. Vafai and J. Ettefagh. Thermal and fluid flow instabilities in buoyancy-driven flows in open-ended cavities. *International Journal of Heat and Mass Transfer*, 33: 2329–2344, 1990.

[73] A. Koca. Numerical analysis of conjugate heat transfer in a partially open square cavity with a vertical heat source. *International Communications in Heat and Mass Transfer*, 35: 1385–1395, 2008.

[74] J. F. Hinojosa Palafox. Natural convection and surface thermal radiation in a tilted open shallow cavity. *Revista mexicana de física*, 58: 19–28, 2012.

[75] S. N. Singh and S. P. Venkateshan. Numerical study of natural convection with surface radiation in side-vented open cavities. *International Journal of Thermal Sciences*, 43: 865–876, 2004.

[76] C. Balaji and S. P. Venkateshan. Interaction of radiation with free convection in an open cavity. *International Journal of Heat and Fluid Flow*, 15: 317–324, 1994.

[77] J. S. Lim and A. Bejan. Natural convection with radiation in a cavity with open top end. *Journal of heat transfer*, 114: 479, 1992.

[78] M. A. Hossain, S. Asghar, and R. Subba Reddy Gorla. Buoyancy-driven flow of a viscous incompressible fluid in an open-ended rectangular cavity with permeable horizontal surfaces. *International Journal of Numerical Methods for Heat & Fluid Flow*, 20: 759–772, 2010.

[79] A. A. Mohamad, M. El-Ganaoui, and R. Bennacer. Lattice boltzmann simulation of natural convection in an open ended cavity. *International Journal of Thermal Sciences*, 48: 1870–1875, 2009.

[80] I. Sezai and A. A. Mohamad. Three-dimensional simulation of natural convection in cavities with side opening. *International Journal of Numerical Methods for Heat & Fluid Flow*, 8: 800–813, 1998.

[81] D. Angirasa, M. J. B. M. Pourquie, and F. T. M. Nieuwstadt. Numerical study of transient and steady laminar buoyancy-driven flows and heat transfer in a square open cavity. *Numerical Heat Transfer*, 22: 223–239, 1992.

[82] Y. L. Chan and C. L. Tien. A numerical study of two-dimensional laminar natural convection in shallow open cavities. *International Journal of Heat and Mass Transfer*, 28: 603–612, 1985.

[83] Y. L. Chan and C. L. Tien. A numerical study of two-dimensional natural convection in square open cavities. *Numerical Heat Transfer*, 8: 65–80, 1985.

[84] J. F. Hinojosa and J. Cervantes-de Gortari. Numerical simulation of steady-state and transient natural convection in an isothermal open cubic cavity. *Heat and Mass Transfer*, 46: 595–606, 2010.

[85] S. K. S. Boetcher and E. M. Sparrow. Buoyancy-induced flow in an open-ended cavity: Assessment of a similarity solution and of numerical simulation models. *International Journal of Heat and Mass Transfer*, 52: 3850–3856, 2009.

[86] D. Angirasa, J. G. M. Eggels, and F. T. M. Nieuwstadt. Numerical simulation of transient natural convection from an isothermal cavity open on a side. *Numerical Heat Transfer, Part A: Applications*, 28: 755–767, 1995.

[87] F. Penot. Numerical calculation of two-dimensional natural convection in isothermal open cavities. *Numerical Heat Transfer, Part A Applications*, 5: 421–437, 1982.

[88] O. Polat and E. Bilgen. Laminar natural convection in inclined open shallow cavities. *International Journal of Thermal Sciences*, 41: 360–368, 2002.

[89] E. Bilgen and H. Oztop. Natural convection heat transfer in partially open inclined square cavities. *International Journal of Heat and Mass Transfer*, 48: 1470–1479, 2005.

[90] É. Fontana, A. da Silva, and V. C. Mariani. Natural convection in a partially open square cavity with internal heat source: An analysis of the opening mass flow. *International Journal of Heat and Mass Transfer*, 54: 1369–1386, 2011.

[91] W. Chakroun, M. M. Elsayed, and S. F. Al-Fahed. Experimental measurements of heat transfer coefficient in a partially/fully opened tilted cavity. *Journal of Solar Energy Engineering*, 119, 1997.

[92] M. M. Elsayed and W. Chakroun. Effect of aperture geometry on heat transfer in tilted partially open cavities. *Transactions-American Society of Mechanical Engineers Journal of Heat Transfer*, 121: 819–827, 1999.

[93] M. Montiel-Gonzlez, J. F. Hinojosa, H. I. Villafn-Vidales, A. Bautista-Orozco, and C.A. Estrada. Theoretical and experimental study of natural convection with surface thermal radiation in a side open cavity. *Applied Thermal Engineering*, 75: 1176–1186, 2015.

[94] V. M. Maytorena, A. Piña-Ortiz, and J. F. Hinojosa. Experimental and numerical study of turbulent natural convection in an open cubic cavity. *Heat and Mass Transfer*, 51: 1205–1217, 2015.

[95] A. E. Gill. The boundary-layer regime for convection in a rectangular cavity. *Journal of Fluid Mechanics*, 26: 515–536, 1966.

[96] C. J. Ho and Y. H. Lin. Natural convection of cold water in a vertical annulus with constant heat flux on the inner wall. *Journal of heat transfer*, 112: 117–123, 1990.

[97] S. Wakitani. Development of multicellular solutions in natural convection in an air-filled vertical cavity. *Transactions-American Society Of Mechanical Engineers Journal Of Heat Transfer*, 119: 97–101, 1997.

[98] S. Wakitani. Flow patterns of natural convection in an air-filled vertical cavity. *Physics of Fluids*, 10: 1924–1928, 1998.

[99] S. Kimura and A. Bejan. The boundary layer natural convection regime in a rectangular cavity with uniform heat flux from the side. *Journal of heat transfer*, 106: 99, 1984.

[100] J. C. Patterson and J. Imberger. Unsteady natural convection in a rectangular cavity. *Journal of Fluid Mechanics*, 100: 65–86, 9 1980.

[101] S. G. Schladow, J. C. Patterson, and R. L. Street. Transient flow in a side-heated cavity at high Rayleigh number: a numerical study. *Journal of Fluid Mechanics*, 200: 121–148, 1989.

[102] W. Lin and S. W. Armfield. Scaling laws for unsteady natural convection cooling of fluid with Prandtl number less than one in a vertical cylinder. *Physical Review E*, 72: 016306, 2005.

[103] W. Lin, S. W. Armfield, and J. C. Patterson. Unsteady natural convection boundary-layer flow of a linearly-stratified fluid with Pr$<$ 1 on an evenly heated semi-infinite vertical plate. *International Journal of Heat and Mass Transfer*, 51: 327–343, 2008.

[104] J. C. Patterson, C. Lei, S. W. Armfield, and W. Lin. Scaling of unsteady natural convection boundary layers with a non-instantaneous initiation. *International Journal of Thermal Sciences*, 48: 1843–1852, 2009.

[105] T. P. Bednarz, W. Lin, and S. C. Saha. Scaling of thermo-magnetic convection. In *13th Asian Congress of Fluid Mechanics*, 798–800, Dhaka, Bangladesh, 2010.

[106] T. P. Bednarz, W. Lin, J. C. Patterson, C. Lei, and S. W. Armfield. Scaling for unsteady thermo-magnetic convection boundary layer of paramagnetic fluids of Pr $>$ 1 in micro-gravity conditions. *International Journal of Heat and Fluid Flow*, 30: 1157–1170, 2009.

[107] T. Aberra, S. W. Armfield, and M. Behnia. Prandtl number scaling of the natural convection flow over an evenly heated vertical plate (Pr $>$ 1). In *CHT-08 ICHMT Fourth International Symposium on Advances in Computational Heat Transfer*, Connecticut, USA: Begell House Inc., 2008.

[108] S. C. Saha, R. J. Brown, and Y. T. Gu. Scaling for the Prandtl number of the natural convection boundary layer of an inclined flat plate under uniform surface heat flux. *International Journal of Heat and Mass Transfer*, 55: 2394–2401, 2012.

[109] S. C. Saha, J. C. Patterson, and C. Lei. Scaling of natural convection of an inclined flat plate : sudden cooling condition. *Journal of Heat Transfer*, 133: 041503–041511, 2011.

[110] S. C. Saha. Scaling of free convection heat transfer in a triangular cavity for Pr $>$ 1. *Energy and Buildings*, 43: 2908–2917, 2011.

[111] S. C. Saha, R. J. Brown, and Y. Gu. Prandtl number scaling of the unsteady natural convection boundary layer adjacent to a vertical flat plate for Pr $>$ 1 subject to ramp surface heat flux. *International Journal of Heat and Mass Transfer*, 55: 7046–7055, 2012.

[112] W. Lin, S. W. Armfield, J. C. Patterson, and C. Lei. Prandtl number scaling of unsteady natural convection boundary layers for Pr $>$ 1 fluids under isothermal heating. *Physical Review E*, 79: 066313, 2009.

[113] W. Lin and S. W. Armfield. Scalings for unsteady natural convection boundary layers on an evenly heated plate with time-dependent heating flux. *Physical Review E*, 88: 063013, 2013.

[114] R. Viskanta, D. M. Kim, and C. Gau. Three-dimensional natural convection heat transfer of a liquid metal in a cavity. *International journal of heat and mass transfer*, 29: 475–485, 1986.

[115] S. Arcidiacono, I. D. Piazza, and M. Ciofalo. Low-Prandtl number natural convection in volumetrically heated rectangular enclosures: II. square cavity, AR=1. *International Journal of Heat and Mass Transfer*, 44: 537–550, 2001.

[116] I. D. Piazza and M. Ciofalo. Low-Prandtl number natural convection in volumetrically heated rectangular enclosures: I. slender cavity, AR = 4. *International Journal of Heat and Mass Transfer*, 43: 3027–3051, 2000.

[117] A. Koca, H. F. Oztop, and Y. Varol. The effects of Prandtl number on natural convection in triangular enclosures with localized heating from below. *International Communications in Heat and Mass Transfer*, 34: 511–519, 2007.

[118] A. T. Kirkpatrick and M. Bohn. An experimental investigation of mixed cavity natural convection in the high Rayleigh number regime. *International Journal of Heat and Mass Transfer*, 29: 69–82, 1986.

[119] H. S. Dol and K. Hanjali. Computational study of turbulent natural convection in a side-heated near-cubic enclosure at a high Rayleigh number. *International Journal of Heat and Mass Transfer*, 44: 2323–2344, 2001.

[120] O. V. Trevisan and A. Bejan. Mass and heat transfer by high Rayleigh number convection in a porous medium heated from below. *International Journal of Heat and Mass Transfer*, 30: 2341–2356, 1987.

[121] C. Quon. High Rayleigh number convection in an enclosurea numerical study. *The Physics of Fluids*, 15: 12–19, 1972.

[122] H. N. Dixit and V. Babu. Simulation of high Rayleigh number natural convection in a square cavity using the lattice boltzmann method. *International Journal of Heat and Mass Transfer*, 49: 727–739, 2006.

[123] F. A. Kulacki and A. A. Emara. *High Rayleigh number convection in enclosed fluid layers with internal heat sources*. The University of Michigan, 1975.

[124] Y. Le Peutrec and G. Lauriat. Effects of the heat transfer at the side walls on natural convection in cavities. *Journal of Heat Transfer*, 370–378, 1990.

[125] V. C. Mariani and A. D. Silva. Natural convection: analysis of partially open enclosures with an internal heated source. *Numerical Heat Transfer, Part A: Applications*, 52: 595–619, 2007.

[126] T. Basak, S. Roy, and A. R. Balakrishnan. Effects of thermal boundary conditions on natural convection flows within a square cavity. *International Journal of Heat and Mass Transfer*, 49: 4525–4535, 2006.

[127] M. M. Ganzarolli and L. F. Milanez. Natural convection in rectangular enclosures heated from below and symmetrically cooled from the sides. *International Journal of Heat and Mass Transfer*, 38: 1063–1073, 1995.

[128] M. Sathiyamoorthy, T. Basak, S. Roy, and N. C. Mahanti. Effect of the temperature difference aspect ratio on natural convection in a square cavity for nonuniform thermal boundary conditions. *Journal of Heat Transfer*, 129: 1723–1728, 2007.

[129] B. Calcagni, F. Marsili, and M. Paroncini. Natural convective heat transfer in square enclosures heated from below. *Applied Thermal Engineering*, 25: 2522–2531, 2005.

[130] O. Aydin, A. Ünal, and T. Ayhan. Natural convection in rectangular enclosures heated from one side and cooled from the ceiling. *International Journal of Heat and Mass Transfer*, 42: 2345–2355, 1999.

[131] B. Farouk and T. Fusegi. Natural convection of a variable property gas in asymmetrically heated square cavities. *Journal of Thermophysics and Heat Transfer*, 3: 85–87, 1989.

[132] Y. Varol, A. Koca, and H. F. Oztop. Natural convection in a triangle enclosure with flush mounted heater on the wall. *International Communications in Heat and Mass Transfer*, 33: 951–958, 2006.

[133] I. Ishihara, T. Fukui, and R. Matsumoto. Natural convection in a vertical rectangular enclosure with symmetrically localized heating and cooling zones. *International Journal of Heat and Fluid Flow*, 23: 366–372, 2002.

[134] K. B. Nasr, R. Chouikh, C. Kerkeni, and A. Guizani. Numerical study of the natural convection in cavity heated from the lower corner and cooled from the ceiling. *Applied Thermal Engineering*, 26: 772–775, 2006.

[135] O. Aydin and W. J. Yang. Natural convection in enclosures with localized heating from below and symmetrical cooling from sides. *International Journal of Numerical Methods for Heat and Fluid Flow*, 10: 518–529, 2000.

[136] G. R. Ahmed and M. Yovanovich. Numerical study of natural convection from discrete heat sources in a vertical square enclosure. *Journal of thermophysics and heat transfer*, 6: 121–127, 1992.

[137] M. Hasnaoui, E. Bilgen, and P. Vasseur. Natural convection heat transfer in rectangular cavities partially heated from below. *Journal of Thermophysics and Heat Transfer*, 6: 255–264, 1992.

[138] P. K. B. Chao, H. Ozoe, S. W. Churchill, and N. Lior. Laminar natural convection in an inclined rectangular box with the lower surface half-heated and half-insulated. *Journal of Heat Transfer*, 105: 425–432, 1983.

[139] M. M. El-Refaee, M. M. Elsayed, N. M. Al-Najem, and A. A. Noor. Natural convection in partially cooled tilted cavities. *International Journal for Numerical Methods in Fluids*, 28: 477–499, 1998.

[140] H. H. S. Chu, S. W. Churchill, and C. V. S. Patterson. Effect of heater size, location, aspect ratio, and boundary conditions on two-dimensional, laminar, natural convection in rectangular channels. *Journal of Heat Transfer*, 98 Ser C: 194–201, 1976.

[141] H. Trkoglu and N. Ycel. Effect of heater and cooler locations on natural convection in square cavities. *Numerical Heat Transfer, Part A: Applications*, 27: 351–358, 1995.

[142] A. Valencia and R. L. Frederick. Heat transfer in square cavities with partially active vertical walls. *International Journal of Heat and Mass Transfer*, 32: 1567–1574, 1989.

[143] K. S. Hwang, J. H. Lee, and S. P. Jang. Buoyancy-driven heat transfer of water-based al2o3 nanofluids in a rectangular cavity. *International Journal of Heat and Mass Transfer*, 50: 4003–4010, 2007.

[144] H. F. Oztop and E. Abu-Nada. Numerical study of natural convection in partially heated rectangular enclosures filled with nanofluids. *International Journal of Heat and Fluid Flow*, 29: 1326–1336, 2008.

[145] K. Khanafer, K. Vafai, and M. Lightstone. Buoyancy-driven heat transfer enhancement in a two-dimensional enclosure utilizing nanofluids. *International Journal of Heat and Mass Transfer*, 46: 3639–3653, 2003.

[146] R. Y. Jou and S. C. Tzeng. Numerical research of nature convective heat transfer enhancement filled with nanofluids in rectangular enclosures. *International Communications in Heat and Mass Transfer*, 33: 727–736, 2006.

[147] G. Polidori, S. Fohanno, and C. T. Nguyen. A note on heat transfer modelling of newtonian nanofluids in laminar free convection. *International Journal of Thermal Sciences*, 46: 739–744, 2007.

[148] N. Putra, W. Roetzel, and S. K. Das. Natural convection of nano-fluids. *Heat and Mass Transfer*, 39: 775–784, 2003.

[149] D. Wen and Y. Ding. Formulation of nanofluids for natural convective heat transfer applications. *International Journal of Heat and Fluid Flow*, 26: 855–864, 2005.

[150] A. G. Nnanna. Experimental model of temperature-driven nanofluid. *Journal of Heat Transfer*, 129: 697–704, 2007.

[151] C. H. Li and G. P. Peterson. Experimental studies of natural convection heat transfer of Al_2O_3/DI water nanoparticle suspensions (nanofluids). *Advances in Mechanical engineering*, 2010.

[152] C. J. Ho, D. S. Chen, W. M. Yan, and O. Mahian. Buoyancy-driven flow of nanofluids in a cavity considering the ludwig–soret effect and sedimentation: Numerical study and experimental validation. *International Journal of Heat and Mass Transfer*, 77: 684–694, 2014.

[153] M. Jahanshahi, S. F. Hosseinizadeh, M. Alipanah, A. Dehghani, and G. R. Vakilinejad. Numerical simulation of free convection based on experimental measured conductivity in a square cavity using $water/SiO_2$ nanofluid. *International Communications in Heat and Mass Transfer*, 37: 687–694, 2010.

[154] R. Anderson and G. Lauriat. Horizontal natural convection boundary layer regime in a closed cavity. In *International Heat Transfer Conference*, volume 4, 1453–1458, 1986.

[155] F. Arpino, N. Massarotti, and A. Mauro. High Rayleigh number laminar-free convection in cavities: New benchmark solutions. *Numerical Heat Transfer, Part B: Fundamentals*, 58: 73–97, 2010.

[156] A. Bari. Transient natural 2D convection in a cylindrical cavity with the upper face cooled by thermoelectric peltier effect following an exponential law. *Applied Thermal Engineering*, 23: 431–447, 2003.

[157] D. K. Edwards and Ivan Catton. Prediction of heat transfer by natural convection in closed cylinders heated from below. *International Journal of Heat and Mass Transfer*, 12: 23–30, 1969.

[158] C. Lei, S. W. Armfield, and J. C. Patterson. Unsteady natural convection in a water-filled isosceles triangular enclosure heated from below. *International Journal of Heat and Mass Transfer*, 51: 2637–2650, 2008.

[159] T. Basak, S. Roy, and Ch. Thirumalesha. Finite element analysis of natural convection in a triangular enclosure: Effects of various thermal boundary conditions. *Chemical Engineering Science*, 62: 2623–2640, 2007.

[160] C. P. Chiu and W. R. Chen. Transient natural convection heat transfer between concentric and vertically eccentric spheres. *International Journal of Heat and Mass Transfer*, 39: 1439–1452, 1996.

[161] Y. Varol, H. F. Oztop, and I. Pop. Natural convection in right-angle porous trapezoidal enclosure partially cooled from inclined wall. *International Communications in Heat and Mass Transfer*, 36: 6–15, 2009.

[162] F. Almeida and D. Naylor. Experimental study of free convection in a window with a heated between-panes blind. *Energy and Buildings*, 43: 2647–2655, 2011.

[163] K. D. Aldridge and H. Yao. Flow features of natural convection in a parallelogrammic enclosure. *International Communications in Heat and Mass Transfer*, 28: 923–931, 2001.

[164] H. Saleh, A. I. Alsabery, and I. Hashim. Natural convection in polygonal enclosures with inner circular cylinder. *Advances in Mechanical Engineering*, 7, 2015.

[165] A. Bari and J. M. Garca de Mara. Numerical and experimental study of steady state free convection generated by constant heat flux in tilted hemispherical cavities. *International Journal of Heat and Mass Transfer*, 66: 355–365, 2013.

[166] Y. Shiina, K. Fujimura, T. Kunugi, and N. Akino. Natural convection in a hemispherical enclosure heated from below. *International Journal of Heat and Mass Transfer*, 37: 1605–1617, 1994.

[167] E. H. Ridouane and A. Campo. Numerical simulation of the 3d behavior of thermal buoyant airflows in pentahedral spaces. *International Journal of Heat and Fluid Flow*, 29: 1360–1368, 2008.

[168] J. M. Hyun and B. S. Choi. Transient natural convection in a parallelogram-shaped enclosure. *International Journal of Heat and Fluid Flow*, 11: 129–134, 1990.

[169] L. Iyican, Y. Bayazitoglu, and L. C. Witte. An analytical study of natural conwectiwe heat transfer within a trapezoidal enclosure. *Journal of Heat Transfer*, 102: 640–647, 1980.

[170] E. F. Kent. Numerical analysis of laminar natural convection in isosceles triangular enclosures for cold base and hot inclined walls. *Mechanics Research Communications*, 36: 497–508, 2009.

[171] E. Fuad Kent, E. Asmaz, and S. Ozerbay. Laminar natural convection in right triangular enclosures. *Heat and Mass Transfer*, 44: 187, 2007.

[172] J. E. Hart. Stability of the flow in a differentially heated inclined box. *Journal of Fluid Mechanics*, 47: 547–576, 1971.

[173] R. A. Kuyper, Th. H. Van Der Meer, C. J. Hoogendoorn, and R. A. W. M. Henkes. Numerical study of laminar and turbulent natural convection in an inclined square cavity. *International Journal of Heat and Mass Transfer*, 36: 2899–2911, 1993.

[174] K. G. T. Hollands and L. Konicek. Experimental study of the stability of differentially heated inclined air layers. *International Journal of Heat and Mass Transfer*, 16: 1467–1476, 1973.

[175] J. N. Arnold, I. Catton, and D. K. Edwards. Experimental investigation of natural convection in inclined rectangular regions of differing aspect ratios. *Journal of Heat Transfer*, 98 Ser C: 67–71, 1976.

[176] S. M. ElSherbiny, G. D. Raithby, and K. G. T. Hollands. Heat transfer by natural convection across vertical and inclined air layers. *Journal of Heat Transfer*, 104: 96–102, 1982.

[177] A. Kalendar and P. H. Oosthuizen. Natural convective heat transfer from an inclined isothermal square cylinder with an exposed top surface mounted on a flat adiabatic base. In *ASME 2009 Heat Transfer Summer Conference collocated with the InterPACK09 and 3rd Energy Sustainability Conferences*, 115–122. American Society of Mechanical Engineers, 2009.

[178] M. Nateghi and S. W. Armfield. Natural convection flow of air in an inclined open cavity. In Jagoda Crawford and A. J. Roberts, editors, *11th Computational Techniques and Applications Conference CTAC-2003*, volume 45, C870–C890, 2004.

[179] N. Williamson, S. W. Armfield, W. Lin, and M. P. Kirkpatrick. Stability and nusselt number scaling for inclined differentially heated cavity flow. *International Journal of Heat and Mass Transfer*, 97: 787–793, 2016.

[180] W. H. Leong, K. G. T. Hollands, and A. P. Brunger. Experimental nusselt numbers for a cubical-cavity benchmark problem in natural convection. *International Journal of Heat and Mass Transfer*, 42: 1979–1989, 1999.

[181] D. W. Pepper and K. G. T. Hollands. Summary of benchmark numerical studies for 3-d natural convection in an air-filled enclosure. *Numerical Heat Transfer: Part A: Applications*, 42: 1–11, 2002.

[182] P. Le Quéré, C. Weisman, H. Paillère, J. Vierendeels, E. Dick, R. Becker, M. Braack, and J. Locke. Modelling of natural convection flows with large temperature differences: a benchmark problem for low mach number solvers. part 1. reference solutions. *ESAIM: Mathematical Modelling and Numerical Analysis*, 39: 609–616, 2005.

[183] R. Becker and M. Braack. Solution of a stationary benchmark problem for natural convection with large temperature difference. *International journal of thermal sciences*, 41: 428–439, 2002.

[184] N. B. Cheikh, B. B. Beya, and T. Lili. Benchmark solution for time-dependent natural convection flows with an accelerated full-multigrid method. *Numerical Heat Transfer, Part B: Fundamentals*, 52: 131–151, 2007.

[185] G. De Vahl Davis. Natural convection of air in a square cavity: A benchmark numerical solution. *International Journal for Numerical Methods in Fluids*, 3: 249–264, 1983.

[186] F. Ampofo and T. G. Karayiannis. Experimental benchmark data for turbulent natural convection in an air filled square cavity. *International Journal of Heat and Mass Transfer*, 46: 3551–3572, 2003.

[187] S. Wakashima and T. S. Saitoh. Benchmark solutions for natural convection in a cubic cavity using the high-order time–space method. *International Journal of Heat and Mass Transfer*, 47: 853–864, 2004.

[188] S. J. M. Linthorst, W. M. M. Schinkel, and C. J. Hoogendoorn. Flow structure with natural convection in inclined air-filled enclosures. *Journal of Heat Transfer*, 103: 535, 1981.

[189] P. LeQuere and T. De Roquefort. Transition to unsteady natural convection of air in differentially heated vertical cavities. In *Numerical Methods in Laminar and Turbulent Flow*, 841–852, Swansea, U.K., 1985. Pineridge Press.

[190] P. LeQuere and T. De Roquefort. Transition to unsteady natural convection of air in differentially heated vertical cavities. *significant questions in buoyancy affected enclosure or cavity flows*, 60: 29–36, 1986.

[191] D. Kuhn and P. Oosthuizen. Transient natural convective flow in a rectangular enclosure with a uniformly heated vertical wall. In *24th Annual Meeting of the Society of Engineering Science*, Salt Lake City, Utah, U.S.A., 1987.

[192] A. A. Mohamad and R. Viskanta. Transient natural convection of low-Prandtl-number fluids in a differentially heated cavity. *International Journal for Numerical Methods in Fluids*, 13: 61–81, 1991.

[193] J. C. Patterson and S. W. Armfield. Transient features of natural convection in a cavity. *Journal of Fluid Mechanics*, 219: 469–497, 1990.

[194] J. Ma and F. Xu. Transient flows around a fin at different positions. *Procedia Engineering*, 126: 393–398, 2015.

[195] S. Jiracheewanun, S. W. Armfield, M. Behnia, and G. McBain. The transient behaviour of a differentially heated cavity with isoflux boundaries. In *15th Australasian Fluid Mechanics Conference AFMC 2004*, Australia: University of Sydney, 2004.

[196] J. Rostami. Unsteady natural convection in an enclosure with vertical wavy walls. *Heat and Mass Transfer*, 44: 1079–1087, 2007.

[197] M. N. Hasan, S. C. Saha, and Y. Gu. Unsteady natural convection within a differentially heated enclosure of sinusoidal corrugated side walls. *International Journal of Heat and Mass Transfer*, 55: 5696–5708, July 2012.

[198] N. Nithyadevi, P. Kandaswamy, and S. Sivasankaran. Natural convection in a square cavity with partially active vertical walls: Time-periodic boundary condition. *Mathematical Problems in Engineering*, 2006: 1–16, 2006.

[199] D. Kizildag, C. Perez-Segarra, A. Oliva, and I. Rodrguez. Numerical simulations of natural convection flow in a rectangular cavity under transient boundary conditions. In *5th European Congress on Computational Methods in Applied Sciences and Engineering*, Venice, Italy, 2008.

[200] O. Younis, J. Pallares, and F. X. Grau. Transient natural convection cooling of a high Prandtl number fluid in a cubical cavity. *Meccanica*, 46: 989–1006, 2010.

[201] W. Lin. *Scaling analysis and direct simulation of unsteady weak fountains and natural convection flow*. PhD thesis, The Department of Mechanical and Mechatronic Engineering, The University of Sydney, 2000.

[202] W. Lin and S. W. Armfield. Direct simulation of natural convection cooling in a vertical circular cylinder. *International Journal of Heat and Mass Transfer*, 42: 4117–4130, 1999.

[203] W. Lin and S. W. Armfield. Direct simulation of weak axisymmetric fountains in a homogeneous fluid. *Journal of Fluid Mechanics*, 403: 67–88, 2000.

[204] W. Lin and S. W. Armfield. Natural convection cooling of rectangular and cylindrical containers. *International Journal of Heat and Fluid Flow*, 22: 72–81, 2001.

[205] D. Poulikakos and A. Bejan. Natural convection experiments in a triangular enclosure. *Journal of heat transfer*, 105: 652–655, 1983.

[206] D. Poulikakos and A. Bejan. The fluid dynamics of an attic space. *Journal of Fluid Mechanics*, 131: 251–269, 1983.

[207] H. Salmun. Convection patterns in a triangular domain. *International Journal of Heat and Mass Transfer*, 38: 351–362, 1995.

[208] Y. E. Karyakin, Y. A. Sokovishin, and O. G. Martynenko. Transient natural convection in triangular enclosures. *International Journal of Heat and Mass Transfer*, 31: 1759–1766, 1988.

[209] S. C. Saha. Unsteady natural convection in a triangular enclosure under isothermal heating. *Energy and Buildings*, 43: 695–703, 2011.

[210] E. H. Ridouane and A. Campo. Formation of a pitchfork bifurcation in thermal convection flow inside an isosceles triangular cavity. *Physics of Fluids*, 18: 074–102, 2006.

[211] E. H. Ridouane and A. Campo. Relationship between thermal convection intensity and aspect ratio of two triangular cavities inscribed in horizontal rectangular cavities. *International Journal of Numerical Methods for Heat & Fluid Flow*, 16: 338–355, 2006.

[212] C. Lei and J. C. Patterson. Unsteady natural convection in a triangular enclosure induced by absorption of radiation. *Journal of Fluid Mechanics*, 460: 181–209, 2002.

[213] C. Lei and J. C. Patterson. Unsteady natural convection in a triangular enclosure induced by surface cooling. *International Journal of Heat and Fluid Flow*, 26: 307–321, 2005.

[214] S. C. Saha, J. C. Patterson, and C. Lei. Natural convection and heat transfer in attics subject to periodic thermal forcing. *International Journal of Thermal Sciences*, 49: 1899–1910, 2010.

[215] S. C. Saha, J. C. Patterson, and C. Lei. Natural convection in attics subject to instantaneous and ramp cooling boundary conditions. *Energy and Buildings*, 42: 1192–1204, 2010.

[216] J. Imberger. Natural convection in a shallow cavity with differentially heated end walls. part 3. experimental results. *Journal of Fluid Mechanics*, 65: 247–260, 1974.

[217] P. Filis and D. Poulikakos. An experimental study of the effect of wall temperature nonuniformity on natural convection in an enclosure heated from the side. *International journal of heat and fluid flow*, 7: 258–265, 1986.

[218] N. Ramesh and S. P. Venkateshan. Experimental study of natural convection in a square enclosure using differential interferometer. *International Journal of Heat and Mass Transfer*, 44: 1107–1117, 2001.

[219] I. Tanasawa. Experimental techniques in natural convection. *Experimental Thermal and Fluid Science*, 10: 503–518, 1995.

[220] R. A. V. Ramos, T. Dias, and L. F. Milanez. Numerical and experimental analysis of natural convection in a cavity with flush mounted heat sources on a side wall. In *Thermal and Thermomechanical Phenomena in Electronic Systems*, 130–134, 1998.

[221] F. Corvaro and M. Paroncini. Experimental analysis of natural convection in square cavities heated from below with 2D-PIV and holographic interferometry techniques. *Experimental Thermal and Fluid Science*, 31: 721–739, 2007.

[222] S. J. Lee and S. Kim. Application of holographic interferometry and 2D-PIV for HSC convective flow diagnostics. *Measurement Science and Technology*, 15: 664–672, 2004.

[223] Y. S. Tian and T. G. Karayiannis. Low turbulence natural convection in an air filled square cavity part i: The thermal and fluid flow fields. *International Journal of Heat and Mass Transfer*, 43: 849–866, 2000.

[224] B. F. Armaly, A. Li, and J. H. Nie. Measurements in three-dimensional laminar separated flow. *International Journal of Heat and Mass Transfer*, 46: 3573–3582, 2003.

[225] P. L. Betts and I. H. Bokhari. Experiments on turbulent natural convection in an enclosed tall cavity. *International Journal of Heat and Fluid Flow*, 21: 675–683, 2000.

[226] D. Saury, N. Rouger, F. Djanna, and F. Penot. Natural convection in an air-filled cavity: Experimental results at large Rayleigh numbers. *International Communications in Heat and Mass Transfer*, 38: 679–687, 2011.

[227] C. G. Jeevaraj and J. C. Patterson. Experimental study of transient natural convection of glycerol-water mixtures in a side heated cavity. *International Journal of Heat and Mass Transfer*, 35: 1573–1587, 1992.

[228] L. Kolsi, M. B. B. Hamida, W. Hassen, A. K. Hussein, M. N. Borjini, S. Sivasankaran, S. C. Saha, M. M. Awad, F. Fathinia, and H. B. Aissia. Experimental and numerical investigations of transient natural convection in differentially heated air-filled tall cavity. *American Journal of Modern Energy*, 1: 30–43, 2015.

[229] G. N. Ivey. Experiments on transient natural convection in a cavity. *Journal of Fluid Mechanics*, 144: 389–401, 7 1984.

[230] T. D. Upton and D. W. Watt. Experimental study of transient natural convection in an inclined rectangular enclosure. *International Journal of Heat and Mass Transfer*, 40: 2679–2690, 1997.

[231] C. F. Henze and Hess R. H. Experimental investigation of natural convection losses from open cavities. *Journal of Heat Transfer*, 106: 333–368, 1984.

[232] R. Yewell, D. Poulikakos, and A. Bejan. Transient natural convection experiments in shallow enclosures. *Journal of Heat Transfer*, 104: 533–538, 1982.

[233] J. Salat, S. Xin, P. Joubert, A. Sergent, F. Penot, and P. Le Qur. Experimental and numerical investigation of turbulent natural convection in a large air-filled cavity. *International Journal of Heat and Fluid Flow*, 25: 824–832, 2004.

[234] D. Z. Jeng, C. S. Yang, and C. Gau. Experimental and numerical study of transient natural convection due to mass transfer in inclined enclosures. *International Journal of Heat and Mass Transfer*, 52: 181–192, 2009.

[235] H. F. Oztop, Z. Zhao, and B. Yu. Conduction-combined forced and natural convection in lid-driven enclosures divided by a vertical solid partition. *International Communications in Heat and Mass Transfer*, 36: 661–668, 2009.

[236] S. Ostrach. Natural convection in enclosures. In James P. Hartnett and Thomas F. Irvine, editors, *Advance heat transfer*, volume 8 of *Advances in Heat Transfer*, 161–227. 1972.

[237] Ş. Bilir and A. Ateş. Transient conjugated heat transfer in thick walled pipes with convective boundary conditions. *International Journal of Heat and Mass Transfer*, 46: 2701–2709, 2003.

[238] Y. Varol, H. F. Oztop, and A. Koca. Effects of inclination angle on conductionnatural convection in divided enclosures filled with different fluids. *International Communications in Heat and Mass Transfer*, 37: 182–191, 2010.

[239] E. Papanicolaou and Y. Jaluria. Mixed convection from simulated electronic components at varying relative positions in a cavity. *Journal of Heat Transfer*, 116: 960–970, 1994.

[240] A. Missoum, M. Elmir, A. Belkacem, M. Nabou, and B. Draoui. Numerical simulation of heat transfer through a double-walled facade building in arid zone. *Energy Procedia*, 36: 834–843, 2013.

[241] R. Viskanta and M. Abrams. Thermal interaction of two streams in boundary-layer flow separated by a plate. *International Journal of Heat and Mass Transfer*, 14: 1311–1321, 1971.

[242] G. S. H. Lock and R. S. Ko. Coupling through a wall between two free convective systems. *International Journal of Heat and Mass Transfer*, 16: 2087–2096, 1973.

[243] R. Anderson and A. Bejan. Natural confection on both sides of a vertical wall separating fluids at different temperatures. *Journal of Heat Transfer*, 102: 631, 1980.

[244] A. Bejan and R. Anderson. Heat transfer across a vertical impermeable partition imbedded in porous medium. *International Journal of Heat and Mass Transfer*, 24: 1237–1245, 1981.

[245] A. Bejan and R. Anderson. Natural convection at the interface between a vertical porous layer and an open space. *Journal of Heat Transfer*, 105: 124–129, 1983.

[246] H. T. Chen and S. M. Chang. Numerical simulation for conjugate problem of natural convection on both sides of a vertical wall. *International journal of heat and mass transfer*, 39: 383–390, 1996.

[247] R. Viskanta and D. W. Lankford. Coupling of heat transfer between two natural convection systems separated by a vertical wall. *International Journal of Heat and Mass Transfer*, 24: 1171–1177, 1981.

[248] F. J. Higuera and I. Pop. Conjugate natural convection heat transfer between two porous media separated by a vertical wall. *International journal of heat and mass transfer*, 40: 123–129, 1996.

[249] J. H. Merkin and I. Pop. Conjugate free convection on a vertical surface. *International Journal of heat and Mass transfer*, 39: 1527–1534, 1996.

[250] X. Chen and P. Han. A note on the solution of conjugate heat transfer problems using simple-like algorithms. *International Journal of Heat and Fluid Flow*, 21: 463–467, 2000.

[251] A. A. Mamun, Z. R. Chowdhury, M. A. Azim, and M. A. Maleque. Conjugate heat transfer for a vertical flat plate with heat generation effect. *Nonlinear Analysis: Modelling and Control*, 13: 213–223, 2008.

[252] A. Belzizia, S. Benissaad, and S. Abboudi. Effect of wall conductivity on conjugate natural convection in a square enclosure with finite vertical wall thickness. *Advances in Theoretical and Applied Mechanics*, 5: 179–190, 2012.

[253] N. H. Saeid. Conjugate natural convection in a porous enclosure: effect of conduction in one of the vertical walls. *International Journal of Thermal Sciences*, 46: 531–539, 2007.

[254] W. S. Fu, J. C. Perng, and W. J. Shieh. Transient laminar natural convection in an enclosure partitioned by an adiabatic baffle. *Numerical Heat Transfer, Part A: Applications*, 16: 325–350, 1989.

[255] W. S. Fu, J. C. Perng, and W. J. Shieh. Transient laminar natural convection in a partitioned enclosure heated by uniform flux. *Heat and Mass Transfer*, 25: 233–243, 1990.

[256] F. Xu, J. C. Patterson, and C. Lei. Transient natural convection in a differentially heated cavity with a thin fin of different lengths on a sidewall. In *Proceedings of the 16th Australasian Fluid Mechanics Conference, 16AFMC*, 402–405, 2007.

[257] F. Xu. Unsteady coupled thermal boundary layers induced by a fin on the partition of a differentially heated cavity. *International Communications in Heat and Mass Transfer*, 67: 59–65, 2015.

[258] N. Williamson and S. W. Armfield. Stability characteristics of conjugate natural convection boundary layers. *ANZIAM Journal*, 52: 696–709, 2011.

[259] F. Xu, J. C. Patterson, and C. Lei. Heat transfer through coupled thermal boundary layers induced by a suddenly generated temperature difference. *International Journal of Heat and Mass Transfer*, 52: 4966–4975, 2009.

[260] S. C. Saha, Y. Gu, and M. A. Hossain. Free convection heat transfer through coupled thermal boundary layers in a partitioned triangular enclosure. In *International Conference on Mechanical Engineering*, Dhaka, Bangladesh, December 2011.

[261] C. J. Ho and Y. L. Yih. Conjugate natural convection heat transfer in an air-filled rectangular cavity. *International Communications in Heat and Mass Transfer*, 14: 91–100, 1987.

[262] S. Acharya and C. H. Tsang. Natural convection in a fully partitioned, inclined enclosure. *Numerical Heat Transfer*, 8: 407–428, 1985.

[263] H. Trkoglu and N. Ycel. Natural convection heat transfer in enclosures with conducting multiple partitions and side walls. *Heat and Mass Transfer/Waerme- und Stoffuebertragung*, 32: 1–8, 1996.

[264] P. K. Ghosh, A. Sarkar, and V. M. K. Sastri. Natural convection heat transfer in an enclosure with a partition-a finite-element analysis. *Numerical Heat Transfer*, 21: 231–248, 1992.

[265] T. W. Tong and F. M. Gerner. Natural convection in partitioned air-filled rectangular enclosures. *International Communications in Heat and Mass Transfer*, 13: 99–108, 1986.

[266] A. Kangni, R. B. Yedder, and E. Bilgen. Natural convection and conduction in enclosures with multiple vertical partitions. *International Journal of Heat and Mass Transfer*, 34: 2819–2825, 1991.

[267] K. Kahveci. A differential quadrature solution of natural convection in an enclosure with a finite-thickness partition. *Numerical Heat Transfer, Part A: Applications*, 51: 979–1002, 2007.

[268] F. Xu, Q. Yang, and P. Yu. Numerical studies of transition from steady to unsteady coupled thermal boundary layers. *International Journal of Computational Methods*, 11: 1344002, 2014.

[269] D. M. Cuckovic-Dzodzo, M. B. Dzodzo, and M. D. Pavlovic. Laminar natural convection in a fully partitioned enclosure containing fluid with nonlinear thermophysical properties. *International Journal of Heat and Fluid Flow*, 20: 614–623, 1999.

[270] T. Nishimura, M. Shiraishi, F. Nagasawa, and Y. Kawamura. Natural convection heat transfer in enclosures with multiple vertical partitions. *International Journal of Heat and Mass Transfer*, 31: 1679–1686, 1988.

[271] K. Hanjali, S. Kenjere, and F. Durst. Natural convection in partitioned two-dimensional enclosures at higher Rayleigh numbers. *International Journal of Heat and Mass Transfer*, 39: 1407–1427, 1996.

[272] M. W. Nansteel and R. Greif. Natural convection in undivided and partially divided rectangular enclosures. *Journal of Heat Transfer*, 103: 623–629, 1981.

[273] Nishimura T., Shiraishi M., and Kawamura Y. Natural convection heat transfer in enclosures with an off-center partition. *International Journal of Heat and Mass Transfer*, 30: 1756–1758, 1987.

[274] M. Khatamifar, R. D'Urso, W. Lin, D. Holmes, S. W. Armfield, and M. P. Kirkpatrick. A numerical and experimental study on the unsteady conjugate natural convection boundary layers in a water filled rectangular cavity with a conducting partition wall at varied locations. In Harun Chowdhury and Firoz Alam, editors, *19th Australasian Fluid Mechanics Conference*, 1–4, Melbourne, VIC, 2014. Australasian Fluid Mechanics Society.

[275] F. Xu, J. C. Patterson, and C. Lei. An experimental study of the coupled thermal boundary layers adjacent to a partition in a differentially heated cavity. *Experimental Thermal and Fluid Science*, 54: 12–21, 2014.

[276] F. H. Harlow and J. E. Welch. Numerical calculation of time-dependent viscous incompressible flow of fluid with free surface. *Physics of Fluids*, 8: 2182–2189, 1965.

[277] S. Patankar. *Numerical Heat Transfer and Fluid Flow*. Series in computational methods in mechanics and thermal sciences. Taylor & Francis, 1980.

[278] B. P. Leonard. A stable and accurate convective modelling procedure based on quadratic upstream interpolation. *Computer Methods in Applied Mechanics and Engineering*, 19: 59–98, 1979.

[279] K. Diethelm, N. J. Ford, and A. D. Freed. A predictor-corrector approach for the numerical solution of fractional differential equations. *Nonlinear Dynamics*, 29: 3–22, 2002.

[280] Victor J. K. The history of stokes' theorem. *Mathematics Magazine*, 52: 146–156, 1979.

[281] D. B. Spalding. A novel finite difference formulation for differential expressions involving both first and second derivatives. *International Journal for Numerical Methods in Engineering*, 4: 551–559, 1972.

[282] B. P. Leonard. A stable and accurate convective modelling procedure based on quadratic upstream interpolation. *Computer methods in applied mechanics and engineering*, 19: 59–98, 1979.

[283] A. D. Gosman and F. J. K. Ideriah. Teach-t: A general computer program for two-dimensional. *Turbulent, Recirculating Flows, Dept. of Mechanical Engineering, Imperial College, London*, 1976.

[284] T. J. Craft, S. E. Gant, H. Iacovides, and B. E. Launder. A new wall function strategy for complex turbulent flows. *Numerical Heat Transfer, Part B: Fundamentals*, 45: 301–318, 2004.

[285] G. De Vahl Davis and I. P. Jones. Natural convection in a square cavity: A comparison exercise. *International Journal for Numerical Methods in Fluids*, 3: 227–248, 1983.

[286] C. Wan, B. S. V. Patnaik, and D. G. W. Wei. A new benchmark quality solution for the buoyancy-driven cavity by discrete singular convolution. *Numerical Heat Transfer: Part B: Fundamentals*, 40: 199–228, 2001.

[287] D. R. Chenoweth and S. Paolucci. Natural convection in an enclosed vertical air layer with large horizontal temperature differences. *Journal of Fluid Mechanics*, 169: 173–210, 1986.

[288] P. Le Quéré and T. A. De Roquefortt. Computation of natural convection in two-dimensional cavities with chebyshev polynomials. *Journal of Computational Physics*, 57: 210–228, 1985.

[289] P. Le Quéré. Accurate solutions to the square thermally driven cavity at high Rayleigh number. *Computers & Fluids*, 20: 29–41, 1991.

[290] Riccardo Puragliesi. *Numerical investigation of particle-laden thermally driven turbulent flows in enclosure*. PhD thesis, Faculty of Engineering Science and Technology, 2010.

[291] M. T. Manzari. An explicit finite element algorithm for convection heat transfer problems. *International Journal of Numerical Methods for Heat & Fluid Flow*, 9: 860–877, 1999.

[292] D. A. Mayne, A. S. Usmani, and M. Crapper. h-adaptive finite element solution of high Rayleigh number thermally driven cavity problem. *International Journal of Numerical Methods for Heat & Fluid Flow*, 10: 598–615, 2000.

[293] American Society for Testing, Materials, R. S. Graves, and R. R. Zarr. *Insulation Materials, Testing and Applications, 3rd Volume*. ASTM Special Technical Publication. American Society for Testing Materials, 1911.

[294] Aerogel Technologies LLC. Silica aerogel, 1999.

[295] M. R. Ravi, R. A. W. M. Henkes, and C. J. Hoogendoorn. On the high-Rayleigh-number structure of steady laminar natural-convection flow in a square enclosure. *Journal of Fluid Mechanics*, 262: 325–351, 1994.

[296] B. A. Meyer, J. W. Mitchell, and M. M. El-Wakil. The effect of thermal wall properties on natural convection in inclined rectangular cells. *Journal of Heat Transfer*, 104: 111–117, 1982.

[297] A. Rohatgi. Webplotdigitizer - extract data from plots, images, and maps.

[298] R. Anderson and A. Bejan. Heat transfer through single and double vertical walls in natural convection - Theory and experiment. *International Journal of Heat and Mass Transfer*, 24: 1611–1620, 1981.

[299] D. Duxbury. *An interferometric study of natural convection in enclosed plane air layers with complete and partial central vertical divisions.* PhD thesis, University of Salford, 1979.

[300] A. Ranganathan. The levenberg-marquardt algorithm. *Tutoral on LM algorithm*, 11: 101–110, 2004.

[301] J. J. Moré. The levenberg-marquardt algorithm: implementation and theory. In *Numerical analysis*, 105–116. Springer, 1978.

Appendix A

Variables in the code

Table A.1: Global variables in the code with their description.

Variable name	Variable type	Description
GREAT/ SMALL	double	a large number/ a small number (preventing division by zero)
INCALU, INCALV, INCALP, INCALT, INCALB	bool	activate the corresponding method which are horizontal velocity, vertical velocity, pressure, temperature and buoyancy term methods, respectively.
NI, NJ, NIM1, NJM1	int	total number of grids and total number of grids minus one in the x and y direction.
INPART	bool	activate partition in the cavity
IT,JT	int	the maximum values of NI and NJ
SPa, EPa	int	the cell number of left and right side of a vertical partition, respectively.

Variable name	Variable type	Description
AN, ANN, AS, ASS, AE, AEE, AW, AWW	double	the main coefficients of descretized formula at north, far north, south, far south, east, far east, west and far west, respectively.
SP, SU	double	coefficients of linearized source term.
APO, AP	double	Coefficient for old time step, summation of the main coefficients and APO and SP.
U, UO, UOO, V, VO, VOO, T, TO, TOO	double	horizontal velocity, vertical velocity and temperature values at current, previous and two time steps ago.
X, XU, Y, YV	double	x coordinate of main grid, x coordinate at storage location of u, y coordinate of main grid, y coordinate at storage location of v, respectively.
P, PP, PO	double	pressure, pressure correction and pressure value at previous time step.
DU, DV	double	coefficients of velocity correction term for u and v.
DEN, DENO, VIS	double	density of fluid at current and previous time step and viscosity of fluid.
INHY, INCEN, INQUK	bool	activate the hybrid, central and QUICK schemes respectively.
INDPRI	int	output frequency
TSTEP	double	time step
SF	double	stream function
STEADY	bool	activate steady or unsteady solution.

Variable name	Variable type	Description
DXEP, DXPW	double	consecutive main grid distances in x direction from $X(1)$ to $X(NIM1)$ and from $X(2)$ to $X(NI)$
DYNP, DYPS	double	consecutive main grid distances in y direction from $Y(1)$ to $Y(NJM1)$ and from $Y(2)$ to $Y(NJ)$
DXEPU, DXPWU	double	consecutive staggered grid distances in x direction from $XU(2)$ to $XU(NIM1)$ and from $XU(3)$ to $XU(NI)$
DYNPV, DYPSV	double	consecutive staggered grid distances in y direction from $YV(2)$ to $YV(NJM1)$ and from $YV(3)$ to $YV(NJ)$
SEW, SNS	double	area of main grid control volume in x and y direction respectively.
SEWU, SNSV	double	area of staggered grid control volume in x and y direction respectively.
URFU, URFV, URFT, URFP;	double	under-relaxation factor for u, v, θ and p.
Kr	double	thermal conductivity ratio of partition to fluid

Table A.2: Main local variables in the code with their description.

Variable name	Variable type	Description
NFTSTP, NLTSTP	int	the first and last iteration step
ELBYH	double	aspect ratio of the cavity

Variable name	Variable type	Description
NIM2, NJM2	int	the total number of grids minus two in the x and y direction.
MeshParCoef1	int	grid stretching frequency for sin function mapping
MeshParCoef2	double	controlling the grid stretching value for sin function mapping
MESH_TYPE1	int	grid mapping method selection. 1: sin function mapping, 2: linear function mapping 3: uniform grid and 4: manually defined mapping
IXC, JXC	int	location of sign changing at the linear function grid mapping in the x and y direction.
ISTRENGTH, JSTRENGTH	double	grid strength for linear function grid mapping
XP, TP	double	partition distance from left and partition thickness
RALI, PRANDL	double	Rayleigh and Prandtl number respectively.
IPREF, JPREF	int	grid number where pressure is fixed in x and y directions respectively.
SORMAX	double	the convergence criterion
VALUE	int	0: activate pause ability, 1: inactivate pause ability
K_fluid, K_solid	double	thermal conductivity of fluid and solid

Appendix B

Code

B.1 Horizontal velocity method (u)

```
1    // CALCULATE U
2        static void CALCU(double[] R1, double NSWPU, int ITSTEP)
3        {
4            int NIM1, NJM1;
5            double AREANS, AREAEW, VOL;
6            double GN, GNW, GS, GSW, GE, GP, GW;
7            double CN, CS, CE, CW;
8            double DN, DS, DE, DW;
9            double VISN, VISS;
10           double SMP, CP, CPO;
11           double GAMP, GAMM, RESOR, SORVOL;
12           double DUDXP, DUDXM, DVDXM, DVDXP;
13           NIM1 = G.NI - 1;
14           NJM1 = G.NJ - 1;
15           for (int I = 3; I <= NIM1; I++)
16           {
17               for (int J = 2; J <= NJM1; J++)
```

```
18              {
19                  //COMPUTE AREAS AND VOLUME
20                  AREANS = G.SEWU[I];
21                  AREAEW = G.SNS[J];
22                  VOL = G.SEWU[I] * G.SNS[J];
23                  // CONVECTION COEFFICIENT
24                  GN = 0.5 * (G.DEN[I, J + 1] + G.DEN[I, J]) * G.V[I, J + 1];
25                  GNW = 0.5 * (G.DEN[I - 1, J] + G.DEN[I - 1, J + 1]) * G.V[I
                        - 1, J + 1];
26                  GS = 0.5 * (G.DEN[I, J - 1] + G.DEN[I, J]) * G.V[I, J];
27                  GSW = 0.5 * (G.DEN[I - 1, J] + G.DEN[I - 1, J - 1]) * G.V[I
                        - 1, J];
28                  GE = 0.5 * (G.DEN[I + 1, J] + G.DEN[I, J]) * G.U[I + 1, J];
29                  GP = 0.5 * (G.DEN[I, J] + G.DEN[I - 1, J]) * G.U[I, J];
30                  GW = 0.5 * (G.DEN[I - 1, J] + G.DEN[I - 2, J]) * G.U[I - 1,
                        J];
31                  CN = (0.5 * (GN + GNW) * AREANS) ;
32                  CS = (0.5 * (GS + GSW) * AREANS) ;
33                  CE = (0.5 * (GE + GP) * AREAEW) ;
34                  CW = (0.5 * (GP + GW) * AREAEW) ;
35                  // DIFFUSION COEFFICIENT
36                  VISN = 0.25 * (G.VIS[I, J] + G.VIS[I, J + 1] + G.VIS[I - 1,
                        J] + G.VIS[I - 1, J + 1]);
37                  VISS = 0.25 * (G.VIS[I, J] + G.VIS[I, J - 1] + G.VIS[I - 1,
                        J] + G.VIS[I - 1, J - 1]);
38                  DN = R1[I] * VISN * AREANS / G.DYNP[J];
39                  DS = R1[I] * VISS * AREANS / G.DYPS[J];
40                  DE = R1[I] * G.VIS[I, J] * AREAEW / G.DXEPU[I];
41                  DW = R1[I] * G.VIS[I - 1, J] * AREAEW / G.DXPWU[I];
42                  // SOURCE TERMS
43                  SMP = CN - CS + CE - CW;
```

```
44                  // BLOCKED-OFF REGION (partition)
45                  if (G.INPART)
46                  {
47                      if (I >= G.SPa && I <= G.EPa)
48                      {
49                          SMP = G.GREAT;
50                      }
51
52                  }
53                  CP = Math.Max(0.0, SMP);
54                  CPO = CP;
55                  // ASSEMBLE
56                  // HYBRID
57                  if (G.INHY)
58                  {
59                      G.AN[I, J] = DN * Math.Max(0.0, 1 - 0.5 * Math.Abs(CN /
                            DN)) + Math.Max(-CN, 0.0);
60                      G.AS[I, J] = DS * Math.Max(0.0, 1 - 0.5 * Math.Abs(CS /
                            DS)) + Math.Max(CS, 0.0);
61                      G.AE[I, J] = DE * Math.Max(0.0, 1 - 0.5 * Math.Abs(CE /
                            DE)) + Math.Max(-CE, 0.0);
62                      G.AW[I, J] = DW * Math.Max(0.0, 1 - 0.5 * Math.Abs(CW /
                            DW)) + Math.Max(CW, 0.0);
63                      G.AWW[I, J] = G.AEE[I, J] = G.ASS[I, J] = G.ANN[I, J] =
                            0.0;
64                  }
65                  // CENTRAL
66                  if (G.INCEN)
67                  {
68                      G.AN[I, J] = Math.Max(-CN, 0.0) + DN - 0.5 *
                            Math.Abs(CN);
```

```
69                      G.AS[I, J] = Math.Max(CS, 0.0) + DS - 0.5 *
                            Math.Abs(CS);
70                      G.AE[I, J] = Math.Max(-CE, 0.0) + DE - 0.5 *
                            Math.Abs(CE);
71                      G.AW[I, J] = Math.Max(CW, 0.0) + DW - 0.5 *
                            Math.Abs(CW);
72                      G.AWW[I, J] = G.AEE[I, J] = G.ASS[I, J] = G.ANN[I, J] =
                            0.0;
73                  }
74                  // QUICK
75                  if (G.INQUK)
76                  {
77                      // FOR BOUNDARYS HYBRID SCHEME AND FOR THE REST OF
                            DOMAIN QUICK SCHEME
78                      if (I <= 5 || J <= 4 || I <= NIM1 - 2 || J <= NIM1 - 2)
79                      {
80                          G.AN[I, J] = Math.Max(-CN, 0.0) + DN - 0.5 *
                                Math.Abs(CN);
81                          G.AS[I, J] = Math.Max(CS, 0.0) + DS - 0.5 *
                                Math.Abs(CS);
82                          G.AE[I, J] = Math.Max(-CE, 0.0) + DE - 0.5 *
                                Math.Abs(CE);
83                          G.AW[I, J] = Math.Max(CW, 0.0) + DW - 0.5 *
                                Math.Abs(CW);
84                          G.AWW[I, J] = G.AEE[I, J] = G.ASS[I, J] = G.ANN[I,
                                J] = 0.0;
85                      }
86                      else
87                      {
88                          if (CE > 0 && CW > 0)
89                          {
```

```
90                          G.AE[I, J] = DE - CE * (0.5 - (G.DXPWU[I] / (8 *
                                G.DXPW[I])));
91                          G.AW[I, J] = DW + CW * (0.5 + (G.DXPWU[I - 1] /
                                (8 * G.DXPW[I - 1])) + (G.DXPWU[I - 1] *
                                G.DXPWU[I - 1] / (8 * G.DXPW[I - 1] *
                                G.DXPWU[I - 2]))) + CE * ((G.DXPWU[I] *
                                G.DXPWU[I] / (8 * G.DXPW[I] * G.DXPWU[I -
                                1])));
92                          G.AWW[I, J] = -CW * (G.DXPWU[I - 1] * G.DXPWU[I
                                - 1] / (8 * G.DXPW[I - 1] * G.DXPWU[I - 2]));
93                      }
94                      else
95                      {
96                          G.AE[I, J] = DE - CE * (0.5 + (G.DXPWU[I] / (8 *
                                G.DXPW[I + 1])) + (G.DXPWU[I] * G.DXPWU[I] /
                                (8 * G.DXPW[I + 1]) * G.DXPWU[I + 1]));
97                          G.AW[I, J] = DW + CW * (0.5 - (G.DXPWU[I - 1] /
                                (8 * G.DXPW[I])));
98                          G.AEE[I, J] = (G.DXPWU[I] * G.DXPWU[I] / (8 *
                                G.DXPW[I + 1]) * G.DXPWU[I + 1]);
99                      }
100                     if (CN > 0 && CS > 0)
101                     {
102                         G.AN[I, J] = DN - CN * (0.5 - (G.DYPSV[J] / (8 *
                                G.DYPS[J])));
103                         G.AS[I, J] = DS + CS * (0.5 + (G.DYPSV[J - 1] /
                                (8 * G.DYPS[J - 1])) + (G.DYPSV[J - 1] *
                                G.DYPSV[J - 1] / (8 * G.DYPS[I - 1] *
                                G.DYPSV[J - 2]))) + CN * ((G.DYPSV[J] *
                                G.DYPSV[J] / (8 * G.DYPS[J] * G.DYPSV[J -
                                1])));
```

```
104                         G.ASS[I, J] = -CS * (G.DYPSV[J - 1] * G.DYPSV[J
                                - 1] / (8 * G.DYPS[J - 1] * G.DYPSV[J - 2]));
105                     }
106                     else
107                     {
108                         G.AN[I, J] = DN - CN * (0.5 + (G.DYPSV[J] / (8 *
                                G.DYPS[J + 1])) + (G.DYPSV[J] * G.DYPSV[J] /
                                (8 * G.DYPS[J + 1]) * G.DYPSV[J + 1]));
109                         G.AS[I, J] = DS + CS * (0.5 - (G.DYPSV[J - 1] /
                                (8 * G.DYPS[J])));
110                         G.ANN[I, J] = (G.DYPSV[I] * G.DYPSV[J] / (8 *
                                G.DYPS[J + 1]) * G.DYPSV[J + 1]);
111                     }
112                 }
113             }
114             if (G.STEADY)
115             {
116                 G.APO[I, J] = 0.0;
117             }
118             else
119             {
120                 G.APO[I, J] = G.DEN[I, J] * VOL / G.DT[ITSTEP];
121             }
122             G.DU[I, J] = AREAEW;
123
124             G.SU[I, J] = CPO * G.U[I, J] + G.DU[I, J] * (G.P[I - 1, J]
                    - G.P[I, J]) + 1.5 * (G.APO[I, J] * G.UO[I, J]) - 0.5 *
                    (G.APO[I, J] * G.UOO[I, J]) + G.ANN[I, J] * G.U[I, J +
                    2] + G.ASS[I, J] * G.U[I, J - 2] + G.AWW[I, J] * G.U[I
                    - 2, J] + G.AEE[I, J] * G.U[I + 2, J];
125             G.SP[I, J] = -CP;
```

```
126                 DUDXP = (G.U[I + 1, J] - G.U[I, J]) / G.DXEPU[I];
127                 DUDXM = (G.U[I, J] - G.U[I - 1, J]) / G.DXPWU[I];
128                 DVDXP = (G.V[I, J + 1] - G.V[I - 1, J + 1]) / G.DXPW[I];
129                 DVDXM = (G.V[I, J] - G.V[I - 1, J]) / G.DXPW[I];
130                 G.SU[I, J] = R1[I] * (G.VIS[I, J] * DUDXP - G.VIS[I - 1, J]
                        * DUDXM) / G.SEWU[I] * VOL + G.SU[I, J];
131                 GAMP = 0.25 * (G.VIS[I, J] + G.VIS[I - 1, J] + G.VIS[I, J +
                        1] + G.VIS[I - 1, J + 1]);
132                 GAMM = 0.25 * (G.VIS[I, J] + G.VIS[I - 1, J] + G.VIS[I, J -
                        1] + G.VIS[I - 1, J - 1]);
133                 G.SU[I, J] = R1[I] * (GAMP * DVDXP - GAMM * DVDXM) /
                        G.SNS[J] * VOL + G.SU[I, J];
134             }
135
136         }
137         // MODIFICATION U
138         // TOP WALL
139         for (int I = 3; I <= NIM1; I++)
140         {
141             G.U[I, G.NJ] = 0.0;
142         }
143         // WEST WALL
144         for (int J = 2; J <= NJM1; J++)
145         {
146             G.U[2, J] = 0.0;
147         }
148         //BOTTOM WALL
149         for (int I = 3; I <= NIM1; I++)
150         {
151             G.U[I, 1] = 0.0;
152         }
```

```
153             //EAST WALL
154             for (int J = 2; J <= NJM1; J++)
155             {
156                 G.U[G.NI, J] = 0.0;
157             }
158             // RESIDUAL
159             G.RESORU = 0.0;
160             for (int I = 3; I <= NIM1; I++)
161             {
162                 for (int J = 2; J <= NJM1; J++)
163                 {
164                     G.AP[I, J] = G.AN[I, J] + G.AS[I, J] + G.AE[I, J] + G.AW[I,
                            J] + G.APO[I, J] + G.ANN[I, J] + G.ASS[I, J] + G.AEE[I,
                            J] + G.AWW[I, J] - G.SP[I, J];
165                     G.DU[I, J] = G.DU[I, J] / G.AP[I, J];
166                     RESOR = G.AN[I, J] * G.U[I, J + 1] + G.AS[I, J] * G.U[I, J
                            - 1] + G.AE[I, J] * G.U[I + 1, J] + G.AW[I, J] * G.U[I
                            - 1, J] - G.AP[I, J] * G.U[I, J] + G.SU[I, J];
167                     VOL = G.SEW[I] * G.SNS[J];
168                     SORVOL = G.GREAT * VOL;
169                     if (Math.Abs(G.SP[I, J]) > 0.5 * SORVOL)
170                     {
171                         RESOR = RESOR / SORVOL;
172                     }
173                     G.RESORU = G.RESORU + Math.Abs(RESOR);
174
175                     G.AP[I, J] = G.AP[I, J] / G.URFU;
176                     G.SU[I, J] = G.SU[I, J] + (1.0 - G.URFU) * G.AP[I, J] *
                            G.U[I, J];
177                     G.DU[I, J] = G.DU[I, J] * G.URFU;
178                 }
```

```
179             }
180                 // USE THOMAS ALGORITHM FOR PRESSURE EQUATION
181                 for (int N = 1; N <= NSWPU; N++)
182                 {
183                     LISOLV(3, 2, G.U);
184                 }
185         }
```

B.2 Vertical velocity method (v)

```
1     // CALCULATE V
2         static void CALCV(double[] R1, double NSWPV, double TREF, int ITSTEP)
3         {
4             int NIM1, NJM1;
5             double AREANS, AREAEW, VOL;
6             double GN, GS, GSW, GE, GP, GW, GSE;
7             double CN, CS, CE, CW;
8             double DN, DS, DE, DW;
9             double VISE, VISW;
10            double SMP, CP, CPO;
11            double RGAMP, RGAMM, GAMP, GAMM, RESOR, SORVOL;
12            double DUDYP, DUDYM, DVDYP, DVDYM;
13            double BUOYA;
14            NIM1 = G.NI - 1;
15            NJM1 = G.NJ - 1;
16            for (int I = 2; I <= NIM1; I++)
17            {
18                for (int J = 3; J <= NJM1; J++)
19                {
20                    //COMPUTE AREAS AND VOLUME
```

```
21                  AREANS = G.SEW[I];
22                  AREAEW = G.SNSV[J];
23                  VOL = G.SEW[I] * G.SNSV[J];
24                  // CONVECTION COEFFICIENT
25                  GN = 0.5 * (G.DEN[I, J + 1] + G.DEN[I, J]) * G.V[I, J + 1];
26                  GP = 0.5 * (G.DEN[I, J] + G.DEN[I, J - 1]) * G.V[I, J];
27                  GS = 0.5 * (G.DEN[I, J - 1] + G.DEN[I, J - 2]) * G.V[I, J -
                        1];
28                  GE = 0.5 * (G.DEN[I + 1, J] + G.DEN[I, J]) * G.U[I + 1, J];
29                  GSE = 0.5 * (G.DEN[I, J - 1] + G.DEN[I + 1, J - 1]) * G.U[I
                        + 1, J - 1];
30                  GW = 0.5 * (G.DEN[I, J] + G.DEN[I - 1, J]) * G.U[I, J];
31                  GSW = 0.5 * (G.DEN[I, J - 1] + G.DEN[I - 1, J - 1]) *
                        G.U[I, J - 1];
32                  CN = (0.5 * (GN + GP) * AREANS) ;
33                  CS = (0.5 * (GS + GP) * AREANS) ;
34                  CE = (0.5 * (GE + GSE) * AREAEW) ;
35                  CW = (0.5 * (GSW + GW) * AREAEW) ;
36                  // DIFFUSION COEFFICIENT
37                  VISE = 0.25 * (G.VIS[I, J] + G.VIS[I + 1, J] + G.VIS[I, J -
                        1] + G.VIS[I + 1, J - 1]);
38                  VISW = 0.25 * (G.VIS[I, J] + G.VIS[I - 1, J] + G.VIS[I, J -
                        1] + G.VIS[I - 1, J - 1]);
39                  DN = R1[I] * G.VIS[I, J] * AREANS / G.DYNPV[J];
40                  DS = R1[I] * G.VIS[I, J - 1] * AREANS / G.DYPSV[J];
41                  DE = R1[I] * VISE * AREAEW / G.DXEP[I];
42                  DW = R1[I] * VISW * AREAEW / G.DXPW[I];
43                  // SOURCE TERMS
44                  SMP = CN - CS + CE - CW;
45                  // BLOCKED-OFF REGION (PARTITION DIFINATION)
46                  if (G.INPART)
```

```
47                  {
48                      if (I >= G.SPa && I <= G.EPa)
49                      {
50                          SMP = G.GREAT;
51                      }
52
53                  }
54                  CP = Math.Max(0.0, SMP);
55                  CPO = CP;
56                  // ASSEMBLE
57                  //HYBRID
58                  if (G.INHY)
59                  {
60                      G.AN[I, J] = DN * Math.Max(0.0, 1 - 0.5 * Math.Abs(CN /
                            DN)) + Math.Max(-CN, 0.0);
61                      G.AS[I, J] = DS * Math.Max(0.0, 1 - 0.5 * Math.Abs(CS /
                            DS)) + Math.Max(CS, 0.0);
62                      G.AE[I, J] = DE * Math.Max(0.0, 1 - 0.5 * Math.Abs(CE /
                            DE)) + Math.Max(-CE, 0.0);
63                      G.AW[I, J] = DW * Math.Max(0.0, 1 - 0.5 * Math.Abs(CW /
                            DW)) + Math.Max(CW, 0.0);
64                      G.AWW[I, J] = G.AEE[I, J] = G.ASS[I, J] = G.ANN[I, J] =
                            0.0;
65
66                  }
67                  // CENTRAL
68                  if (G.INCEN)
69                  {
70                      G.AN[I, J] = Math.Max(-CN, 0.0) + DN - 0.5 *
                            Math.Abs(CN);
```

```
71                      G.AS[I, J] = Math.Max(CS, 0.0) + DS - 0.5 *
                            Math.Abs(CS);
72                      G.AE[I, J] = Math.Max(-CE, 0.0) + DE - 0.5 *
                            Math.Abs(CE);
73                      G.AW[I, J] = Math.Max(CW, 0.0) + DW - 0.5 *
                            Math.Abs(CW);
74                      G.AWW[I, J] = G.AEE[I, J] = G.ASS[I, J] = G.ANN[I, J] =
                            0.0;
75
76                  }
77                  // QUICK
78                  if (G.INQUK)
79                  {
80                      // FOR BOUNDARYS HYBRID SCHEME AND FOR THE REST OF
                            DOMAIN QUICK SCHEME
81                      if (I <= 5 || J <= 4 || I <= NIM1 - 2 || J <= NIM1 - 2)
82                      {
83                          G.AN[I, J] = Math.Max(-CN, 0.0) + DN - 0.5 *
                                Math.Abs(CN);
84                          G.AS[I, J] = Math.Max(CS, 0.0) + DS - 0.5 *
                                Math.Abs(CS);
85                          G.AE[I, J] = Math.Max(-CE, 0.0) + DE - 0.5 *
                                Math.Abs(CE);
86                          G.AW[I, J] = Math.Max(CW, 0.0) + DW - 0.5 *
                                Math.Abs(CW);
87                          G.AWW[I, J] = G.AEE[I, J] = G.ASS[I, J] = G.ANN[I,
                                J] = 0.0;
88                      }
89                      else
90                      {
91                          if (CE > 0 && CW > 0)
```

```
92                          {
93                              G.AE[I, J] = DE - CE * (0.5 - (G.DXPWU[I] / (8 *
                                    G.DXPW[I])));
94                              G.AW[I, J] = DW + CW * (0.5 + (G.DXPWU[I - 1] /
                                    (8 * G.DXPW[I - 1])) + (G.DXPWU[I - 1] *
                                    G.DXPWU[I - 1] / (8 * G.DXPW[I - 1] *
                                    G.DXPWU[I - 2]))) + CE * ((G.DXPWU[I] *
                                    G.DXPWU[I] / (8 * G.DXPW[I] * G.DXPWU[I -
                                    1])));
95                              G.AWW[I, J] = -CW * (G.DXPWU[I - 1] * G.DXPWU[I
                                    - 1] / (8 * G.DXPW[I - 1] * G.DXPWU[I - 2]));
96                          }
97                          else
98                          {
99                              G.AE[I, J] = DE - CE * (0.5 + (G.DXPWU[I] / (8 *
                                    G.DXPW[I + 1])) + (G.DXPWU[I] * G.DXPWU[I] /
                                    (8 * G.DXPW[I + 1]) * G.DXPWU[I + 1]));
100                             G.AW[I, J] = DW + CW * (0.5 - (G.DXPWU[I - 1] /
                                    (8 * G.DXPW[I])));
101                             G.AEE[I, J] = (G.DXPWU[I] * G.DXPWU[I] / (8 *
                                    G.DXPW[I + 1]) * G.DXPWU[I + 1]);
102                         }
103                         if (CN > 0 && CS > 0)
104                         {
105                             G.AN[I, J] = DN - CN * (0.5 - (G.DYPSV[J] / (8 *
                                    G.DYPS[J])));
106                             G.AS[I, J] = DS + CS * (0.5 + (G.DYPSV[J - 1] /
                                    (8 * G.DYPS[J - 1])) + (G.DYPSV[J - 1] *
                                    G.DYPSV[J - 1] / (8 * G.DYPS[I - 1] *
                                    G.DYPSV[J - 2]))) + CN * ((G.DYPSV[J] *
                                    G.DYPSV[J] / (8 * G.DYPS[J] * G.DYPSV[J -
```

```
                                1])));
107                         G.ASS[I, J] = -CS * (G.DYPSV[J - 1] * G.DYPSV[J
                                - 1] / (8 * G.DYPS[J - 1] * G.DYPSV[J - 2]));
108                     }
109                     else
110                     {
111                         G.AN[I, J] = DN - CN * (0.5 + (G.DYPSV[J] / (8 *
                                G.DYPS[J + 1])) + (G.DYPSV[J] * G.DYPSV[J] /
                                (8 * G.DYPS[J + 1]) * G.DYPSV[J + 1]));
112                         G.AS[I, J] = DS + CS * (0.5 - (G.DYPSV[J - 1] /
                                (8 * G.DYPS[J])));
113                         G.ANN[I, J] = (G.DYPSV[I] * G.DYPSV[J] / (8 *
                                G.DYPS[J + 1]) * G.DYPSV[J + 1]);
114                     }
115                 }
116             }
117             if (G.STEADY)
118             {
119                 G.APO[I, J] = 0.0;
120             }
121             else
122             {
123                 G.APO[I, J] = G.DEN[I, J] * VOL / G.DT[ITSTEP];
124             }
125             G.DV[I, J] = AREANS;
126             G.SU[I, J] = CPO * G.V[I, J] + G.DV[I, J] * (G.P[I, J - 1]
                - G.P[I, J]) + 1.5 * (G.APO[I, J] * G.VO[I, J]) - 0.5 *
                (G.APO[I, J] * G.VOO[I, J]) + G.ANN[I, J] * G.V[I, J +
                2] + G.ASS[I, J] * G.V[I, J - 2] + G.AWW[I, J] * G.V[I
                - 2, J] + G.AEE[I, J] * G.V[I + 2, J];
127             // BUOYANCY TERM
```

```
128                     TREF = 0.0;
129                     if (G.INCALB)
130                     {
131                         BUOYA = (0.5 * (G.T[I, J] + G.T[I, J - 1]) - TREF);
132                         G.SU[I, J] = G.SU[I, J] + BUOYA * VOL;
133                     }
134                     G.SP[I, J] = -CP;
135                     DUDYP = (G.U[I + 1, J] - G.U[I + 1, J - 1]) / G.DYPS[J];
136                     GAMP = 0.25 * (G.VIS[I, J] + G.VIS[I + 1, J] + G.VIS[I, J -
                            1] + G.VIS[I + 1, J - 1]);
137                     GAMM = 0.25 * (G.VIS[I, J] + G.VIS[I - 1, J] + G.VIS[I, J -
                            1] + G.VIS[I - 1, J - 1]);
138                     DUDYM = (G.U[I, J] - G.U[I, J - 1]) / G.DYPS[J];
139                     DVDYP = (G.V[I, J + 1] - G.V[I, J]) / G.DYNPV[J];
140                     DVDYM = (G.V[I, J] - G.V[I, J - 1]) / G.DYPSV[J];
141                     G.SU[I, J] = R1[I] * (GAMP * DUDYP - GAMM * DUDYM) /
                            G.SEW[I] * VOL + G.SU[I, J];
142                     RGAMP = G.VIS[I, J]; RGAMM = G.VIS[I, J - 1];
143                     G.SU[I, J] = R1[I] * (RGAMP * DVDYP - RGAMM * DVDYM) /
                            G.SNSV[J] * VOL + G.SU[I, J];
144                 }
145
146             }
147             // MODIFICATION V
148             // WEST WALL
149             for (int J = 3; J <= NJM1; J++)
150             {
151                 G.V[1, J] = 0.0;
152             }
153             // TOP WALL
154             for (int I = 2; I <= NIM1; I++)
```

```
155             {
156                 G.V[I, G.NJ] = 0.0;
157             }
158             //EAST WALL
159             for (int J = 3; J <= NJM1; J++)
160             {
161                 G.V[G.NI, J] = 0.0;
162             }
163             //BOTTOM WALL
164             for (int I = 2; I <= NIM1; I++)
165             {
166                 G.V[I, 2] = 0.0;
167             }
168             // RESIDUAL
169             G.RESORV = 0.0;
170             for (int I = 2; I <= NIM1; I++)
171             {
172                 for (int J = 3; J <= NJM1; J++)
173                 {
174                     G.AP[I, J] = G.AN[I, J] + G.AS[I, J] + G.AE[I, J] + G.AW[I,
                            J] + G.APO[I, J] + G.ANN[I, J] + G.ASS[I, J] + G.AEE[I,
                            J] + G.AWW[I, J] - G.SP[I, J];
175                     G.DV[I, J] = G.DV[I, J] / G.AP[I, J];
176                     RESOR = G.AN[I, J] * G.V[I, J + 1] + G.AS[I, J] * G.V[I, J
                            - 1] + G.AE[I, J] * G.V[I + 1, J] + G.AW[I, J] * G.V[I
                            - 1, J] - G.AP[I, J] * G.V[I, J] + G.SU[I, J];
177                     VOL = G.SEW[I] * G.SNS[J];
178                     SORVOL = G.GREAT * VOL;
179                     if (Math.Abs(G.SP[I, J]) > 0.5 * SORVOL)
180                     {
181                         RESOR = RESOR / SORVOL;
```

```
182                     }
183                     G.RESORV = G.RESORV + Math.Abs(RESOR);
184
185                     G.AP[I, J] = G.AP[I, J] / G.URFV;
186                     G.SU[I, J] = G.SU[I, J] + (1.0 - G.URFV) * G.AP[I, J] *
                            G.V[I, J];
187                     G.DV[I, J] = G.DV[I, J] * G.URFV;
188                 }
189             }
190                 // USE THOMAS ALGORITHM FOR PRESSURE EQUATION
191                 for (int N = 1; N <= NSWPV; N++)
192                 {
193                     LISOLV(2, 3, G.V);
194                 }
195         }
```

B.3 Pressure method (p)

```
1     // CALCULATE P
2         static void CALCP(int IPREF, int JPREF, int NSWPP, int ITSTEP)
3         {
4             int NIM1, NJM1;
5             double AREANS, AREAEW, VOL;
6             double CN, CS, CE, CW;
7             double DENN, DENS, DENE, DENW;
8             double SMP;
9             double PPREF;
10            NIM1 = G.NI - 1;
11            NJM1 = G.NJ - 1;
12            G.RESORM = 0.0;
```

```
13              for (int I = 2; I <= NIM1; I++)
14              {
15                  for (int J = 2; J <= NJM1; J++)
16                  {
17                      //COMPUTE AREAS AND VOLUME
18                      AREANS = G.SEW[I];
19                      AREAEW = G.SNS[J];
20                      VOL = G.SEW[I] * G.SNS[J];
21                      // CONVECTION COEFFICIENT
22                      DENN = 0.5 * (G.DEN[I, J + 1] + G.DEN[I, J]);
23                      DENS = 0.5 * (G.DEN[I - 1, J] + G.DEN[I, J]);
24                      DENE = 0.5 * (G.DEN[I, J] + G.DEN[I + 1, J]);
25                      DENW = 0.5 * (G.DEN[I, J] + G.DEN[I - 1, J]);
26                      G.AN[I, J] = DENN * AREANS * G.DV[I, J + 1];
27                      G.AS[I, J] = DENS * AREANS * G.DV[I, J];
28                      G.AE[I, J] = DENE * AREAEW * G.DU[I + 1, J];
29                      G.AW[I, J] = DENW * AREAEW * G.DU[I, J];
30                      CN = DENN * G.V[I, J + 1] * AREANS;
31                      CS = DENS * G.V[I, J] * AREANS;
32                      CE = DENE * G.U[I + 1, J] * AREAEW;
33                      CW = DENW * G.U[I, J] * AREAEW;
34
35                      SMP = CN - CS + CE - CW;
36                      G.SP[I, J] = 0.0;
37                      if (G.STEADY)
38                      {
39                          G.SU[I, J] = -SMP;
40                      }
41                      else
42                      {
```

```
43                      G.SU[I, J] = -SMP + (G.DENO[I, J] - G.DEN[I, J]) * VOL
                            / G.DT[ITSTEP];
44                  }
45              }
46          }
47          for (int I = 2; I <= NIM1; I++)
48          {
49              for (int J = 2; J <= NJM1; J++)
50              {
51                  G.AP[I, J] = G.AN[I, J] + G.AS[I, J] + G.AE[I, J] + G.AW[I,
                        J] - G.SP[I, J];
52                  G.RESORM = G.RESORM + Math.Abs(G.SU[I, J]); // campute sum
                        of absolute mass sources
53
54              }
55          }
56          // USE THOMAS ALGORITHM FOR PRESSURE EQUATION
57          for (int N = 1; N <= NSWPP; N++)
58          {
59              LISOLV(2, 2, G.PP);
60
61          }
62          for (int I = 2; I <= NIM1; I++)
63          {
64              for (int J = 2; J <= NJM1; J++)
65              {
66                  if (I != 2)
67                  {
68                      G.DU[I, J] = G.DU[I, J] * (G.PP[I - 1, J] - G.PP[I, J]);
69                      G.U[I, J] = G.U[I, J] + G.DU[I, J];
70                  }
```

```
71                  if (J != 2)
72                  {
73                      G.DV[I, J] = G.DV[I, J] * (G.PP[I, J - 1] - G.PP[I, J]);
74                      G.V[I, J] = G.V[I, J] + G.DV[I, J];
75                  }
76              }
77          }
78          if (IPREF > 0.0 && JPREF > 0.0)
79          {
80              PPREF = G.PP[IPREF, JPREF];
81              for (int I = 2; I <= NIM1; I++)
82              {
83                  for (int J = 2; J <= NJM1; J++)
84                  {
85                      G.P[I, J] = G.P[I, J] + G.URFP * (G.PP[I, J] - PPREF);
86                      G.PP[I, J] = 0.0;
87                  }
88              }
89          }
90          else
91          {
92              for (int I = 2; I <= NIM1; I++)
93              {
94                  for (int J = 2; J <= NJM1; J++)
95                  {
96                      G.P[I, J] = G.P[I, J] + G.URFP * (G.PP[I, J]);
97                      G.PP[I, J] = 0.0;
98                  }
99              }
100         }
101     }
```

B.4 Temperature method (θ)

```
// CALCULATE T
    static void CALCT(double R2, double NSWPT, int ITSTEP)
    {
        int NIM1, NJM1;
        double AREANS, AREAEW, VOL;
        double CN, CS, CE, CW;
        double GN, GS, GE, GW;
        double DN, DS, DE, DW;
        double SMP, CP, CPO;
        double GAMN, GAMS, GAME, GAMW;
        double RESOR, SORVOL;
        NIM1 = G.NI - 1;
        NJM1 = G.NJ - 1;
        for (int I = 2; I <= NIM1; I++)
        {
            for (int J = 2; J <= NJM1; J++)
            {
                //COMPUTE AREAS AND VOLUME
                AREANS = G.SEW[I];
                AREAEW = G.SNS[J];
                VOL = G.SEW[I] * G.SNS[J];
                // CONVECTION COEFFICIENT
                GN = 0.5 * (G.DEN[I, J + 1] + G.DEN[I, J]) * G.V[I, J + 1];
                GS = 0.5 * (G.DEN[I, J - 1] + G.DEN[I, J]) * G.V[I, J];
                GE = 0.5 * (G.DEN[I + 1, J] + G.DEN[I, J]) * G.U[I + 1, J];
                GW = 0.5 * (G.DEN[I - 1, J] + G.DEN[I, J]) * G.U[I, J];
                CN = (GN * AREANS);
                CS = (GS * AREANS);
                CE = (GE * AREAEW);
```

```
30                  CW = (GW * AREAEW) ;
31                  GAMN = 0.5 * (G.GAMH[I, J] + G.GAMH[I, J + 1]);
32                  GAMS = 0.5 * (G.GAMH[I, J] + G.GAMH[I, J - 1]);
33                  GAME = 0.5 * (G.GAMH[I, J] + G.GAMH[I + 1, J]);
34                  GAMW = 0.5 * (G.GAMH[I, J] + G.GAMH[I - 1, J]);
35                  DN =  GAMN * AREANS / G.DYNP[J];
36                  DS =  GAMS * AREANS / G.DYPS[J];
37                  DE =  GAME * AREAEW / G.DXEP[I];
38                  DW =  GAMW * AREAEW / G.DXPW[I];
39                  // SOURCE TERMS
40                  SMP = CN - CS + CE - CW;
41                  CP = Math.Max(0.0, SMP);
42                  CPO = CP;
43                  // ASSEMBLE
44                  //HYBRID
45                  if (G.INHY)
46                  {
47                      G.AN[I, J] = DN * Math.Max(0.0, 1 - 0.5 * Math.Abs(CN /
                            DN)) + Math.Max(-CN, 0.0);
48                      G.AS[I, J] = DS * Math.Max(0.0, 1 - 0.5 * Math.Abs(CS /
                            DS)) + Math.Max(CS, 0.0);
49                      G.AE[I, J] = DE * Math.Max(0.0, 1 - 0.5 * Math.Abs(CE /
                            DE)) + Math.Max(-CE, 0.0);
50                      G.AW[I, J] = DW * Math.Max(0.0, 1 - 0.5 * Math.Abs(CW /
                            DW)) + Math.Max(CW, 0.0);
51                  }
52                  // CENTRAL
53                  if (G.INCEN)
54                  {
55                      G.AN[I, J] = Math.Max(-CN, 0.0) + DN - 0.5 *
                            Math.Abs(CN);
```

```
56                      G.AS[I, J] = Math.Max(CS, 0.0) + DS - 0.5 *
                            Math.Abs(CS);
57                      G.AE[I, J] = Math.Max(-CE, 0.0) + DE - 0.5 *
                            Math.Abs(CE);
58                      G.AW[I, J] = Math.Max(CW, 0.0) + DW - 0.5 *
                            Math.Abs(CW);
59                  }
60                  // QUICK
61                  if (G.INQUK)
62                  {
63                      // FOR BOUNDARYS HYBRID SCHEME AND FOR THE REST OF
                            DOMAIN QUICK SCHEME
64                      if (I <= 5 || J <= 4 || I <= NIM1 - 2 || J <= NIM1 - 2)
65                      {
66                          G.AN[I, J] = Math.Max(-CN, 0.0) + DN - 0.5 *
                                Math.Abs(CN);
67                          G.AS[I, J] = Math.Max(CS, 0.0) + DS - 0.5 *
                                Math.Abs(CS);
68                          G.AE[I, J] = Math.Max(-CE, 0.0) + DE - 0.5 *
                                Math.Abs(CE);
69                          G.AW[I, J] = Math.Max(CW, 0.0) + DW - 0.5 *
                                Math.Abs(CW);
70                          G.AWW[I, J] = G.AEE[I, J] = G.ASS[I, J] = G.ANN[I,
                                J] = 0.0;
71                      }
72                      else
73                      {
74                          if (CE > 0 && CW > 0)
75                          {
76                              G.AE[I, J] = DE - CE * (0.5 - (G.DXPWU[I] / (8 *
                                    G.DXPW[I])));
```

```
77                      G.AW[I, J] = DW + CW * (0.5 + (G.DXPWU[I - 1] /
                            (8 * G.DXPW[I - 1])) + (G.DXPWU[I - 1] *
                            G.DXPWU[I - 1] / (8 * G.DXPW[I - 1] *
                            G.DXPWU[I - 2]))) + CE * ((G.DXPWU[I] *
                            G.DXPWU[I] / (8 * G.DXPW[I] * G.DXPWU[I -
                            1])));
78                      G.AWW[I, J] = -CW * (G.DXPWU[I - 1] * G.DXPWU[I
                            - 1] / (8 * G.DXPW[I - 1] * G.DXPWU[I - 2]));
79                  }
80                  else
81                  {
82                      G.AE[I, J] = DE - CE * (0.5 + (G.DXPWU[I] / (8 *
                            G.DXPW[I + 1])) + (G.DXPWU[I] * G.DXPWU[I] /
                            (8 * G.DXPW[I + 1]) * G.DXPWU[I + 1]));
83                      G.AW[I, J] = DW + CW * (0.5 - (G.DXPWU[I - 1] /
                            (8 * G.DXPW[I])));
84                      G.AEE[I, J] = (G.DXPWU[I] * G.DXPWU[I] / (8 *
                            G.DXPW[I + 1]) * G.DXPWU[I + 1]);
85                  }
86                  if (CN > 0 && CS > 0)
87                  {
88                      G.AN[I, J] = DN - CN * (0.5 - (G.DYPSV[J] / (8 *
                            G.DYPS[J])));
89                      G.AS[I, J] = DS + CS * (0.5 + (G.DYPSV[J - 1] /
                            (8 * G.DYPS[J - 1])) + (G.DYPSV[J - 1] *
                            G.DYPSV[J - 1] / (8 * G.DYPS[I - 1] *
                            G.DYPSV[J - 2]))) + CN * ((G.DYPSV[J] *
                            G.DYPSV[J] / (8 * G.DYPS[J] * G.DYPSV[J -
                            1])));
90                      G.ASS[I, J] = -CS * (G.DYPSV[J - 1] * G.DYPSV[J
                            - 1] / (8 * G.DYPS[J - 1] * G.DYPSV[J - 2]));
```

```
91                          }
92                          else
93                          {
94                              G.AN[I, J] = DN - CN * (0.5 + (G.DYPSV[J] / (8 *
                                    G.DYPS[J + 1])) + (G.DYPSV[J] * G.DYPSV[J] /
                                    (8 * G.DYPS[J + 1]) * G.DYPSV[J + 1]));
95                              G.AS[I, J] = DS + CS * (0.5 - (G.DYPSV[J - 1] /
                                    (8 * G.DYPS[J])));
96                              G.ANN[I, J] = (G.DYPSV[I] * G.DYPSV[J] / (8 *
                                    G.DYPS[J + 1]) * G.DYPSV[J + 1]);
97                          }
98                      }
99                  }
100                 if (G.STEADY)
101                 {
102                     G.APO[I, J] = 0.0;
103                 }
104                 else
105                 {
106                     G.APO[I, J] = G.DEN[I, J] * VOL / G.DT[ITSTEP];
107                 }
108                 G.SU[I, J] = CPO * G.T[I, J] + 1.5 * (G.APO[I, J] * G.TO[I,
                        J]) - 0.5 * (G.APO[I, J] * G.TOO[I, J]) + G.ANN[I, J] *
                        G.T[I, J + 2] + G.ASS[I, J] * G.T[I, J - 2] + G.AWW[I,
                        J] * G.T[I - 2, J] + G.AEE[I, J] * G.T[I + 2, J];
109                 G.SP[I, J] = -CP;
110             }
111         }
112         // MODIFICATION T
113         //TOP WALL
114         for (int I = 2; I <= NIM1; I++)
```

```
115             {
116                 G.T[I, G.NJ] = G.T[I, NJM1];
117                 G.AN[I, NJM1] = 0.0;
118             }
119             // WEST WALL
120             for (int J = 2; J <= NJM1; J++)
121             {
122                 G.T[1, J] = 1.0;
123             }
124             //BOTTOM WALL
125             for (int I = 2; I <= NIM1; I++)
126             {
127                 G.T[I, 1] = G.T[I, 2];
128                 G.AS[I, 2] = 0.0;
129             }
130             //EAST WALL
131             for (int J = 2; J <= NJM1; J++)
132             {
133                 G.T[G.NI, J] = 0.0;
134             }
135             // RESIDUAL
136             G.RESORT = 0.0;
137             for (int I = 2; I <= NIM1; I++)
138             {
139                 for (int J = 2; J <= NJM1; J++)
140                 {
141                     G.AP[I, J] = G.AN[I, J] + G.AS[I, J] + G.AE[I, J] + G.AW[I,
                            J] + G.APO[I, J] + G.ANN[I, J] + G.ASS[I, J] + G.AEE[I,
                            J] + G.AWW[I, J] - G.SP[I, J];
142                     RESOR = G.AN[I, J] * G.T[I, J + 1] + G.AS[I, J] * G.T[I, J
                            - 1] + G.AE[I, J] * G.T[I + 1, J] + G.AW[I, J] * G.T[I
```

```
                        - 1, J] - G.AP[I, J] * G.T[I, J] + G.SU[I, J];
143                 VOL = G.SEW[I] * G.SNS[J];
144                 SORVOL = G.GREAT * VOL;
145                 if (Math.Abs(G.SP[I, J]) > 0.5 * SORVOL)
146                 {
147                     RESOR = RESOR / SORVOL;
148                 }
149                 G.RESORT = G.RESORT + Math.Abs(RESOR);
150                 G.AP[I, J] = G.AP[I, J] / G.URFT;
151                 G.SU[I, J] = G.SU[I, J] + (1.0 - G.URFT) * G.AP[I, J] *
                        G.T[I, J];
152             }
153         }
154         for (int N = 1; N <= NSWPT; N++)
155         {
156             LISOLV(2, 2, G.T);
157         }
158     }
```

Appendix C

TDMA method

```
1   static  void LISOLV(int ISTART, int JSTART, double[,] PHI)
2         {
3             int NIM1, NJM1;
4             double[] A = new double[G.IT];
5             double[] B = new double[G.IT];
6             double[] C = new double[G.IT];
7             double[] D = new double[G.IT];
8             double TERM;
9             NIM1 = G.NI - 1;
10            NJM1 = G.NJ - 1;
11            int JSTM1 = JSTART - 1;
12            int ISTM1 = ISTART - 1;
13            A[JSTM1] = 0.0;
14            // W-E SWEEP
15            for (int I = ISTART; I <= NIM1; I++)
16            {
17                C[JSTM1] = PHI[I, JSTM1];
18                // S-N TRAVERSE
19                for (int J = JSTART; J <= NJM1; J++)
20                {
```

```
21                  A[J] = G.AN[I, J];
22                  B[J] = G.AS[I, J];
23                  C[J] = G.AE[I, J] * PHI[I + 1, J] + G.AW[I, J] * PHI[I - 1,
                        J] + G.SU[I, J];
24                  D[J] = G.AP[I, J];
25                  TERM = 1.0 / (D[J] - B[J] * A[J - 1]);
26                  A[J] = A[J] * TERM;
27                  C[J] = (C[J] + B[J] * C[J - 1]) * TERM;
28              }
29              // NEW PHI
30              for (int JJ = JSTART; JJ <= NJM1; JJ++)
31              {
32                  int J = G.NJ + JSTM1 - JJ;
33                  PHI[I, J] = A[J] * PHI[I, J + 1] + C[J];
34              }
35          }
36          A[ISTM1] = 0.0;
37          // S-N SWEEP
38          for (int J = JSTART; J <= NJM1; J++)
39          {
40              C[ISTM1] = PHI[ISTM1, J];
41              // W-E TRAVERSE
42              for (int I = ISTART; I <= NIM1; I++)
43              {
44                  A[I] = G.AE[I, J];
45                  B[I] = G.AW[I, J];
46                  C[I] = G.AN[I, J] * PHI[I, J + 1] + G.AS[I, J] * PHI[I, J -
                        1] + G.SU[I, J];
47                  D[I] = G.AP[I, J];
48                  TERM = 1.0 / (D[I] - B[I] * A[I - 1]);
49                  A[I] = A[I] * TERM;
```

```
50                  C[I] = (C[I] + B[I] * C[I - 1]) * TERM;
51              }
52              // NEW PHI
53              for (int II = ISTART; II <= NIM1; II++)
54              {
55                  int I = G.NI + ISTM1 - II;
56                  PHI[I, J] = A[I] * PHI[I + 1, J] + C[I];
57              }
58          }
59      }
```